# Surface Rupture Morphology and Paleoseismology of the Western Hope Fault and Characteristics of Coseismically-Displaced Boulders in the Port Hills, South Island, New Zealand

---

A thesis submitted in fulfillment of the requirements for the degree of

Doctor of Philosophy in Geology in the University of Canterbury

By

**Narges Khajavi**

September 2015

---

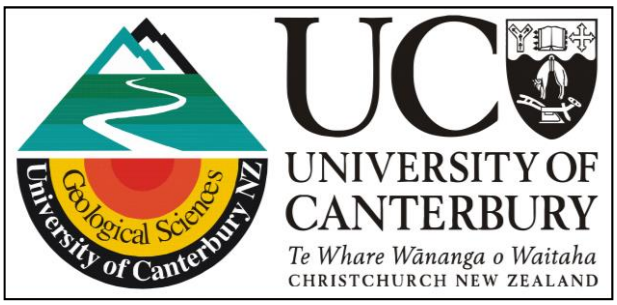

For my husband

**Amir**

And my parents

**Abdolhossein and Parvaneh**

I couldn’t have done this without your support

And for my little baby

**Daniel**

I have done this because your presence inspired me

# FRONTISPIECE

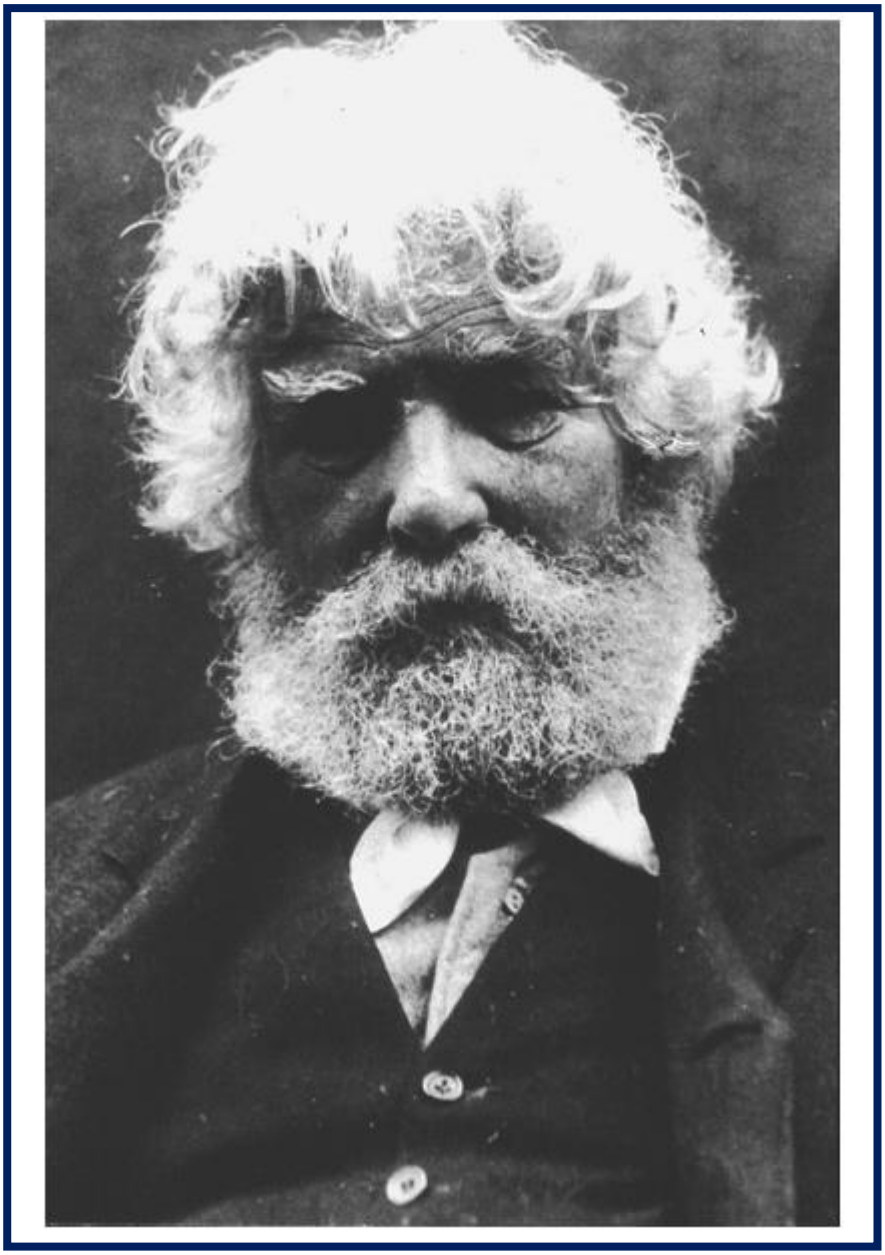

Alexander McKay (1841-1917), an assistant government geologist (1885-1892) in New Zealand. He was the first geologist who started investigations on the 1888 North Canterbury (Amuri) earthquake on the Hope Fault. Photo: Published by Rodney Grapes (2006).

# FRONTISPIECE

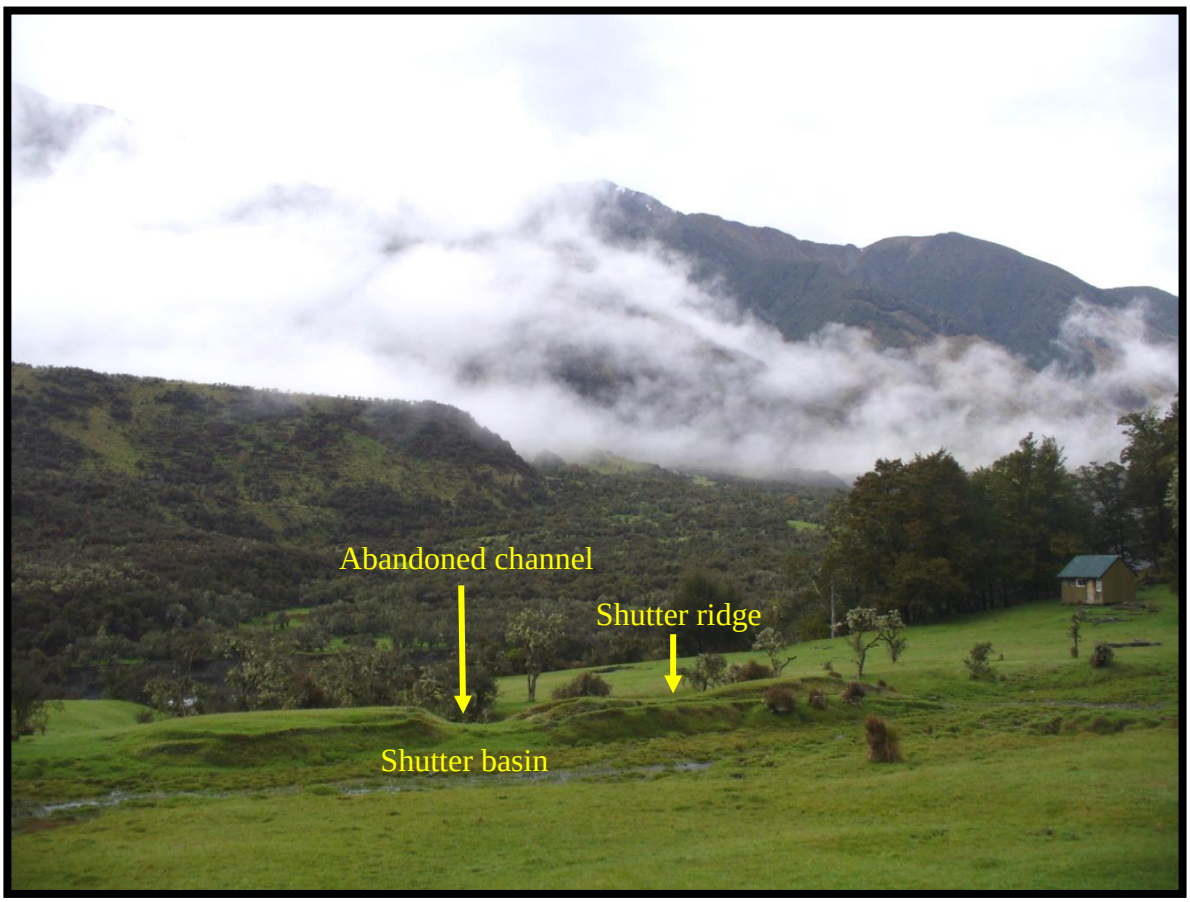


Field photograph looking southwest showing the Hope Fault shutter ridge and basin in the Hope Valley.

# FRONTISPIECE

Field photograph after the September 4th, 2010 Darfield (Canterbury) earthquake showing a coseismically-displaced boulder in the Hoon Hay Scenic Reserve, Port Hills. Note the gap between the displaced boulder and its host soil socket.

# ABSTRACT

Documenting earthquake-induced ground deformation is significant to assess the characteristics of past and contemporary earthquakes and provide insight into seismic hazard. This study uses airborne light detection and ranging (LiDAR) and conducts multi-disciplinary field techniques to document the surface rupture morphology and evaluate the paleoseismicity and seismic hazard parameters of the Hurunui segment of the Hope Fault in the northern South Island of New Zealand. It also documents and evaluates seismically induced features and ground motion characteristics of the 2010 Darfield and 2011 Christchurch earthquakes in the Port Hills, south of Christchurch. These two studies are linked in that they investigate the near-field coseismic features of large ($M_w$ ~7.1) earthquakes in New Zealand and produce data for evaluating seismic hazards of future earthquakes.

In the northern South Island of New Zealand, the Australian-Pacific plate boundary is characterised by strike-slip deformation across the Marlborough Fault System (MFS). The ENE-striking Hope Fault (length: ~230 km) is the youngest and southernmost fault in the MFS, and the second fastest slipping fault in New Zealand. The Hope Fault is a major source of seismic hazard in New Zealand and has ruptured (in-part) historically in the $M_w$ 7.1 1888 Amuri earthquake. In the west, the Hurunui segment of the Hope Fault is covered by beech forest. Hence, its seismic hazard parameters and paleoearthquake chronology were poorly constrained and it was unknown whether the 1888 earthquake ruptured this segment or not and if so, to what extent.

Utilising LiDAR and field data, a 29 km-long section of the Hurunui segment of the Hope Fault is mapped. LiDAR-mapping clearly reveals the principal slip zone (PSZ) of the fault and a suite of previously unrecognised structures that form the fault deformation zone (FDZ). FDZ width measurements from 415 locations reveal a spatially-variable, active FDZ up to ~500 m wide with an average width of 200 m. Kinematic analysis of the fault structures shows that the Hurunui segment strikes between 070° and 075° and is optimally oriented for dextral strike-slip within the regional stress field. This implies that the wide FDZ observed is unlikely to result from large-scale fault mis-orientation with respect to regional stresses. The analysis of FDZ width indicates that it increases with increased hanging wall topography and increased topographic relief suggesting that along-strike topographic perturbations to fault geometry and stress states increase fault zone complexity and width. FDZ width also

increases where the tips of adjacent PSZ strands locally vary in strike, and where the thickness of alluvial deposits overlying bedrock increases.

LiDAR- and photogrammetrically-derived topographic mapping indicates that the boundary between the Hurunui and Hope River segments is characterised by a ~850-m-wide right stepover and a 9º-14° fault bend. Paleoseismic trenching at Hope Shelter site reveals that 6 earthquakes occurred at A.D. 1888, 1740-1840, 1479-1623, 819-1092, 439-551, and 373-419. These rupture events have a mean recurrence interval of ~298 ± 88 yr and inter-event times ranging from 98 to 595 yrs. The variation in the inter-event times is explained by (1) coalescing rupture overlap from the adjacent Hope River segment on to the Hurunui segment at the study site, (2) temporal clustering of large earthquakes on the Hurunui segment, and/or (3) 'missing' rupture events. It appears that the first two options are more plausible to explain the earthquake chronologies and rupture behaviour on the Hurunui segment, given the detailed nature of the geologic and chronologic investigations. This study provides first evidence for coseismic multi-segment ruptures on the Hope Fault by identifying a rupture length of 44-70 km for the 1888 earthquake, which was not confined to the Hope River segment (primary source for the 1888 earthquake).

LiDAR data is also used to identify and measure dextral displacements and scarp heights from the PSZ and structures within the FDZ along the Hurunui segment. Reconstruction of large dextrally-offset geomorphic features shows that the vertical component of slip accounts for only ~1% of the horizontal displacements and confirms that the fault is predominantly strike-slip. A strong correlation exists between the dextral displacements and elevations of geomorphic features suggesting the possibility of age correlation between the geomorphic features. A mean single event displacement (SED) of 3.6 ± 0.7 m is determined from interpretation of sets of dextral displacements of ≤ 25 m. Using the available surface age data and the cumulative dextral displacements from Matagouri Flat, McKenzie Fan, Macs Knob and Hope River sites, and the mean SED, a mean slip rate of 12.2 ± 2.4 mm/yr, and a mean recurrence interval of ~320 ± 120 yr, and a potential earthquake magnitude of $M_w$ 7.2 are determined for the Hurunui segment. This study suggests that the fault slip rate has been constant over the last ~15000 yr.

Strong ground motions from the 2010 Darfield (Canterbury) earthquake displaced boulders and caused ground damage on some ridge crests in the Port Hills. However, the 2011 Christchurch earthquake neither displaced boulders nor caused ground damage at the same ridge crests. Documentation of locations (~400 m a.s.l.), lateral displacements (8-970

cm), displacement direction (250° ± 20°) of displaced boulders, in addition to their hosting socket geometries (< 1 cm to 50 cm depth), the orientation of the ridges (000°-015°) indicate that boulders have been displaced in the direction of instrumentally recorded transient peak ground horizontal displacements nearby and that the seismic waves have been amplified at the study sites. The co-existence of displaced and non-displaced boulders at proximal sites suggests small-scale ground motion variability and/or varying boulder-ground dynamic interactions relating to shallow phenomena such as variability in soil depth, bedrock fracture density and/or microtopography on the bedrock-soil interface. Shorter shaking duration of the 2011 Christchurch event, differing frequency contents and different source characteristics were all factors that may have contributed to generating circumstances less favourable to boulder displacement in this earthquake. Investigating seismically induced features, fault behaviour, site effects on the rupture behaviour, and site response to the seismic waves provides insights into fault rupture hazards.

# CONTENTS

Frontispiece ..... II

Frontispiece ..... III

Frontispiece ..... IV

Abstract ..... V

Contents ..... VIII

List of Figures ..... XVI

List of Tables ..... XIX

Acknowledgments ..... XX

List of publications ..... XXII

Co-authorship forms ..... XXV

Thesis Prologue ..... 1

1.1 Scientific context ..... 1

1.2 Thesis structure ..... 6

1.3 Scientific contributions arising from this PhD and related work ..... 10

1.4 Originality ..... 10

Part one: The Hope Fault ..... 11

CHAPTER 1. Influence of topography and basement depth on surface rupture morphology revealed from LiDAR and field mapping, Hope Fault, New Zeland ..... 12

1.1 Abstract ..... 13

1.2 Introduction ..... 14

1.3 Tectonic and geologic setting ..... 16

1.4 LiDAR data ..... 21

1.5 Methodology ..... 22

1.5.1 Geomorphic mapping ..... 22

1.5.2 Fault mapping and classification ..... 22

1.5.3 Relationship between fault orientation, kinematics, and FDZ width ..... 25
1.5.4 Relationship between topography and FDZ width ..... 26
1.5.5 Structure contours of PSZ strand to constraint near-surface fault dip ..... 28
1.5.6 Relationship between depth-to-basement and FDZ width ..... 28
1.6 Results ..... 29
1.6.1 Fault length and orientations ..... 30
1.6.2 FDZ width and asymmetry ..... 35
1.6.3 Relationship between FDZ and PSZ orientation ..... 35
1.6.4 Relationship between FDZ width and topography ..... 36
1.6.5 PSZ subsurface geometry and segmentation ..... 37
1.6.6 Relationship between FDZ width and sediment thickness ..... 38
1.7 Discussion and complications ..... 38
1.7.1 Relationship of fault orientations and kinematics with respect to local and regional stress fields ..... 41
1.7.2 Sackungen origin for secondary faults? ..... 45
1.7.3 Topographic influence on near surface fault geometry and surface rupture morphology ..... 46
1.7.4 Depth-to-bedrock influence on surface rupture morphology ..... 49
1.7.5 Fault maturity, FDZ width, slip measurements, and paleoseismic implications ..... 50
1.8 Conclusions ..... 51
CHAPTER 2. Late Holocene rupture behavour and earthquake chronology on the Hope Fault, New Zealand ..... 53
2.1 Abstract ..... 54
2.2 Introduction ..... 55
2.3 Tectonic setting and background ..... 58
2.3.1 The Hope Fault and Marlborough Fault System ..... 58

2.3.2 The 1888 Amuri earthquake: background and reassessment of McKay's observations ..... 60
2.3.3 Paleoseismicity of the Hope Fault ..... 62
2.3.4 Geomorphology of the Mid-Hope Valley and the Hope Fault ..... 63
2.4 Methodology ..... 64
2.4.1 Background, fault mapping and site selection ..... 64
2.4.2 Dating techniques ..... 65
2.4.3 Oxcal modelling of radiocarbon ages ..... 68
2.5 Results ..... 68
2.5.1 Geomorphic Descriptions of the Hope Shelter Site ..... 68
2.5.2 Structural description of the Hope Shelter site ..... 69
2.5.3 Slip Measurement at the Hope Shelter Site ..... 69
2.5.4 Hope Shelter trenches ..... 70
2.5.4.1 Trench 1 ..... 70
2.5.4.1.1 Trench 1-Stratigraphy ..... 70
2.5.4.1.2 Trench 1-Faulting ..... 74
2.5.4.2 Trench 2 ..... 76
2.5.4.2.1 Trench 2-Stratigraphy ..... 76
2.5.4.2.2 Trench 2-Faulting ..... 78
2.5.5 Age of surface features ..... 80
2.5.5.1 Age of the Holocene terrace and fan at the Hope Shelter site 80
2.5.5.2 Age of the debris deposit at the Hope Shelter site ..... 82
2.5.5.3 Age of the surfaces near Parakeet Stream ..... 85
2.5.5.4 OxCal modeling of radiocarbon ages ..... 86
2.6 Discussion ..... 89
2.6.1 Paleoearthquakes on the Hurunui segment ..... 89
2.6.2 Most recent faulting event: the 1888 Amuri earthquake ..... 93

2.6.3 Relationship between surface and subsurface data and slip rate estimation 95

2.6.4 Periodic versus Episodic Earthquake Recurrence ..... 95

2.6.5 Rupture segmentation: evidence for a geometric barrier between the two segments? ..... 98

2.7 Conclusions ..... 99

CHAPTER 3. Post-last glacial slip rate along the western Hope Fault, South Island, New Zealand ..... 101

3.1 Abstract ..... 102

3.2 Introduction ..... 103

3.3 Review of the Hope Fault slip rates and regional offsets ..... 106

3.4 Methodology ..... 108

3.4.1 Geomorphic features and measuring displacements ..... 108

3.4.2 Horizontal versus vertical displacements ..... 110

3.4.3 Radiocarbon data ..... 113

3.5 Results ..... 114

3.5.1 Location and characteristics of the displacements measured along the Hurunui segment ..... 114

3.5.2 Vertical displacements of the fault at Macs Knob and Parakeet Stream sites ..... 115

3.5.3 Relationship between elevation and dextral displacements of the geomorphic features ..... 120

3.5.4 Distribution of dextral displacements and available surface ages ..... 122

3.5.5 Estimates of slip rate ..... 122

3.5.6 Estimate of single event displacement and recurrence interval ..... 126

3.6 Discussion ..... 132

3.6.1 Slip rate of the Hurunui segment ..... 132

3.6.2 Single event displacement and recurrence interval of the Hurunui segment ..... 133

3.6.3 Spatiotemporal variation in the Hope Fault slip rate ..... 136

3.6.4 Earthquake magnitude, fault segmentation and slip model ..... 137

3.7 Conclusion ..... 138

Part two: The coseismically- displaced boulders in the port hills ..... 140

CHAPTER 4. Seismically induced boulder displacements in the Port Hills, New Zealand during the 2010 Darfield (Canterbury) earthquake ..... 141

4.1 Abstract ..... 142

4.2 Introduction ..... 143

4.3 Boulder displacement in the Darfield earthquake ..... 144

4.3.1 Methodology ..... 144

4.3.2 Field observations ..... 146

4.3.3 Analysis of displacement data ..... 148

4.4 Possible role of topographic amplification ..... 149

4.4.1 Methodology ..... 149

4.4.2 Results and interpretation ..... 151

4.5 Concluding discussion ..... 151

CHAPTER 5. Conclusions ..... 154

5.1 Introduction ..... 155

5.2 Key findings ..... 155

5.2.1 How accurate are the fault structures and geomorphic features mapped along the Hurunui segment using LiDAR data? ..... 156

5.2.2 How wide is the deformation zone? ..... 157

5.2.3 What are the structures within the fault deformation zone and how are their kinematics interpreted in the context of the regional stress field? ..... 157

5.2.4 Why has the mature Hope Fault developed a wide deformation zone instead of a simple thoroughgoing structure? What factors affect the spatial distribution of the fault deformation zone? ..... 158

5.2.5 Are valuable sites to conduct further paleoseismic studies identified on the western Hope Fault using LiDAR data? ..... 160

5.2.6 What is the structural configuration of the fault at the proposed segment boundary area? ..... 160

5.2.7 Did the 1888 earthquake rupture through the segment boundary? ..... 161

5.2.8 Can the segment-to-segment rupture scenarios be resolved to provide a Holocene rupture behaviour of the western Hope Fault? ..... 162

5.2.9 How faulted geomorphic features, their displacements and surface age can be compared along the entire Hurunui segment? ..... 164

5.2.10 What are the seismic hazard parameters of the fault? ..... 166

5.2.11 Are geomorphic, geodetic and paleoseismic slip rates consistent? ..... 166

5.2.12 Is there along-strike spatiotemporal variation in the slip rate? How the slip rate varies from segment-to-segment? ..... 167

5.2.13 How estimates of seismic hazard parameters are improved by integrating field and LiDAR data? ..... 168

5.2.14 What characteristics should be mapped and what is the relationship between those? ..... 169

5.2.15 What is the relation between coseismic displacement of boulders, the transient peak ground horizontal displacement recorded at the nearby stations, and the permanent post-seismic horizontal ground displacement? ..... 170

5.2.16 Did topography influence the boulder displacement? ..... 171

5.2.17 Suggestions for future work ..... 173

References ..... 174

Appendixes ..... 193

Appendix to Chapter 2: Late Holocene rupture behaviour and earthquake chronology on the Hope Fault, New Zealand ..... 194

Appendix 2.1: Key observations of Mckay (1890) and Jones (1933) regarding the 1888 North Canterbury (Amuri) earthquake ..... 195

Appendix 2.2: Trench unit descriptions ..... 199

Appendix 2.3: Details of OxCal Modelling....200

Appendix to Chapter 3: Post-last glacial slip rate along the western Hope Fault, South Island, New Zealand....202

Appendix 3.1: Measured Displacements along the fault....203

Supplements....220

Supplement to Chapter 1: Influence of topography and basement depth on surface rupture morphology revealed from LiDAR and field mapping, Hope Fault, New Zealand....221

S1.1 Supplementary figures....222

S1.2 Relationship between fault scarps and kinematics....223

S1.3 A comparison of secondary structures associated with faults....224

S1.3.1 Secondary structures associated with the Alpine Fault....224

S1.3.2 Secondary structures associated with the Conway segment of the Hope Fault....224

S1.4 Detailed site investigations....225

S1.4.1 McKenzie Fan....225

S1.4.2 Boundary Stream....226

S1.5 References....228

Supplement to Chapter 2: Late Holocene rupture behaviour and earthquake chronology on the Hope Fault, New Zealand....229

S2.1 Supplementary data: beech seeds in peat sample....230

S2.2 Supplementary data: Matagouri bush....231

S2.3 Supplementary data: pit logs....231

S2.3.1 Pit 1 (branch trench)....231

S2.3.2 Pit 3....233

S2.3.3 Pit 4....234

S2.4 Supplementary data: Schmidt hammering....234

S2.4.1 Schmidt hammer....234

S2.4.2 Methodology ..... 234

S2.4.3 References ..... 237

S2.5 Supplementary data: fault bend ..... 238

S2.6 Supplementary data: Parakeet Stream site ..... 240

S2.6.1 Fallen boulder due to the coseismic shaking associated with the 1888 event? ..... 242

S2.6.2 References ..... 242

S2.7 Supplementary data: calculating the mean recurrence interval time for the preferred earthquakes timings ..... 243

S2.7.1 References ..... 244

Supplement to Chapter 4: Seismically induced boulder displacement in the Port Hills, New Zealand during the 2010 Darfield (Canterbury) earthquake ..... 245

S4.1 Supplementary tables ..... 246

S4.2 Supplementary methodology used in the 2D FLAC modelling ..... 249

S4.2.1 References ..... 249

S4.3 Complete results of topographic amplification models ..... 251

S4.4 Selected pictures of broken and displaced boulders and rockfalls in the Port Hills ..... 252

# LIST OF FIGURES

Figure 1.1. Geological setting of New Zealand ..... 17

Figure 1.2. Geomorphic location of the LiDAR strip. ..... 20

Figure 1.3. Recorded structures associated with strike-slip systems are compared with structures associated with the dextral strike-slip Hurunui segment of the Hope Fault. ..... 23

Figure 1.4. Rose diagrams showing the significant azimuthal distribution of the PSZ and inferred PSZ strands ..... 25

Figure 1.5. Width of the FDZ with respect to the PSZ, strike of the PSZ strands, and the range of significant azimuthal distribution of the PSZ (right axis) are shown along the fault ..... 26

Figure 1.6. Detailed analysis of the FDZ associated with the Hurunui segment of the Hope Fault. ..... 27

Figure 1.7. Uninterpreted LiDAR strip (~7 km long, from Landslip Stream to McMillan Stream) and structural geomorphic map of the two key sites.. ..... 31

Figure 1.8. Uninterpreted LiDAR strip (~7 km long, from McMillan Stream to Three Mile Stream) and structural geomorphic map of the two key sites.. ..... 32

Figure 1.9. Uninterpreted LiDAR strip (~7 km long, from Three Mile Stream to Lodge Stream) and structural geomorphic map of the two key sites. ..... 33

Figure 1.10. Uninterpreted LiDAR strip (it is ~8 km long, from Lodge Stream to the eastern extent of the LiDAR swath) and structural geomorphic map of the key site.. ..... 34

Figure 1.11. Cross-sections AA' to FF' showing fault models at depth. ..... 39

Figure 1.12. Cross-sections GG' to LL' showing fault models at depth. ..... 40

Figure 1.13. Impact of average depth of the cover deposits beneath the FDZ on the FDZ width and fault density within the FDZ. ..... 41

Figure 1.14. 3-D models of small portions of the LiDAR swath showing fault branching depths where the fault cuts flanks of mountains. ..... 50

Figure 2.1. Geological setting of New Zealand ..... 57

Figure 2.2. Observations of McKay (1890) has been mapped. ..... 59

Figure 2.3. Structural map of the western Hope Fault including the overlapping area of the two segments are presented. ..... 61

Figure 2.4. Details of the Hope Shelter site are presented. ..... 66

Figure 2.5. Trench T-1 and Trench T-2 pictures (A-B) and photo-logs (C-F). ..... 67

Figure 2.6. The full log of Trench T-1. ..... 71

Figure 2.7. Simplified stratigraphy and age of the units from Hope Shelter site trenches.. .... 72

Figure 2.8. The first three meters of Trench T-1 are shown in details. ..... 73

Figure 2.9. Trench T-2 and augur locations are shown.. ..... 79

Figure 2.10. Hope River downcutting curve for the Hope River Valley is presented ..... 82

Figure 2.11. The results of the dendro-chronologic study are shown. ..... 84

Figure 2.12. The results of OxCal modelling (Trench 1- model 1) including dates plots, plots of RI times between each two events, and average RI time are presented. ..... 87

Figure 2.13. The results of OxCal modelling (Trench 1- model 2) including dates plots, plots of RI times between each two events, and average RI time are presented. ..... 88

Figure 2.14. The results of OxCal modelling (Trench 2) including dates plots, plots of RI times between each two events, and average RI time are presented. ..... 89

Figure 2.15. The timing of late Holocene paleoearthquake histories for the Hurunui and Hope River segments of the Hope Fault including the 1888 Amuri earthquake. ..... 91

Figure 3.1. Geological setting of New Zealand ..... 105

Figure 3.2. Macs Knob area (the middle section of the Hurunui segment). ..... 112

Figure 3.3. Parakeet Stream area (the middle section of the Hurunui segment to the east of Macs Knob). ..... 113

Figure 3.4. Continuous structurally-interpreted LiDAR hillshade strips from the western limit of LiDAR swath toward the east. ..... 116

Figure 3.5. Continuous structurally-interpreted LiDAR hillshade strips from east of McKenzie Fan toward the east. ..... 117

Figure 3.6. Continuous structurally-interpreted LiDAR hillshade strips from east of the eastern branch of McMillan Stream toward the east. ..... 118

Figure 3.7. Continuous structurally-interpreted LiDAR hillshade strips from east of the Parakeet Stream toward the eastern end of the LiDAR swath ..... 119

Figure 3.8. Plot of dextral displacements versus elevations of 59 displaced features ..... 121

Figure 3.9. Dextral slip distribution along the PSZ of the Hurunui segment ..... 123

Figure 3.10. Slip rate estimates for the Hurunui segment of the Hope Fault. ..... 129

Figure 3.11. Displacement plot for the Hurunui segment. ..... 130

Figure 3.12. Slip rate estimates from Hurunui and Hope River segments are compared along ~40 km of the western Hope Fault.. ..... 135

Figure 4.1. General view of the Port Hills. ..... 145

Figure 4.2. Displaced boulders at Hoon Hay site.. ..... 145

Figure 4.3. Plots of displacement distance of boulders versus (A), Mass and socket depth and (B), azimuth and slope. ..... 146

Figure 4.4. A comparison of observed and instrumentally recorded displacement directions.. ..... 150

Figure 4.5. Results of topographic amplification modelling along profiles AA' and BB'.. .. 151

Figure 4.6. Seismograms in the frequency domain for Darfield and Christchurch earthquakes at LPCC site. ..... 153

# LIST OF TABLES

Table 1.1. Comparison of deformation zones and slip rates of selected strike-slip faults. . 15

Table 1.2. Characteristics of the deformation zone north and south of the fault.. ..... 35

Table 1.3. Structural and morphological characteristics of the cross-sections..... 42

Table 2.1. Known paleoseismic histories along the segments of the Hope Fault ..... 63

Table 2.2. Radiocarbon dating results from the Hope Shelter trenches. ..... 76

Table 2.3. The results of OSL samples from Trench 1 and Pit 1. ..... 80

Table 2.4. Radiocarbon dating results from the Parakeet Stream site..... 85

Table 2.5. Paleoseismic history of trenches 1 and 2 modelled using OxCal program.. ..... 90

Table 3.1. The most recent paleoseismic data for the Hope Fault. ..... 108

Table 3.2. Criteria to assign quality indices to the dextral displacements. ..... 110

Table 3.3. A summary of the published radiocarbon data by previous studies..... 114

Table 3.4. The number of measured dextral displacements, ..... 120

Table 3.5. Slip rate estimates from different sites along the Hurunui segment..... 127

Table 3.6. Estimates of recurrence intervals from different sites..... 131

Table 4.1. Seismic characteristics of Darfield and Christcurch earthquakes.. ..... 144

Table 4.2. Azimuth measurements in ten places along the Port Hill ridgeline.. ..... 146

# ACKNOWLEDGMENTS

I am greatly thankful to my supervisors Mark Quigley, Robert Langridge, and Jarg Pettinga. Mark and Rob deserve special acknowledgement for their great supervisions and being fantastic source of academic inspiration. Mark was an excellent support through my research challenges and taught me how to be strong and professionally contribute into science. Mark, your high expectations of my work encouraged me to develop my scientific brain and look at scientific questions differently. I thank you for all of that. I am sincerely grateful to Rob, who introduced me to the attractive world of strike-slip faults, patiently taught me advanced field skills, allowed me to develop my ideas, treated me as a friend rather than a student, and engaged me with a group of awesome scientists at GNS Science. Rob, your academic support and enthusiasm for my work and your friendship are greatly appreciated.

I would love to express my deep gratitude to the University of Canterbury, GNS Science, New Zealand Natural Hazard Platform, New Zealand Earthquake Commission, and the Department of Geological Sciences for providing me with a Doctoral scholarship and research funds to do my research and publish my work.

I am grateful to the academic, technical, and retired staff of the Departments of Geological Sciences, Physics and Astronomy, Civil and Forestry at the University of Canterbury. They were friendly, supportive, and welcoming. Jarg Pettinga, Robert Hurst, David Norton, Andy Nicol, Tim Davies, David Bell, Jocelyn Campbell, Brendan Duffy, Brendon Bradley, Pat Roberts, Janet Warburton, John Southward, Anekant Wandres, Stefan Winkler, Kate Pedley, Maree Hemmingsen, Cathy Higgins, Vanessa Tappenden, Sacha Baldwin-Cunningham, Kerry Swanson, Lachlan Kirk, and Vicki Wilton deserve special thanks. I thank great researchers such as Kevin Furlong, Mike Oskin, Chris Smart, and Fidel Martín González who came to the Department of Geological Sciences or to GNS Science as visitors and improved the quality of my work by helping me with modern methods of data analysis, discussing interesting subjects, getting involved with my field work and providing relevant papers from the scientific literature.

I wish to thank the Department of Conservation in New Zealand for providing all the required permits to conduct my research in Lake Sumner Forest Parks. I also would like to thank Kevin Henderson, the owner of the Poplars Station, for site access.

I would like to acknowledge some of my fellow doctoral candidates at the University of Canterbury, Eric Bilderback, Sam McColl, Tim Stahl, Danilo Moretti, Arul Arumugam, Grant Wilson, Jonathan Davidson, with whom I had many academic discussions and developed wonderful friendships.

I would like to express my appreciation to my husband, Amir, who was also my permanent field assistant. Amir believed in me and supported my academic wishes, from Iran to New Zealand, and never gave up; however, this was a challenging journey to go through. A thank you goes also to my little baby, Daniel, who was my inspiration to try to finalise my thesis. To my parents Abdolhossein and Parvaneh: I cannot think of any worthy words which could express the gratitude I have for the love, support, kindness and patience that you have shown me.

# LIST OF PUBLICATIONS

My thesis resulted in a suite of peer-reviewed articles, conference talks, and posters. I am the lead author on all of the peer-reviewed articles from my PhD research and led the field and laboratory work, data collection and analysis, results, discussion, writing of the articles and dealing with the review comments. I contributed to an additional peer-reviewed article led by R. Langridge. My supervisors Dr. Mark Quigley and Dr. Robert Langridge helped me in the field and contributed significantly to reviewing and structuring the manuscripts. Details on the co-author's contribution on the peer-reviewed articles are listed on the "co-authorship forms" section.

## Journal articles from my PhD research

1- **Khajavi, N.,** Langridge R.M., Quigley, M., Smart, C., Rezanejad, A., Martín-González, F., (2015, accepted manuscript by the GSA Bulletin). Late Holocene rupture behaviour and earthquake chronology on the Hope Fault, New Zealand. **(Chapter 2)**

2- **Khajavi, N.,** Quigley, M., Langridge, R.M., (2014). Influence of topography and basement depth on surface rupture morphology revealed from LiDAR and field mapping, Hope fault, New Zealand. Tectonophysics, Vol.630, PP: 265-284. **(Chapter 1)**

3- **Khajavi, N.,** Quigley, M., McColl S.T., Rezanejad, A., (2012). Seismically-induced boulder displacement in the Port Hills, New Zealand during the 2010 Darfield (Canterbury) earthquake, New Zealand Journal of Geology and Geophysics, Vol.55, No.3, PP. 271- 278. **(Chapter 4)**

4- **Khajavi, N.,** Langridge, R., Quigley, M., (intended for submission to Tectonophysics, 2015). Postglacial slip rate along the western Hope Fault, South Island, New Zealand **(Chapter 3)**

## Other journal articles

Langridge, R.M., Ries, W.F., Farrier, T., Barth, N.C., **Khajavi, N.,** De Pascale, G.P., 2014. Developing sub 5-m LiDAR DEMs for forested sections of the Alpine and Hope faults, South Island, New Zealand: Implications for structural interpretations. Journal of Structural Geology 64, 53-66.

## Conferences

1- **Khajavi, N.,** Langridge R.M., Quigley, M., (2015). Late Holocene rupture behaviour and earthquake chronology on the Hope Fault, New Zealand, Geosciences 2015 Conference, Wellington, New Zealand. Geoscience Society of New Zealand Miscellaneous Publication X: P. X. *(Oral Presentation)*

1- **Khajavi, N.,** Quigley, M., Langridge R.M., (2013). Deformation zone of the Hurunui segment of the Hope fault, New Zealand, revealed from LiDAR, Geosciences 2013 Conference, Christchurch, New Zealand. Geoscience Society of New Zealand Miscellaneous Publication 136A: P. 56. *(Oral Presentation)*

2- Langridge, R.M, **Khajavi, N.,** Quigley, M., Almond, P., Duncan, R. (2013). Timing and recurrence of late Holocene earthquakes on the Hope Fault, New Zealand, highlighting insights from LiDAR and paleoseismic studies. San Francisco, CA, USA: American Geophysical Union Fall Meeting (AGU), 3-7 Dec 2013. *(Oral presentation)*

3- **Khajavi, N.,** Langridge, R.M, Quigley, M. (2012). New insights into the rupture history of the Hope fault, New Zealand. San Francisco, CA, USA: American Geophysical Union Fall Meeting (AGU), 3-7 Dec 2012. *(Oral presentation)*

4- **Khajavi, N.,** Quigley, M., McColl S.T., Rezanejad, A., (2012). Coseismic displacement of boulders in the Port Hills, New Zealand during the 2010 Darfield earthquake; implications for field estimates of shaking intensity, Geosciences 2012 Conference, Hamilton, New Zealand. Geoscience Society of New Zealand Miscellaneous Publication 134A: P. 50. *(Oral Presentation)*

5- Langridge, R.M., **Khajavi, N.,** Hemphill-Haley, M.A. Almond, P. Duncan, R. (2012) Paleoseismicity and slip rate of the strike-slip Hope Fault, South Island: A well-segmented and frequent earthquake source in New Zealand. PANAF 2012 Conference, Turkey. *(Oral Presentation)*

6- **Khajavi, N.,** Langridge, R.M, Quigley, M. (2011). Geomorphic and structural mapping of the western Hope fault using LiDAR, Geosciences 2011 Conference, Nelson, New Zealand. Geoscience Society of New Zealand Miscellaneous Publication 130A: P. 60. *(Poster Presentation)*

7- **Khajavi, N.,** Quigley, M. (2011). LiDAR of the western Hope Fault, LiDAR workshop at GNS, New Zealand, on the 28th October 2011. *(Oral Presentation and Report)*

8- **Khajavi, N.,** Quigley, M., Furlong, K., Rezanejad, A., Davies, T. (2011). "Ground-Motion Intensity Inferred From Upthrow of Boulders and Rockfalls during the 2010 Darfield Earthquake, Port Hills, New Zealand", European Geosciences Union General Assembly 2011, Austria, Vienna. *(Oral Presentation)*

9- Stahl, T., Bilderback, E., **Khajavi, N.,** McColl, S., Massey, C., Quigley, M., Nobes, D., Noble, D., (2011). "Don't head for the hills: Coseismic landsliding during the September 4th Darfield Earthquake", Oamaru conference, New Zealand. *(Oral Presentation)*

# CO-AUTHORSHIP FORMS

Deputy Vice-Chancellor's Office
Postgraduate Office

UNIVERSITY OF CANTERBURY
*Te Whare Wānanga o Waitaha*
CHRISTCHURCH NEW ZEALAND

## Co-Authorship Form

This form is to accompany the submission of any thesis that contains research reported in co-authored work that has been published, accepted for publication, or submitted for publication. A copy of this form should be included for each co-authored work that is included in the thesis. Completed forms should be included at the front (after the thesis abstract) of each copy of the thesis submitted for examination and library deposit.

**Chapter 1, Supplement to chapter 1:** Influence of topography and basement depth on the surface rupture morphology revealed from LiDAR and field mapping, Hope Fault, New Zealand

**Published in: Tectonophysics (Year 2014, Volume 630, pages 265–284).**

Chapter 1 contains this article.

Supplementary data associated with this article can be found in the online version at http://dx.doi.org/10.1016/j.tecto.2014.05.032 as well as in this thesis. This article includes a Google map (Kml file) of the most important areas described in this article. The Kml file is attached to this thesis as a digital appendix (Appendix A).

A preliminary version of the structural and geomorphological maps in this chapter was sent to the GNS by Narges Khajavi as a report as part of the LiDAR project which was led by Dr. Robert Langridge (the co-supervisor to this PhD thesis).

The published article was written by **Narges Khajavi**

Dr. Mark Quigley and Dr. Robert Langridge contributed significantly to reviewing and structuring the manuscript. Dr. Langridge helped with the field work.

Estimated candidate contribution in writing and revising, data analysis and figures, field work, and execution of research: 90%

**Certification by Co-authors:**

If there is more than one co-author then a single co-author can sign on behalf of all

The undersigned certifies that:

- The above statement correctly reflects the nature and extent of the PhD candidate's contribution to this co-authored work
- In cases where the candidate was the lead author of the co-authored work he or she wrote the text

Name: *Mark Quigley* Signature: 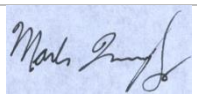 Date: *18/8/201518*

Deputy Vice-Chancellor's Office
Postgraduate Office

UNIVERSITY OF CANTERBURY
*Te Whare Wānanga o Waitaha*
CHRISTCHURCH NEW ZEALAND

# Co-Authorship Form

This form is to accompany the submission of any thesis that contains research reported in co-authored work that has been published, accepted for publication, or submitted for publication. A copy of this form should be included for each co-authored work that is included in the thesis. Completed forms should be included at the front (after the thesis abstract) of each copy of the thesis submitted for examination and library deposit.

**Chapter 2, Appendix to chapter 2, Supplement to chapter 2, digital supplement to chapter 2**: Late Holocene rupture behaviour and earthquake chronology on the Hope Fault, New Zealand

**Accepted in: Geological Society of America Bulletin (GSA bulletin) (year 2015)**

Chapter 2 contains this article.

Digital appendix (Appendix B) includes the laboratory OSL and radiocarbon age dating used in this chapter.

The accepted manuscript was written by **Narges Khajavi**

Dr. Mark Quigley and Dr. Robert Langridge contributed significantly to reviewing and structuring the manuscript. All co-authors helped with the field work. OxCal modelling and dendrochronology results benefitted from discussions with Dr. Robert Langridge. Dr. Quigley heavily revised 2 pages (the last 2 paragraphs under the section "Periodic versus Episodic Earthquake Recurrence" and the relevant part in the abstract) of the manuscript out of 68 pages.

Estimated candidate contribution in writing and revising, data collection and analysis and figures, field work, and execution of research: 90%

**Certification by Co-authors:**

If there is more than one co-author then a single co-author can sign on behalf of all

The undersigned certifies that:

- The above statement correctly reflects the nature and extent of the PhD candidate's contribution to this co-authored work
- In cases where the candidate was the lead author of the co-authored work he or she wrote the text

Name: *Mark Quigley* Signature: 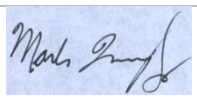 Date: *18/08/2015*

Deputy Vice-Chancellor's Office
Postgraduate Office

UNIVERSITY OF CANTERBURY
*Te Whare Wānanga o Waitaha*
CHRISTCHURCH NEW ZEALAND

# Co-Authorship Form

This form is to accompany the submission of any thesis that contains research reported in co-authored work that has been published, accepted for publication, or submitted for publication. A copy of this form should be included for each co-authored work that is included in the thesis. Completed forms should be included at the front (after the thesis abstract) of each copy of the thesis submitted for examination and library deposit.

**Chapter 3**, **Appendix to chapter 3:** Post-last glacial slip rate along the western Hope Fault, South Island, New Zealand.

**Intended for submission to: Tectonophysics (soon)**

Chapter 3 contains this manuscript

The manuscript was written by **Narges Khajavi**

Dr. Mark Quigley and Dr. Robert Langridge contributed to reviewing and structuring the manuscript. Dr. Langridge and Dr. Mark Quigley helped with the field work and developing the ideas.

Estimated candidate contribution in writing and revising, data collection and analysis and figures, field work, and execution of research: 90%

**Certification by Co-authors:**

If there is more than one co-author then a single co-author can sign on behalf of all

The undersigned certifies that:

- The above statement correctly reflects the nature and extent of the PhD candidate's contribution to this co-authored work
- In cases where the candidate was the lead author of the co-authored work he or she wrote the text

Name: *Mark Quigley* Signature: 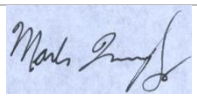 Date: *18/08/2015*

Deputy Vice-Chancellor's Office
Postgraduate Office

UNIVERSITY OF CANTERBURY
*Te Whare Wānanga o Waitaha*
CHRISTCHURCH NEW ZEALAND

# Co-Authorship Form

This form is to accompany the submission of any thesis that contains research reported in co-authored work that has been published, accepted for publication, or submitted for publication. A copy of this form should be included for each co-authored work that is included in the thesis. Completed forms should be included at the front (after the thesis abstract) of each copy of the thesis submitted for examination and library deposit.

**Chapter 4, Supplement to chapter 4:** Seismically induced boulder displacements in the Port Hills, New Zealand during the 2010 Darfield (Canterbury earthquake)

**Published in: New Zealand Journal of geology and Geophysics (NZJGG) (Year 2012, Volume 55, No 3, pages 271-278)**

Chapter 4 contains this article

The published article was written by **Narges Khajavi**

Dr Sam McColl contributed significantly to Flac modelling and the interpretation of the results. He also helped with the field work. Dr Mark Quigley contributed significantly in reviewing and structuring the manuscript. Mr Amir Rezanejad helped with the field work.

Estimated candidate contribution in writing and revising, data collection and analysis and figures, field work, and execution of research: 80%

**Certification by Co-authors:**

If there is more than one co-author then a single co-author can sign on behalf of all

The undersigned certifies that:

- The above statement correctly reflects the nature and extent of the PhD candidate's contribution to this co-authored work
- In cases where the candidate was the lead author of the co-authored work he or she wrote the text

Name: *Mark Quigley* Signature: 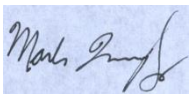 Date: *18/08/2015*

# THESIS PROLOGUE

This thesis is devoted to understanding the earthquake hazard and paleosesimicity of strike-slip faults. This thesis was mainly funded by the New Zealand Natural Hazard Platform to use airborne light detection and ranging (LiDAR) and advanced field techniques to investigate the surface rupture morphology and paleoseismology of the western Hope Fault in the northern South Island of New Zealand. When I started my PhD research, the $M_w$ 7.1 Darfield (Canterbury) earthquake of 4 September 2010 occurred on a dextral strike-slip fault and struck the city of Christchurch and wider Canterbury region. As I was part of the Tectonics group at the University of Canterbury, I additionally pursued research related to this earthquake. That research was defined to document immediately the characteristics of the coseismically-displaced boulders and ground damage in the Port Hills, south of Christchurch to ensure the quality of scientific data was not lost. Therefore, this thesis includes two parts. Although these parts are related to two different study areas (Fig. P.1) which are separated by more than one hundred kilometre and present different geologic, coseismic, and geomorphic phenomena, they both conduct studies on evaluating and addressing seismological problems. In addition, they both show that documenting earthquake-induced modifications of the earth surface are significant to assess the characteristics of the past and contemporary earthquakes and provide insight into seismic hazard analysis. In one area, paleoearthquake chronology, fault slip rate and coseismically-formed fault structures are investigated and mapped, and in the other area, coseismic phenomena farther away from the source fault are documented, mapped and analysed. In particular, this research provides: (1) robust data on the earthquake chronology, recurrence interval, slip pattern, slip rate, rupture length and magnitude of large earthquakes on the western part of the Hope Fault, which are applicable to the New Zealand national seismic hazard model, and (2) data on the strong ground motion characteristics of the faults for assessing future coseismic displacements and related fault rupture hazard to infrastructure adjacent to known active faults (e.g., Honegger et al., 2004; Van Dissen et al., 2013) including design of fault set-back distances (e.g., Villamor et al., 2012).

## 1.1 **Scientific context**

Accurate evaluation of surface rupture morphology of a fault is crucial for evaluating cumulative slip on the surface and conducting paleoseismic investigations. In general, active faults have been mapped using field techniques and from aerial photographs. However,

detecting the faults and their deformation zone comprising smaller-scale structures in areas of dense vegetation requires other techniques. Airborne LiDAR technology, which has been developed in the last 15 years, has significantly improved the recognition of faults and their surface morphology in densely vegetated areas (Chan et al., 2007; Zachariasen and Prentice, 2008; Arrowsmith and Zielke, 2009; Begg and Mouslopoulou, 2010; Barth et al., 2012; Haddad et al., 2012; Nissen et al., 2012; Oskin et al., 2012; Quigley et al., 2012; Duffy et al., 2013; Gold et al., 2013; Langridge et al., 2013, 2014; Khajavi et al., 2014).

Assessing seismic hazard parameters including fault length, slip rate, single event displacement, and recurrence interval for faults with large magnitude earthquakes and successive surface ruptures requires investigations on the spatiotemporal accumulation of slip preserved along geomorphic features (Weldon and Sieh, 1985; Langridge and Berryman, 2005; Kozaci et al., 2007; Langridge et al., 2010; Rizza et al., 2011; Ninis et al., 2013; Barth et al., 2014; Khajavi et al., 2014; Rittase et al., 2014; Manighetti et al., 2015; Zielke et al., 2015) and paleoseismological analysis (Hartleb et al., 2006; Scharer et al., 2007; McCalpin, 2009; Berryman et al., 2012; Langridge et al., 2013; Khajavi et al., accepted manuscript).

New Zealand occupies the boundary between the Australian and Pacific tectonic plates (Fig. P.1A). The Marlborough Fault System (MFS) in the northern South Island of New Zealand is a strike-slip plate boundary transfer zone which links the Hikurangi subduction zone to its north with the dextral strike-slip Alpine Fault to its south (Van Dissen and Yeats, 1991; Berryman et al., 1992; Knuepfer, 1992; Nicol and Van Dissen, 2002) (Fig. P.1B). Nearly pure strike-slip deformation occurs across the MFS (Beavan et al., 2002; DeMets et al., 1994, 2010; Wallace et al., 2007, 2012). The MFS is characterized by four major dextral strike-slip faults (Wairau, Awatere, Clarence, and Hope faults) that transfer the motion between the Alpine Fault in the west and Hikurangi subduction zone in the east (Berryman and Beanland, 1991; Pettinga et al., 2001; Van Dissen and Yeats, 1991; Wallace et al., 2007, 2012; Yeats and Berryman, 1987). The ENE-striking Hope Fault is one of the longest (~230 km) and fastest slipping (~8-27 mm/ yr) active faults in New Zealand (Cowan and McGlone, 1991; Langridge et al., 2003, Langridge and Berryman, 2005). The Hope Fault consists of five geometrically-defined segments (from west to east: Taramakau, Hurunui, Hope River, Conway, and Seaward) (Fig. P.1B) that are separated by fault stepovers and changes in strike. Evidence for segmented rupture behaviour along the Hope Fault includes: (1) the 1888 $M_w$ 7.1 Amuri earthquake, which ruptured the Hope Fault for an estimated length of between 13 and150 km (McKay, 1890; 1920; Berryman, 1984; Knuepfer, 1984; Cowan, 1991), (2) along-

fault variations in slip rate (i.e., from ~8-15 mm/yr (Hurunui segment) to ~10-17 mm/yr (Hope River segment) to ~19-27 mm/yr (Conway segment), and (3) along-fault variations in the timing and estimated recurrence interval of paleoearthquakes, which varies from ~81 to 500 yr (Cowan and McGlone, 1991; Langridge et al, 2003; Langridge and Berryman, 2005).

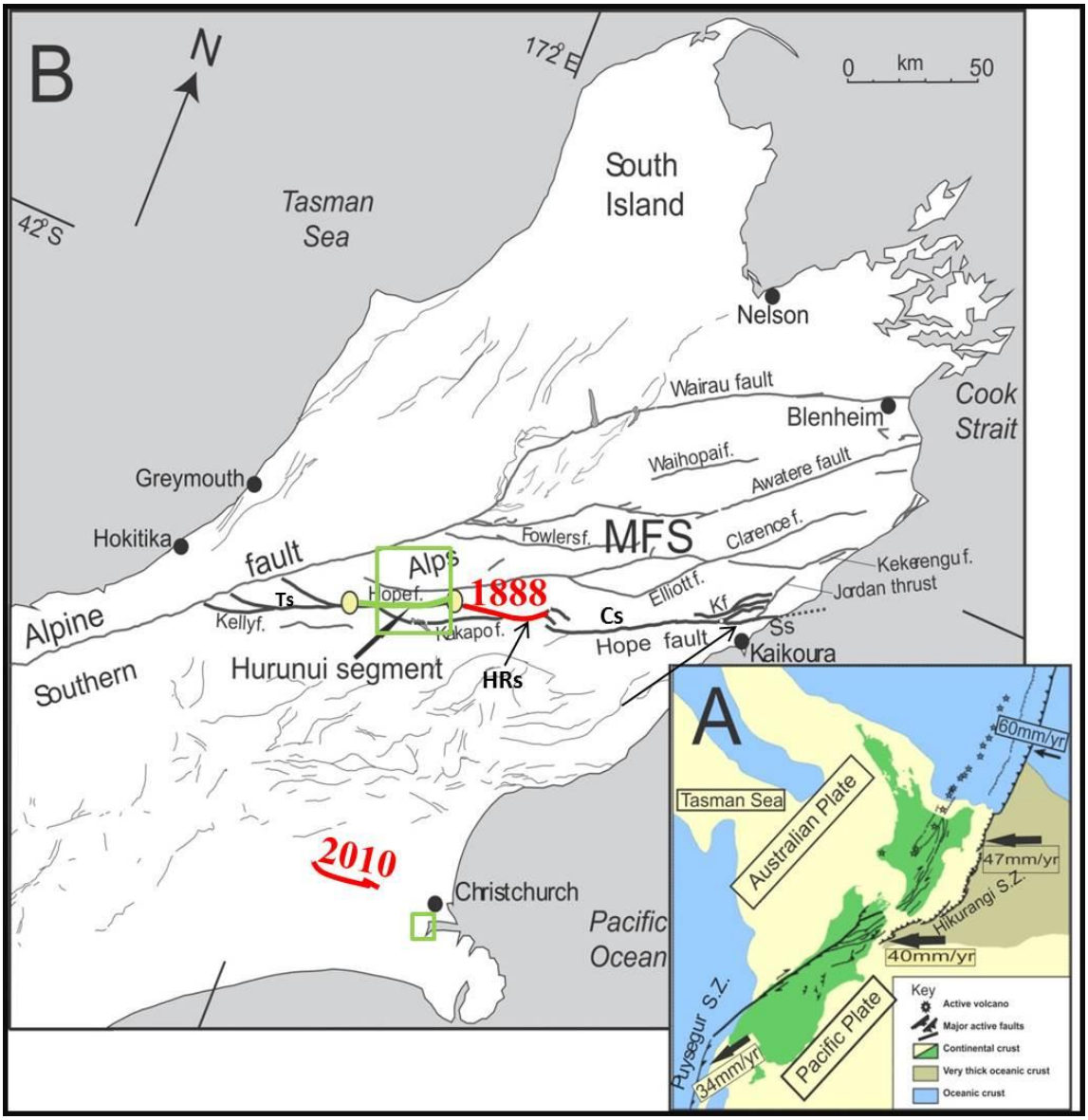


Figure. P.1. Geological setting of New Zealand and active faults in the northern South Island. (A), New Zealand plate boundary including subduction zones and major faults. Nuvel-1 plate rates (mm/yr) and orientations are after DeMets et al. (1994). (B), Location of active faults within the northern South Island. Marlborough Fault System (MFS) and the Alpine Fault are highlighted. Hope Fault is heavily highlighted; modified from Langridge and Berryman (2005). Green boxes show the principal field sites within this thesis. The 1888 earthquake on the Hope River segment (HRs) of the Hope Fault and the 2010 earthquake on the Greendale Fault are highlighted. Abbreviations: Ts: Taramakau segment; Cs: Conway segment; Ss: Seaward segment.

The Hurunui segment of the Hope Fault, which has an estimated length of ~42 km (Fig. P.1B) is covered by beech forest and located in a remote mountainous area so that not much information was available on the fault geometry and earthquake history prior to this study. Freund (1971), Langridge (2004), Langridge and Berryman (2005), and Langridge et al. (2007, 2013) had already documented major fault strands and scarps and near-fault geomorphic features and those structures were previously identified on regional geologic maps (Bowen, 1964; Gregg, 1964; Lensen, 1962; Nathan et al., 2002; Rattenbury et al., 2006; Warren, 1967). In addition, Langridge and Berryman (2005) and Langridge et al. (2013) conducted research on the slip rate and paleosesimicity of the Hurunui segment at two sites along the Hurunui segment. This segment of the fault is adjacent to the Hope River segment which has recorded one historical earthquake, i.e., the 1888 Amuri earthquake with an estimated magnitude of $M_w$ 7.1 (Stirling et al., 2012) (Fig. P.1B). As briefly mentioned already, the estimated rupture length associated with this earthquake varied by an order of magnitude, therefore more knowledge was required to better resolve the western extension of the surface rupture of this earthquake in the context of fault segmentation and future seismic hazard posed by the fault. This thesis aims to improve the current knowledge by: (1) providing a detailed structural map of the Hurunui segment and its deformation zone, (2) conducting more paleoseismic investigations to discover the paleoearthquake chronology of the western Hope Fault, and (3) producing the most updated seismic hazard parameters for the western Hope Fault.

Displaced boulders have been reported and mapped in association with large earthquakes all around the world (e.g., Japan, India, Italy, Iran and California) (Oldham, 1899; Clark, 1972; Bolt and Hansen, 1977; Umeda et al., 1987; Iio and Yoshioka, 1992; Ohmachi and Midorikawa, 1992; Bouchon et al., 2000). The observed displaced boulders in the Port Hills, south of Christchurch (Fig. P.1B), provide excellent information on the ground motion variability and origin of the seismic shaking, as well as on the engineering of earthquake-resistant structures. This phenomenon can be used as a proxy of earthquake motion in areas lacking arrays of seismometers. Five month after the Darfield earthquake, another fault ruptured under the Port Hills that caused even more intense shaking and landsliding, but no further damage or boulder displacement in the study site. This provides baseline knowledge on the characteristics of the seismic source and sites which has been damaged and or record different coseismic phenomena.

This thesis has aimed to answer the following research questions (Table P.1) regarding the Hope Fault and coseismically displaced boulders in the Port Hills.

Table P.1. Research questions regarding the Hope Fault and displaced boulders in the port Hills, South Island, New Zealand.

| **Goal/Scientific contribution** | **Research questions** | **Relevant chapter** |
|---|---|---|
| Defining the fault deformation zone associated with the Hurunui segment of the Hope Fault and investigating the faults' structural complexities | How accurate are the fault structures and geomorphic features mapped along the Hurunui segment using LiDAR data? | Chapter 1 |
| | How wide is the deformation zone? | |
| | What are the structures within the fault deformation zone and how are their kinematics interpreted in the context of the regional stress field? | |
| | Why has the mature Hope Fault developed a wide deformation zone instead of a simple thoroughgoing structure? What factors affect the spatial distribution of the fault deformation zone? | |
| | Are valuable sites to conduct further paleoseismic studies identified on the western Hope Fault using LiDAR data? | |
| Obtaining an earthquake chronology for the Hurunui segment using paleoseismic trenching and other Quaternary techniques and explore the fault behaviour | What is the structural configuration of the fault at the proposed segment boundary area? | Chapter 2 |
| | Did the 1888 earthquake rupture through the segment boundary? | |
| | Can the segment-to-segment rupture scenarios be resolved to provide Holocene rupture behaviour of the western Hope Fault? | |
| Measuring dextral displacements along the Hurunui segment, obtaining slip history, single event displacement, slip rate, recurrence interval, and the magnitude potential of the Hurunui segment | How faulted geomorphic features, their displacements and surface age can be compared along the entire Hurunui segment? | Chapter 1, Chapter 2 and Chapter 3 |
| | What are the seismic hazard parameters of the fault? | |
| | Are geomorphic, geodetic and paleoseismic slip rates consistent? | |
| | Is there along-strike spatiotemporal variation in the slip rate? How does the slip rate vary from segment-to-segment? | |
| | How are estimates of seismic hazard parameters improved by integrating field and LiDAR data? | |
| Documenting the characteristics of displaced boulders and ground damage observed in the Port Hills and investigate the possible factors affecting boulder displacement | What characteristics should be mapped and what is the relationship between those? | Chapter 4 |
| | What is the relation between coseismic displacement of boulders, the transient peak ground horizontal displacement recorded at the nearby stations, and the permanent post-seismic horizontal ground displacement? | |
| | Did topography influence the boulder displacement? | |

## 1.2 **Thesis structure**

This thesis includes 2 parts and 5 chapters; **Part I** (Chapters 1-3) is on the Hope Fault, **Part II** (Chapter 4) is on the documentation of the coseismically-displaced boulders in the Port Hills, southeast of Christchurch, and Chapter 5 summarises the main conclusions of this thesis and provides suggestions for future research.

**In Part I,** LiDAR data, different field techniques, and computer programmes are used to: (1) document the fault deformation zone associated with the Hurunui segment of the Hope Fault concealed beneath beech forest, (2) investigate the key factors that affect the fault zone complexity observed along the Hurunui segment of the Hope Fault, (3) investigate the paleoseismology of the western Hope Fault via trenching and other techniques in the area which is proposed to be a segment boundary between the Hurunui and Hope River segments of the Hope Fault (McKay, 1890; Cowan, 1991; Langridge and Berryman, 2005; Langridge et al., 2013), (4) document the surface slip pattern along the Hurunui segment of the Hope Faut, and (5) estimate slip rates from different sites and investigate the spatiotemporal variation in the slip rate along the Hurunui segment of the Hope Fault.

**Chapter 1** uses LiDAR data to map the surface rupture patterns associated with major earthquakes on the Hurunui segment of the Hope Fault. This segment of the fault is largely concealed beneath beech forest meaning that details of the fault deformation zone were poorly mapped prior to this study. Structures within the fault deformation zone are mapped and classified and their kinematics are analysed in the context of the regional stress field. Although the Hope Fault is a structurally mature (Cowan et al., 1996), well-established and fast-slipping active fault with a recurrence interval of ~81-500 years (Cowan and McGlone, 1991; Langridge et al., 2003; Langridge and Berryman, 2005; Langridge et al., 2013), a deformation zone of up to ~500 m wide with an average width of ~200 m is mapped along the Hurunui segment. Many studies suggest that structurally mature active faults should have relatively narrow and simple rupture morphologies compared to less evolved and more segmented faults. Taking that into account, the impact of fault orientation, topography, and depth-to-bedrock on the fault deformation zone width and geometry are investigated. This chapter concludes that the Hurunui segment strikes between 070° and 075° and is optimally oriented for dextral strike-slip within the regional stress field. Therefore, the observed variation in the fault deformation zone resulted from: (1) increased hanging wall topography;

high topography loads the fault plane and deflects it from its favourable orientation for strike-slip motion so that it branches off to adjust itself and accommodate the local oblique motion exerted by topography, (2) increased topographic relief; proximity of the fault to major river valleys creates spatial variations in gravitational loads that may perturb near-surface stress fields, (3) increasing thickness of alluvial deposits overlying bedrock, and (4) local changes in the fault strike.

**Chapter 2** provides new data that are valuable to the New Zealand national seismic hazard model. The true extent of the 1888 Amuri surface rupture has been debated by geologists, with estimations ranging from 13 km (from the Hope-Boyle confluence to the Hope-Waiau confluence) to 150 km (from the junction of the Alpine and Hope faults to the east of Hanmer Basin) (McKay, 1890; 1920; Berryman, 1984; Knuepfer, 1984) and no clear structural data was available for the area which is proposed to be a segment boundary (Cowan, 1991; Langridge et al., 2013) between the Hurunui and Hope River segments of the Hope Fault. This chapter uses a variety of field techniques and computer programmes to identify the structural configuration of the segment boundary area, resolve the surface rupture extent of the 1888 Amuri earthquake, and investigate the paleoseismicity of the Hurunui segment and rupture behaviour of this segment in relation to the Hope River segment which is adjacent to it. High-resolution LiDAR- and photogrammetrically-derived hillshade models are used to better constrain both the surface rupture morphology of the eastern end of the Hurunui segment and the segment boundary area. Historical accounts of the 1888 Amuri earthquake (McKay, 1890) are reinterpreted in conjunction with the structures observed on the hillshade models from the area between the two segments. Fault zone maps from Chapter 1 are used to determine suitable and accessible places to excavate trenches and pits to acquire a paleoseismic history. Two paleoseismic trenches and 7 pits are excavated in order to investigate the past earthquake history of the fault and determine a surface rupture length and location in relation to the Hope River and Hurunui segments. Radiocarbon dating and OxCal modelling are used to investigate the timing of the past events and dendrochronology and optically stimulated luminescence (OSL) dating is used to determine the age of faulted sedimentary deposits and further refine the timing of paleoearthquakes. This chapter presents the following results: (1) a small releasing stepover (~850 m wide) and bend (9º-14°) are discovered at the segment boundary area, (2) six earthquakes ruptured the eastern part of the Hurunui segment in the last ~1700 yr with a mean recurrence interval of ~298 ± 88 yr and inter-event times ranging from 98 to 595 yr, (3) the 1888 Amuri earthquake propagated

through the proposed segment boundary; this is the first evidence for coseismic multi-segment ruptures on the Hope Fault, (4) it is likely that the Hurunui segment show earthquake temporal clustering behaviour, (5) the 1888 earthquake ruptured 44 to70 km of the Hope Fault with a magnitude of $M_w$ 7.1 ± 0.1, and (6) the geometrically-defined segment boundary between the Hurunui and Hope River segments does not always act as barrier to rupture propagation, and analogous geometric discontinuities may not limit rupture dimensions elsewhere along the Hope Fault, implying that the magnitude of future earthquakes may in some instances exceed estimates based on lengths of individual fault segments.

**Chapter 3** utilises LiDAR data and geomorphically-interpreted maps from Chapter 1 to: investigate dextral displacements along a 29 km-long section of the Hurunui segment of the Hope Fault, assess vertical component of slip on the fault in relation to the horizontal slip, provide slip rate estimates for the sites including high-quality cumulative dextral displacement and age data, correlate ages between faulted geomorphic features, compare the geomorphic, geodetic and paleoseismic slip rates, examine slip history and recurrence interval of the fault, and evaluate the magnitude of earthquakes of the Hurunui segment. Prior to this study, slip rate estimates were available for two sites along the Hurunui segment and fault displacement data were limited to the accessible sites and known fault traces and the most identifiable faulted landforms within the vegetated terrain (mainly, active and abandoned channels) (Langridge and Berryman, 2005). Those data were insufficient to derive the fault slip history and evaluate the spatiotemporal variability in the slip rate. This chapter provides one of the biggest collections of dextral displacement data (in addition to the study conducted by Manighetti et al., (2015)) along the Hope Fault (see Appendix 3.1). These displacement data are analysed to calculate the seismic hazard parameters for the Hurunui segment. The main outcomes of this chapter are: (1) reconstruction of geomorphic features with large horizontal displacements shows that the vertical component of motion is only ~ 1% (i.e., H:V ~100) and confirms that the fault is predominantly strike-slip; this is consistent with the results of Chapter 1, (2) the mean slip rate of the Hurunui segment is determined to be 12.2 ± 2.4 mm/yr, (3) the mean single event displacement (SED) along the Hurunui segment is determined to be 3.6 ± 0.7 m, (4) the mean recurrence interval of the Hurunui segment is determined to be ~200 to 440 yr which is consistent with the mean recurrence interval (i.e., ~210-386) obtained in Chapter 2, and (5) it is inferred that both adjacent segments of the fault (Hurunui and Hope River segments) follow a constant slip rate (12.5 ± 2.1 mm/yr) with earthquake rupture of ≥ $M_w$ ~7.

**In Part II,** characteristics of the coseismically-displaced boulders, and other forms of ground damage in the Port Hills during the 2010 Darfield (Canterbury) earthquake are documented and some of the major controls on spatial ground motion variability at non-instrumented locations are examined.

**Chapter 4** documents the location, physical attributes, hosting socket geometries, displacement directions and displacement azimuths of displaced boulders, and characteristics of coseismic shattered ridges, landslides and other forms of ground damage in the Port Hills (~35 km southeast of the earthquake epicentre), approximately two weeks after the 2010 $M_w$ 7.1 Darfield earthquake. The key sites were revisited from two days following the 2011 $M_w$ 6.2 Christchurch earthquake to see whether any modification (i.e., further displacement) had occurred or not. This chapter presents descriptive analysis of documented data, non-instrumental constraints on the variability, distribution and origin of strong ground motion during major earthquakes, and investigates the possible roles of topographic amplification on boulder displacement by comparing the characteristics of two earthquakes and two adjacent sites; one including displaced boulders and the other including non-displaced boulders. This chapter concludes that: (1) boulder displacement are observed on N-striking (000°-015°) ridges above ~400 m elevation but not on NE-, NW- and SE-striking ridges, (2) the prevailing boulder horizontal displacement azimuth is subparallel with the direction of instrumentally recorded transient peak ground horizontal displacements, (3) the lateral displacement of many boulders from low slope ground surfaces on ridge crests exceeds nearby instrumentally recorded peak ground displacements at lower elevations by up to an order of magnitude, implying that seismic waves were amplified at the study sites, (4) the co-existence of displaced and non-displaced boulders at proximal sites suggests small-scale ground motion variability and/or varying boulder-ground dynamic interactions relating to shallow phenomena such as variability in soil depth, bedrock fracture density and/or microtopography on the bedrock-soil interface, (5) revisiting the boulders following the 2011 $M_w$ 6.2 Christchurch earthquake reveals no subsequent relocation despite locally recorded horizontal and vertical ground accelerations well in excess of the Darfield earthquake and pervasive rockfalls and landslides elsewhere.

**Chapter 5** summarises the main conclusions of this thesis and provides suggestions for future research.

## 1.3 **Scientific contributions arising from this PhD and related work**

All of the scientific chapters (chapters 1 to 4) in this thesis have been considered for independent peer-reviewed journal articles. At the time of thesis submission, chapters 1 and 4 have been published in peer-reviewed journals (Khajavi et al., 2012; Khajavi et al., 2014) and chapter 2 has been accepted for publication in the GSA Bulletin. Chapter 3 is intended for publication to a peer-reviewed journal (preferably, Tectonophysics) and will be sent to a journal while the thesis review by examiners is in progress. Some parts of chapters 1, 2, and 4 have been presented at domestic and international conferences or used in scientific reports. Each of these chapters include either an appendix or supplementary file or both, which are presented following the "References" section. There are some repetitions in tectonic setting, geomorphic mapping and background in Chapters 1, 2, and 3 as a result of being individual articles. I am co-author in another peer-reviewed journal with my co-supervisor (Langridge et al., 2014). A Kml file (Appendix A) is associated with Chapter 1, and a PDF file (Appendix B) including OSL and radiocarbon laboratory age dating is associated with Chapter 2. These Kml and PDF files are submitted as digital appendixes alongside with this thesis.

## 1.4 **Originality**

The material presented in this thesis has benefitted from many useful discussions with my senior supervisor, co-supervisors, co-authors, and colleagues. LiDAR data was funded by the New Zealand Natural Hazard Platform and provided by GNS Science. My senior supervisor, Dr. Mark Quigley, my co-supervisor, Dr. Robert Langridge, and my other co-authors contributed in field works and assisted with trenching, excavating pits, documenting displaced boulders, scientific discussions and editorial input into the manuscripts. Sam McColl helped with setting up the topographic amplification model in Flac software for Chapter 4. He guided me how to interpret the results from Flac modelling. During my PhD research, Dr. Mark Quigley and Dr. Rob Langridge offered directions to develop the research and improve some of the ideas. Apart from these exceptions, this thesis represents field work, data collection, analysis and interpretations, maps, figures, sample preparations, computer models, and articles which are all my own work. The manuscripts and chapters were entirely written by me. I went through all the review comments from the journal reviewers and benefitted from useful discussions with my senior and co-supervisors and Sam McColl. Roles of co-authors in each manuscript have been clarified in "co-authorship forms" section.

# PART ONE: THE HOPE FAULT

# CHAPTER 1. INFLUENCE OF TOPOGRAPHY AND BASEMENT DEPTH ON SURFACE RUPTURE MORPHOLOGY REVEALED FROM LIDAR AND FIELD MAPPING, HOPE FAULT, NEW ZELAND

# Influence of topography and basement depth on surface rupture morphology revealed from LiDAR and field mapping, Hope Fault, New Zealand

**Narges Khajavi[a]*, Mark Quigley[a], Robert Langridge[b]**

[a] Department of Geological Sciences, University of Canterbury, New Zealand

[b] GNS Science, Lower Hut, Wellington, New Zealand

[*]Corresponding author. Email: narges.khajavi@pg.canterbury.ac.nz

Article history:
Submitted to: Tectonophysics
Received 17 December 2013
Received in revised form 21 May 2014
Accepted 28 May 2014
Available online 2 June 2014

## 1.1 Abstract

High-resolution airborne LiDAR and field mapping are used to investigate a 29 km-long section of the Hurunui segment of the Hope Fault concealed beneath beech (*Nothofagus*) forest. Approximately 20 km of the dextral strike-slip principal slip zone (PSZ) is identified as a series of 69 individual fault strands on the LiDAR DEM. Mapping reveals 70 normal, 55 dextral-reverse, and 100 secondary faults, many of which were previously unrecognized. Secondary faults are kinematically linked with the PSZ and comprise a complex surface fault deformation zone (FDZ). A Rose diagram weighted by the lengths of the PSZ strands shows that the Hurunui segment strikes between 070° and 075° and is optimally oriented for dextral strike-slip within the regional stress field. The observed fault zone complexity is thus unlikely to result from large-scale fault mis-orientation with respect to regional stresses. FDZ width measurements from 415 locations reveal a spatially-variable, active FDZ up to ~500 m wide with an average width of 200 m. FDZ width increases with increased hanging wall topography and increased topographic relief (e.g., adjacent to high topography with deeply incised streams), suggesting that along-strike topographic perturbations to fault geometry and stress states increase fault zone complexity and width. Where adjacent PSZ strands strike between 070° and 075°, the FDZ is ≤ 150 m wide; however, FDZ width increases where the tips of adjacent PSZ segments locally vary in strike by ≥ 10°. FDZ width and surface fracture density also appear to increase with increasing thickness of alluvial deposits overlying bedrock. The results indicate that spatial variations in near-fault topography and geology can generate along-strike variability in the morphology of surface ruptures, even in the case of

fast-slipping, structurally mature faults where more confined, simplistic ruptures are expected at seismogenic depths.

## 1.2 **Introduction**

Fault deformation zones (FDZs) typically consist of narrow (< 2-5 m) principal slip zone (s) (PSZ) along which maximum fault slip occurs and a wide (> $10^2$ m) zone of smaller faults, fractures and/ or distributed folding (e.g., Schulz and Evans, 2000; Shipton and Cowie, 2001). Field data (e.g., Tchalenko and Ambraseys, 1970; Martel et al., 1988; Stirling et al., 1996; Kim et al., 2004; Rockwell and Ben-Zion, 2007; Sagy et al., 2007; Joussineau and Aydin, 2009), numerical models (e.g., Aydin and Schultz, 1990; Richard et al., 1991), and analogue experiments (e.g., Riedel, 1929; Tchalenko, 1970; Richard, 1991; Richard et al., 1995) predict that the FDZ should narrow in width and evolve from structurally complex to simple through-going fracture patterns as strain localizes with progressive slip, although alternative models for fault zone widening with cumulative slip have been proposed (e.g., Ben-Zion and Andrews, 1998). In general, the majority of studies suggest that structurally mature active strike-slip faults with large accommodated strain, fast slip rates and more frequent surface ruptures should have relatively narrow and simple rupture morphologies compared to less evolved, more segmented faults with slower slip rates. Although discrete, structurally simple rupture zones of < 30 m width are common along some segments of major fast-slipping active faults (e.g., Sieh and Jahns, 1984; Zhou et al., 2010; Lin et al., 2012), rupture zones along many active faults, including evolved and fast-slipping faults in plate boundary zones, commonly exceed $10^2$-$10^3$ m and contain complex surface rupture morphologies (Table 1.1). Progressive rotation and/or structural overprinting of faults misaligned with regional stresses (Scholz et al., 2010), fault zone segmentation and termination (e.g., Wesnousky, 1988; Kim et al., 2004; Oglesby, 2005; Elliott et al., 2009), and variations in the thickness and material properties of the faulted media (e.g., Richard et al., 1991, 1995; Norris and Cooper, 1997; Shipton and Cowie, 2003; Barth et al., 2012; Oskin et al., 2012) all offer explanations for the width and complexity observed in surface rupture morphology. Shallow (< 1-4 km depth) stress perturbations resulting from topographic loading from mountain ranges and unloading associated with valley systems (Norris and Cooper, 1995; Eusden et al., 2000, 2005; Barth et al., 2012) may also influence surface rupture morphology. Understanding the morphology and causative mechanisms influencing surface ruptures on active faults is important for assessing future coseismic displacements

and related fault rupture hazard to infrastructure adjacent to known active faults (e.g., Honegger et al., 2004; Van Dissen et al., 2013) including design of fault set-back distances (e.g., Villamor et al., 2012).

Table 1.1. Comparison of deformation zones and slip rates of selected strike-slip faults. * includes maximum distance of distributed surface rupturing, including parallel faults, splay faults, and faults not structurally linked to principal fault, that ruptured coevally with the principal fault.

| No | Dextral-slip fault/segment | Fault deformation zone width | Dextral slip rate | Reference |
|---|---|---|---|---|
| 1 | Hurunui geometric segment of the Hope Fault, ***New Zealand*** | ~500 m | ~8-13 mm/yr | This study, Langridge and Berryman (2005) |
| 2 | Conway geometric segment of the Hope Fault, ***New Zealand*** | ~2 km | ~23± 4 mm/yr | McMorran (1991); Ward (2000); Eusden et al. (2000 and 2005); Langridge et al. (2003) |
| 3 | Hope River rupture segment of the Hope Fault, ***New Zealand***<br>Excluding step-overs or bends<br>Including step-overs or bends | <br><br>20-50 m<br>2.3 km | ~10-18 mm/yr | Freund (1971); Cowan (1989), Cowan (1990); Cowan and McGlone (1991) |
| 4 | Central segment of the Alpine Fault, ***New Zealand*** | ~1 km | ~28 mm/yr | Barth (2013); Norris and Cooper (2001) |
| 5 | Central segment of the Wairarapa Fault, ***New Zealand*** | ~350 m | ~12 mm/yr | Carne and Little (2012) |
| 6 | Awatere fault, ***New Zealand*** | ~2 km | ~4-7 mm/yr | Little (1996) |
| 7 | Clarence fault, ***New Zealand*** | ~1.5 km | ~4-8 mm/yr | Browne (1992); Nicol and Van Dissen (2002) |
| 8 | Previously-unidentified Greendale Fault, **New Zealand**<br>Excluding step-overs<br>Including step-overs | <br><br>~300 m<br>~1 km | N/A | Quigley et al. (2012) |
| 9 | Cholame segment of San Andreas fault/USA | ~500 m | ~35 mm/yr | Arrowsmith and Zielke (2009); Lienkaemper (2001) |
| 10* | Newly-formed dextral fault in Gorny Altai/ Russia | ~4 km | N/A | Lunia et al. (2008) |
| 11 | Previously-unidentified Bam fault/Iran | ~500 m | N/A | Binet and Bollinger (2005); Jackson et al. (2006) |
| 12 | Denali fault/Alaska | ~1 km | ~15 mm/yr | Schwartz et al. (2012); Hreinsdóttir et al. (2006) |
| 13 | North Coast segment of San Andreas fault/USA | ~200 m | ~16-24 mm/yr | Zachariasen and Prentice (2008) |
| 14* | Coyote Creek fault, USA | ~2.6 Km | ~10 mm/yr | Dorsey (2002); Petersen et al. (2011) |
| 15* | Imperial fault, Mexico-USA border | ~6 km | ~15-20 mm/yr | Petersen and Wesnousky (1994); Petersen et al. (2011) |
| 16* | Superstition Hills fault and a previously unknown northeast-striking structure, USA | Up to 8.5 km | ~2-6 mm/yr | Williams and Magistrale (1989); Petersen and Wesnousky (1994); Petersen et al. (2011) |
| 17* | Previously- unrecognized Landers fault, US | ~3.8 km | ~0.4-0.6 mm/yr | Petersen and Wesnousky (1994); Petersen et al. (2011) |
| 18* | Nojima fault, Japan | ~4.5 km | ~0.9-1 mm/yr | Murata et al. (2001); Petersen et al. (2011) |
| 19 | Duzce fault, a splay of the North Anatolian fault, Turkey | ~700 m | ~15 mm/yr | Pucci et al. (2008); Petersen et al. (2011) |
| 20* | Lavic Lake and Bullion faults, USA | ~6.8 km | ~0.2-0.6 mm/yr | Treiman et al. (2002); Petersen et al. (2011) |
| 21* | Northern strand (five segments) of the North Anatolian fault, Turkey | ~12 km | ~20-23 mm/yr | Barka et al. (2002); Petersen et al. (2011) |
| 22 | Qingchuan fault of the Long Shan Thrust Belt, China | Generally < 20 m<br>Locally >100m | ~1-1.5 mm/yr for LSTB Faults | Lin et al. (2009); Lin et al. (2012) |

Active faults have traditionally been mapped using field techniques and aerial photography; however, faults in areas of dense vegetation and/or subtle features such as small, secondary faults comprising fault zones were typically challenging to detect (Chan et al., 2007). Recently, airborne LiDAR (light detection and ranging) data has improved the detection of faults in densely vegetated areas and the resolution with which faults can be mapped (Chan et al., 2007; Zachariasen and Prentice, 2008; Arrowsmith and Zielke, 2009; Begg and Mouslopoulou, 2010; Barth et al., 2012; Duffy et al., 2013; Haddad et al., 2012; Nissen et al., 2012; Oskin et al., 2012; Quigley et al., 2012; Gold et al., 2013; Langridge et al., 2013, 2014). In this study, I use LiDAR data to map the surface rupture patterns associated with major earthquakes on the Hurunui segment of the Hope Fault in New Zealand's South Island. I map and classify the structures within the FDZ, analyse their kinematics in the context of the regional stress field, and investigate how the FDZ width and geometry vary as a function of fault orientation, topography, and depth-to-bedrock. I discuss the applicability of the new fault zone maps for characterizing fault paleoseismicity. This study provides explanations for why complex surface ruptures may form on structurally mature faults where kinematically simple slip confined to a discrete rupture may have been expected.

## 1.3 **Tectonic and geologic setting**

New Zealand occupies the boundary between the Australian and Pacific tectonic plates. Nearly pure strike-slip deformation occurs across the Marlborough Fault System in the northern South Island at a rate of 39-48 mm/yr along an azimuth of ~258° (Beavan et al., 2002; DeMets et al., 1994, 2010; Wallace et al., 2007, 2012) (Fig. 1.1). The Marlborough Fault System is characterized by four major dextral strike-slip faults (Wairau, Awatere, Clarence, and Hope faults) that transfer the motion between the Alpine Fault in the west and Hikurangi subduction zone in the east (Yeats and Berryman, 1987; Berryman and Beanland, 1991; Van Dissen and Yeats, 1991; Pettinga et al., 2001; Wallace et al., 2007, 2012) (Fig. 1.1). The Wairau, Awatere and Clarence faults have Quaternary slip rates of ~4-8 mm/yr (Berryman et al., 1992; Knuepfer, 1992; Little and Jones, 1998; Benson et al., 2001; Nicol et al., 2002; Zachariasen et al., 2006). The ENE-striking and NW-dipping Hope Fault is a ~230 km long dextral strike-slip fault that traverses the central South Island of New Zealand from

the Alpine Fault in Westland to the east coast of the South Island near Kaikoura (Fig. 1.1) (Freund, 1971; Van Dissen, 1989; Cowan, 1990; Langridge and Berryman, 2005; Langridge et al., 2003). The Hope Fault has the highest slip rate of 23 ± 4 mm/yr (Langridge et al., 2003) within the Marlborough Fault System.

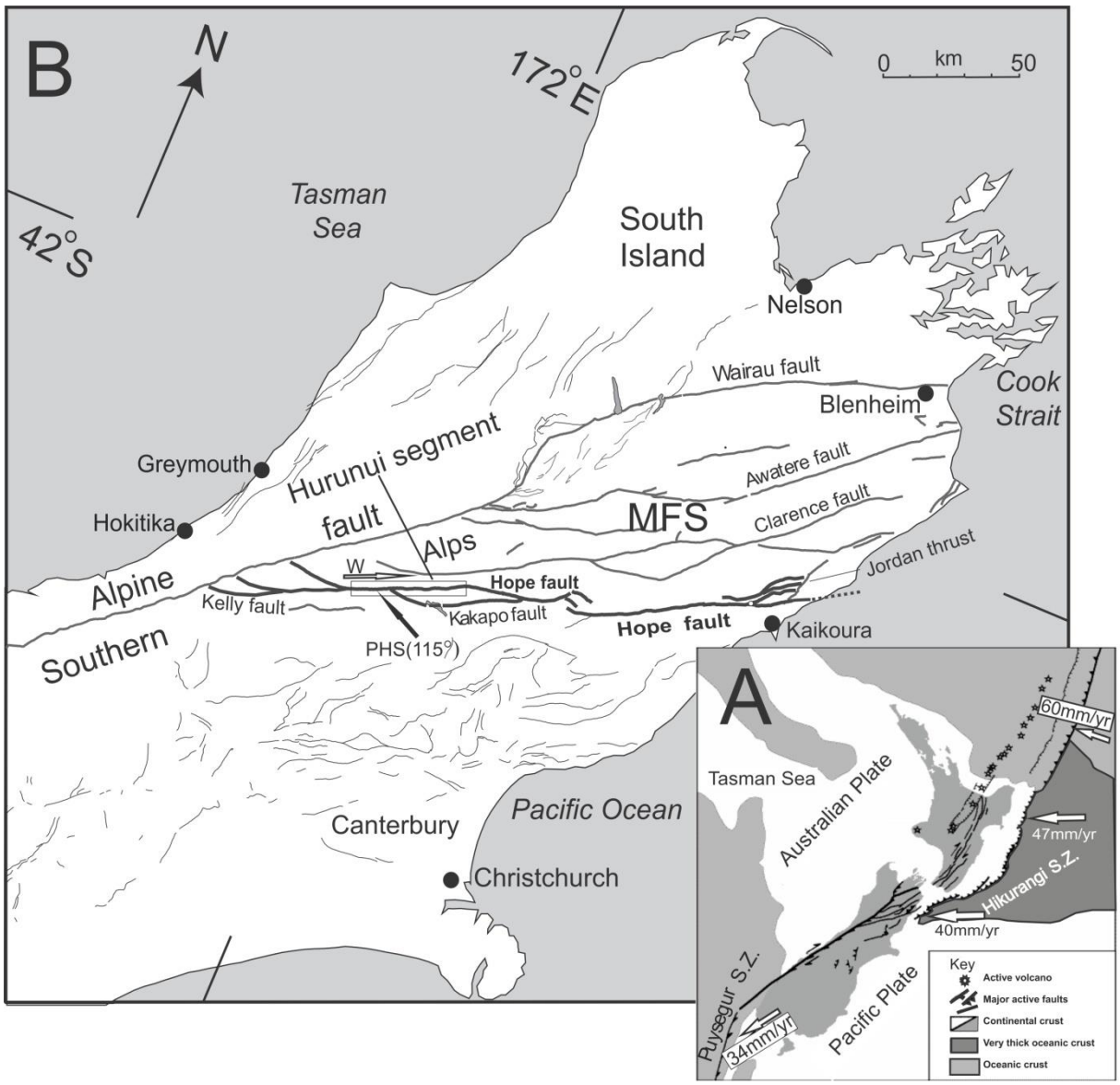


Figure 1.1. Geological setting of New Zealand and active faults in the northern South Island. (A), New Zealand plate boundary including subduction zones and major faults. Nuvel-1 plate rates (mm/yr) and orientations are after DeMets et al. (1994). (B), Location of active faults within the northern South Island. Marlborough Fault System (MFS) and the Alpine Fault are highlighted. Hope Fault is heavily highlighted with the Hurunui segment shown in a rectangle; modified from Langridge and Berryman (2005). The principal horizontal shortening vector (PHS, Nicol and Wise, 1992; Pettinga and Wise, 1994), and the modelled relative slip vector (W, Wallace et al., 2007, 2012) are shown near the Hurunui segment.

The bedrock geology of the Marlborough region consists primarily of sandstones, mudstones and mélange collectively classified as the Torlesse Formation of Triassic to early Cretaceous age (Gregg, 1964; Warren, 1967; Nathan et al., 2002; Barrell and Townsend,

2012). The basement rock is covered with late Quaternary unconsolidated deposits (Barrell and Townsend, 2012) as Tertiary rocks were eroded away. Within the study area, the late Quaternary period is characterized by ice cap and valley glaciers, the latter being the dominant force in forming the Hurunui and Hope valleys (Nathan et al., 2002) (Fig. 1.2). During cold climate periods, glacial ice eroded the mountainous areas while glacial meltwater deposited volumes of sediments in the valleys and basins. Following the Last Glacial Maximum (LGM-Otira glaciation; about 18,000 years ago) (Nathan et al., 2002; Alloway et al., 2007), alluvial aggradation terraces and fans were formed and slopes were stabilized by growth of woody vegetation. Subsequent to this, rivers incised into these surfaces (Knuepfer, 1992; Barrell and Townsend, 2012). Glaciofluvial, alluvial and landslide/debris deposits of late Pleistocene to Holocene age thus predominate in valleys and basins across which the Hope Fault traverses (Nathan et al., 2002). In such a dynamically active landscape, the geomorphic features created are the result of interaction between erosion, deposition and the fast-slipping Hope Fault.

The Hope Fault is the southernmost and youngest major fault within the Marlborough Fault System, and likely initiated ~1-2 Ma ago (Wood et al., 1994; Langridge and Berryman, 2005). The fault consists of several geometric segments and some branching faults (Van Dissen and Yeats, 1991; Yang, 1991; Pettinga et al., 2001; Berryman et al., 2003; Langridge et al., 2003, 2013) (Fig. 1.1). Along the Hope Fault, many geomorphic features preserve dextral, vertical, or oblique displacements resulting from past earthquakes.

The eastern segments of the Hope Fault are more easily mapped (Eusden et al., 2000, 2005; Beauprêtre et al., 2012) due to drier, less forested landscape and anthropogenic activity that has resulted in a largely grass-covered environment (Langridge et al., 2014). A FDZ width of up to 1.3 km including depressions, folds, and wedges has been documented along the eastern parts of the Hope Fault where it is not concealed beneath forest (Freund, 1971; Cowan, 1989; Eusden et al., 2000, 2005). Fault dip angles of 59°-80° NW measured from bedrock exposures have been published for the eastern segments of the Hope Fault (Freund, 1971; Eusden et al., 2000, 2005).

This study focuses on the Hurunui segment of the Hope Fault, which is a 42-km-long geometric segment located between Harper Pass in the west and the Hope-Boyle River confluence in the east (Figs. 1.1-1.2) (Cowan, 1991; Langridge and Berryman, 2005; Langridge et al., 2013). The Hurunui segment is located east of the main divide of the Southern Alps, where average annual rainfall is ~1.5-3m (Langridge et al., 2014). Here, much

of the landscape is covered by native beech (*Nothofagus*) forest (Langridge and Berryman, 2005; Langridge et al., 2013, 2014). The record of large earthquakes on the Hurunui segment is uncertain due to the short historical period (from ca. A.D. 1840) (Langridge et al., 2013) and remote mountainous location of this segment. Documentation of the surface rupture attributes of the fault is thus required to better estimate the fault slip rate and paleoseismic attributes such as magnitude and recurrence interval. Along this segment, major fault strands and scarps, near-fault geomorphic features such as grabens, fissures, sag ponds, and dextrally and vertically offset geomorphic markers such as terrace risers and streams have been documented by Langridge (2004), Langridge and Berryman (2005), and Langridge et al. (2007, 2013). Much of their mapping was undertaken in forested terrain using traditional methods and through re-interpretation of aerial images initially used by Freund (1971) to map the fault. The location of the PSZ and major structures within the FDZ was previously identified on regional geologic maps (Lensen, 1962; Bowen, 1964; Gregg, 1964; Warren, 1967; Nathan et al., 2002; Rattenbury et al., 2006). Dextral displacements along the fault yield a dextral to vertical slip ratio of ~7 ± 2:1 (Langridge and Berryman, 2005), indicating that the fault is predominately strike-slip and likely to be steeply dipping. Bedrock fault exposures show that the Hurunui segment dips steeply to the northwest (strike/dip = 063°/80° NW; Langridge and Berryman, 2005) in a bedrock shear zone near Three Mile Stream (Fig. 1.2) and in an outcrop of intense crushed bedrock including the fault plane (088°/ 72° NW; Browne, 1987) east of the study area (off the LiDAR swath). Langridge and Berryman (2005) estimated two dextral slip rates for the Hurunui segment; 8.1-11 mm/yr for the McKenzie fan site, and 13 ± 1.5 mm/yr for the Macs Knob area (Fig. 1.2). Estimates of the Hurunui segment surface rupture length (42 km), average single event displacement (3.4 m) and seismogenic depth (13 km) applied to earthquake scaling relationships (Hanks and Kanamori, 1979; Wells and Coppersmith, 1994; Langridge and Berryman, 2005; Stirling et al., 2002, 2008;) yield $M_w$ estimates of 7-7.4 (see also Langridge and Berryman, 2005).

In this study, airborne LiDAR data was collected along a 29-km-long and ~1-km wide survey along the centremost part of the Hurunui segment (Langridge et al., 2014). This survey extends from Landslip Stream in the west to near Boundary Stream in the east (Fig. 1.2). In particular, the survey was designed to assess the potential of LiDAR beneath beech (*Nothofagus*) forest in an area that was previously mapped by Langridge (2004), Langridge and Berryman (2005), and Langridge et al. (2007, 2013).

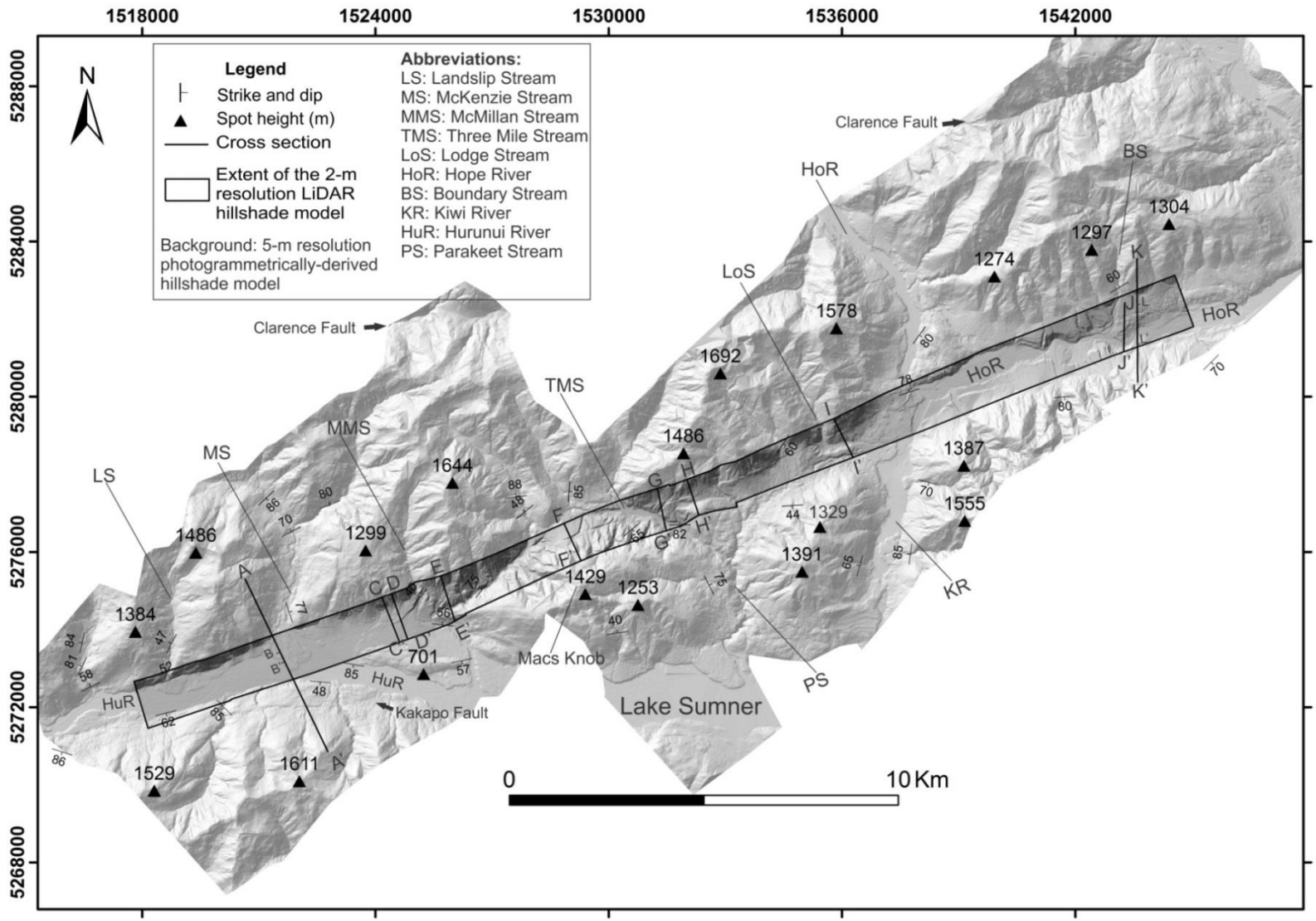


Figure 1.2. Geomorphic location of the LiDAR strip. Base map, which is the photogrammetrically-derived 5-m hillshade model, is used to give a larger view of the landscape.

## 1.4 **LiDAR data**

Airborne LiDAR data and orthophotos were collected along the Hurunui segment in November 2010. The data were acquired with an Optech ALTM 3100EA instrument from a plane at the flight altitude of ~1200 m above ground level (Langridge et al., 2014). For grassland and gravel substrates, the number of ground returns was approximately equal to the signal input, i.e., ~100%. For the forested terrain, up to 3-4 times the number of total returns was counted (Langridge et al., 2014). Unclassified returns collected from the vegetated terrain and were filtered in-house by New Zealand Aerial Mapping Ltd. (NZAM) (Langridge et al., 2014) and automatically classified into ground, first and intermediate returns using TerraSolid LiDAR processing software modules TerraScan, TerraPhoto and TerraModeler. Manual editing was subsequently used to improve the quality of the classified ground control points. Ground return point data for sample areas of gravel, grassland, scrub and beech forest were 1.47, 1.60, 0.78, and 0.7 points/$m^2$ respectively (Langridge et al., 2014). Horizontal and vertical accuracy of LiDAR data points are ± 0.3 m and ± 0.15 m respectively. Ground return point data were used to construct high resolution 2 m DEM and 0.5 m contour lines.

To generate the DEMs and hillshade models for mapping, I used ASCII xyz data from the ground returns and produced feature classes using ArcMap (GIS) software. An inverse distance weighted (IDW) interpolation technique was utilized to build the DEMs. In this method, input parameters of number of points = 12 and maximum distance = 20 were used based on the visible gaps in the dataset. Figure 1.2 shows the extent of the LiDAR-derived 2 m hillshade model that overlaps a photogrammetrically-derived 5 m hillshade model. Socet GXP software (http://www.geospatialexploitationproducts.com/content/products/ socet-gxp) and 2008 aerial images were used to extract the 5 m DEM. The high resolution 5 m hillshade model was used as a background to show geomorphic context of the study area. The 2 m DEM and hillshade models were used to map the fault and geomorphic features. Along with the LiDAR DEM and hillshade models, complementary digitized files such as topographic maps, pre-LiDAR 15 m DEM, the 5 m hillshade model, geological maps (Nathan et al., 2002; Rattenbury et al., 2006), and orthophotos were imported into ArcMap software and a suite of discrete shapefiles were developed to map tectonic and geomorphic features.

## 1.5 **Methodology**

### 1.5.1 Geomorphic mapping

To generate a detailed geomorphic map of the study area, I used all of the complementary maps, examined elevation profiles on the 2 m DEM, used multiple illumination angles in shade models in ArcMap, and field-validated the results. Geomorphically active and abandoned vegetated alluvial fans, active and ephemeral rivers, terraces risers, vegetated (older) and unconsolidated (younger) landslides/debris deposits, active flood plains, swamps, ponds, talus/scree slopes, gravitational failure scarps (arcuate features), cut banks/cliffs, moraine (with less certainty), and tectonic features such as grabens, fold axes, and pop-up (bulge) structures were mapped.

### 1.5.2 Fault mapping and classification

GIS-based mapping was integrated with field checking and previous field studies to identify all fault strands. Following that a classification of the faults based on kinematics, orientation, and spatial distribution with respect to the Hope Fault was required. Generally, FDZs consist of a PSZ and three other main zones; tip damage zone (at tips of the PSZ), linking damage zone (at step-overs), and wall damage zone (around the PSZ) (Kim et al., 2004). There are defined structures that mark each zone that have been well-described in dextral strike-slip fault systems in the field and laboratory experiments (Riedel, 1929; Tchalenko, 1970; Tchalenko and Ambraseys, 1970; Scholz, 1977; Sylvester, 1988; Richard et al., 1991, 1995; Kim et al., 2004). I produced a simple sketch map to show these structures and to provide a foundation for the fault classification (Fig. 1.3).

Figure 1.3A shows a schematic configuration of structures associated with dextral strike-slip systems. Riedel (R) faults (synthetic strike-slip faults), R′ faults (antithetic strike-slip faults; conjugate R), P faults (synthetic minor faults), P′ faults (antithetic minor faults; conjugate P), Y faults (synthetic strike-slip faults subparallel to the PSZ) and T faults (synthetic micro faults subparallel to the PSZ; also called tension gashes or extension fractures) that initiate when shearing begins (Tchalenko, 1970; Scholz, 1977; Sylvester, 1988; Richard et al., 1995; Casas et al., 2001; Kim et al., 2004; Carne and Little, 2012). As shear continues, normal (N) and reverse (Re) faults also form and will be rotated by ongoing shear. All of these structures may be superimposed depending on the natural stress conditions and material properties of the faulted substrate, resulting in a structurally complex fault zone

(Burbank and Anderson, 2006). These faults are mainly part of the wall damage zones. Splay faults (Sp) are branch faults that are dominant in the tip damage zones, and can mainly be in the form of wing cracks, horsetail splays (pinnate fractures), synthetic, and antithetic faults, but sometimes combinations of these forms occur (Kim et al., 2004). Fig. 1.3B shows a schematic configuration of the structures that I mapped on the LiDAR swath along the Hurunui segment. Here, I generally categorize the structures into three groups: (1) continuous fault strands that define the PSZ, (2) fault strands that are near the PSZ and connect to the PSZ on the surface, and (3) fault strands that are within the FDZ, but are farther away from the PSZ and have no directly observable physical connection to it on the surface. I name the third group "secondary faults" (Sf).

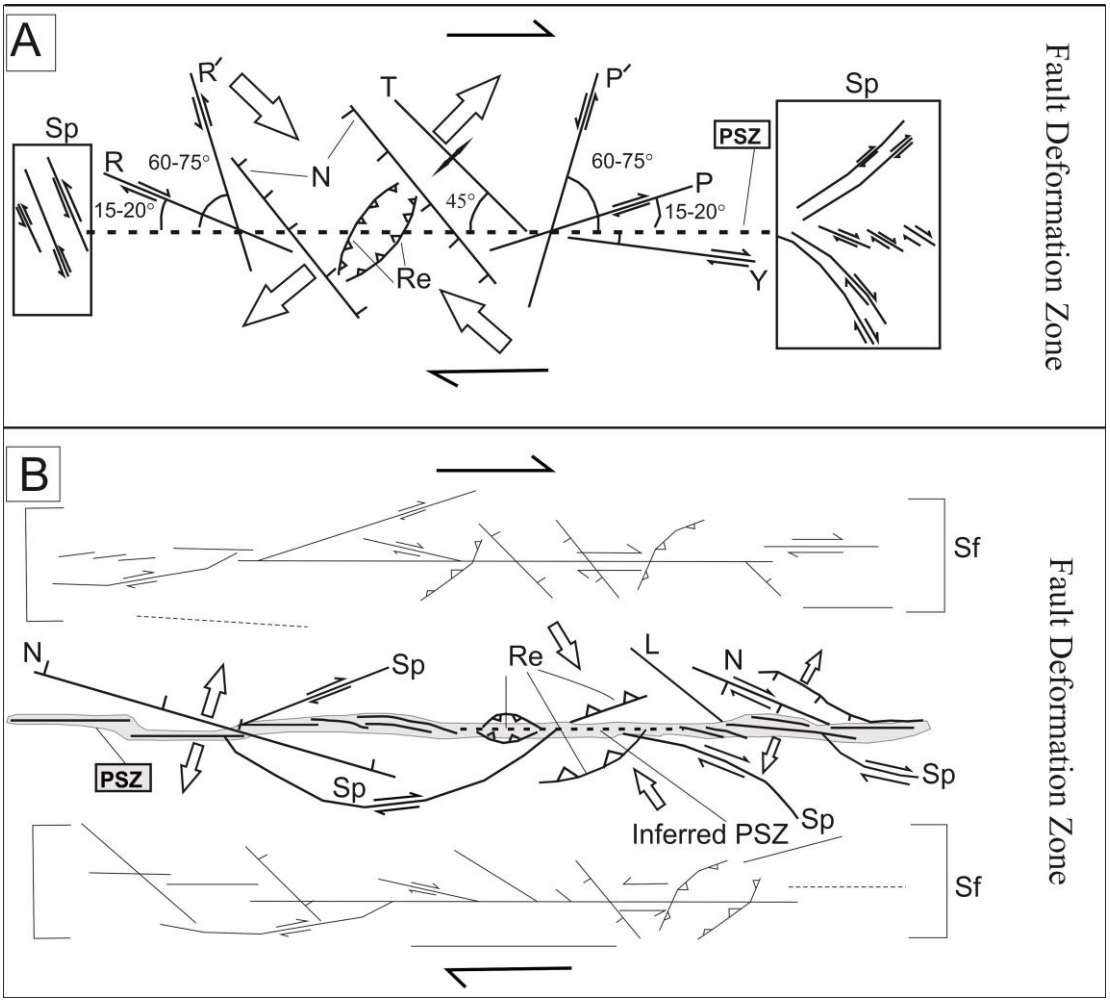


Figure 1.3. Recorded structures associated with strike-slip systems are compared with structures associated with the dextral strike-slip Hurunui segment of the Hope Fault using a simplified sketch map. (A), Structures form in models and natural settings (after Tchalenko, 1970; Scholz, 1977; Sylvester, 1988; Richards et al., 1995; Casas et al., 2001; Kim et al., 2004; Carne and Little, 2012). (B), Structures identified on the LiDAR strip. Abbreviations were explained in detail within the text.

The first group is composed of the PSZ, and inferred PSZ strands. I discriminate the PSZ strands from other faults confidently because they display well-developed surface expression and fault scarps, appear continuous and traceable, and accommodate considerable cumulative dextral and vertical slip measurable along offset geomorphic landmarks. The inferred PSZ strands are those with lesser confidence, but are parallel to, and located along, surface projections of adjacent PSZ strands and thus are likely of similar origin. This group includes continuous short or long strands, or continuous en echelon faults (Fig. 1.3B).

The second group is composed of normal (N), dextral-reverse (Re) and splay (Sp) faults, and some lineaments (L) with no discernible offset. I do not observe an abundance of R shears along the LiDAR swath. This is possibly because erosional or depositional processes have obscured or removed evidence for previous strike-slip displacements more readily than structures with vertical displacement, or that these structures are not a primary feature of coseismic rupture here. The kinematics and orientation of these structures with respect to the PSZ were used to determine whether they are normal, dextral-reverse, splay, or R faults. Kinematic information was obtained from vertical and horizontal displacements of streams, terrace risers, bulges or basins. Orientations of delineated structures (Fig. 1.3B) were compared with orientations of classically defined structures (Fig. 1.3A) with respect to the PSZ. Both the orientation and offsets observed across N, Re and Sp faults indicate that some of these structures include strike-slip components of displacement, and may in some cases be dominated by strike-slip movement where structures are close in orientation to the PSZ. I extended numerous elevation profiles across every structure to examine their kinematics and geomorphology more carefully and field-assessed many of them to improve confidence in fault classifications.

The third group (Sf) is composed of many fault strands that characterize the boundary of the FDZ. These faults are accommodated in the hanging wall (HW) and foot wall (FW) blocks around the PSZ, in a distance of up to 350 m on the steep slopes, and quite often show asymmetric patterns with respect to the PSZ. At some localities along the FDZ, these faults appear in the form of a smaller-scale dextral strike-slip system which includes its own PSZ and related structures (Fig. 1.3B). Since secondary faults display smaller vertical and horizontal displacements along their length, they cannot be mistakenly considered as being the PSZ or the core of the FDZ.

### 1.5.3 Relationship between fault orientation, kinematics, and FDZ width

For kinematic analysis, strikes and lengths of the PSZ and inferred PSZ strands, normal, and dextral-reverse faults were measured on the LiDAR strip. To provide significant azimuthal distribution of the faults in each group (Azzaro et al., 2012; Barth et al., 2012), I weighted the strikes of the faults based on their lengths and present them on Rose diagrams in Fig. 1.4.

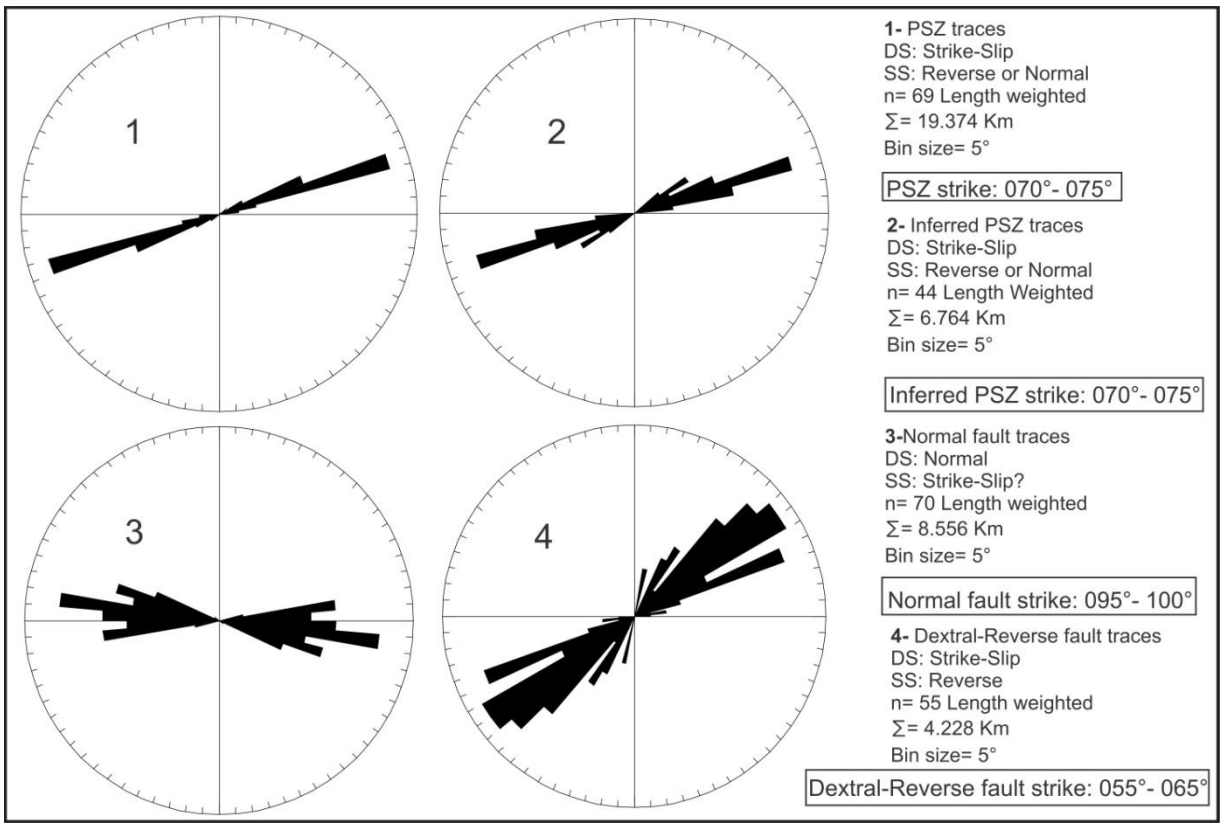


Figure 1.4. Rose diagrams showing the significant azimuthal distribution of the PSZ and inferred PSZ strands, normal and dextral-reverse faults mapped along the Hurunui segment. Details of each group of faults are provided. Abbreviations: DS; Dominant sense of motion, SS; Subordinate sense of motion.

For analysis of the FDZ, I measured the widths of the FDZ, including all of the mapped structures on the LiDAR DEM, along the entire length of the survey (Fig. 1.5). I made ~330 measurements of the FDZ width along the fault length, with an average spacing of 80 m between measurements. Where the FDZ width was highly variable along the PSZ, I increased the number of the measurements to 10 m spacing. Where the FDZ is uniformly narrow (<10 m) along strike and limited to the delineated fault scarp, I decreased the spacing of measurements to 1 km. A detailed graph showing the variations of the FDZ width along the Hurunui segment is presented in Fig. 1.5. To show the spatial distribution of the FDZ width

on the HW and FW blocks, I used a similar methodology as described above except that I made 415 measurements of the FDZ width north and south of the PSZ. I designated positive signs to the values of the FDZ width measured north of the PSZ, and negative signs to the values of the FDZ width measured south of the PSZ to assess the symmetry of the FDZ with respect to the PSZ along the Hurunui segment (Fig. 1.6).

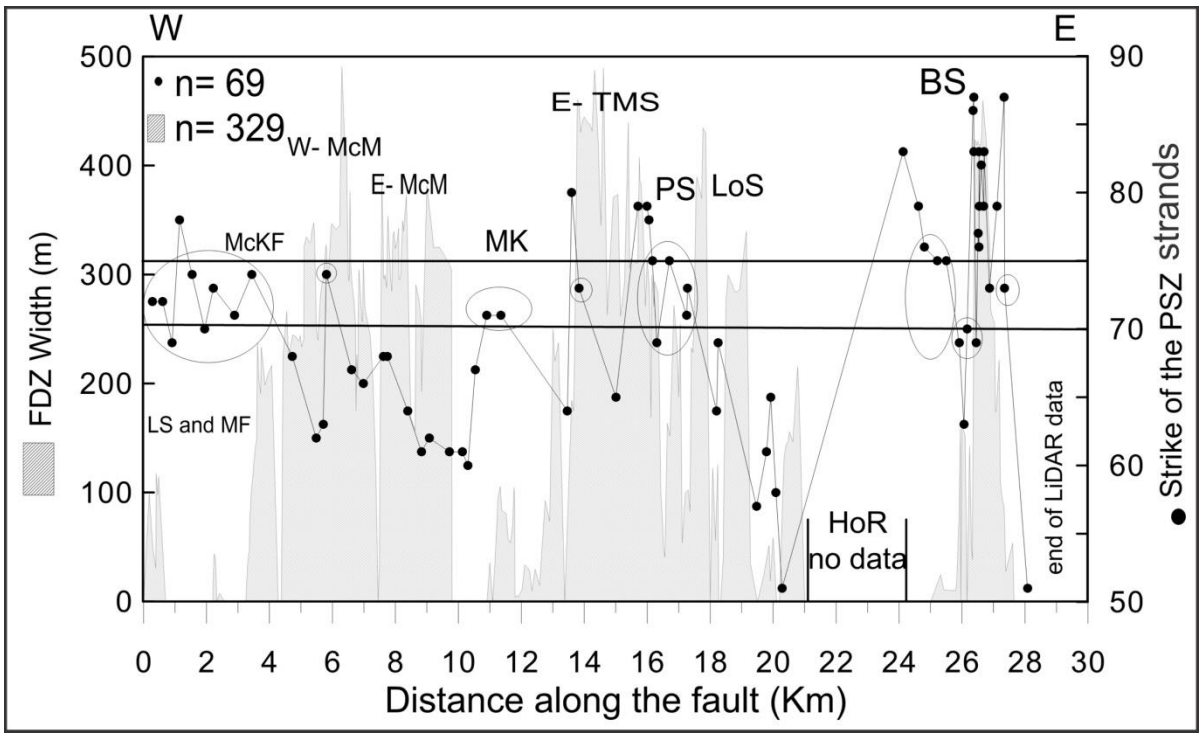


Figure 1.5. Width of the FDZ with respect to the PSZ, strike of the PSZ strands, and the range of significant azimuthal distribution of the PSZ (right axis) are shown along the fault. Width of the FDZ is defined using location of the structures off the PSZ. Abbreviations: LS and MF: Landslip Stream and Matagouri Flat, McKF: McKenzie Fan, W-McM: West McMillan, E-McM: East McMillan, MK: Macs Knob, E-TMS: East Three Mile Stream, PS: Parakeet Stream, LoS: Lodge Stream, HoR: Hope River, BS: Boundary Stream.

For evaluating the effect of fault strike on width of the FDZ, I plotted the strikes of the PSZ strands along the fault length. The plot was then overlain on the graph that shows the variations of the FDZ width along the fault (black closed circles on Fig. 1.5). To assess if the local variations in strikes of the PSZ strands can influence the FDZ width or its spatial distribution, I considered the difference between strikes of the adjacent PSZ strands and plotted the differential values as a bar graph along the fault length (red bars on Fig. 1.6).

### 1.5.4 Relationship between topography and FDZ width

For evaluating the effect of topography on the FDZ width, I extended two PSZ-parallel topographic profiles, with the same length, on the 2 m LiDAR DEM at 300 m distance north

and south of the PSZ. Each profile is used to represent the average near-field topography south or north of the fault. To avoid confusion by adding these two topographic profiles, I made a differential topographic profile and overlaid it on Fig. 1.6 (DT1; blue profile). This differential profile is the result of subtracting the southern profile from the northern one. Therefore, where this profile shows values > 0, north of the fault is higher in elevation than south of it, where it shows values < 0, south of the fault is higher in elevation than north of it, and where there is no difference in the elevation of north and south of the fault, the profile shows zero (0) values.

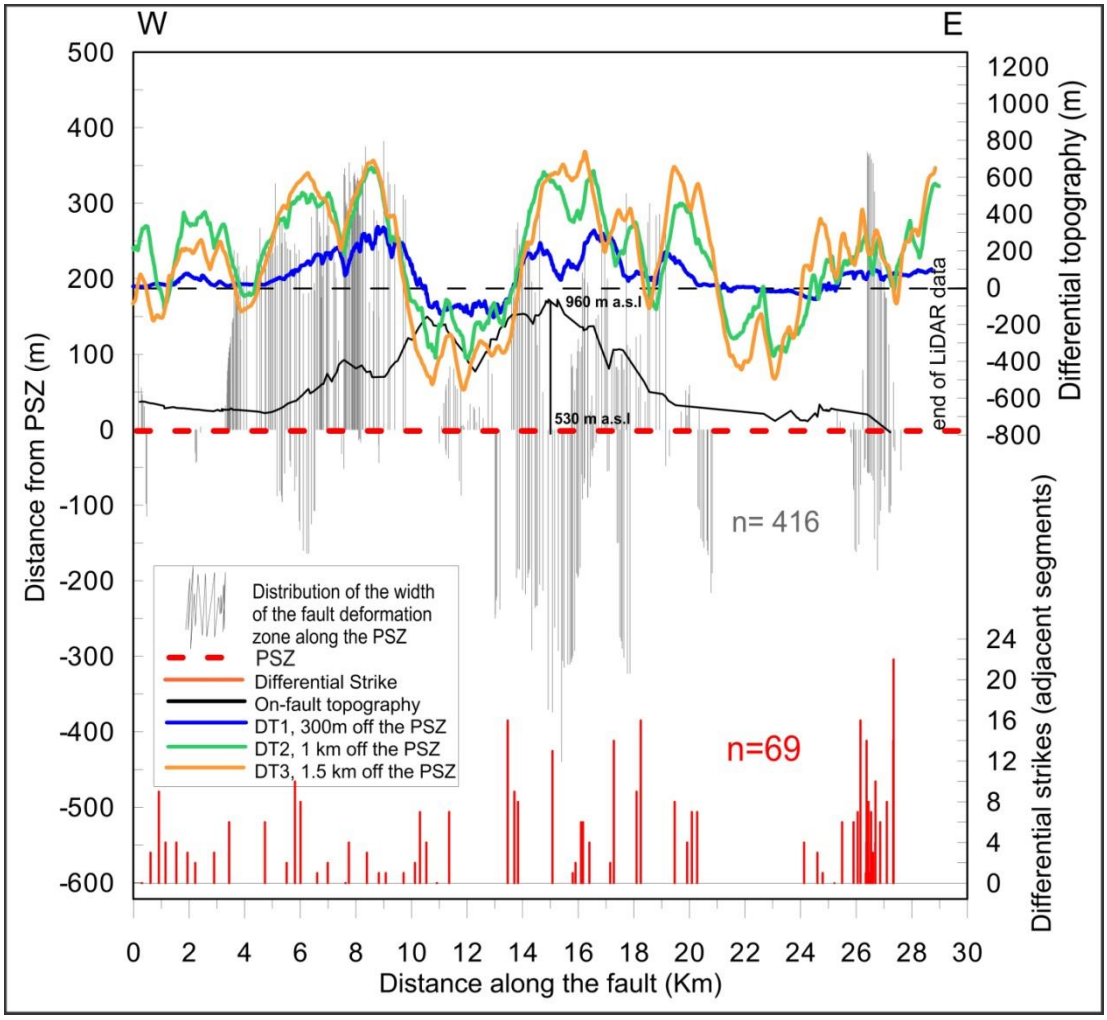


Figure 1.6. Detailed analysis of the FDZ associated with the Hurunui segment of the Hope Fault. Width of the FDZ is defined using location of the structures off the PSZ. Changes in strike of the adjacent fault strands (i.e., differential strike which reflects step-overs or bends) and differential topography were examined against each other. Northern (positive values) and southern (negative values) portions of the FDZ with respect to the PSZ (grey bar graph), differential topographic profiles (DT1-3), on-fault topographic profile, and differential strikes (red bar graph) are shown.

Additionally, I extended 4 other PSZ-parallel topographic profiles; two of which were produced from the photogrammetrically derived 5 m DEM at 1 km distance north and south of the PSZ, and two others on the 15 m DEM at 1.5 km distance north and south of the PSZ. Using a similar methodology to that described above, I made 2 more differential profiles and overlaid them on Fig. 1.6 (DT2; the green profile and DT3; the orange profile). The reason for adding extra profiles is that they represent the farther-field topography of south and north of the PSZ. The 5 m DEM had much better resolution for extracting distal elevation profiles, but its width was variable along the PSZ forcing me to use the 15 m DEM for the distal profiles. I also extracted the on-fault topography from the LiDAR DEM and added it to Fig. 1.6 to show the elevation of the landscape cut by the fault. By overlaying the differential profiles on Fig. 1.6, I could qualitatively assess the spatial relationships between topography adjacent to the fault and the width of the FDZ.

### 1.5.5 Structure contours of PSZ strand to constraint near-surface fault dip

Structural contours were constructed along the length of the PSZ to provide estimates of near-surface fault dip. I estimated the fault dip from three locations; east of McMillan Stream (distance 7.5-9 km on Figs. 1.2 and 1.5), Macs Knob (distance 10-13.5 km on Figs. 1.2 and 1.5), and Lodge Stream (distance 18-20 km on Figs. 1.2 and 1.5). Measurements of near-surface dip were then compared with nearby measurements of bedrock fault zones or fractures (e.g., Langridge, 2004) to estimate fault subsurface geometries through the cover and into the bedrock (see Section 1.9.6).

### 1.5.6 Relationship between depth-to-basement and FDZ width

For evaluating the effect of sediment thickness (overlying bedrock) on FDZ width, I first selected sites along the LiDAR swath to construct cross-sections. Three characteristics were considered in sample site selection: (1) the existence of abundant or complex structures, (2) the appearance of different styles of faulting such as N-facing vs. S-facing scarps, and en echelon vs. confined PSZ traces, and (3) areal coverage of different parts of the landscape, i.e., young, active alluvial valleys cut by the fault versus active mountain fronts cut by the fault. The sites, from west to east, are McKenzie fan, east and west of McMillan Stream, Macs Knob, and east of Three Mile, Lodge, and Boundary Streams (Fig. 1.2).

To generate accurate profiles and structural cross-sections of the sample sites, I used both the 2 m LiDAR and the 5 m DEMs as basemaps depending on the extent of the profiles.

Cross-sections AA′ to LL′ were extended across the PSZ through the selected sites (Fig. 1.2). Exposed bedrock slopes (BS) were uniformly extrapolated down to the base of the profiles assuming constant dip to estimate the depth-to-bedrock along the cross-section. I have no direct constraints on the depth and shape of the bedrock interface beneath alluvial deposits, thus this is an extrapolated model only. The hypothesized geometry of the cover deposits beneath the FDZ is used to calculate the average depth-to-bedrock. For example; where geometry of cover deposits is a simple triangle (Figs. 1.11-1.12), the average bedrock depth will be two thirds of the triangle height, but where cover geometry is complex I split it into several simpler shapes and calculate average depth to bedrock. For cross-section EE′, where up-slope portions of the FDZ are in the bedrock, the cross-sectional areas of the sediment wedges (beneath lower-slope portions of the FDZ) were converted to a rectangular area with uniform depth and the average depth-to-bedrock beneath the FDZ width was computed using this area and the FDZ width. I also added the orientation of bedding to some of the cross-sections where strike and dip data were available (see Fig. 1.2, strikes and dips from Nathan et al., 2002; Langridge, 2004; Rattenbury et al., 2006). The dip angle of the fault in the near surface was estimated using structure contours (see Section 1.9.5) and was also constrained at two sites in excavated trenches near Boundary Stream (BS), and west of the McKenzie fan in the flood plain of the Hurunui River (Fig. 1.2), where the fault dip is vertical (Langridge et al., 2013; Khajavi et al., accepted manuscript). In the cross-sections, I use a uniform dip of the fault in bedrock of 85° NW for the PSZ, dextral Sf, and dextral Sp structures in bedrock between distances 0 to 10 km and 14 to 30 km on Fig. 1.5 as indicated from bedrock fault exposures and the trenches east and west of the study area, and 80° SE between distances 10 to 14 km on Fig. 1.5, analogous to structures exposed elsewhere on other segments of the Hope Fault (e.g., Cowan, 1989; Eusden et al., 2000, 2005). For N faults I use a dip of 60° and for Re faults I use a dip of 45°; consistent with shallow structures that merge with the PSZ in the cover sequence or near the bedrock cover interface. These cross-sectional models were used to examine the influence of bedrock depth on the FDZ width and on the ratio of the number of faults/fractures to the FDZ width. The average depth-to-bedrock beneath the FDZ is examined against FDZ width.

## 1.6 **Results**

A detailed structural geomorphic map was produced for the LiDAR strip (Figs. 1.7-1.10; see also the Kml file in the digital Appendix A). These figures show continuous

uninterpreted LiDAR hillshade model strips (from west to east), that include sample sites (selected windows on the strips; A and B), and the equivalent geomorphic-structural maps of the sites so that uninterpreted and interpreted datasets can be visually compared.

### 1.6.1 Fault length and orientations

Fault mapping and classification reveal that the total length of the PSZ identifiable on the LiDAR swath is ~20 km (69% of the entire swath). The PSZ consists of 69 fault strands. The length of these fault strands expressed as tip-to-tip measurements of continuous rupture strands varies from 30 to 1500 m. Nine PSZ strands are longer than 500 m and 3 are longer than 1 km. The mean length of the PSZ strands is 280 m. The total combined length of the inferred PSZ strands (not visible on LiDAR but able to be linearly traced between adjacent mapped strands; shown as dashed lines) is ~7 km (24% of the entire swath). The remaining 7% of the total length of the Hurunui segment is not identifiable on the LiDAR swath and is inferred to have been eroded away or buried by active alluvial and colluvial processes (Figs. 1.2 and 1.5-1.6). PSZ step-over widths were measured perpendicular to the PSZ strike at 8 locations where adjacent PSZ lengths were greater than 300 m; widths ranged from 17 to 90 m (average = 58 m).

In addition to the PSZ and inferred PSZ strands, 70 normal faults and 55 dextral-reverse faults, with total lengths of 8.5 km and 4.2 km were mapped respectively. Normal faults are more abundant north of the PSZ and dextral-reverse faults are typically more abundant south of the PSZ. Many secondary (n = 100) and splay (n = 13) faults of different scale and style of motion were also mapped. Secondary faults have higher distribution north of the fault and appear mainly parallel to subparallel to the PSZ; however, splay faults are almost of the same size and appear near the small-scale step-overs or near the tips of the PSZ or inferred PSZ strands (Figs. 1.7-1.10).

Length-weighted Rose diagrams (Fig. 1.4) indicate that the longest segments of the PSZ and inferred PSZ are those with strikes of 070° to 075°, the longest segments of the normal faults are those with strikes of 095° to 100°, and the longest segments of the dextral-reverse faults are those with strikes of 055° to 065°. Disregarding the effect of weighting, the PSZ strike varies from 070° to 075°, the inferred PSZ strike varies from 065° to 075°, the normal fault strike varies from 090° to 100°, and the dextral-reverse fault strike varies from

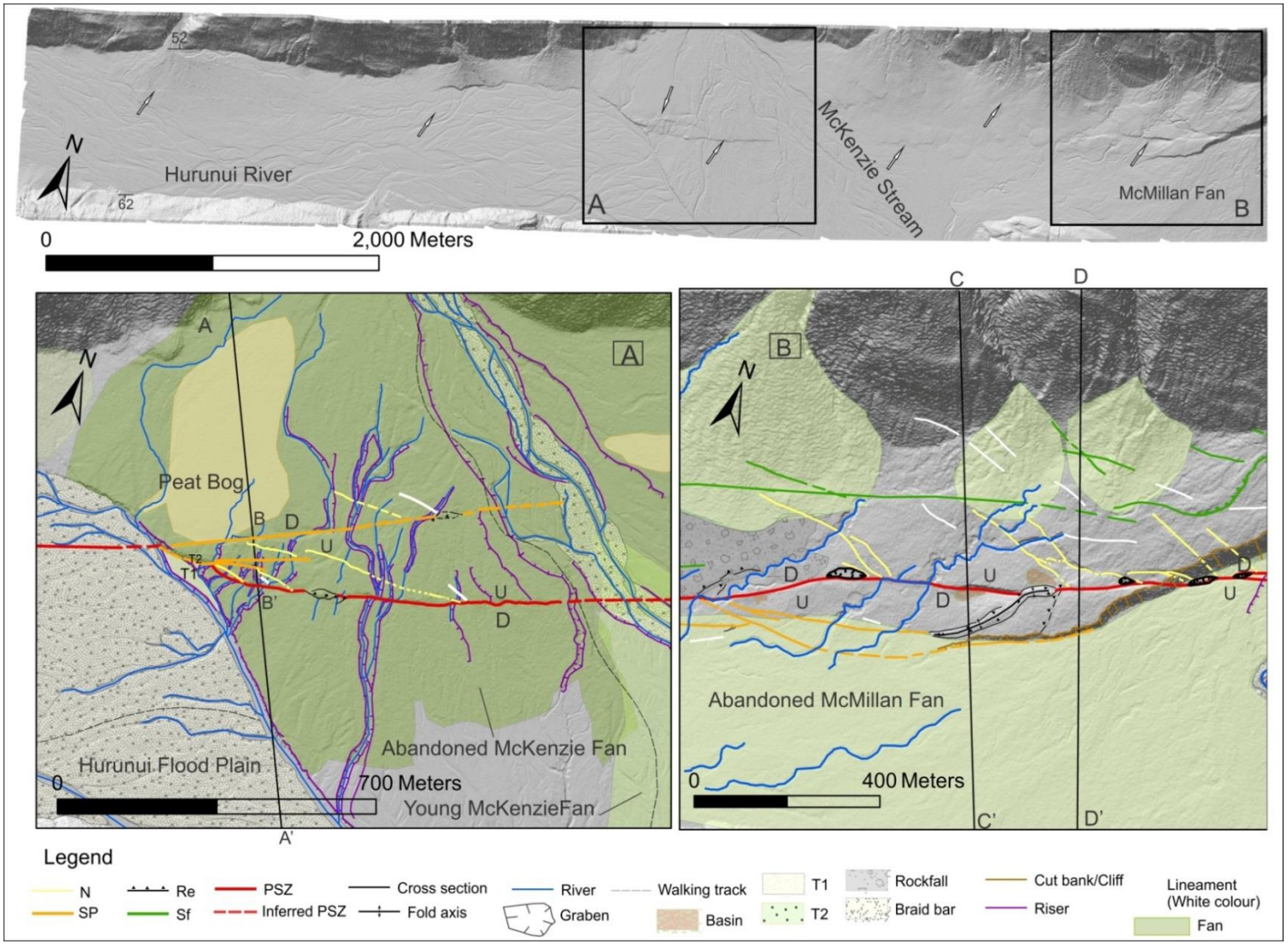


Figure 1.7. Uninterpreted LiDAR strip (~7 km long, from Landslip Stream to McMillan Stream) and structural geomorphic map of the two key sites. Arrows point to the fault strands. (A), McKenzie fan and location of cross-section AA' and BB'. (B), West of McMillan Stream and locations of cross-sections CC' and DD'.

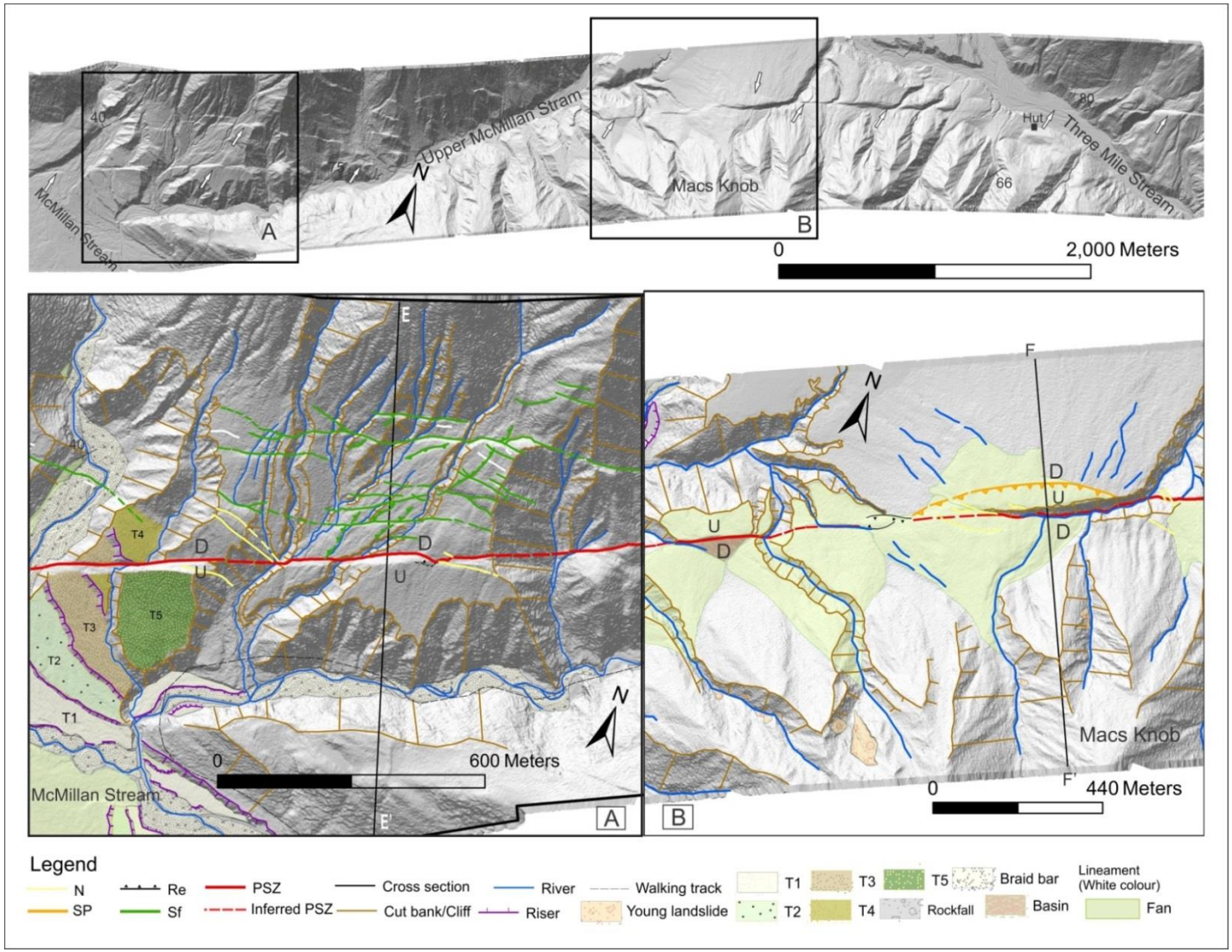


Figure 1.8. Uninterpreted LiDAR strip (~7 km long, from McMillan Stream to Three Mile Stream) and structural geomorphic map of the two key sites. Arrows point to the fault strands. (A), East of McMillan Stream and location of cross-section EE'. (B), Macs Knob and location of cross-section FF'.

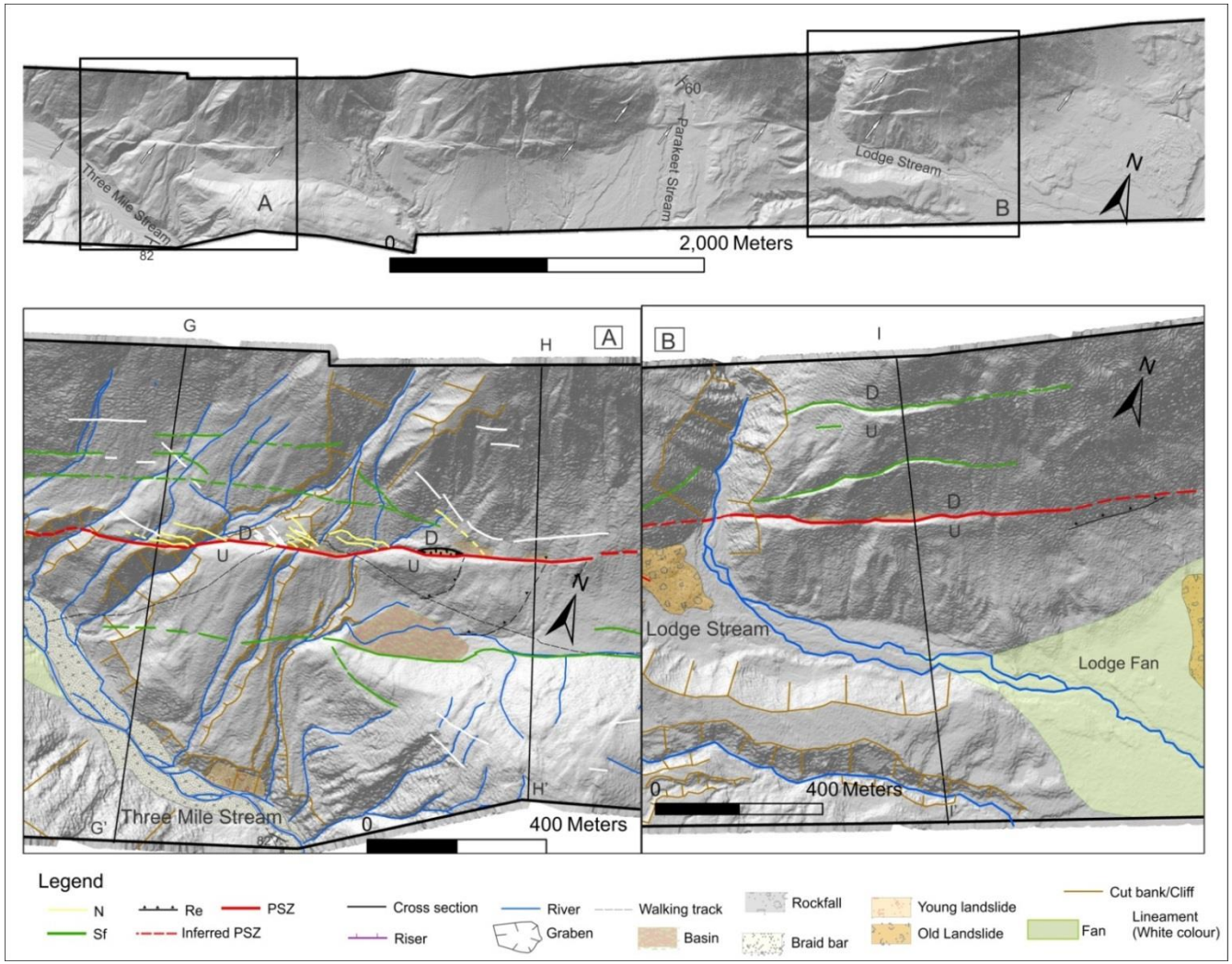


Figure 1.9. Uninterpreted LiDAR strip (~7 km long, from Three Mile Stream to Lodge Stream) and structural geomorphic map of the two key sites. Arrows point to the fault strands. (A), East of Three Mile Stream and locations of cross-sections GG' and HH'. (B), East of Lodge Stream and location of cross-section II'.

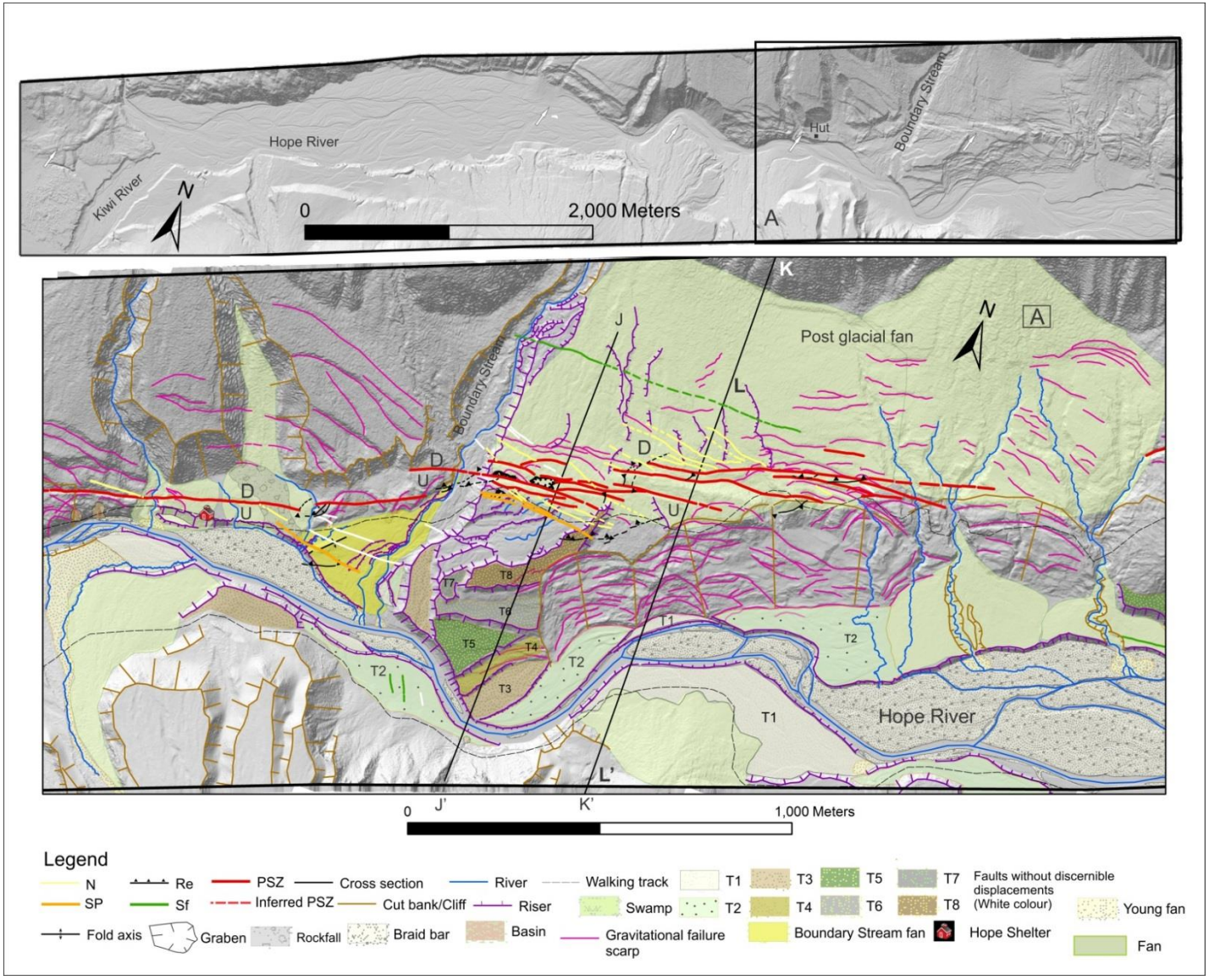


Figure 1.10. Uninterpreted LiDAR strip (it is ~8 km long, from Lodge Stream to the eastern extent of the LiDAR swath) and structural geomorphic map of the key site. Arrows point to the fault strands. (A), Hope Shelter and Boundary Stream and locations of cross-sections JJ', KK' and LL'.

045° to 050°. The result of the strike analysis shows that normal fault strands are oriented at an angle of 20°-30° (average 25°) clockwise with respect to the PSZ. Dextral-reverse fault strands are oriented at an angle of 5°-20° (average 12.5°) counter-clockwise with respect to the PSZ.

### 1.6.2 FDZ width and asymmetry

The results reveal that the FDZ width is spatially variable along the fault length with three major peaks (Figs. 1.5-1.6). The FDZ width varies from a few metres, where it is equivalent to the PSZ width, to up to 500 m including the three fault groups described in the methodology section (Fig. 1.5). The average width of the FDZ is ~200 m. The results of the FDZ width measurements with respect to the PSZ are presented in Table 1.2 and Fig. 1.6. In total, 57% of the measurements were taken north of PSZ and 33% were taken south of the PSZ (Table 1.2). The remainder of measurements (10%) was centrally distributed with respect to the PSZ (Figs. 1.5-1.6, Table 1.2). At locations where landforms of equivalent age enabled structures to be compared to the north and south of the PSZ (Fig. 1.6) there is considerable spatial variability in terms of the degree of symmetry about the PSZ. For instance, at distances ~5-8 km and ~26-28 km (Fig. 1.6), the FDZ is wider north of the PSZ than south of it, whereas at distance ~14.5-16 km (Fig. 1.6) the FDZ is wider to the south of the PSZ. Over much of the strike length, the FDZ as currently expressed in the landscape is highly asymmetric with respect to the PSZ. Similar asymmetry is commonly observed in exhumed strike-slip fault zones (e.g., Schulz and Evans, 2000).

Only 30% of the FDZ width north of the fault is narrower than 100 m, 55% of it is wider than 200 m and narrower than 300 m, and 15% of it is wider than 300 m (Table 1.2). In contrast, 48% of the FDZ width south of the fault is narrower than 100 m, 43% of it is wider than 200 m and narrower than 300 m, and only 9% of it is wider than 300 m (Table 1.2). The FDZ is distributed more to the north of the PSZ, and is on average wider there, compared to the FDZ on the south side of the PSZ.

### 1.6.3 Relationship between FDZ and PSZ orientation

Where strikes of the PSZ strands are in the range of 070°-075° the FDZ width is typically a few metres to ~200 m wide (Fig. 1.5). In contrast, where strikes of the PSZ strands deflect away from 070° to 075°, the FDZ width is wider and increases up to ~500 m. Differential strikes graph shows three major peaks along the fault length that are fairly

concordant with wider distribution of the FDZ (Fig. 1.6). Differential strikes vary from 0° to 22° with an increasing trend from west to east of the LiDAR swath. The maximum local changes in strike are up to 10° in the west, 16° near the middle, and 22° toward the eastern end of the study area (Fig. 1.6).

Table 1.2. Characteristics of the deformation zone north and south of the fault. In total, 415 measurements were done. Number, percentage and distribution of measurements north and south of the fault are shown. Detailed classification of the FDZ shows that how much of it is narrower than 100 m, between 100-200 m wide, between 300-400 m wide, and wider than 400 m north and south of the fault. Along 10 percent of the PSZ, the FDZ is only limited to the heights of scarps (FDZ is a few meter wide).

| | | | **Distribution of the FDZ with respect to the PSZ** | **Number and percentage of Values ≤ 100 m** | **Number and percentage of values > 100 and ≤ 200 m** | **Number and percentage of values > 200 and ≤ 300 m** | **Number and percentage of values > 300 and ≤ 400 m** | **Number and percentage of Values > 400 m** |
|---|---|---|---|---|---|---|---|---|
| **Measurements of the FDZ width along the fault length (Total = 415)** | **Number of measurements with positive values (north of the fault)** | 236 | 57% of the FDZ is located north of the fault | 70, 30% | 47, 20% | 82, 35% | 37, 15% | 0, 0% |
| | **Number of measurements with negative values (south of the fault)** | 138 | 33% of the FDZ is located south of the fault | 66, 48% | 39, 28% | 21, 15% | 11, 8% | 1, 1% |
| | **Number of measurements where FDZ is equal to the PSZ** | 41 | 10% of the PSZ shows FDZ equal to the PSZ | ---------- | ---------- | ---------- | ---------- | ---------- |

### 1.6.4 Relationship between FDZ width and topography

The fault occupies open valleys and rangefronts and cuts across topography at elevations ranging from 530 to 960 m a.s.l. (Fig. 1.6). The results of evaluating the effect of varying topography on the FDZ width reveal that the narrowest parts of the FDZ are located where it crosses both the lowest elevation and youngest deposits (near Landslip Stream, at McKenzie fan, and near Hope Shelter) and the highest elevation and oldest alluvial fan deposits (at Macs Knob and west of Hope-Kiwi River confluence) in the study area (Figs. 1.2 and 1.5-1.6) indicating that the FDZ width shows no systematic relationship with landscape age or elevation. Where steep (≥ 25° slope) HW (north of the fault) topographic relief is present and exceeds FW relief near river valleys, secondary faults are abundant and the FDZ width is ~300-450 m (Figs. 1.8A and 1.9A-B, cross-sections GG′ and II′, and Fig. 1.10, cross-section JJ′). Under the same topographic configuration but farther away from the river valleys, the FDZ width is narrower, i.e. 200-250 m (Fig. 1.9A, cross-section HH′ and Fig. 1.10, cross-sections KK′-LL′, and Figs. 1.5-1.6). In Macs Knob, where steep (≥ 25° slope) HW (south of the fault) topographic relief is present and exceeds FW relief far from river valleys, secondary faults are rare and the FDZ width is confined to a surface rupture up to ~100 m wide (Fig. 1.8B, cross-section FF′, and Figs. 1.5-1.6). In areas of low HW and FW

topographic relief (e.g., modern stream beds or late Holocene surfaces) the FDZ width is either nearly similar to the former (Fig. 1.7B, see cross-sections CC′ and DD′) or more confined than the latter (Fig. 1.7A, cross-section AA′, and Fig. 1.10A, see the single fault strand near the Hope Shelter, and Figs. 1.5-1.6).

The higher differential strikes correlate with the higher differential topographic peaks and the wider FDZ (e.g., east of Macs Knob, the differential strike range is 0°-16°, DT1 peak is 300, DT2 peak is 650, DT3 peak is 700, and the FDZ is up to 500 m wide), and the lower differential strikes correlate with the lower differential topographic peaks and the narrower FDZ (e.g., at Macs Knob, the differential strike range is 0°-7°, DT1 peak is 0, DT2 peak is -300, DT3 peak is -500, and the FDZ is up to 100 m wide) (Fig. 1.6).

### 1.6.5 PSZ subsurface geometry and segmentation

The PSZ strand across Macs Knob bends slightly to the north with increased elevation and in several locations the strand is observed to migrate upstream across stream valley bottoms, indicating a southerly fault dip of this strand (Fig. 1.8B). Structure contours indicate a dip of 65° SE for the PSZ strand across Macs Knob and 35° SE for the thrust flake. Nearby bedrock shear zones and fractures dip 80-85° S (Langridge, 2004). The cross-section FF′ through Macs Knob presents a model to reconcile these fault orientations, showing a near-surface shallowing in the fault dip (Fig. 1.11).

The PSZ across Lodge Stream and east of McMillan Stream areas bends slightly to the south with increasing elevation and locally migrates upstream across stream valley bottoms, indicating an overall northerly fault dip (Fig. 1.9A-B). Structure contours indicate a near-surface fault dip of 60° NW at the Lodge Stream area and 63° NW at the east of McMillan Stream area for the PSZ. The cross-sections in the Three Mile Stream, Macs Knob, east of McMillan stream and Lodge Stream areas portray my interpretation of a shallowing fault dip in the cover deposits compared to the underlying bedrock fault (Figs. 1.11-1.12). In these instances the near surface fault dip inferred from PSZ structural contours is shallower than the inferred dip in the underlying bedrock, with a ‘downslope rotation’ away from the proximal topographic high. The strike continuity of the PSZ trace throughout the Hurunui segment despite different dip directions suggests that the Hurunui segment of the Hope Fault is likely to consist of smaller, oppositely dipping faults (i.e. sub-segments) that are structurally linked and enable through-going rupture propagation. The propagation of coseismic strike-slip ruptures through multiple faults is commonly observed in historical

earthquakes (e.g., 2001 Kunlun earthquake, Lin et al., 2003; 1991 Landers earthquake, Sieh et al., 1993; 1999 Hector Mine earthquake; Li et al., 2003).

### 1.6.6 Relationship between FDZ width and sediment thickness

The estimated depth-to-bedrock across the FDZ (average thickness of cover integrated over FDZ width) varies from ~0 to 250 m (Figs. 1.11-1.12 and Table 1.3). Figure 1.13 shows two diagrams that examine the effect of estimated depths-to-bedrock on the FDZ width, and on the ratio of the amount of fractures/faults to the FDZ width for any particular sample site (cross-section). Figure 1.13A shows two different linear correlations; one between cross-sections AA′, FF′ and KK′ and one between the rest of the cross-sections. The smaller group is composed of those cross-sections with the PSZ strikes of 071°-074° and more importantly the strikes of the PSZ segments here show a small variation with the strikes of their adjacent segments (e.g., min. and max. variations are 0°-5°, Table 1.3). The larger group is composed of those cross-sections with the PSZ strikes of 067°-085° and more importantly the strikes of the PSZ segments here show a bigger variation with the strikes of their adjacent segments (e.g., min. and max. variations are 6°-15°, Table 1.3). The data from both groups indicate an increase in FDZ width with increased sediment thickness, with an additional role of fault orientation and strike variation. For a constant sediment thickness, significant variation in FDZ width is likely to reflect fault geometry (existence of step-overs or fault bends vs. a long linear PSZ). A partial correlation between the depths to bedrock and the ratio of the number of fault/fractures to the FDZ width is shown on Fig. 1.13B.

## 1.7 **Discussion and complications**

A comparison of LiDAR fault mapping with the previous field mapping (Lensen, 1962; Bowen, 1964; Gregg, 1964; Warren, 1967; Nathan et al., 2002; Langridge and Berryman, 2005; Rattenbury et al., 2006; Langridge et al., 2013, 2014) indicates that the use of LiDAR has enabled large improvements in the detection and mapping of the entire FDZ in this densely forested terrain. The high-resolution mapping of the Hurunui segment surface rupture provides new evidence for previously unknown structures and displacements. Good examples of this include the secondary structures (off the PSZ), the en echelon structures, the gravitational failure scarps, the normal and reverse faults associated with the PSZ, and the

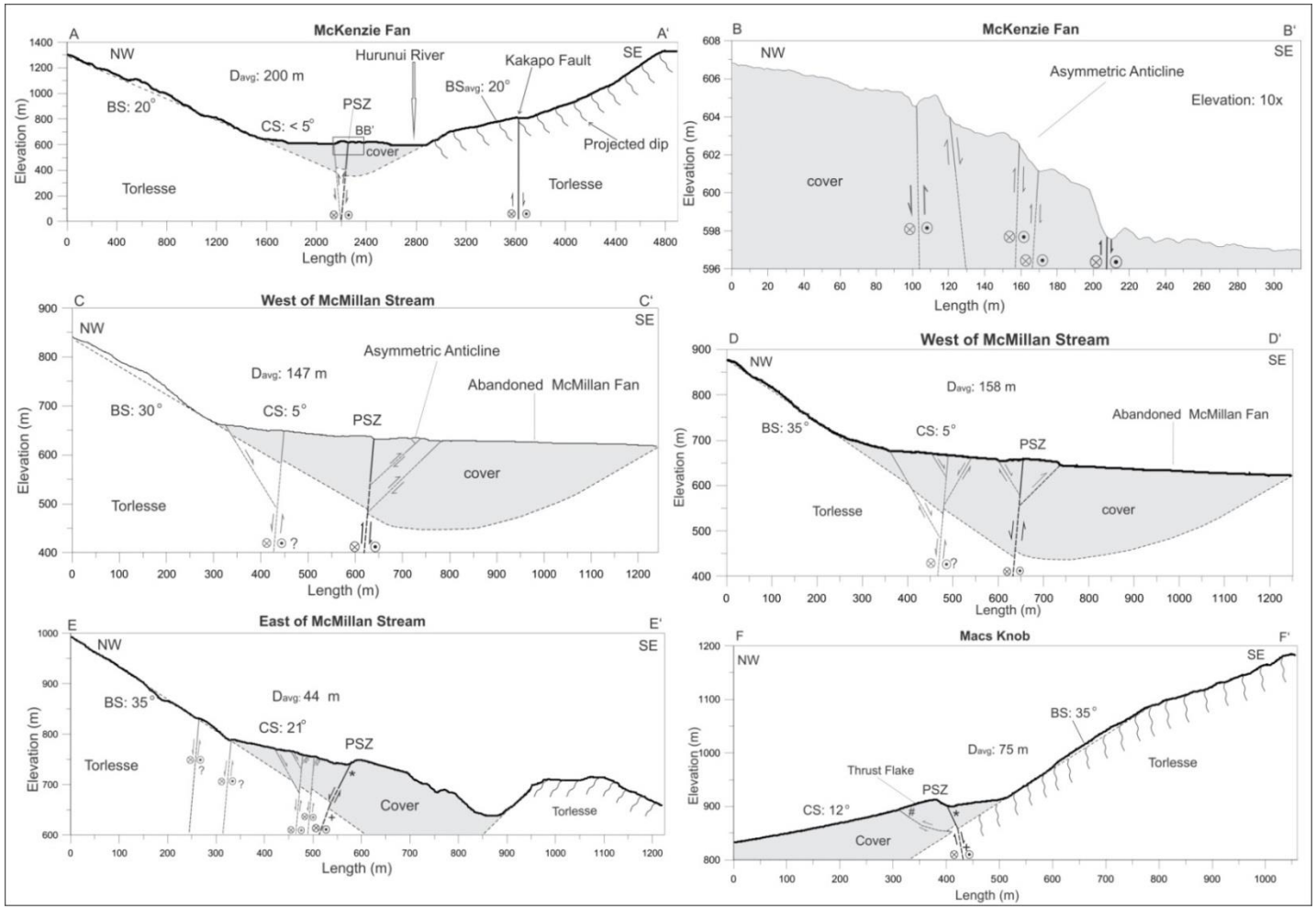


Figure 1.11. Cross-sections AA' to FF' showing fault models at depth. Dip angle of the PSZ considered being 85° in both bedrock and covering deposits where no other data were available. Abbreviations: BS: Bedrock Slope, CS: Cover Slope, Davg: average depth of the cover deposits beneath the FDZ. Symbols in cross-section EE': +, dip angle of 70° NW for the PSZ measured from bedrock in the field by Langridge (2004), *, dip angle of 63° NW for the PSZ measured from LiDAR-derived structural contours. Symbols in cross-section FF': *, dip angle of 65° SE for the PSZ measured from LiDAR-derived structural contours, #, dip angle of 35° SE for the thrust flake measured from LiDAR-derived structural contours, +, dip angle of 80° SE for the PSZ measured from bedrock in the field by Langridge (2004).

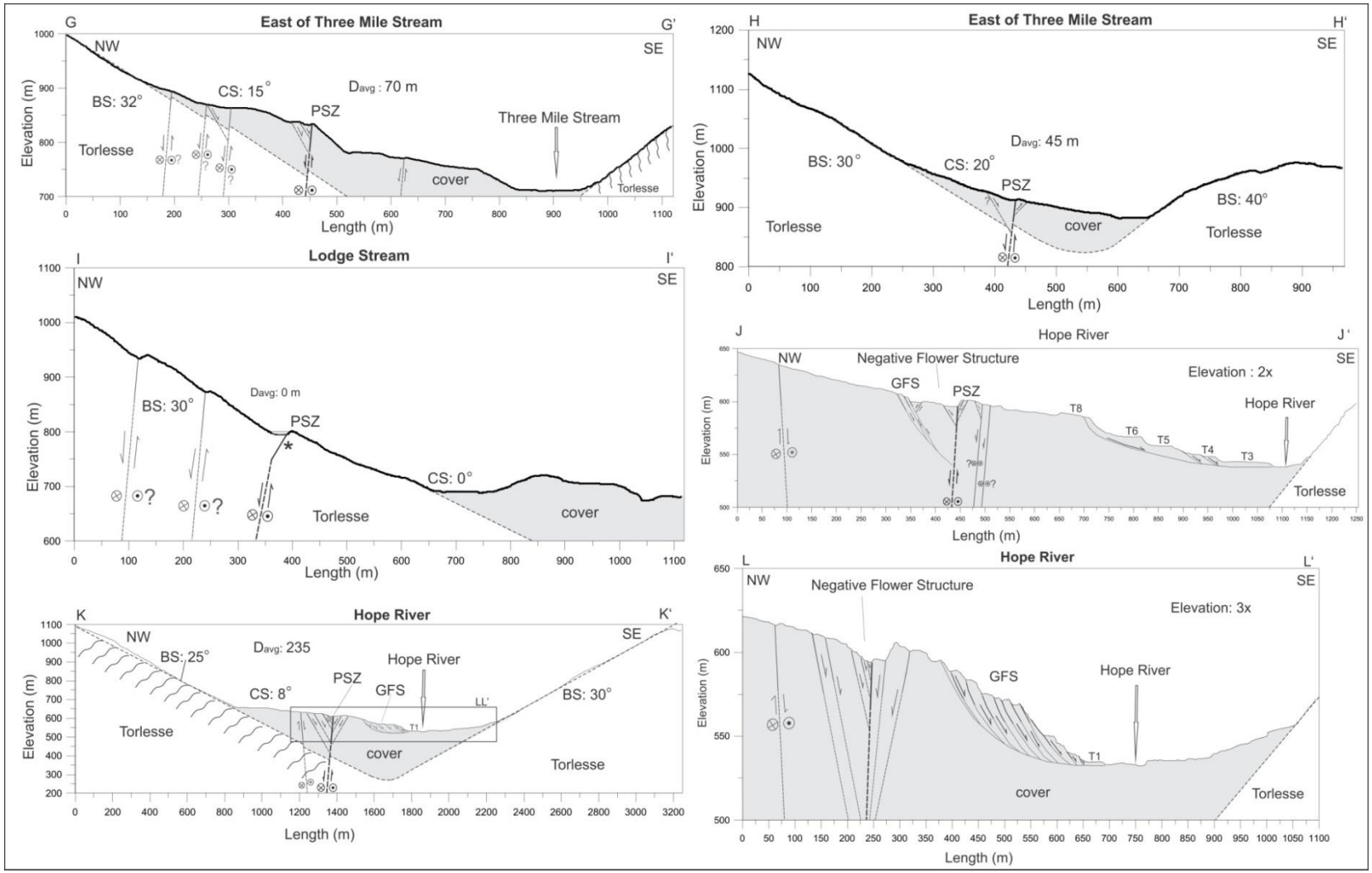


Figure 1.12. Cross-sections GG' to LL' showing fault models at depth. Dip angle of the PSZ is considered to be 85° in both bedrock and cover deposits where no other data were available. Abbreviations: BS: Bedrock Slope, CS: Cover Slope, $D_{avg}$: average depth of the cover deposits beneath the FDZ, GFS: Gravity Failure Scarps. Symbol * in cross-section II': dip angle of 60° NW for the PSZ measured from LiDAR-derived structural contours.

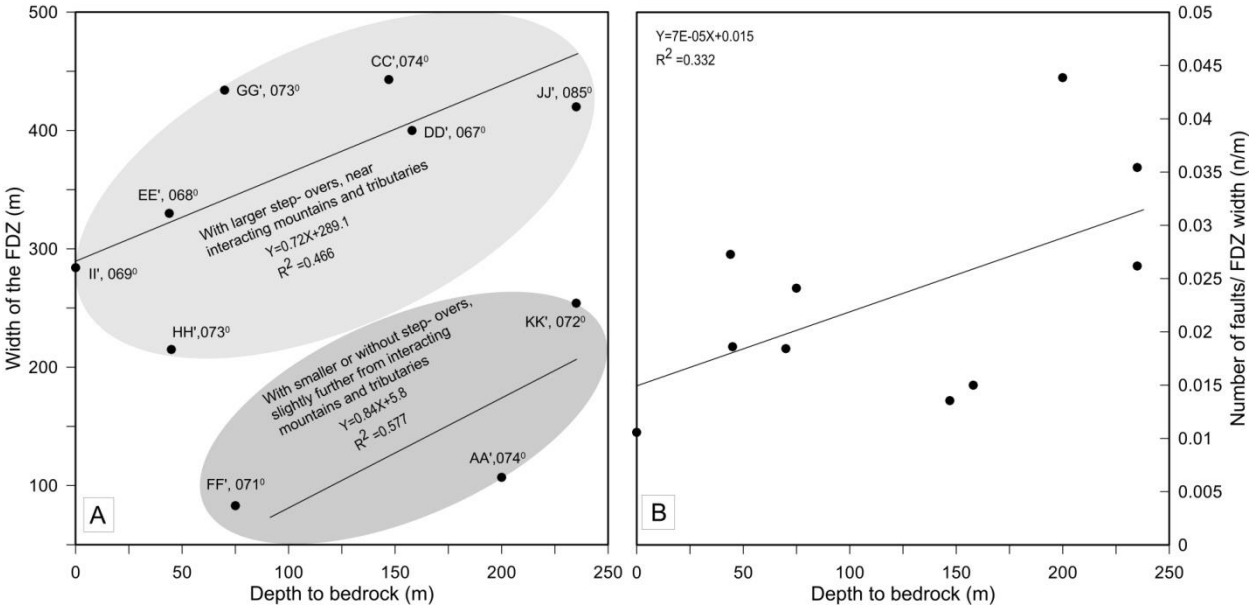


Figure 1.13. Impact of average depth of the cover deposits beneath the FDZ on the FDZ width and fault density within the FDZ. (A), Two groups of cross-sections with correlations between their samples are identified. These groups have different characteristics (see Table 1.3 and comments related to each cross-section). Cross-sections are presented with their ID and the strike of the PSZ strand. For Example: AA, 074° means that cross-section AA' includes a PSZ strand that strikes 074°. (B), A partial relationship appears between the average depth-to-bedrock beneath the PSZ and the number of faults included within the FDZ in each cross-section.

displaced terraces and risers to the east of McMillan Stream under thick vegetation (Figs. 1.7-1.10). Many of these features had neither been observed from aerial photos, nor seen in the forest during previous reconnaissance studies that focused mainly on the PSZ (e.g., Freund, 1971; Browne, 1987; Langridge, 2004; Langridge and Berryman, 2005). Here, I use the mapped structures as proxies of the fault kinematics and near-surface geometry, and discuss their distribution and abundance in relation to topography, fault strike and thickness of poorly consolidated cover.

### 1.7.1 Relationship of fault orientations and kinematics with respect to local and regional stress fields

Transpressive and transtensive faults can be characterized by the angle α (obliquity angle) between the PSZ and the horizontal convergence or extension directions respectively (Woodcock and Fischer, 1986; Cunningham and Mann, 2007; Scholz et al., 2010; Carne and Little, 2012). Analogue models show kinematic and geometric differences between structures forming at low angles of obliquity ($0° \leq \alpha \leq 15°$) and structures forming at high angles of obliquity ($30° \leq \alpha \leq 90°$) (Casas et al., 2001). Where α is ≤ 15°, deformation is more focused on a steeply dipping (> 70°) PSZ and structures are typical of the Riedel model of simple

shear (Fig. 1.3A), but where α is ≥ 15°, an asymmetric deformation zone is distributed over a shallowly dipping (< 40°) PSZ (Casas et al., 2001). This distributed deformation zone could be in the form of uplift resulting from transpression, or in the form of basin resulting from transtension, depending on the stress regime.

Table 1.3. Structural and morphological characteristics of the cross-sections.

| **Cross-sections and comments** | **Fault Strike** | **Average depth of cover deposits under the PSZ** | **Fault density (no)** | **FDZ width** | **Slope** |
|---|---|---|---|---|---|
| **AA'- BB'** Right step-over, 3° change in strike, situated in valley | 74° | 200 | 5 | 107at the cross-section | < 5° |
| **CC'** 10° fault bend, situated in valley | 64°-74° | 147 | 6 | 443 | 5° |
| **DD'** Left step-over, 8° change in strike, situated in valley | 67 | 158 | 6 | 400 | 5° |
| **EE'** Situated at the mountain flank, near 2 large branches of McMillan Stream and some smaller tributaries | 68 | 44 | 9 | 330 | 21° |
| **FF'** Situated at the mountain flank, oldest part of the landscape, nearly at the same distance to McMillan and Three Mile Stream (not very close to large streams) | 71 | 75 | 2 | 83 | 12° |
| **GG'** Left step-over, 9° change in strike, situated at the mountain flank, near Three Mile Stream and its tributaries | 73 | 70 | 8 | 434 | 15° |
| **HH'** Left step-over, 6° change in strike, situated at the mountain flank, not very close to Three Mile Stream and its tributaries | 73 | 45 | 4 | 215 | 20° |
| **II'** Left step-over, 10° change in strike, situated at the mountain flank, near Lodge Stream | 69 | 0 | 3 | 284 | 30° |
| **JJ'** Left step-over, 15° bend, en echelon structures, situated at the mountain flank, near Boundary Stream and Hope River | 85 | 235? | 11 | 420 | 8° |
| **KK'** En echelon structures, 5° change in strike of the main PSZ strands, situated at the mountain flank, at a greater distance to Boundary Stream (with respect to JJ') and near Hope River | 72 | 235 | 9 | 254 | 8° |

With this in mind, the strike analysis of the PSZ strands, using LiDAR data, shows that the primary azimuthal direction of the PSZ (070°-075°) is at an angle of 1°-6° to the Pacific plate slip vector orientation calculated at the fault (249°; DeMets et al., 2010). The Hurunui segment appears as a near-continuous fault along its length on LiDAR with a favourable orientation to transfer strike-slip motion between the Hikurangi subduction zone and the Alpine Fault (Fig. 1.1). In a general view, the fault is remarkably straight with a gentle curve in its middle (Figs. 1.2 and 1.8). I do not observe large-sized basins, uplift zones, or major step-overs. Generally, I observe structures expected for strike-slip systems that are physically connected to the PSZ, and in some areas, a clear superposition of structures is recognized around the PSZ (Fig. 1.7B). However, the distribution of these structures looks different than the models particularly in terms of fault-normal distribution of structures with respect to the PSZ (Fig. 1.3A) (e.g., the majority of normal faults are located south of the fault and the majority of reverse faults are located north of the fault instead of forming both north and south of the PSZ). Together, the PSZ and structures within the second group (see fault classifications) make a narrower deformation zone of up to ~250 m wide, which is nearly symmetric along the PSZ. However, the entire FDZ including all structures is up to ~500 m wide and definitely asymmetric along the PSZ. Dextral displacements along the PSZ are well preserved and the ratio of horizontal to vertical displacements indicates primarily strike-slip (~7 ± 2:1, Langridge and Berryman, 2005). All of the described characteristics above confirm that the fault is predominantly dextral strike-slip and steeply dipping toward the NW, which is supported by field data (see Methodology section).

Near-fault stress fields may differ from regional stresses (e.g., Holt et al., 2013) due to coseismic slip variations and variations in fault strike and geometry (Lunina et al., 2008), variations in thickness and material properties of faulted media (e.g., Richard et al., 1991, 1995; Norris and Cooper, 1997; Shipton and Cowie, 2003; Barth et al., 2012), and variations in topography (Norris and Cooper, 1995; Eusden et al., 2000, 2005; Barth et al., 2012). Furthermore, fault rotation with progressive displacement can result in cumulative fault kinematic histories that do not directly relate to the present fault orientation and/or slip in the most recent event. The existence of high and variable near-fault surface topography, variable fault strikes and geometries, and variations in sediment thickness adjacent to the Hurunui segment all provide potential influences on near fault stresses in this instance. With this in mind, I use LiDAR-derived orientations and kinematics of the PSZ and normal and dextral-reverse faults connected to the PSZ to derive information about the near-fault stress field.

Assuming that the orientation and kinematics of mapped faults can be used to calculate a strain ellipse that reflects the stress field, and that the $\sigma_2$ is vertical in strike-slip faulting, I estimate $\sigma_1$ = 100-105° and $\sigma_3$ = 010°-015°. Geodetic measurements of incremental strain near the Hope Fault used as a proxy for the contemporary stress field indicate $\sigma_1$ is oriented between 100° and 110° (Fig. 1.1; see W vector) (Wallace et al., 2007, 2012). Paleostress tensors derived from focal mechanisms of shallow crustal earthquakes in the northern South Island (Fig. 1.1; see PHS vector) similarly indicate $\sigma_1$ near the Hurunui segment trends 115° (Nicol and Wise, 1992; Pettinga and Wise, 1994). The contemporary stress field calculated by Sibson et al. (2011) using stress inversions from earthquake focal mechanisms shows $\sigma_1$ at 115° ± 16° for North Canterbury-Marlborough region. From these data I conclude that the Hurunui segment of the Hope Fault is optimally oriented for dextral strike-slip within the regional stress field.

Mapped normal faults along the Hurunui segment range in length from 18 to 360 m (average = 122 m), have accumulated maximum vertical displacements of 0.2 to 6 m, and have orientations of 095° to 100° (Fig. 1.4). Where normal fault scarps are present on the youngest parts of the landscape (e.g., on the active alluvial plain of the Hurunui River) adjacent to parts of the PSZ that record only the most recent surface rupture (Langridge et al., 2013), the normal fault lengths are 80 to 85 m, the vertical displacements are 0.2 to 0.5 m, and the orientations are ~100°. Only four of the 70 identified normal faults contain some evidence for dextral displacement, 31 contain features that have not been laterally offset (i.e., have purely dip slip kinematics), and 35 faults do not contain features that enable assessment of whether lateral displacement is present. In general, it appears that the orientation and kinematics of many of the identified normal faults are best explained by a vertical $\sigma_1$, and a $\sigma_3$ orientation of 005°-010° that is perpendicular to the regional $\sigma_1$ orientation. In particular, the $\sigma_3$ orientation derived from single-event normal faults where no near-field variations in topography or sediment thickness are present indicates consistency between the near-fault coseismic and regional stress fields in the absence of local conditions that could perturb the stress field.

Mapped dextral-reverse faults range in length from 8 to 364 m (average = 76 m) with total accumulated maximum slips of 0.5 to 4 m. Thirteen of the 55 identified dextral-reverse faults are associated with pop-up structures, 7 contain features that have not been laterally offset, 10 faults contain features with unambiguous evidence of dextral displacement, and 25 faults do not contain features that enable assessment of whether lateral displacement is

present. The average orientation of these faults (055°-065°; Fig. 1.4) is typically within 5°-20° of the PSZ and 35°-55° of the regional $\sigma_1$, consistent with oblique (rather than purely reverse) displacement.

### 1.7.2 Sackungen origin for secondary faults?

Sackungen are uphill-facing structures located on the upper parts of mountains and produced by gravitational spreading in slopes (McCalpin, 2003; Li et al., 2010). In the past, this terminology was used for the actual deep-seated gravitational slope deformation that is expressed on the surface by linear features, first introduced by Zischinsky (1966, 1969). McCalpin (2003) introduced three origins for sackungen formation: (1) tectonic origin (resulting from surface faulting), (2) earthquake origin (resulting from coseismic shaking), and (3) neither tectonic nor earthquake origins.

Uphill-facing scarps near the Hope Fault (called mountain faults, or antislope scarps or ridge rents) have been observed by Clayton (1965), Beck (1968) and Freund (1971). Clayton (1965) and Beck (1968) suggested that these features formed due to earthquake shaking on slopes that were oversteepened following LGM, and propagated laterally. Freund (1971) suggested that they are tectonic in origin because they were also observed on low elevation hills and areas where the valleys were lower than threshold steepness.

The secondary faults associated with the Hurunui segment have characteristics implying that they are tectonic in origin: (1) they are preferentially located at lower parts of mountains in a close proximity (i.e. within 300 m) to the PSZ, (2) they are linear, long, and fault-parallel so that they can easily be discriminated from arcuate uphill-facing features occupying higher elevations and slopes (near ridge crests) in the study site, (3) some of them have apparently dextrally displaced streams, (4) they are typically associated with kinematically linked smaller-scale structures, (5) their surface traces occasionally cut through different slopes along strike, which is not typical in the classical definition of sackungen (McCalpin, 2003), and (6) their orientation and kinematics indicate strain orientations consistent with formation by regional stresses (as opposed to topographic stresses alone). I thus attribute these features to tectonic faulting, as opposed to sackungen.

### 1.7.3 Topographic influence on near surface fault geometry and surface rupture morphology

In this section I discuss the possibility that topography exerts a fundamental influence on the observed characteristics of the FDZ including the formation of secondary structures. These secondary structures are smaller in size than the second order faults in the study of Barth et al. (2012), and they are more linear than the normal faults shown by Eusden et al. (2000, 2005). I observe that the FDZ is composed of a series of dextral, dextral–normal and normal faults that form negative flower structures. The FDZ is wider both where the strike of the PSZ deflects away from 070° to 075° (Fig. 1.5) and where mountain flanks have been incised by tributary streams (Figs. 1.7-1.10). Moreover, the FDZ has an asymmetric distribution with respect to the PSZ with a wider zone of deformation accommodated where topographic relief is greater. It appears that, where high topography deflects the PSZ in a way to align it with the plate boundary vector, the FDZ is narrowest. However, at many places where high topography locally misaligns segments of the PSZ with the plate boundary vector, the FDZ is wider (Figs. 1.5 and 1.14A). This is consistent with the obliquity concept explained by several authors (Woodcock and Fischer, 1986; Cunningham and Mann, 2007; Scholz et al., 2010; Carne and Little, 2012). I suggest that the width of the resulting deformation zone is spatially variable due to two factors: (1) proximity of the PSZ to tributary stream canyons (see Norris and Cooper, 1995, 1997 for the Alpine Fault), and (2) size of the tributary stream canyons (Norris and Cooper, 1995). For example; the FDZ is the widest where the misaligned PSZ segments are near larger stream canyons (like McMillan and Three Mile streams), narrower where it is near smaller stream canyons (like Parakeet and Lodge streams), and narrowest where it is more distal to stream canyons (see Fig. 1.2 for locations, and Figs. 1.7-1.10 for explanations). This is in agreement with the stress perturbation concept as streams form canyons that are different from steep mountainous topography elsewhere along the fault.

Topographic relief creates spatial variations in gravitational loads that may perturb near-surface and regional stress fields (McTigue and Mei, 1981; McTigue and Stein, 1984; Savage et al., 1985; Savage and Swolfs, 1986; Liu and Zoback, 1992). McTigue and Mei (1981) used 2D models to compute the magnitude and orientation of the topographically-induced perturbed tectonic stresses in the upper crust. Their results suggested that regional horizontal compression can be modified (decreased or changed to tension) in the proximity of high topography. Savage et al. (1985) modelled the near-surface gravity-induced stresses for

an isolated symmetric ridge and valley. Their results revealed that horizontal compressive stresses form near the ridge top and decline with increasing Poisson's ratio. In comparison, horizontal tensile stresses form beneath the valley; however, they reduce and change to compressive with increasing Poisson's ratio. They also showed that the magnitude of the gravity-induced stresses is approximately equal to ρgb, where ρ is the mass per unit volume, g is the gravitational acceleration, and b is the height of the ridge or the depth of the valley. Savage and Swolfs (1986) modelled the effect of tectonic and gravitational stress in long symmetric ridges and valleys. Their results also showed that topography decreases regional tectonic compression near the ridge top and can change it to tension where the slope is steep, but the regional tectonic stress focuses in the valleys. When the effect of topography on regional tectonic stresses is added to the effect of topography on gravitational stresses, the lateral components of the gravity-induced compressive stress at the ridge top are slightly increased while the gravity-induced tensile stress beneath the valley is slightly decreased (Savage and Swolfs, 1986). Norris and Cooper (1995, 1997) also discussed the effect of topographically perturbed stresses on developing serial and parallel partitioning of the central segment of the dextral-reverse Alpine Fault and suggested a depth of 1-4 km for stress perturbation around the fault (they considered the depth of stress disturbance to be one to two times the valley relief (Savage and Swolfs, 1986)). In all of the above studies, the relationship between topographic relief and the FDZ width has not been investigated specifically; however, mechanistic explanations linking topography with the state of stress on and around faults are presented.

I argue based on the mapping data that if the zone of high shear stress on the valley sides is strong enough, it can rotate the fault plane, thereby influencing rupture propagation and possibly causing fault bifurcation into separate segments, resulting in enhanced fault geometric complexities and increasing deformation zone width. The local valley relief adjacent to the Hurunui segment is 700-1100 m (Fig. 1.6) suggesting that the near-fault stress field could be perturbed to depths of ~1-2 km. The modelled cross-sections using field data show that shallower (< 85°) dip angles of the PSZ (e.g., 63°, cross-section EE′ and 65° cross-section FF′), occur in cover deposits at depths generally < 100-200 m; although, I cannot dismiss the possibility of additional fault rotation at depth. The results strongly suggest that the Hurunui segment is dominantly strike-slip with a dip angle of ~85° NW at depth (along much of its length) or SE at a shallower depth (in Macs Knob), but can appear as a dextral-reverse or dextral–normal fault with dip angle of 60°-65° near the surface depending on the

existence of high topography south or north of the fault or thickness of deposits. The existence of an asymmetric FDZ along the PSZ also confirms the fault should be dipping more gently near the surface especially where it enters the cover deposits. The secondary faults are mostly parallel to sub-parallel to the PSZ, uphill-facing, small scale (average length = 160 m with only two of them being around 2 km long), and are only up to 500 m off the PSZ. They are likely to join with the dextral strike-slip PSZ at a shallow depth. If I project the faults downdip with the dip angles assumed in the methodology section, both the faults that are connected to the PSZ on the surface (e.g., normal and dextral-reverse faults) and the very small-scale faults that are connected to the secondary faults on the surface merge into a single PSZ strand or into their relevant major secondary fault at depths of ~50-200 m (see cross-sections BB′, CC′, DD′, EE′, FF′, GG′, JJ′ and KK′). In contrast, the larger dextral strike-slip secondary and splay faults (see other near-vertical dextral faults around the PSZ; cross-sections AA′, CC′, DD′, EE′, GG′, II′, JJ′, and KK′) would merge with the PSZ at deeper depths beyond the cross-sectional views. This is consistent with the suggestion of the stress perturbation depth around the fault in this area. The subsurface interaction of the majority of the faults (the branching depth) in most instances seems to be close to, or at the basement-cover interface, i.e., 50-200 m depth.

Scarps associated with some of the secondary faults range from ~0.1 to 6 m in height. The vertical single event displacement (along the PSZ) and recurrence interval time of the Hurunui segment, calculated by Langridge and Berryman (2005), are ~0.2 m and 300-500 years respectively. Therefore, some of the secondary faults with large vertical slip have likely ruptured and/or reactivated during multiple events, i.e., being coseismic features. It appears that at least many of them are well-established structures that accommodate slip during earthquake ruptures. The characteristics of many of the secondary features observed here are not consistent with the post-seismic collapse features documented by Eusden et al. (2000, 2005) (see S1.3.2 in Supplementary file). In contrast, their characteristics are consistent with the mapped and interpreted coseismic dextral-normal faults (third order faults) associated with the Alpine Fault (e.g., similar surface patterns and lengths, no cross-cutting relationship between the faults, locating on the range-ward side of the fault, large uphill-facing scarps) (Barth et al., 2012). The results of this study show that topography extending to fault-normal distances up to 1.5 km is important in influencing the morphologic properties of the FDZ. At locations where DT1 is around 0, but DT2 and DT3 yield highly positive or negative values, a relatively wide FDZ is still recorded. Topographic profiles DT1, DT2 and DT3 (Fig. 1.6),

all show that north of the PSZ is higher in elevation than south of it. The only exception is the Macs Knob region, in which higher mountains are south of the PSZ. I observe a strong correlation between the upthrown side of the fault and high topography along the entire length of the Hurunui segment, i.e., scarps are uphill-facing. I present a model (the 3D block diagram in Fig. 1.14A-B, see figures description) to explain the fault kinematics. In this model, high topography exerts a load on the fault plane and forces it to deflect away from the mountains. By variably loading the PSZ by differential topography along strike, the fault strike will vary and its dip can no longer remain very steep at very shallow depth near the base or on the flanks of the mountain so that it branches off to adjust itself and accommodate the local oblique motion exerted by topography. This model explains the production of uphill-facing scarps. The model and the results of the geomorphic mapping and topographic analysis suggest that the surface geometry of the PSZ and FDZ is locally controlled and independent of large-scale regional stress.

### 1.7.4 Depth-to-bedrock influence on surface rupture morphology

Field observations (e.g., Kunlun earthquake, Lin et al., 2003; El Mayor-Cucapah earthquake, Oskin et al., 2012) and models (e.g., Richard et al., 1991, 1995) indicate that fault zones are typically wider in unconsolidated cover deposits compared to consolidated deposits and basement rocks. The results of this study indicate that the thickness of the unconsolidated cover deposits is an important factor in influencing the FDZ width. However, the wide FDZ exposed along the cross-sections CC′, DD′, EE′, GG′, HH′, and JJ′ (Figs. 1.11-1.12 and Table 1.3) is not only a result of the thickness of cover deposits, but also related to the changes in fault strike (6°-15°) where there are step-overs or bends. The changes in the strike of the fault are resulted from different responses of the fault to the existing variable topography along it. Therefore, I believe that the thickness of cover deposits is a second order control (after topography relief) on the FDZ both at the flanks of mountains and adjacent to valleys. The latter implies that the existence of the fault step-overs or bends along the strike of the fault is the first order control on the FDZ (e.g., McKenzie and McMillan sites; Fig. 1.7A-B). An important first order control of topography is also illustrated by the 1888 Hope Fault rupture; the surface rupture is comparably narrow and straight where it traverses areas with minimal surface relief (i.e. no topographic loading) despite significant thicknesses of underlying unconsolidated outwash deposits, and is more complex (more fault step-overs and/or bends) in areas of higher topographic relief (Cowan, 1990; Cowan and McGlone, 1991).

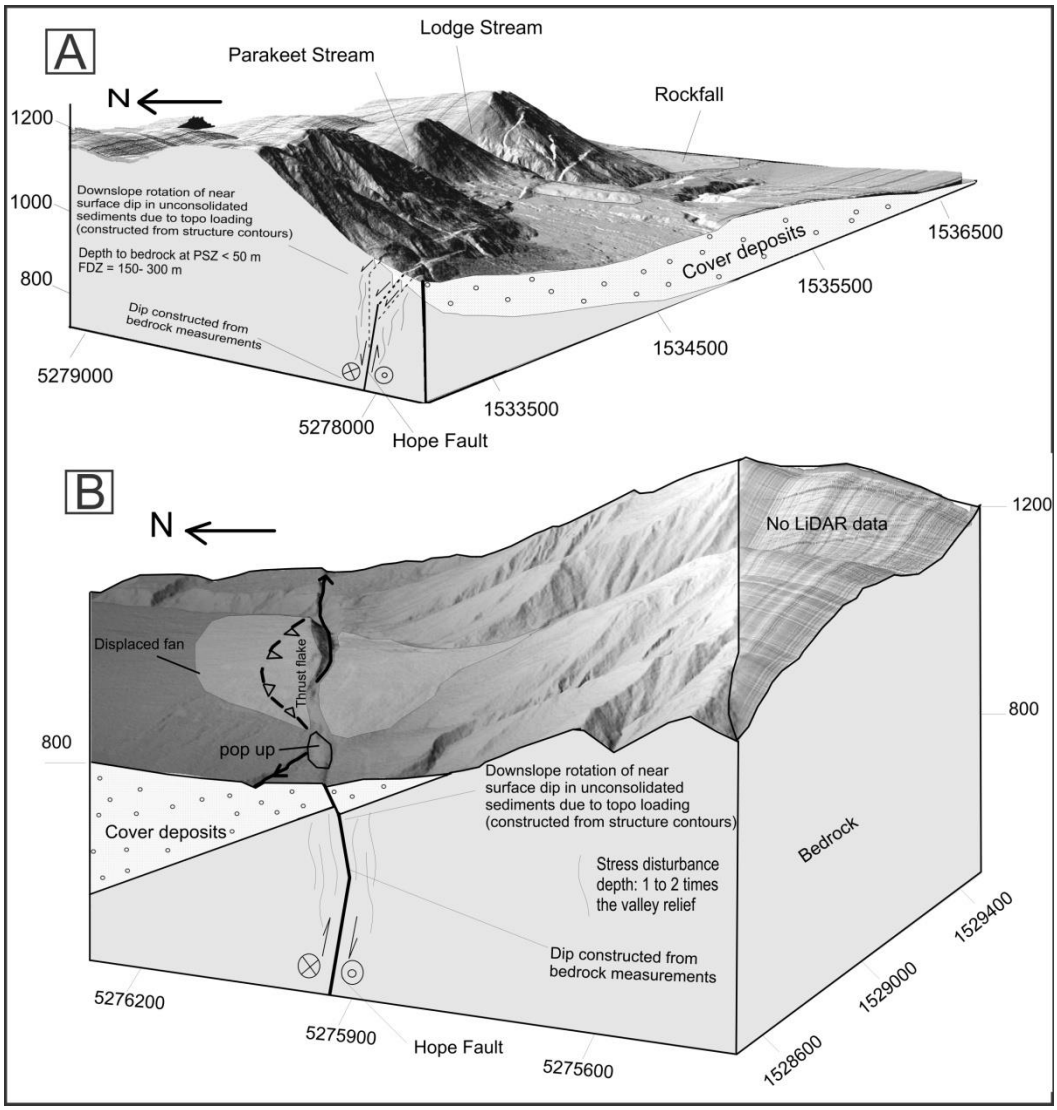


Figure 1.14. 3-D models of small portions of the LiDAR swath showing fault branching depths where the fault cuts flanks of mountains. The block diagrams were built using xyz LiDAR data and Surfer software. Note that all of the fault scarps are uphill-facing. I interpret that the fault escapes from topography as it propagates through the surface. (A), Parakeet site; high topography is north of the fault, more branching occurs where topography misaligned the fault strike with the regional stress orientation, deeper branching occurs in bedrock. (B), Macs Knob site; high topography is south of the fault, no deep branching occurs in bedrock because topography aligned the fault strike with the regional stress orientation and this site is the oldest part of the landscape (slip has been localized on a single fault strand over time), the branching depth is limited to the thickness of cover deposits (see cross-section FF').

### 1.7.5 Fault maturity, FDZ width, slip measurements, and paleoseismic implications

The Hope Fault is a structurally mature (Cowan et al., 1996), well-established and fast-slipping active fault with a recurrence interval of ~81-500 years (Cowan and McGlone, 1991; Langridge et al., 2003; Langridge and Berryman, 2005; Langridge et al., 2013). Despite this, deformation zones of up to ~2 km wide including transpressive wedges along the Conway

segment (Eusden et al., 2000, 2005), and up to 2.3 km wide including depressions and constraining bends along the Hope River segment (Freund, 1971; Cowan, 1989, 1990), and up to ~500 m wide including secondary structures along the Hurunui segment (this study) have been identified. As shown in Table 1.1, other mature strike-slip faults can also develop wide deformation zones. Therefore, it is important to study the key controlling factors, except the existence of step-overs or bends (fault complex geometries), on the rupture patterns and to investigate if there is a similar pattern.

In this study, I illustrate that along-strike variability in FDZ width and surface rupture complexity reflects variations in topographic loading and sediment thickness that alter the near-fault stress fields, fault geometries, and mechanical properties of the faulted substrate at shallow (< 1-2 km) depths. Significant near surface rupture complexity and possible variations in surface slip on any given structure may result despite simple, uniform slip on a confined, structurally simple underlying fault at seismogenic depths (e.g., Graymer et al., 2007). For this reason, it is possible in some instances that the total finite slip measured in previous investigations may not have captured all of the total displacement that was measured on the LiDAR. Furthermore, I do not account for possible distributed deformation that was not reflected by discrete surface rupture (e.g., Quigley et al., 2010, 2012; Van Dissen et al., 2011). As a consequence, previous slip rates estimated using slip measurements limited to the PSZ alone may have underestimated the slip rate in some instances along the Hope Fault (see also Oskin et al., 2012 as an example for the El Mayor-Cucapah surface rupture).

## 1.8 **Conclusions**

Quantitative and detailed LiDAR-derived mapping presented in this work confirm the value of LiDAR as a robust tool for the detailed mapping of fault structures under forest cover. Field-based studies, orthophotos and aerial images also played an important role in the fault and geomorphic mapping and interpretation. A detailed structural geomorphic map was produced for the entire LiDAR strip in this study. This study reveals that the Hurunui segment of the Hope Fault trends 070°-075° and is favourably oriented for dextral strike slip with respect to the orientation of the Pacific plate slip vector. The fault has evolved as a spatially diverse deformation zone that varies in width from a few metres to up to 500 m. This deformation zone has locally been controlled by the oblique component of slip resulting from topographic loading on the fault plane and deflecting it from its favourable orientation for strike-slip motion, the proximity of the fault to the major river valleys and thickness of

cover deposits. Large displacements on the structures forming the FDZ record multiple earthquakes since the late Pleistocene. The normal and dextral-reverse faults join with the dextral strike-slip PSZ close to, or at the basement-cover interface, i.e., ~50-200 m depth, indicating that the surface rupture zone complexity results from shallow (1-2 km) fault zone widening and bifurcation. The PSZ-parallel to -subparallel dextral secondary structures (average length = 160 m) forming wedges and dextral strike-slip splay faults could possibly merge with the dextral strike-slip PSZ at depths that are still within the expected penetration depth of topographically-influenced stress perturbations.

## Acknowledgements

I wish to thank NZ Natural Hazards Research Platform Grant 2010-GNS-01-NHRP and the New Zealand Earthquake Commission Capability Fund for funding this research. I thank the Department of Conservation and land owner of the Poplar Station Kevin Henderson for site access. I thank our field assistants Amir Rezanejad and Fidel Martín González and acknowledge Jocelyn Campbell, Chris Smart, Jarg Pettinga, Brendan Duffy, and Nic Barth for academic discussions. I also thank Mike Oskin and An Yin for constructive comments on this manuscript.

# CHAPTER 2. LATE HOLOCENE RUPTURE BEHAVOUR AND EARTHQUAKE CHRONOLOGY ON THE HOPE FAULT, NEW ZEALAND

# Late Holocene rupture behaviour and earthquake chronology on the Hope Fault, New Zealand

**Narges Khajavi[1,*], Robert M. Langridge[2], Mark C. Quigley[1, 6], Chris Smart[3], Amir Rezanejad[4], Fidel Martín-González[5]**

[1]Department of Geological Sciences, University of Canterbury, New Zealand
[2]GNS Science, Lower Hut, Wellington, New Zealand
[3]Department of Geography, University of Western Ontario, London, Canada
[4]Department of Civil Engineering, University of Canterbury, New Zealand
[5]Área de Geología -ESCET-, Universidad Rey Juan Carlos, Spain
[6]Now at School of Earth Sciences, The University of Melbourne, Australia
[*]Corresponding author. Email: narges.khajavi@pg.canterbury.ac.nz

Article history:
Submitted to: the Geological Society of America Bulletin in September 2014
Submitted in revised form in February 2015
Accepted in July 2015
Submitted in the final revised form in December 2015

## 2.1 Abstract

The Hope Fault is the most active and southernmost splay of the Marlborough Fault System (MFS) in the northern South Island of New Zealand. The fault comprises five geometrically-defined segments. Paleoseismic trenching and radiocarbon dating of faulted late Holocene sediments on the Hurunui segment of the Hope Fault are used to derive an earthquake chronology that extends from the historic 1888 $M_w$ 7.1 Amuri earthquake to ~300 A.D., thereby providing the longest chronologic record of earthquakes on the Hope Fault to date. Earthquake event horizons are identified by upward fault terminations, colluvial wedges, unconformities, and/or progressive folding of shutter basin deposits. Six earthquakes identified at A.D. 1888, 1740-1840, 1479-1623, 819-1092, 439-551, and 373-419 indicate a mean recurrence interval of ~298 ± 88 yr with successive median inter-event times ranging from 98 to 595 yrs. The large variance in inter-event times with respect to mean recurrence interval is explained by: (1) coalescing rupture overlap from the adjacent Hope River segment on to the Hurunui segment at the study site (including the 1888 $M_w$ 7.1 Amuri earthquake, sourced primarily from the Hope River segment), that results in apparently shorter inter-event times at the study site compared to mean recurrence intervals from adjacent fault segments, and (2) earthquake temporal clustering on the Hurunui segment, which could result in inter-event times that are significantly shorter or longer than inter-event times and mean recurrence intervals predicted by a periodic earthquake rupture model, and/or

(3) ‘missing’ events, which could result in inter-event times and mean recurrence intervals at the study site that are longer than the actual mean recurrence interval. While I cannot exclude option (3) as a possibility, I prefer options (1) and (2) to explain earthquake chronologies and rupture behaviour on the Hurunui segment of the Hope Fault, given the detailed nature of the geologic and chronologic investigations. By demonstrating that the 1888 Amuri earthquake propagated through a proposed segment boundary, I provide first evidence for coseismic multi-segment ruptures on the Hope Fault. In contrast, the penultimate earthquake ruptured the Hurunui segment at 1740-1840 A.D. with no known rupture of the Hope River segment. Paleoearthquake records near geometrically complex segment structural boundaries on major strike-slip faults may show temporal recurrence distributions resulting from earthquake ruptures that variably arrest or propagate through proposed segment boundaries. I point that earthquake recurrence along major strike-slip plate boundary faults may vary between more periodic and more episodic end-members, even on adjacent, geometrically-defined segments.

## 2.2 **Introduction**

Earthquake moment magnitude ($M_w$) scales with the source rupture area (length x width) and average coseismic displacement (e.g., Kanamori, 1977; Wells and Coppersmith, 1994; Leonard, 2010). A major focus of paleoseismic fault trenching is therefore to document the surface rupture lengths and coseismic displacements of historic and prehistoric earthquake surface ruptures to determine past earthquake $M_w$ for integration into seismic hazard models (e.g., McCalpin, 2009). However the interpretation of paleoseismic trench data and event chronology can be complicated due to: (1) the complex nature of fault ruptures propagating through heterogeneous packages of sediments (Quigley et al., 2012), (2) variable topography (Khajavi et al., 2014) combined with surface processes that can lead to incomplete, spatially variable, or ambiguous evidence for earthquake events over short or long fault distances, even for structurally mature faults (Scharer et al., 2007; Hartleb et al., 2003, 2006), and (3) rupture segmentation on large strike-slip fault systems, which are typically composed of multiple segments with intervening stepovers or bends that can impede rupture propagation (Wesnousky, 1988, 2006; Oglesby, 2005; Elliott et al., 2009). Slip distributions from earthquake ruptures on adjacent fault segments may overlap, resulting in re-rupture at the overlapping zone at time-scales that are relatively short (i.e. months to decades) compared to the expected return times of major earthquakes on individual segments. Examples of this are: the 1999 Izmit and Düzce earthquakes (Hartleb et al., 2002; Langridge

et al., 2002), 1939 Erzincan and 1951 earthquakes, 1939 and 1942 earthquakes on the North Anatolian fault (Barka, 1996; 2003), 2013 Scotia Sea earthquakes (Vallée and Satriano, 2014) and 1812 and 1857 San Andreas earthquakes (Weldon et al., 2005). Fault re-rupture due to overlapping slip from adjacent ruptures may introduce disorder into the apparent recurrence interval of earthquakes (Ben-Zion and Rice, 1995) and complicate the discrimination of periodic from clustered earthquake recurrence (Grant and Sieh, 1994; Rockwell et al., 2000). Variations in the extent to which ruptures overlap along segmented active faults may result in apparent contradictions in paleoseismic earthquake chronologies along the length of these faults (Seitz et al., 1997, 2013; Fumal et al., 2002; Hartleb et al., 2003; Biasi and Weldon, 2009). Robust earthquake records proximal to geometrically-defined fault segment boundaries are thus needed to compare with earthquake records from central parts of fault segments in order to better constrain our understanding of rupture behaviour.

The Hope Fault is one of the longest (~230 km) and fastest slipping (~8-27 mm/yr) active faults in New Zealand (Fig. 2.1) (Cowan and McGlone, 1991; Langridge et al., 2003; Langridge and Berryman, 2005). Field, aerial phototographic, and light detection and ranging (LiDAR) mapping (McKay, 1890; Freund, 1971; Cowan, 1989; Langridge et al., 2003; Langridge and Berryman, 2005; Langridge et al., 2013; Beauprêtre et al., 2012; Khajavi et al., 2014) indicate that the Hope Fault is highly segmented. The fault consists of five geometrically-defined segments (from west to east: Taramakau, Hurunui, Hope River, Conway, and Seaward) of ~20 to 70 km length that are separated by fault stepovers of up to ~7 km in width (Figs 2.1-2.2) and changes in strike in excess of 15 degrees. Evidence for segmented rupture behaviour along the Hope Fault includes: (1) the 1888 $M_w$ 7.1 Amuri earthquake, which ruptured the Hope Fault (total length ~ 230km) for an estimated length of 13 to 150 km (6 to 65 % of total Hope Fault length) (McKay, 1890, 1920; Berryman, 1984; Knuepfer, 1984; Cowan, 1991), (2) along-fault variations in slip rate from ~8-15 mm/yr (Hurunui segment) to ~10-17 mm/yr (Hope River segment) to ~19-27 mm/yr (Conway segment), and (3) along-fault variations in the timing and estimated recurrence interval of paleoearthquakes, which varies from ~81 to 500yr (Cowan and McGlone, 1991; Langridge et al, 2003; Langridge and Berryman, 2005). Available data makes the best possible estimates of the seismic hazard for the Hope Fault very uncertain. The geometry of the Hope Fault system suggests a segmentation model seem viable. However, it is unclear whether the segmentation model is useful for estimating seismic hazard from the Hope Fault.

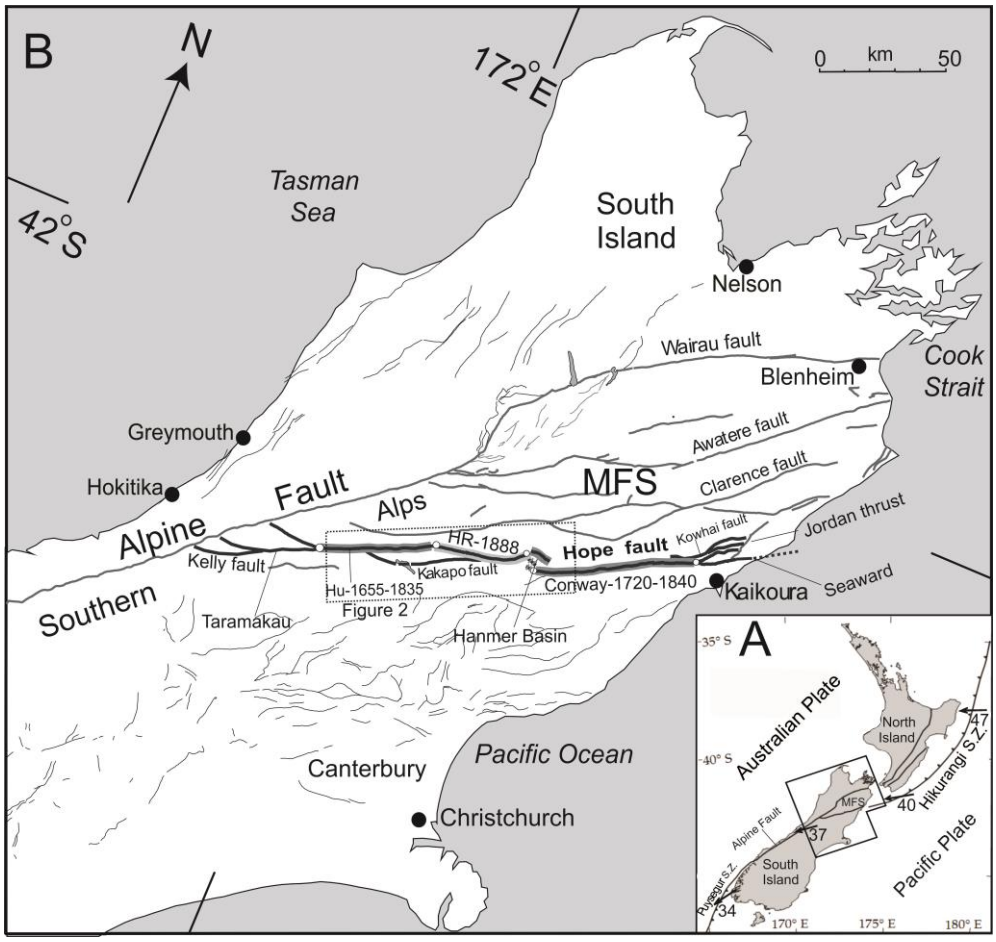


Figure 2.1. Geological setting of New Zealand and active faults in the northern South Island. (A), New Zealand plate boundary including subduction zones and major faults. Nuvel-1 plate rates (mm/yr) and orientations are after DeMets et al. (1994). (B), Location of active faults within the northern South Island are shown; Marlborough Fault System (MFS) and the Alpine Fault are highlighted; and the Hope Fault is heavily highlighted; modified from Langridge et al. (2005). The timings of the most recent events along the Hurunui, Hope River and Conway segments are presented in yr A.D. and their related segments are colored in gray bold (with historic event) and black bold (with known event). Box shows area of Fig. 2.2.

In this study, I develop new data that could lead to an improved geologic basis for hazard estimation. In detail, digital elevation models (DEMs) derived from LiDAR and photogrammetry are used to better constrain the surface rupture morphology of the eastern end of the Hurunui segment of the Hope Fault adjacent to the proposed segment boundary with the Hope River segment (Cowan, 1991; Langridge et al., 2013). Historical accounts of the 1888 Amuri earthquake (McKay, 1890) are reinterpreted in conjunction with my observations to determine a better surface rupture length and location in relation to the Hope River and Hurunui segments. Two closely spaced (~4 m apart) paleoseismic trenches are excavated at the study site. Radiocarbon dating and OxCal modelling are used to investigate

the timing of the past events at the study site. Dendrochronology and optically stimulated luminescence (OSL) dating are used to determine the age of the earthquake-displaced sedimentary deposits and further refine the timing of paleoearthquakes. These results are combined with new off-fault data and previously published paleoseismic trenching data to compare earthquake chronologies on the Hope River and Hurunui segments. The extent to which the proposed geometric boundary between these segments terminates or impedes rupture propagation on the Hope Fault is explored.

## 2.3 **Tectonic setting and background**

### 2.3.1 The Hope Fault and Marlborough Fault System

New Zealand occupies the boundary between the Australian and Pacific tectonic plates in the SW Pacific. Nearly pure strike-slip deformation occurs across the Marlborough Fault System (MFS) in the northern South Island at rates of ~39-48 mm/yr (DeMets et al., 1994, 2010; Beavan et al., 2002; Yeats and Berryman, 1987; Berryman and Beanland, 1991; Van Dissen and Yeats, 1991; Pettinga et al., 2001; Wallace et al., 2007, 2012) (Fig. 2.1). The MFS comprises four major dextral strike-slip faults: the Wairau, Awatere, Clarence, and Hope faults, which transfer the motion between the Alpine Fault in the west and the Hikurangi subduction zone in the east (Fig. 2.1).

The ENE-striking Hope Fault is the youngest and southernmost fault in the MFS, likely initiated ~1-2 Myr ago (Freund, 1971; Van Dissen, 1989; Cowan, 1990; Wood et al., 1994; Langridge and Berryman, 2005), and has the second highest slip rate of an onshore fault in New Zealand. The Hope Fault is geometrically segmented (Langridge et al., 2013) and includes branching faults (Kelly, Kakapo and Kowhai faults), pull apart basins, stepovers, and structural bends (Yang, 1991; Van Dissen and Yeats, 1991; Pettinga et al., 2001; Berryman et al., 2003) (Fig. 2.1). Movement along strike-slip segments of the fault has developed transpressional duplexes (Eusden et al., 2000, 2005), and pull-apart basins such as Hanmer Basin (Figs. 2.1-2.2), which, globally, is one of the best known examples of a depression forming at a releasing stepover (Wood et al., 1994). Typically, the Hope Fault comprises a deformation zone of up to 1.3 km width including depressions, folds, and wedges that have previously been documented or structurally investigated along the length of the fault (Freund, 1971; Cowan, 1989; Eusden et al., 2000, 2005; Khajavi et al., 2014). Measured slip rates along the fault indicate that it accommodates nearly half of the plate-tectonic motion across the Marlborough region (Cowan, 1990; Cowan and McGlone, 1991; Van

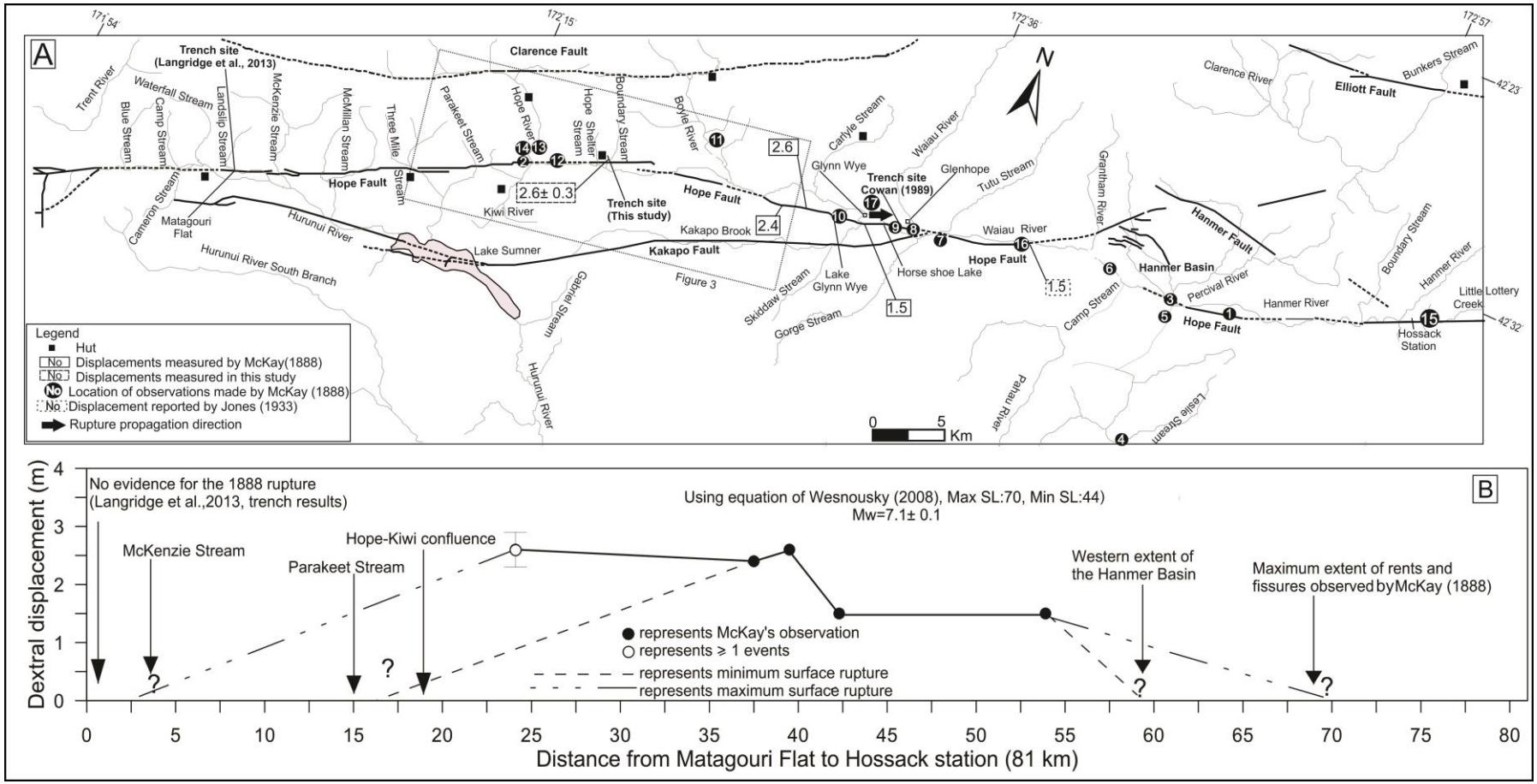


Figure 2.2. Observations of McKay (1890) has been mapped. (A), Geographical map showing the location of observations (1-16), certain (solid black lines) and uncertain (dashed lines) faults, trench sites, and measured along-fault slips. McKay's quotes related to his observations were presented in Appendix 2.1. (B), Slip distribution associated with the 1888 event. Eastern and Western extents of the surface rupture are estimated using McKay's observations and the results of Langridge et al. (2013), and this study.Box shows area of Fig. 2.3.

Dissen and Yeats, 1991; Knuepfer, 1992; Langridge et al., 2003; Langridge and Berryman, 2005).

### 2.3.2 The 1888 Amuri earthquake: background and reassessment of McKay's observations

A large earthquake occurred on the Hope Fault, on September 1, 1888 (McKay, 1890, 1902). That historical earthquake (termed the North Canterbury or Amuri earthquake) ruptured the Hope River segment of the fault and produced displacements ranging from 1.5 to 2.6 m, (McKay, 1890; Cowan, 1991) (Fig. 2.2). The true extent of the 1888 Amuri surface rupture has been debated by geologists, with estimations ranging from 13 km (from the Hope-Boyle confluence to the Hope-Waiau confluence) to 150 km (from the junction of the Alpine and Hope Faults to the east of Hanmer Basin) (McKay, 1890, 1920; Berryman, 1984; Knuepfer, 1984). Cowan (1991) argued that the rupture length was probably 30±5 km, i.e., from the Hope-Boyle confluence to the Hanmer Basin (Figs. 2.1-2.2), based on the observed and reported damage and reports of aftershock concentration patterns. He also argued that the rupture was initiated beneath the Hope-Boyle confluence (Fig. 2.2) which was considered to be a 4 km-wide tectonic basin formed at a releasing bend along the Hope Fault (Clayton, 1966). Estimates of the moment magnitude of the Amuri earthquake are $M_w$ 7-7.3 (Cowan, 1991) and $M_w$ 7.1 (Stirling et al., 2012).

The post-earthquake observations of McKay (1890), presented in Appendix 2.1, and subsequent interpretations of earthquake rupture length (Berryman, 1984; Knuepfer, 1984; Cowan, 1991) provide important information relevant to this study. The trench site (Figs. 2.2-2.3) falls along the known or suspected zone of faulting associated with the 1 September 1888 Amuri earthquake. McKay's report includes terms such as *"line of greatest disturbance", "line of greater dislocation", "earthquake-fracture", "old and new earth-fractures", "ground-rents", "earth-rents", "fissures", "slips", "rents and openings", "old line of dislocation", "recently-formed earth-rents", "recently-formed fractures", "old earthquake-rents", "traces of earthquake-action"* to describe prehistoric (pre-1888) and the 1888 Amuri earthquake-induced surface features (Appendix 2.1). McKay clearly refers to the 1888 Amuri surface fractures resulting from fault rupture (e.g., *"line of dislocation or greatest disturbance", "earthquake fracture or rents"*), ground failure (e.g., *"rents", "opening", "slips", "fissures"*), and those for which no specific origin is inferred (e.g., *"ground-rent", "earth-rent"*). In this study, I interpret the terms *"line of greater*

*dislocation"*, *"line of greatest disturbance"* and *"earthquake-fracture"* to refer to a surface rupture (Appendix 2.1: 1, 2 and 14), and term *"old line of dislocation"* to refer to a former surface rupture (Appendix 2.1: 1, 10 and 15). The term *"slip"* is commonly used in New Zealand to refer to a landslide (Appendix 2.1: 1, 4, 10, 13 and 14). Figure 2.2 shows documented observations and measured single event displacements between the Hope-Kiwi area and Hanmer Plain, which encompasses parts of both the Hurunui and Hope River segments. Quotes from the words of McKay (1890), which are related to locations 1-16 and displacements identified in Fig. 2.2, appear in Appendix 2.1.

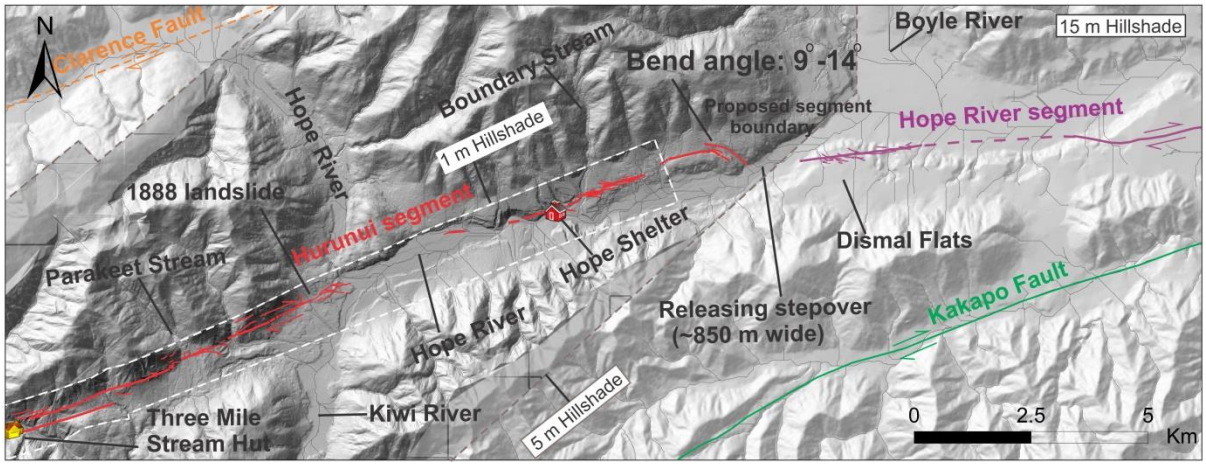


Figure 2.3. Structural map of the western Hope Fault including the overlapping area of the two segments are presented. Location of the fault bend and releasing stepover are shown in between the two segments. Defined western extension of the 1888 rupture (Cowan, 1989) is shown. Location of the 1888 landslide (McKay, 1890) is shown on the map near the Hope-Kiwi confluence.

Based on McKay's observations and comments, it can be inferred that: (1) the clearest evidence of the western limit of the 1888 Amuri surface rupture is near the Hope-Kiwi confluence (Fig. 2.2 and Appendix 2.1: 2 and 15), and (2) its eastern limit is identified by rents and fissures at the eastern end of the Hanmer Basin, but not as far as the area between the Hanmer River and Lottery Creek (Fig. 2.2 and Appendix 2.1: 15). In his opinion, the 1888 Amuri surface rupture commenced at some point to the west of Glynn Wye (maybe even farther west than the Hope-Kiwi confluence), propagated to the east with increasingly strong ground motions to Glynn Wye and Glenhope, with decreased ground damage from Glenhope toward the eastern end of the Hanmer Plain (Appendix 2.1: 15). Near the Hope-Kiwi confluence (location 2 on Fig. 2.2), McKay mentioned the earthquake fracture, snapped, broken, and thrown-down trees, and a possible continuation of the fault for a mile or more into the forest west of the Hope-Kiwi confluence (Appendix 2.1: 13).

These observations conflict with the interpretations of Cowan (1991) who placed the western limit of the surface rupture at the Hope-Boyle confluence (Fig. 2.2). Based on my reinterpretation of McKay's account (1890), the most reasonable interpretation is that the 1888 Amuri earthquake is likely to have ruptured through the trench site in the Hope Valley. This hypothesis is examined further in this study. Figure 2.2 highlights the surface slip distribution associated with this event, shows my reinterpretation of the fault rupture length and adds one slip measurement near the trench site to the slip gradient.

### 2.3.3 Paleoseismicity of the Hope Fault

The spatial and temporal patterns of large earthquakes on the Hope Fault are uncertain due to the scarcity of historical records (starting from ca. A.D. 1840) (Langridge et al., 2013) and difficulty in undertaking paleoseismic investigations in the mountainous terrain that the fault passes through. Langridge et al. (2003) measured the cumulative and single event displacements on the surface near their trench sites on the eastern Conway segment and used the radiocarbon dates obtained from trenches to conclude that the Conway segment has a recurrence interval of 180-310 years and is capable of generating $\geq M_w$ 7 earthquakes. Beauprêtre et al. (2012) measured the surface and subsurface displacements using 3-dimensional GPR (ground penetrating radar) and LiDAR to analyse part of the Conway segment. Their results suggested that the Conway segment has a mean recurrence interval of ~200 years and can generate earthquakes with magnitudes of at least $M_w$ 7-7.4. Langridge and Berryman (2005) measured surface displacements using traditional techniques (tape measure, compass, hand-held GPS) and dated surfaces using radiocarbon samples to estimate the fault parameters. Their results revealed that the Hurunui segment has an average recurrence interval of 310-490 years and is capable of generating $M_w$ 7.2-7.4 earthquakes.

Cowan and McGlone (1991) excavated a trench across the Hope River segment and interpreted that five temporally characteristic (i.e. periodic) events (including the Amuri earthquake) with an average recurrence interval of ~140 years occurred on the Hope River segment during the last 700 yr (Table 2.1). Langridge et al. (2013) subsequently reinterpreted Cowan's trench and argued that only 2 events had ruptured the Hope River segment during the last ~400-900 yr, and that the other three events had been caused by strong shaking alone (Table 2.1). Trenching investigations on the eastern Conway and western Hurunui segments by Langridge et al. (2003, 2013) did not show any evidence of the 1888 Amuri earthquake

surface rupture on these segments, but showed evidence for 2 events in the last ~600 yr on the Hurunui segment and 3 events in the last ~800 yr on the Conway segment (Table 2.1).

Table 2.1. Known paleoseismic histories along the segments of the Hope Fault

| Segments | Events and Timing (A.D.) | Reference |
|---|---|---|
| Hurunui | 2 events in the last ~ 600 yr<br>1655-1835 and 1425-1625 | Langridge et al., 2013 |
| Hope River | 5 events in the last ~ 700yr<br>1888,1745, 1602,1459, 1316 | Cowan 1989, Cowan & McGlone 1991 |
| Hope River reinterpreting Cowan's trench data and using OxCal to recalculate the events timings | From the five events (i.e., 1888, 1654-1844, 1565-1829, 1443-1718, and 1118-1609), only 2 were surface faulting events (i.e., 1888 and 1118–1609) in the last ~ 900yr, and the rest were shaking events | Langridge et al., 2013 |
| Conway | 3 events in the last ~ 800 yr<br>1720-1840, 1295- 1405, Before 1220 | Langridge et al., 2003 |

### 2.3.4 Geomorphology of the Mid-Hope Valley and the Hope Fault

The bedrock lithology consists primarily of sandstones, mudstones, and mélange collectively grouped as the Torlesse Composite Terrane of Triassic age (Nathan et al., 2002). During the Last Glacial Maximum (LGM-Otira glaciation; about 18,000 years ago) (Nathan et al., 2002; Alloway et al., 2007), the Hope Valley was filled by ice. Immediately following the LGM, when glaciers retreated, the Hope Valley was partly infilled with sediments deposited by glacial meltwater and/ or adjoining alluvial fans. During the Holocene, rivers have incised into these aggradational surfaces, creating suites of fluvial degradational terraces (Barrell and Townsend, 2012). Glaciofluvial, alluvial and landslide/debris deposits of late Pleistocene to Holocene age comprise the majority of post-LGM sediment in the valley (Langridge et al., 2013).

The approximate location of the main trace of the Hope Fault appeared on early regional geological maps (Lensen, 1962; Bowen, 1964; Gregg, 1964; Warren, 1967) and a more detailed fault trace appeared on regional geological maps (Nathan et al., 2002; Rattenbury et al., 2006). Cowan (1989) used aerial images and field observations, and Khajavi et al. (2014) used airborne LiDAR, photogrammetry, and field observations to produce detailed maps of the fault zone along the Hope River and Hurunui segments of the Hope Fault, respectively. Figure 2.3 presents a simplified version of the main fault traces and structural complexities between the Hurunui and Hope River segments. Based on the numerous en echelon structures identifiable on the LiDAR DEM located near the eastern end

of the Hurunui segment on the north side of the Hope River, Khajavi et al. (2014) argued that this area may represent a linking damage zone between the two fault segments (Fig. 2.3).

## 2.4 **Methodology**

### 2.4.1 Background, fault mapping and site selection

No paleoseismic studies have been conducted in the area proposed to be a segment boundary between the Hope River and Hurunui segments (Fig. 2.3). For this reason, this study focuses on the eastern end of the Hurunui segment including the area of the proposed segment boundary (Fig. 2.1) (Mckay, 1890; Cowan, 1991; Langridge and Berryman, 2005; Langridge et al., 2013). The Hurunui segment is located east of the main divide of the Southern Alps. Along the Hurunui segment, the average annual rainfall is ~1.5-3 m (Langridge et al., 2014) and native beech (Nothofagus) forest covers and obscures much of the fault trace and underlying morphology (Langridge and Berryman, 2005; Langridge et al., 2013, 2014). Documentation of the surface rupture attributes of the fault was thus required for identifying the best sites for paleoseismic trenching. For this, I used airborne LiDAR (see also Langridge et al., 2014; Khajavi et al., 2014) to extract accurate surface topography from beneath forest cover. The LiDAR survey did not cover the entire area between the Hope River and Hurunui segments in its eastern extent and thus high-resolution photogrammetry was used to map potential fault traces in the area where the two segments overlap. Georectified aerial photographs (taken in November 2008) covering the same area as LiDAR plus an extra ~4.5 km of coverage to the east and SOCET GXP 3.2 photogrammetry software were used to create a 5-m DEM and associated hillshade model (Fig. 2.3) (Khajavi et al., 2014). The resulting DEM has vertical and horizontal accuracies of ±1.6 and ±0.9 m respectively, shows the majority of the structures that are observed on the LiDAR DEM, and proved sufficient for identifying fault structures under beech forest. In the overlapping area of the two segments, a ~ 850-m-wide right stepover in the fault associated with a ~9º-14° degree fault bend was discovered (Fig. 2.3). Khajavi et al. (2012) surmised that this bend and stepover could play an important role in influencing the dynamics and extent of rupture termination or propagation (e.g., in the 1888 Amuri earthquake).

I mapped fault traces near the segment boundary using three overlapping hillshade models (derived from the 2-m LiDAR, the 5-m SOCET GXP, and an existing national coverage 15-m DEMs) (Fig. 2.3). Geomorphic features and their relations were assessed using standard geomorphic mapping techniques and manipulation of DEMs (e.g., Khajavi et

al., 2014). Based on these data, I selected a site for paleoseismic study at the eastern end of the LiDAR swath and named it "Hope Shelter" (due to its proximity to the Hope Shelter hut in the mid Hope Valley). The Hope Shelter site is ~8 km west of the Hope-Boyle confluence (Figs. 2.2-2.3). Structurally, the Hope Shelter site proved an optimal location for trenching the fault because of the single sharp linear fault trace that blocked a natural drainage creating a swamp with a potential source of datable material. The site was also selected due to its sparse vegetation.

Two narrow (<1m wide) trenches were excavated at the Hope Shelter site (Figs. 2.4B and 2.5A-F). Trench 1 (T-1; 9 m long by 1 m deep, Figs. 2.6-2.8) was excavated in February 2012 by backhoe across the shutter ridge within a small wind gap (formed by an abandoned channel) (Fig. 2.5A). At this location the scarp height is ~0.5 m and the width of the swampy basin is ~10 m. Trench T-1 was located ~50 m from the western edge of the debris deposit (Fig. 2.4). T-1 had a branch trench (I named "pit 1") (Fig. 2.5A) which was excavated within the wind gap in the scarp to understand the geometry and age of any channelized deposits within it (see Fig. S2.3 in Supplementary file). Trench 2 (T-2, ~2.5 m long by 1.3 m deep, Figs. 2.7 and 2.9) was excavated by hand in February 2013 in an attempt to understand some of the stratigraphic and age anomalies observed from T-1 (Fig. 2.5C-D). T-2 was excavated into the scarp and shutter basin deposits adjacent to T-1. At this location the scarp was steep with a height of ~1.1 m. The width of the swampy basin there is ~7 m. The log of the east wall of T-2 (Fig. 2.9) was supplemented by several auger holes to extend the depth and continuity of units. Both trenches were limited in their extents into the shutter basin by the presence of flowing water at the ground surface (Figs. 2.6 and 2.8).

### 2.4.2 Dating techniques

A variety of dating techniques were applied to see whether they could help constrain the prehistoric and 1888 rupture earthquakes. These techniques are: (1) radiocarbon dating: samples from two on-fault trenches excavated across the fault scarp at the Hope Shelter site and four off-fault auger holes at swamps south of the fault near Parakeet Stream (see Figs. 2.2-2.4, and Figs. S2.9-S2.10 in Supplementary file for location and details) were radiocarbon dated, (2) optically stimulated luminescence (OSL) dating: samples from the Hope Shelter site, extracted from one of the trenches on the shutter ridge fan and a pit excavated into the Holocene terrace (see Fig. 2.4, and Fig. S2.5 in Supplementary file) were OSL dated, (3) Schmidt hammering: Schmidt hammer 'rebound values' (e.g., Stahl et al., 2014) were used to

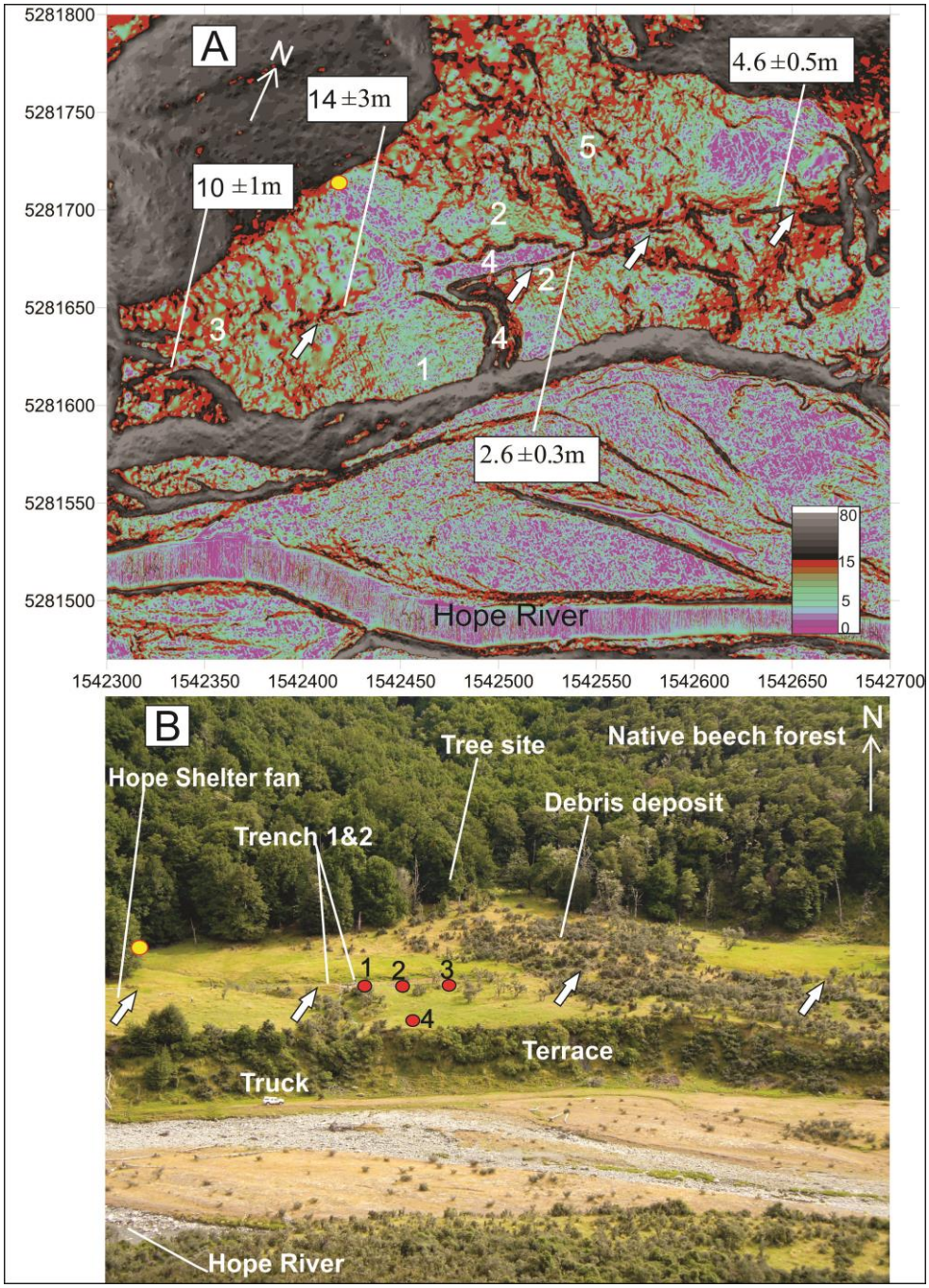


Figure 2.4. Details of the Hope Shelter site are presented. (A), 0.1-m slope map which is made up of the 1-m LiDAR DEM is shown. Morphologies of the five features are identifiable by different surface slopes. Numbers on the map are; 1: terrace, 2: trench site fan, 3: Hope Shelter fan, 4: channel and shutter basin, and 5: debris deposit. Location of the measured displacements and the hot spring (yellow solid circle) are shown. (B), A photograph that shows the five geomorphic features, Trench 1 and Trench 2, pits locations (1-4; red solid circles), hot spring, and the tree site (where I carried out a dendro-chronologic work). Arrows point to the fault trace.


Figure 2.5. Trench T-1 and Trench T-2 pictures (A-B) and photo-logs (C-F). Numbers represent units (see Appendix 2.2 for details).

calibrate the age of the debris deposit relative to a pre-1888 debris deposit at the Hope-Kiwi confluence (see Part 4 in Supplementary file), and (4) dendrochronology: trees and bushes at the Hope Shelter site were examined. Native beech trees are absent in the central part of the site; however, Matagouri (*Discaria toumatou*) scrub is abundant on the debris deposit (Fig. 2.4B). I found no documentation to confirm that the central part of the site might have been deforested by pastoralists. Despite having wide trunks, Matagouri bushes are substantially younger than the 1888 Amuri earthquake event according to a tree-ring count conducted as

part of this study; the age of the sampled bush was 82 yr (1930) (see Fig. S2.2 in Supplementary file). However, uphill and surrounding the site, Red Beech (*Nothofagus fusca*) trees have colonised the upper end of the debris deposit at the mouth of the gully (Fig. 2.4B). Dendrochronology was used to date the trees growing on the upper side of the debris deposit (see Fig. 2.4B for location).

### 2.4.3 Oxcal modelling of radiocarbon ages

In order to develop a refined chronology of paleoseismic events at the Hope Shelter site a Bayesian statistical approach that draws on the strengths of stratigraphic observation and age data was applied. Using the OxCal 4.2.3 program (Bronk Ramsey, 2013) I developed age models that use the radiocarbon dates from the paleoseismic trenches, along with dendro-chronological and historical age constraints in a Bayesian framework (e.g., Biasi and Weldon, 1994; Biasi et al., 2002, Howarth et al., 2014). Bayesian sequence statistics can systematically reduce the age uncertainty of individual and collective dates and event distributions (Scharer et al., 2007; Langridge et al., 2013). In this study, the two trench walls were independently modelled to avoid any error resulting from miscorrelating the horizons.

## 2.5 **Results**

### 2.5.1 Geomorphic Descriptions of the Hope Shelter Site

The results of geomorphic analysis at the Hope Shelter site are presented here. Important surfaces and deposits around the Hope Shelter site include: (1) a faulted Holocene terrace (17 m above the modern Hope River), (2) a faulted low-gradient Holocene fan (here I call it the shutter ridge fan) that emanates from a rangefront catchment and grades to the terrace, (3) another faulted Holocene fan (here I call it the Hope Shelter fan) at the west of the site that overlies the terrace and has preserved a cumulative dextral displacement, (4) a channel and a shutter basin that has formed behind the shutter scarp on the surfaces of the Hope Shelter fan and the shutter ridge fan; I interpret the deeply-incised channel as being related to a small hot spring, therefore I cannot assess discrete displacement associated with this channel, and (5) a faulted debris deposit at the middle of the site that overlies the shutter ridge fan and part of the shutter basin (Fig. 2.4A-B). There is one major ephemeral drainage line that flows along the shutter scarp in the shutter basin/swamp that is joined by a smaller drainage line sourced from the hot spring near the rangefront (Fig. 2.4). During dry months, there is little surface runoff into the swamp and in these conditions, peat accumulation occurs

over the entire swamp floor. During wetter periods, there is a source of water entering the swamp, depositing sands and silts into the middle of the swamp, preventing peat accumulation there, but near the swamp edges, away from sedimentation, peat accumulation continues.

### 2.5.2 Structural description of the Hope Shelter site

The Hope Fault at the Hope Shelter site is structurally simpler compared to the adjacent areas. A fault trace with a strike of 075º is clearly visible on aerial photographs, on the ground and on the LiDAR hillshade model. It is characterised by an uphill-facing scarp that forms a shutter ridge with variable height ranging from 0.2 m to 1.5 m. A single trace of the fault cuts the Hope Shelter and shutter ridge fans and the debris deposits, and splays/bends off towards the east (near Boundary Stream) before ascending a postglacial alluvial fan (Fig. 2.3). On the postglacial alluvial fan, the fault appears as a series of en echelon uphill-facing scarps (Khajavi et al., 2014). Scarp heights in this area vary from 0.2 to ~14 m.

### 2.5.3 Slip Measurement at the Hope Shelter Site

A series of dextral displacements were measured at this site between a large stream to the west (here, I informally name it Hope Shelter Stream, Figs. 2.2 and 2.4A) and Boundary Stream to the east in order to understand the slip pattern at the Hope Shelter site. These field measurements from west to east are 10 ± 1 m, 14 ± 3 m, 2.6 ± 0.3 m, and 4.6 ± 0.5 m, located in the vicinity of the trench site. From west to east, the 10 ± 1 m displacement was measured along a displaced gravitational failure scarp, the 14 ± 3 m displacement was measured along the displaced toe of the Hope Shelter fan adjacent to the Hope Shelter hut, the 2.6 ± 0.3 m displacement was measured along the edge of the debris deposit near the trenches, and the 4.6 ± 0.5 m displacement was measured along an abandoned channel on the terrace surface (Fig. 2.4A). The cumulative displacement of the Hope Shelter fan is considered to estimate the slip rate because, as mentioned before, I cannot assess discrete displacement associated with the incised channel (Fig. 2.4) south of the fault trace as I am not confident of its match on the north side of the fault. The smallest measured displacement is consistent with the highest displacement (2.6 m) measured by McKay (1890) following the 1888 event, and with the average single-event displacement (3.4 m) measured by Langridge and Berryman (2005) at the McKenzie fan site, and with the single-event displacement (3 ± 0.4 m) measured by Khajavi (2015, see Chapter 3) at Matagouri Flat along the western Hurunui segment (Fig.

2.2). However, the 2.6 ± 0.3 m displacement at the Hope Shelter site is quite smaller than the single-event displacement (4.5 ± 0.6 m) measured by Langridge et al. (2013) at Matagouri Flat (Fig. 2.2).

### 2.5.4 Hope Shelter trenches

A sharp stratigraphic contrast was observed in T-1 and T-2 between the shutter ridge and basin stratigraphy. The stratigraphy of the two trenches is summarised in Figure 2.7. To avoid confusion, fault zone stratigraphy has been separated from the basin stratigraphy. Only the west and east walls of T-1 and T-2 were logged at a scale of 1:10, resulting in two mapped walls ~4 m apart. Both trenches have a similar stratigraphy characterised by: (1) alluvial and colluvial gravels exposed in the shutter ridge/scarp, (2) a fault zone comprising mainly gravels, sands, silts, and colluviums, and (3) shutter basin deposits that were mainly well-bedded sands and silts and peaty soils.

In addition to the two main paleoseismic trenches and pit 1, three pits on the surface of the shutter ridge fan and terrace were dug; two of them (pits 2 and 3) were located on two other subtle wind gaps to the east of T-1 and the other (pit 4) was located on the flattest and smoothest part of the terrace (Fig. 2.4B). Pit 2, which was dug into the wind gap adjacent to Trench 1, was not logged or sampled because there was no evidence of paleochannel deposits, suggesting that the wind gap has been formed by subsequent erosion on the fan surface. Pit 3 showed evidence for a paleochannel. Pit 1 and Pit 3 indicate that at least 2 channels have been abandoned on the fan surface to the west of the debris deposit due to the evolution of the fault scarp. Pit 1 and Pit 4 were used to date the fan and terrace surface. Logs of these pits are included in the Supplementary file.

#### 2.5.4.1 Trench 1

##### 2.5.4.1.1 Trench 1-Stratigraphy

The main focus of the trench was the basin section and its relationship with the main fault zone, exposed across the scarp (Figs. 2.6 and 2.8). The deposits in this part of the trench are dominated by peaty basin materials, fine clastic deposits and scarp-derived colluvial deposits (Fig. 2.8). Detailed unit descriptions are provided in Appendix 2.1. Tie lines in Figure 2.7 were drawn on the basis of stratigraphic position, sequence stratigraphy and also

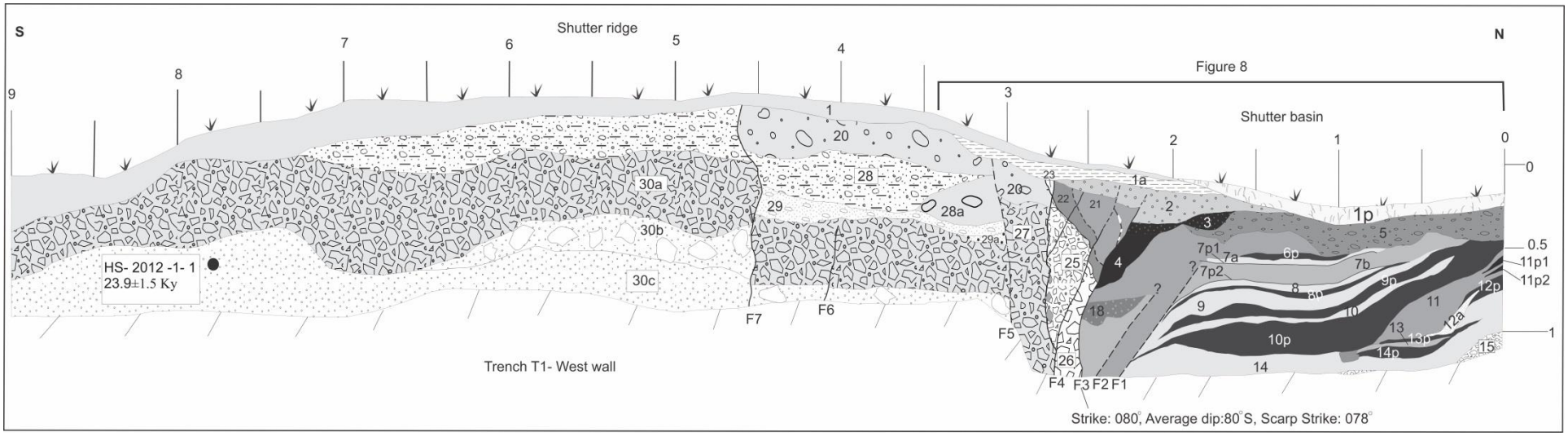


Figure 2.6. The full log of Trench T-1. From meters 2.5 to 9, fan gravels are prevalent and are faulted near the fault scarp. From meter 0 to meter 2.5, swamp deposits are juxtaposed against the fan deposits and are either faulted or deformed.

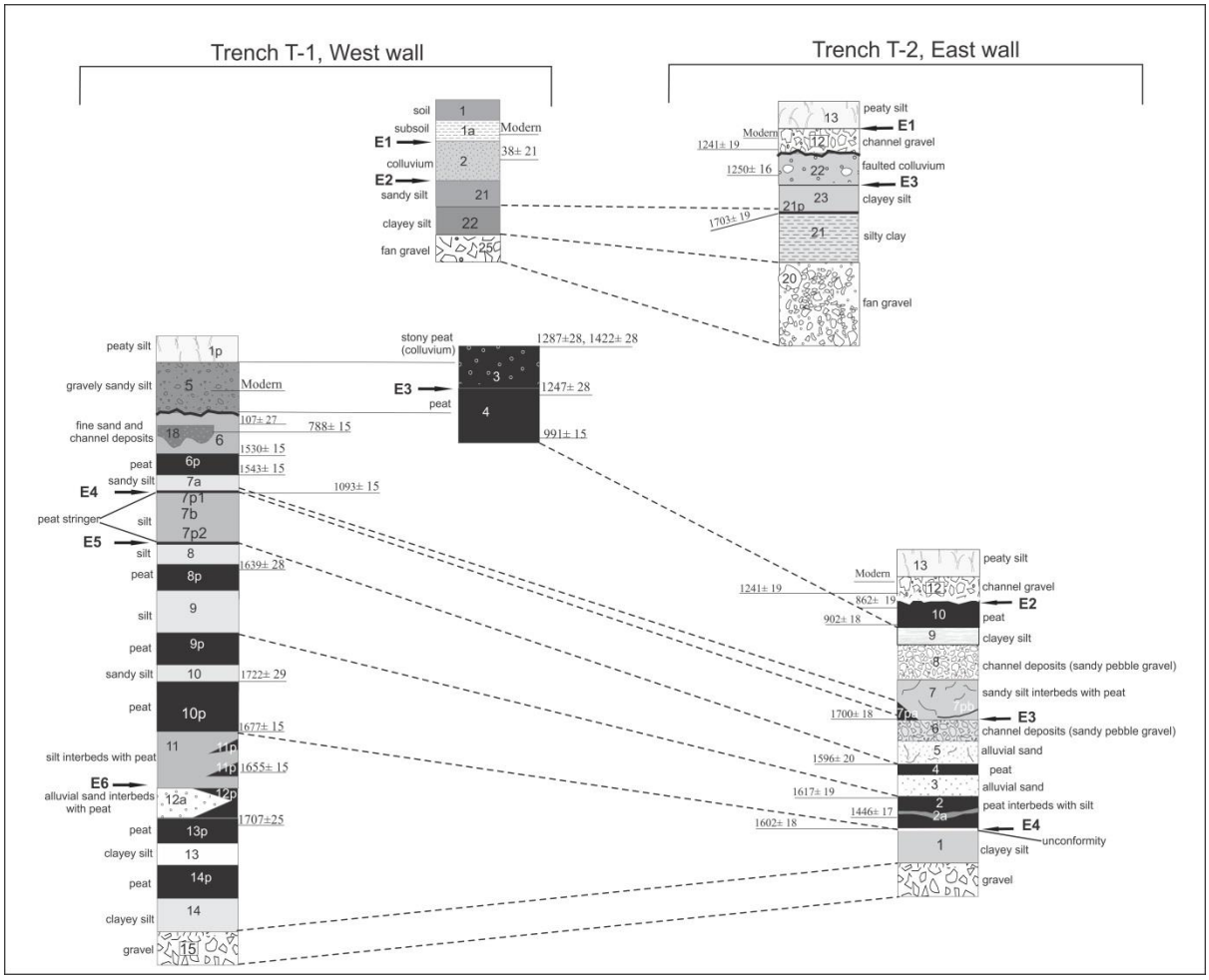


Figure 2.7. Simplified stratigraphy and age of the units from Hope Shelter site trenches. Arrows point to earthquake event horizons described within the text and dashed lines correlate units based on stratigraphic, textural and chronologic grounds. Calibrated radiocarbon ages (years B.P.) of the units are attached to the columns.

chronologic correlations. In general, three variably deformed packages consisting of alternating peat and silt sequences were identifiable in T-1 from meters 0 to 2 (Fig. 2.8).The lowest package begins with gravel (unit 15) and ends with silty alluvium (unit 11) (Figs. 2.7-2.8). The middle package begins with a thick peaty horizon that interfingers with three silt units and ends with silt (unit 8). The uppermost package begins with a thin peaty horizon (unit 7p2) that has a subtle angular unconformity with unit 8p and ends with a thicker peaty horizon (unit 6p). The upward extensions of these packages are overlain by a lower gravelly sandy silt (unit 5) and upper surficial peaty soil (unit 1p) (Fig. 2.8). The southern extents (to the south of T-1) of the silt-peat sequences in the middle package are highly deformed and are juxtaposed against unit 6, a massive, structureless silt deposit. The southern extents of the silt-peat sequences in the uppermost package are less deformed with an upward decreasing deformation pattern. Subtle deformation occurs in the northern extensions of the upper horizons (unit 7p1, 7a, and 6p) in the uppermost package.

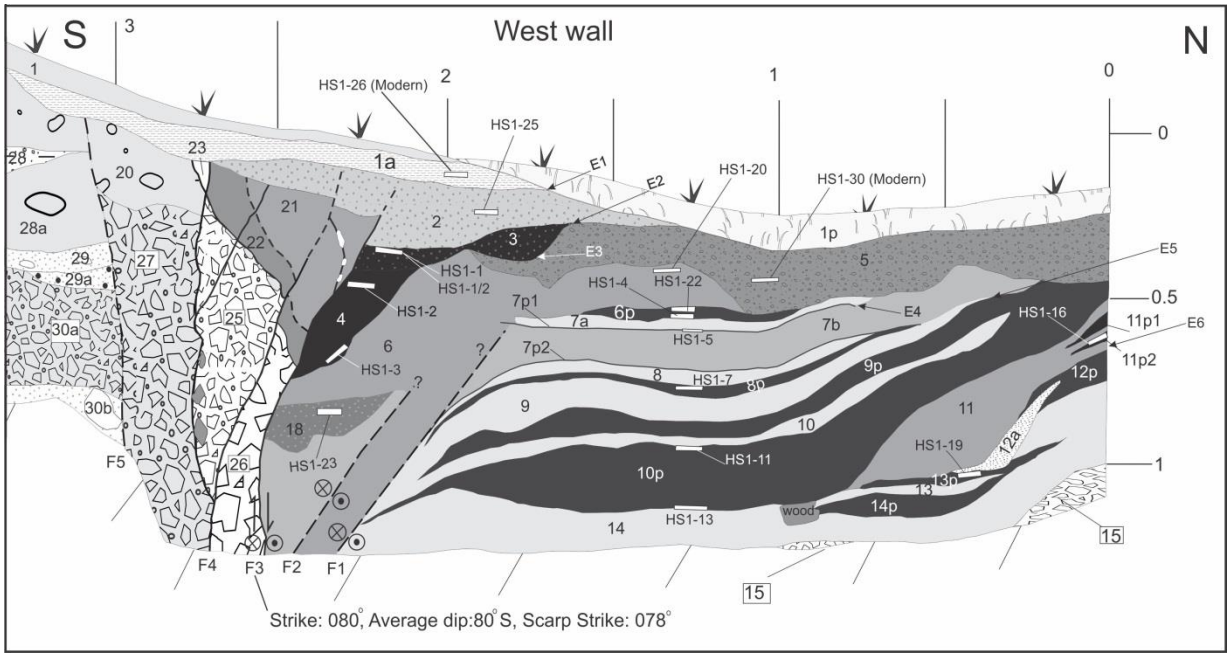


Figure 2.8. The first three meters of Trench T-1 are shown in details. Sample locations and names are included. Black units represent peat and gray units represent silt; see Appendix 2.2 for unit descriptions. Faults are shown in solid lines where certain, and dashed lines where uncertain. Fault F3 is identified as the main fault based on its position in the trench, i.e., it juxtaposes the fan deposits against the swamp deposits.

Seventeen organic samples were radiocarbon dated from T-1. More than half of these dates were in stratigraphic order and are considered to be valid in situ ages. However, several other samples, particularly within and overlying the fault zone, were either out of order, in reverse stratigraphic order or of modern age, making their relevance and interpretation difficult. These dates highlight issues in sampling and assessing multi-event records from strike-slip faults.

Eight samples from the lowest three packages were radiocarbon dated (Figs. 2.7-2.8 and Table 2.2). From the deformed packages towards the main zone of faulting, faulted alluvium (units 6 and 18), faulted gritty peat (unit 4) and sandy to pebbly peat (unit 3) were identified. Unit 6 consists of grey undifferentiated sand to silt deposits that becomes slightly lighter in colour below unit 18. Its upper boundary is marked by an erosional unconformity (Figs. 2.7-2.8). Unit 18 consists of stony sandy silt which is slightly peaty. Five organic samples within these units were dated (Figs. 2.7-2.8 and Table 2.2), and later I dated another piece of material from sample HS1-1 (sample HS1-1/2; Table 2.2) to test the reliability of the reverse order of ages from unit 18 to unit 3. Within the fault zone stratigraphy (Fig. 2.7), the faulted basin units 21 and 22 which consist of sandy silt and clayey silt respectively, are juxtaposed against units 3 and 4. These are the southernmost basin units on the log (Fig. 2.8).

Units 3 and 21 are overlain by colluvium and soil (units 2, 1a and 1, Fig. 2.7). The base of the colluvium, which I interpret as being scarp-derived, has been faulted, while its top is truncated and overlain by more recent material. Two radiocarbon samples from units 2 and 1a were dated, but one was modern in age (Figs. 2.7-2.8 and Table 2.2). To the south of T-1, from meters ~3 to 4.6 (Fig. 2.6), faulted fan gravels (units 25, 26, 27, 28, 28a, 30a and 30b), faulted sandy channel deposits (29, 29a), and faulted scarp-derived colluviums (units 20 and 23) (Figs. 2.6 and 2.8) are prevalent.

#### 2.5.4.1.2 Trench 1-Faulting

The entire zone of faulting in T-1 extends across the width of the scarp for ~3 m width, while the zone of most recent faulting spans as narrow as 1-1.5 m width (Fig. 2.8). The main zone of faulting comprises several vertical and sub-vertical shears F1-F5 (Fig. 2.8). The secondary faults F6 and F7 occur ~1-1.5 m south of the main fault zone at meters 4-5 (Fig. 2.6). Fault F3 in T-1 has a strike of 080º and an average dip of 80º S. On the surface, the fault scarp strikes 078º, as measured in the field. The fault strike measured on the LiDAR hillshade model is 075º.

The most recent faulting event (E1) in T-1 is identified by the upward termination of faults F3 and F4 at or above the base of unit 2, defined as a colluvial wedge. The unit 2 colluvium is likely faulted; alternatively, this colluvium draped across the tips of faults F3 and F4. Unit 1a (subsoil) postdates the most recent faulting event (Fig. 2.8). Sample HS1-26 from unit 1a yielded a modern radiocarbon age. Seeds within unit 2 (sample HS1-25) should be older than or of an equivalent age to the deposition of colluvium indicating that E1 occurred at ~A.D. 1817-1921. Given the reported age distribution, I cautiously attribute E1 to the 1888 Amuri earthquake.

Faulting event 2 (E2) is identified by the generation of the colluvial unit 2 and faulting of the peaty colluvial unit 3 (Fig. 2.8). Sample HS1-25 could either be older or equal to E2 in age because it was deposited in the colluvial unit 2. This event is undoubtedly older than the 1888 event. Therefore, E2 is likely to be older than 1840 (i.e., predates the colonial (historical) period in New Zealand). I dated samples HS1-1 and HS1/2 from unit 3 because the ages of these samples should predate the age of E2 and mark the lower age bracket for it. The calibrated ages of the samples were between ~A.D. 600 and ~A.D. 900. These samples are substantially older than sample HS1-25 and are in the reverse order to samples HS1-2, HS1-3 and HS1-18. This raises three options: (1) unit 4 has been vertically transferred up to

this level; (2) units 3 and 4 have been rotated, thus meaning that the materials dated were originally deposited at the base of these units; or (3) dated materials are reworked and thus older than their hosting sediment. Based on the results from T-2, I think that samples HS1-1 and HS1-2 are reworked materials, but sample HS1-3 could be the most reliable sample because its age is similar to the ages of samples HS2-7 and HS2-8 from peat unit 10 in T-2. Therefore, I favour option 3 above (Table 2.2 and Figs. 2.7-2.9).

Faulting event 3 (E3) is identified by faulting of peat unit 4 and deposition of peaty colluvial unit 3 (Fig. 2.8). Sample HS1-3 predates the event and sample HS1-25 postdates the event, therefore E3 is bracketed between ~A.D. 1034 and 1817. This interpretation is based on accepting the age of the sample HS1-3 as the correct age.

Faulting event 4 (E4) is identified based on the subtle deformation of units 7p1, 7a, and 6p from the uppermost deformed package (Fig. 2.8). Samples HS1-22, HS1-4, and HS1-5 were dated from this package. Samples HS1-22 and HS1-4 from unit 6p have an age overlap and indicate that the peat mean accumulation rate is ~0.5 mm/yr. Sample HS1-5, which comes from a rooty peat stringer, has a much younger age than sample HS1-4. This suggests contamination by roots from plants growing on the upper units. Therefore, I interpret that sample HS1-22 postdates, and sample HS1-3 predates this event; Event 4 is bracketed between ~A.D. 554 and 1151. The fault that caused this event is shown as a dashed fault on the trench log based on the juxtaposition of the three deformed packages of silt-peat sequences against the alluvial unit 6, and the progressive deformation of the three packages towards this contact (Fig. 2.8). However, no clear fault contact was observed at that location.

Faulting event 5 (E5) is identified based on folding that caused the slight angular unconformity where unit 7b drapes over units 7p2 to 9, i.e., between the middle and the uppermost deformed packages (Fig. 2.8). This event should be younger than sample HS1-7 from peat unit 8 and older than sample HS1-4 from peat unit 6p. The event date is bracketed between ~A.D. 412 and 627.

Faulting event 6 (E6) is identified between the middle and lowest deformed packages. The event horizon is unclear, but it is most likely to be between units 10p and 11 or between units 11 and 12-13 (Fig. 2.8). If I restore unit 11 to its horizontal position, it appears that its upper contact with peat unit 10p is convex in shape. In cross-section, units 11 and 12a have the form of a (tilted) paleo-channel with interfingered peat, similar to what can be seen accumulating in the shutter basin today. Since the upper boundary of unit 11 includes clean silt that is slightly peaty, and unit 10p is the thickest peat unit in T-1, I infer that there had

been a slower transition from an alluvial environment to a peatier environment (see units 11 and 10p descriptions in Appendix 2.2). This observation weakens the hypothesis of the event horizon being between units 10p and 11. However, the lower boundary of unit 11, that includes gritty silt with no evidence of peaty fibres, is most likely to be the event horizon. Taking that into account, the event horizon is constrained between samples HS1-19 from unit 13p and sample HS1-13 from unit 10p (Fig. 2.8), i.e., the event date is bracketed between ~A.D. 262 and 534.

#### 2.5.4.2 Trench 2

##### 2.5.4.2.1 Trench 2-Stratigraphy

The stratigraphy in T-2 is consistent with the observations at the surface of the shutter ridge and basin and in T-1, showing that basin sediments were deposited or juxtaposed against the fan gravels derived from the shutter scarp. Detailed unit descriptions are provided in Appendix 2.2. The stratigraphy of T-2 is somewhat simpler than that of T-1 (Figs. 2.7 and 2.9) and comprises one deformed package of sediments. This package (units 1-10) consists of alternating peat, silt, sand and gravel units that are folded into a syncline and vertically-dragged along fault F1 (Figs. 2.5 and 2.9). The lowermost unit within this package is a clayey silt (unit 1) while the uppermost unit is a thick peat (unit 10). Units 1-10 are juxtaposed against fine-grained swampy deposits to the south of fault F1. Observations from the auger holes and the north edge of the trench imply that some of the marginal units in the basin have an interfingering relationship with the units within the deformed package (Fig. 2.9). Figure 2.7 also indicates the possible unit correlations between the two trenches, based on the grain size, relative elevation, and age of those deposits in T-1 and T-2. Differences in the actual elevations of these units can be explained by the possible existence of unconformities, considering the slope (to the west), and likely deformation of units within the basin, especially considering the observed warping adjacent to the fault zone (Figs. 2.8 and 2.9). Taking into account the results of the auguring, dating and unit descriptions, I think that units 1, 2, 3,7, 10, 20, 21, 23, 13 in T-2 are equivalent to units 14, 10p, 9, 7, 4, 25, 22, 21, 1p in T-1 respectively (Figs. 2.7-2.9).

Table 2.2. Radiocarbon dating results from the Hope Shelter trenches (see also digital Appendix B).

| Hope Shelter-Trench 1, C-14 samples, February 2012 | | | | | | | | | | | | |
|---|---|---|---|---|---|---|---|---|---|---|---|---|
| **Sample ID** | **Lab Number** | **$\Delta^{13}C$ (‰)** | **Radiocarbon age (years B.P.)** | **Calibrated age (2σ) A.D.** | | | | **Probability for each 2σ range (%)** | | | | **Sample type and description** |
| HS1-1 | NZA 40297 | -29.6 | 1287±15 | 694-749 | 765-874 | | | 29.5 | 65.5 | | | Peat-degraded plant material |
| HS1-1/2 | NZA 51111 | -27.7 | 1422±28 | 609-692 | 750-763 | | | 92.8 | 2.4 | | | Peat-degraded wood or bark |
| HS1-2 | NZA 51108 | -28.1 | 1247±28 | 721-741 | 770-898 | 922-942 | | 2.9 | 88.7 | 3.3 | | Peat- single woody stalk |
| HS1-3 | NZA 40300 | -27.2 | 991±15 | 1034-1151 | | | | 94.8 | | | | Peat-twig bark fragment |
| HS1-4 | NZA 40305 | -27.1 | 1543±15 | 543-627 | | | | 94.6 | | | | Peat- lump of plant tissue/bark |
| HS1-5 | NZA 40302 | -30.1 | 1093±15 | 987-1023 | | | | 94.7 | | | | Peat- root fragment |
| HS1-7 | NZA 51110 | -29.6 | 1639±28 | 412-549 | | | | 94.9 | | | | Peat- a bulk sample of 12 peat lumps |
| HS1-11 | NZA 51112 | -27.9 | 1722±29 | 257-302 | 317-436 | 491-508 | 520-527 | 10.5 | 82.2 | 1.7 | 0.6 | Peat- 5 small lumps plus a small amount of peaty fagments (treated as bulk) |
| HS1-13 | NZA 40299 | -27.9 | 1677±15 | 390-534 | | | | 94.8 | | | | Peat- slender wood fragment |
| HS1-16 | NZA 40298 | -29.4 | 1655±15 | 415-536 | | | | | | | | Peat- a seed, a short thin twig and 3 small bark fragments (treated as bulk) |
| HS1-19 | NZA 40317 | -26.7 | 1707±25 | 262-280 | 327-461 | 484-532 | | 3 | 83.8 | 8.4 | | Peat- 6 seeds |
| HS1-20 | NZA 51109 | -24.4 | 107±27 | 1698-1725 | 1808-1949 | | | 12.3 | 82.8 | | | A bulk sample of sand-single peaty Raupo root |
| HS1-22 | NZA 40244 | -28.6 | 1530±15 | 554-639 | | | | 94.9 | | | | Peat- wood fragments |
| HS1-23 | NZA 40245 | -28.7 | 788±15 | 1229-1251 | 1261-1290 | | | 17.7 | 77.8 | | | Colluvium- Orangy brown flaky plant tissues |
| HS1-25 | NZA 51076 | -27.4 | 38±21 | 1817-1829 | 1893-1921 | | | 42.6 | 52.4 | | | Colluvium- 4 whole seeds and ~6 small seed fragments and 2 plant materials (treated as bulk) |
| HS1-26 | NZA 51107 | -29.4 | Modern | | | | | | | | | A bulk sample of soil- stalky plant fragment |
| HS1-30 | NZA57002 | -28.2 | Modern | | | | | | | | | A bulk sample of alluvium- small plant fragments (flower head, grass, 5 blades, etc.) |

| Hope Shelter-Trench 2, C-14 samples, February 2013 | | | | | | | | | | |
|---|---|---|---|---|---|---|---|---|---|---|
| **Sample ID** | **Lab Number** | **$\Delta^{13}C$ (AMS)** | **Radiocarbon age (years B.P.)** | **Calibrated age (2σ) A.D.** | | | **Probability for each 2σ range (%)** | | | **Sample type and description** |
| HS2-1 | NZA56458 | -28±0.2 | 1602±18 | 428-548 | 561-570 | | 92.2 | 2.7 | | Peat- stalky plant material |
| HS2-2 | NZA 53421 | -29±0.2 | 1446±17 | 613-667 | | | 95 | | | Peat- twig |
| HS2-3 | NZA54169 | -27.5±0.2 | 1617±19 | 428-555 | | | 94.8 | | | Peat-seeds |
| HS2-4 | NZA 53410 | -37.9±2 | 1596±20 | 431-580 | | | 95 | | | Peat- woody plant material (twigs/stems) |
| HS2-6 | NZA 53411 | -34.4±2 | 1703±19 | 226-274 | 334-440 | 486-531 | 0.9 | 86.8 | 7.3 | Peat- seeds |
| HS2-7 | NZA 53416 | -30.7±2 | 902±18 | 1158-1220 | | | 94.8 | | | Peat- seeds |
| HS2-8 | NZA 53412 | -34.9±2 | 862±19 | 1187-1268 | | | 95.4 | | | Peat- seeds |
| HS2-9 | NZA 53414 | -31.9±2 | 1700±18 | 337-442 | 453-460 | 485-531 | 85.6 | 0.7 | 8.8 | Peat- two small lumps of peat |
| HS2-11 | NZA 53386 | -30.7±0.2 | Modern | | | | | | | A bulk sample of channel/colluvium?- a leafy fragment |
| HS2-13 | NZA54166 | -25.8±0.2 | 1241±19 | 776-895 | | | 94.8 | | | Bark of a piece of dark brown wood |
| HS2-14 | NZA 53384 | -32±2 | 1250±16 | 777-888 | | | 95.4 | | | A bulk sample of colluvium- a leafy looking fragment |

Seven peat samples from the deformed package were dated (Figs. 2.7 and 2.9 and Table 2.2). Within the fault zone stratigraphy (Fig. 2.7), the faulted fine-grained swampy units 24, 23, 21p and 21 that consist of silty clay (shear zone), clayey silt, silty clay and a thin peaty horizon respectively, are juxtaposed against the deformed package to the north and against the fan gravels to the south. These units appear to be equivalent to the faulted ponded? units 21 and 22 in T-1. From unit 21p, sample HS2-6 (comprising 6 small seeds) yields an age of 1703 ± 19 yr B.P. (Fig. 9 and Table 2), which is equivalent in age to the basal units in both T-1 and T-2. These observations allow us to speculate that the stratigraphy within the fault zone can be correlated between the two trenches and also used to estimate the relative vertical displacement across the fault since ~300 A.D. From unit 21 towards the southern end of T-2, faulted fan gravels (unit 20) and colluvial wedge (unit 22) were identified. One organic sample (HS2-14) from this package was radiocarbon dated at 1250 ± 16 yr B.P. (Fig. 2.9 and Table 2.2). An erosional unconformity marks the upper boundary of units 11, 10, 24, 23 which are all overlain by channel gravels and peaty soil (units 12 and 13) (Fig. 2.9). Two organic samples from unit 12 were dated; sample HS2-13 yielded a radiocarbon age of 1241 ± 19 yr B.P., while sample HS2-11 yielded a modern age (Fig. 2.9 and Table 2.2). I concluded that neither of these two dates may reflect the true depositional age of unit 12.

#### 2.5.4.2.2 Trench 2-Faulting

The zone of faulting exposed in T-2 is ~1.1 m wide and comprises shear fractures F1-F3 (Fig. 2.9). Fault F1 in T-2 has a strike of 090º and an average dip of 80º S, which is consistent with faults observed in T-1, and the fault scarp geomorphology. Fault F1 projects upward into a ~9 cm wide zone of shearing (Fig. 2.9) within the silty clay unit 24, which indicates the likelihood of multiple shearing events on this fault strand.

The most recent faulting event (E1) in T-2 is identified by the upward extension of the southernmost fault F3 at the base of the fault scarp, and faulting of the channel gravel (unit 12) and the peaty soil (unit 13?) (Fig. 2.9). This event is the youngest in this trench. Because the ages of samples HS2-7 and HS2-8 are the youngest (~A.D. 1100-1200), most reliable (derived from seeds), are in correct stratigraphic order, and predate the age of E2 in T-1 (because they are equivalent to the age of sample HS1-3) I argue that the most recent faulting event is much younger than the age of sample HS2-8. I acknowledge that I have a poorer estimate of the age of the most recent faulting event in T-2 than I do at T-1.

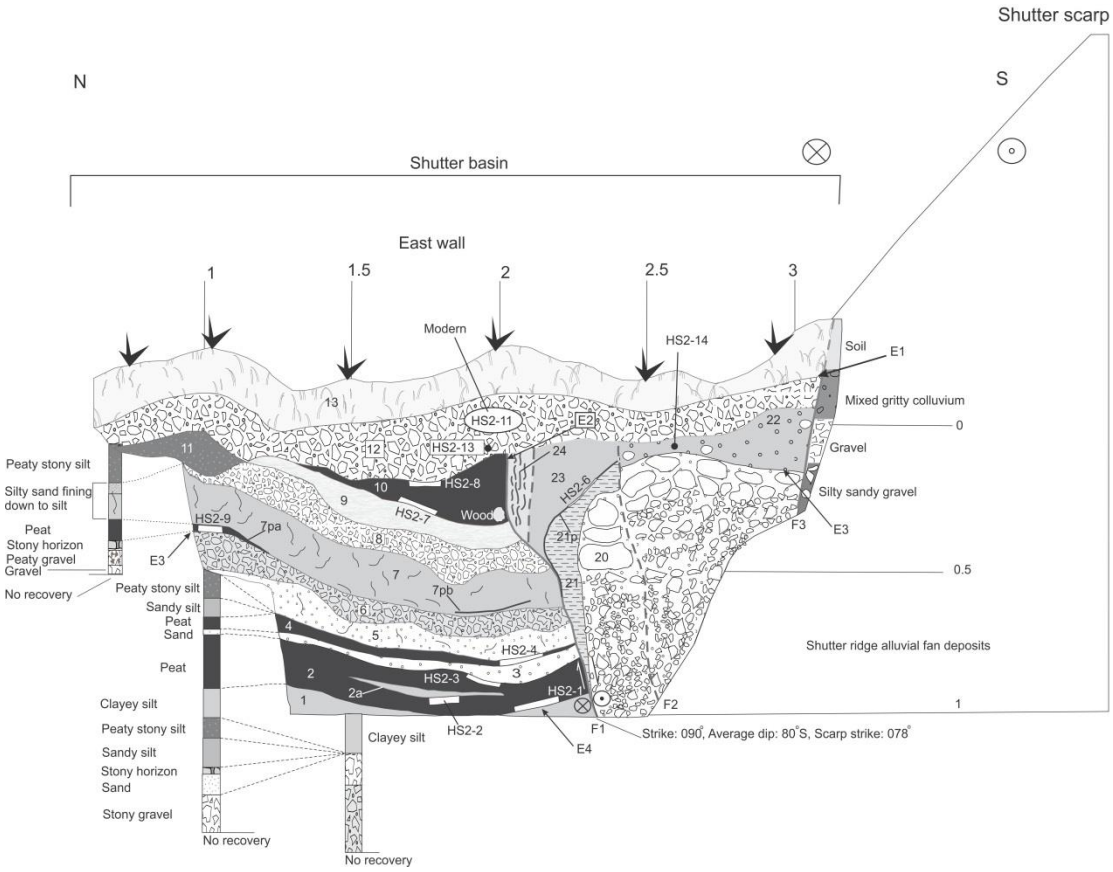


Figure 2.9. Trench T-2 and augur locations are shown. Observations of the back wall of T-2 are described at the right side of the figure. Black units represent peat and gray units represent silt; see Appendix 2.2 for unit descriptions. Faults are shown in solid lines where certain, and dashed lines where uncertain. Fault F1 is identified as the main fault based on its position in the trench, i.e., it cut units 1 to 10 and developed a considerable shear zone.

The penultimate faulting event (E2) is identified by the upward termination of faults F1 and F2, faulting of the top of peat unit 10, and faulting of colluvial unit 22 (Fig. 2.9). Units 1-10 appear to be folded or dragged equally, i.e., they have nearly the same shape and similar dragging style at their southern ends where they contact fault F1. This event must be younger than sample HS2-8 (~A.D. 1187-1268). HS2-8 predates the event because unit 10 existed prior to faulting. Therefore, I am confident that at least two faulting events occurred subsequent to the date obtained for sample HS2-8, because unit 10 is capped by faulted unit 12.

Faulting event 3 (E3) is identified by generation of colluvial unit 22 (Fig. 2.9) and the angular unconformity between units 7pa and 6. This event is bracketed between samples HS2-14 (~A.D. 777-888, unit 22) and HS2-8 (unit 10). I infer that delicate leaf material sampled from within unit 22 probably provides an equivalent age to the deposition of colluvial unit 22. Therefore, event 3 likely occurred around A.D. 777-888. Sample HS2-9 is not in order (may come from reworked materials) so is not used for the age estimation of E3.

Faulting event 4 (E4) is identified by comparing the position of the stoneline within unit 21 in T-1 to the position of the thin peaty horizon (21p) within the faulted fine-grained deposits and the unconformity between units 1 and 2 in T-2 (Fig. 2.9). Unit 21 in T-1 includes an obvious line of stones adjacent to Fault F3, which could be attributed to the oldest faulting event within both trenches. Figure 2.7 shows that unit 21 in T-1 correlates with unit 23 in T-2 implying that the stoneline is probably just above the thin peaty horizon and at or just below the base of the T-2 in the shutter basin. Sample HS2-6 yielded an age of A.D. 226-531. As mentioned already, this age is very similar to the age of basal units in both T-1 and T-2. However, there is ~0.5 m vertical distance between the position of HS2-6 and the basal units. Therefore, I interpret that the thin peat unit 21p has been faulted, folded and displaced vertically. Supporting evidence for vertically-displaced unit 21p is the grain size similarity (clayey silt) between units 21 and 23 and unit 1 (see Appendix 2.2). Therefore, I think that E4 should have occurred during or before the deposition of unit 1, i.e., it is younger than the age of sample HS2-6. Sample HS2-1 from the base of unit 2 provides the minimum age for event E4. Therefore, E4 is bracketed between samples HS2-1 and HS2-6; i.e., A. D. 265-570.

### 2.5.5 Age of surface features

#### 2.5.5.1 Age of the Holocene terrace and fan at the Hope Shelter site

Two samples were dated from the shutter ridge fan and the terrace (17 m above the modern river) using OSL. Sample HS-2012-1-1 (Table 2.3; 23.9 ± 1.5 ka) was taken from the lower sandy unit at 92 cm below the surface in Pit 1 to estimate the age of the fan and shutter ridge (Fig. S2.3 in Supplementary file and Fig. 2.6). This sandy unit correlates with unit 30C on the west wall of T-1. Sample HS-2012-4-1 (Table 3; 16.4 ± 1.2 ka) was taken from a silty unit at a depth of 45 cm below the ground surface in Pit 4 to estimate the age of the distal end of the fan/ terrace (Fig. S2.5 in Supplementary file). Both samples yield glacial or postglacial ages, i.e., ages that are consistent with the last cold climate period in New Zealand and not relating to the valley-filling period characterised by the Holocene deposits. The OSL ages are more consistent with the ages of the highest-elevation postglacial fans (~90 m above the modern river) in this area (12-24 ka; Nathan et al., 2002).

The elevation of the terrace at the trench site, as part of a degradational suite of terraces within the mid-Hope Valley, suggests that it is of mid-Holocene age. To assess the age of the terrace, I developed a river downcutting curve for the Hope River valley following the methodology of Cowan (1989). Here, in addition to his radiocarbon ages, I include a dated

terrace from near the Hope-Kiwi confluence (Langridge and Berryman, 2005) and apply the OSL dates from the Hope Shelter site to the highest-elevation postglacial fan above it, which is the source of deposits for the terrace and shutter ridge fan. I infer that the OSL results provide an accurate representation of the age of the postglacial fan (16-24 ka), rather than the surfaces at the trench site. Heights of the terraces/fan surface were measured from the local river bed. From these data, I developed an average downcutting rate curve of ~4.2 mm/yr spanning the last ~16-24 ka (Fig. 2.10). Using this rate, I predict the age of the terrace below the shutter ridge (~17 m above the Hope River) to be ~3300 (+ 553, - 360) yr. The positive error bar (+ 553) is produced when I allocate the OSL age of 16.4 ± 1.2 ka to the highest-elevation fan, and the negative error bar (- 360) is produced when I allocate the OSL age of 23.9 ± 1.5 ka to the highest-elevation fan. For simplicity, I only show the graph that allocates both OSL ages to the highest-elevation fan. If I eliminate the OSL ages from the graph, the same average age of ~3300 yr will be obtained for the terrace as other data on the graph will still yield the same relation on Fig. 2.10. This age is consistent with the oldest dates from the base of the shutter basin, and considerably younger than the OSL dates from both T-1 and Pit 4. These results confirm that surfaces low in the valley are likely to be of mid- to late-Holocene age. As the fan at the trench site gently grades to the Hope Shelter terrace, I believe that it probably has an age equivalent to the minimum age of the terrace. However, the minimum age of the fan is ~1700 yr based on the radiocarbon age of the base of the swamp formed on its surface.

Table 2.3. The results of OSL samples from Trench 1 and Pit 1 excavated on the low gradient Holocene fan and the Hope Shelter terrace (see also digital Appendix B).

| **Hope Shelter, OSL samples, February 2012** | | | | | |
|---|---|---|---|---|---|
| **Sample ID** | **Lab Number** | **a-value** | **$D_e$ (Gy)** | **Dose Rate (Gy/ka)** | **Age(ka)** |
| HS- 2012- 1- 1 | WLL1046 | 0.06±0.01 | 104.08±4.48 | 4.35±0.21 | 23.9±1.5 |
| HS- 2012- 4- 1 | WLL1037 | 0.06±0.01 | 74.59±4.28 | 4.55±0.19 | 16.4±1.2 |

The older than expected OSL age results may be explained by insufficient bleaching during the remobilisation of the sediment into the Holocene terrace and fan from the highest-elevation postglacial fan or insufficient transport and re-setting down valley. This is not surprising given that rapid sediment remobilisation and redeposition of sediments may be common in this environment. Such high rates and lack of bleaching conditions may arise

because of rapid fan instability triggered by seismic activity or flooding, and short transport distances downvalley.

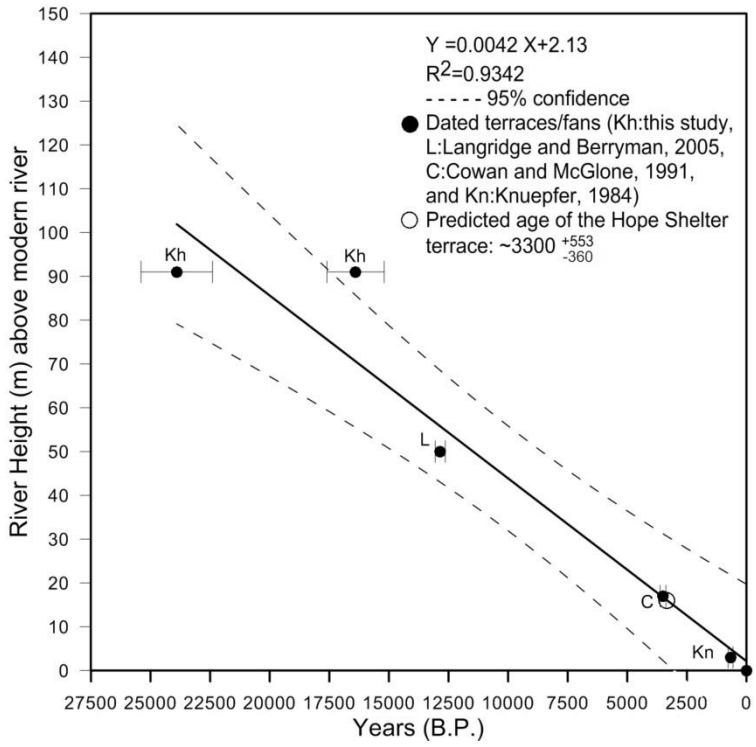


Figure 2.10. Hope River downcutting curve for the Hope River Valley is presented. Age of the Hope Shelter terrace is estimated using the curve.

### 2.5.5.2 Age of the debris deposit at the Hope Shelter site

At the trench site, the debris deposit overlies the middle part of the Holocene shutter ridge fan and the eastern part of the shutter basin (Fig. 2.4). It is composed of large angular boulders and is colonized by beech forest towards its head and Matagouri bushes towards its toe. A linear trough near the toe of the debris deposit, where the boulder clasts have been reorganised, indicates that it is faulted. A dextral offset of 2.6 ± 0.3 m is preserved at the western edge of the debris deposit. Therefore, an age assessment of the debris deposit and the timing of displacement were required.

A Schmidt hammer was used to compare the relative ages of the Hope Shelter debris deposit and a pre-1888 debris deposit near the Hope-Kiwi confluence (see Fig. S2.6 and section S2.4 in Supplementary file). More than 70 boulders were sampled within each debris deposit. The mean values of the Schmidt hammer from the two deposits were compared using one way ANOVA (analysis of variance) (see Table. S2.1 in Supplementary file). The results

of ANOVA imply no significant age difference between the two groups. This suggests that the debris deposit at the Hope Shelter site was not generated during the 1888 event.

Dendrochronology was used to estimate the minimum age of the debris deposit. Sixteen Red Beech (*Nothofagus fusca*) trees growing on the debris deposit were cored and measured in 2012 using standard dendro-chronological techniques, making notes of the growing condition and potential damage within the forest structure (see Fig. 2.4B for tree locations). Trees were cored at the borer height (sternum height of the sampler) of 120 cm. Upon extraction, the cores were stored in plastic tubes (diameter: 7 mm). Following transportation, samples were glued and placed on core mounts; wooden blocks (45× 4× 1.7 cm) thick with two grooves (each groove was ~6 mm wide and ~3 mm deep) in the middle. The samples were sanded down to near their cross-sections where I could see the rings. Ten of the tree cores contained all or some of the central rings of the trees and provide accurate dendro-ages (see Langridge et al., 2007). Six of the tree cores were shorter than the radius of the trees, providing minimum ages. Accurate ages were plotted against the tree diameter at the borer height (dbh) to produce the growth rate curve (Fig. 2.11A). I interpolated the minimum ages on the curve according to their dbh data (Fig. 2.11A). Age uncertainties associated with the interpolated data are shown as error bars with respect to the line of confidence. An age frequency histogram was produced, with accurate and interpolated ages, using a 10 yr bin size (Fig. 2.11B). The age frequency histogram shows a minor peak at ~110 ± 10 yr and a major peak at 130 ± 10 yr. Three trees with interpolated ages affect the gray bars of the histogram adjacent to the 1888 A.D. event (Fig. 2.11A-B). One of the interpolated ages falls after 1888 A.D., one is included within the gray bar just before 1888 A.D. and one is included within the second gray bar before 1888 A.D. According to Fig. 2.11A, these interpolated ages are associated with ± 20 yr of uncertainty, meaning that they can shift or change the peaks, but at this stage, I cannot predict the exact effect of this on the histogram. However, if the ages of the three interpolated data are all overestimated or underestimated by ± 20 yr, two peaks (pre- and post-1888) are still resolvable. Two trees give older ages: 197 yr (A.D. 1815) and 275 yr (A.D. 1737). The age of the oldest tree provides the minimum age for the debris deposit, i.e., 275 ± 10 yr. A distinct period of non-colonisation, i.e. the period between (A. D. 1815-1737), appears on the histogram. The minor peak is consistent with forest re-colonisation immediately post-1888.

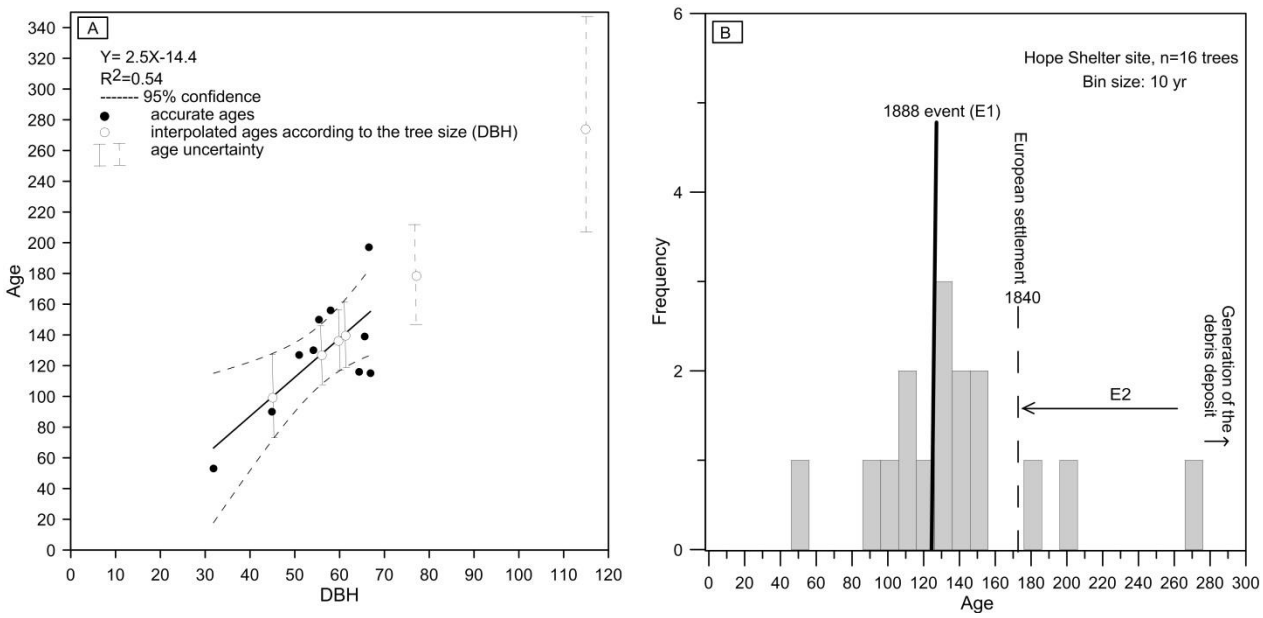


Figure 2.11. The results of the dendro-chronologic study are shown. Abbreviation DBH stands for Diameter at the Borer Height. The 1888 event and historical period (A.D. 1840) are shown on the graph. (A), Shows a linear relationship between DBH and age of the trees. (B), shows one major peak pre 1888 and one minor peak post 1888 using 10 yr bin size.

Apart from earthquakes, many processes including fire, flood, hydrological change, wind, disease, and storm can affect the structure of a forest. Perhaps the most obvious visible effect in the modern forest is windthrow. I expect that windthrow is a significant background effect in the tree structure, which is evident by single tree colonisation every few decades. I am confident that the Hope Shelter site was not deforested by fire at least since the European settlement based on: (1) the absence of any historical report of deforestation at this site, (2) personal accounts of the land owners (pastoralists) that deforestation was unlikely at this site, (3) the absence of any trees that appear to be fire-damaged, in contrast with other sites affected by fire, and (4) the absence of charcoal within either of the trenches at the site.

I examined whether the 2.6 ± 0.3 m displacement of the edge of the debris deposit was from one or more than one event. The toe of the debris deposit occurs on the south side of the fault zone on the pre-existing shutter scarp and then has been faulted (Fig. 2.4). Therefore, it is younger than the pre-existing shutter scarp and basin formed behind the fault scarp and is the youngest displaced geomorphic feature within the study site. The displacement recorded along the western edge of the debris deposit (2.6 ± 0.3 m) is consistent with the measured displacements by McKay (1890) following the 1888 Amuri earthquake (Fig. 2.2). This in combination with the dendrochronology results implies that the debris deposit could have been displaced once or twice since its deposition. If unit 12 (gravel) in T-2 comes from the

reworking of finer-grained material associated with the debris deposit, then the maximum age of the debris deposit would be more than 275 yr, but less than ~800 yr because unit 12 is younger than ~800 years B.P., i.e., younger than sample HS2-8.

### 2.5.5.3 Age of the surfaces near Parakeet Stream

Alluvial surfaces high in the landscape near Parakeet Stream (~800 m a.s.l.), were mapped in detail from LiDAR in order to assess the Holocene slip rate (Khajavi et al., intended for submission, chapter 3). These surfaces have been displaced dextrally along the Hope Fault by several tens of meters (Khajavi, 2015). A series of augers and pits were undertaken to derive the ages of gravel deposition or the abandonment of clastic deposition in favour of peat, which commonly blankets this upland landscape. The stratigraphy of typically shallow (1 m) pits and deeper (1.5 m) augers were logged and organic samples were collected from above and below clastic horizons within these swamps (Fig. S2. 9-10 in Supplementary file). Five radiocarbon samples were dated (Table 2.4). The ages of the samples were all considerably younger than the expected ages for those surfaces offset along the Hope Fault, which would yield unreasonably high slip rates for the fault. Therefore, I reconsidered the stratigraphy and dates from Parakeet Stream in terms of a late Holocene record of off-fault landscape change processes (clastic earthquake-driven pulses overlying stable peaty upland surfaces) as proxies for the timing of surface faulting, rather than as estimates relating to larger cumulative displacements.

Table 2.4. Radiocarbon dating results from the Parakeet Stream site, Western Hope Fault.

| **Parakeet Stream- Pits, C14 samples, February 2013** | | | | | | | | |
|---|---|---|---|---|---|---|---|---|
| Sample ID | Lab Number | $\Delta^{13}C$ (‰) | Radiocarbon age (years B.P.) | Calibrated age (2σ) A.D. | | Probability for each 2σ range (%) | | Sample type and description |
| T3W-1 | NZA 53427 | -27±0.2 | 395±16 | 1460-1512 | 1548-1623 | 44.9 | 49.9 | Peat-seeds |
| T3W-2 | NZA 53430 | -26.5±0.2 | 380±16 | 1479-1627 | | 95.4 | | Colluvium- outer bark of a dark brown twig |
| T4EP-4 | NZA 54174 | -28.9±0.2 | 1624±20 | 425-551 | | 95.2 | | Peat- Peat lumps composed of plant tissues |
| T4WP-3 | NZA 54160 | -28.8±0.2 | 903±19 | 1156-1221 | | 95.1 | | Peat- Wood pieces |
| OCWP-6 | NZA 54154 | -29±2 | 2090±21 | 113BC-50AD | 156BC-134 BC | 91.3 | 3.8 | Peat-seeds |

#### 2.5.5.4 OxCal modeling of radiocarbon ages

Using the OxCal 4.2.3 program (Bronk Ramsey 2013), two models were constructed for T-1 data; T-1 model 1 with six events and T-1 model 2 with 5 events. One model with four events for T-2 was constructed. The models include the historic 1888 Amuri earthquake, the beginning of the historical period (A.D. 1840), and the maximum age of the trees grown on the debris deposit (275 ± 20 yr). Details of the OxCal models (i.e., dates, event horizons, and commands) are presented in Appendix 2.3. The results of modelling T-1 and T-2 data are presented in Figs. 2.12-2.14, respectively. The results from trenches excavated in close proximity (i.e., 4m apart) highlight the challenges in paleoseismic interpretations and imply a different number of events expressed or preserved in trench walls. T-1 provides evidence for 5-6 faulting events during the last ~1700 yr and T-2 provides evidence only for 4 faulting events during the same period (Table 2.5, Figs. 2.7-2.10 and 2.12-2.15). Timing of the events, distribution of the average recurrence interval (RI), mean (μ), median of the average RI, and the minimum and maximum times between the ruptures were calculated by OxCal at the 2 sigma (2σ) level (Table 2.5). The timing of events in the T-1 models were calculated as ~A.D. 298-419, 439-580, 596-1092, 1106-1736 and 1825-1888. A possible sixth event, shown in T-1 model 1, likely occurred at A.D. 1819-1848. The modelled timing of events in T-2 are calculated as A.D. 373-495, 819-1192, 1235-1730 and 1733-1888. Here, the correlations between events from T-1 to T-2 and the differences in the interpretations of these two records are discussed.

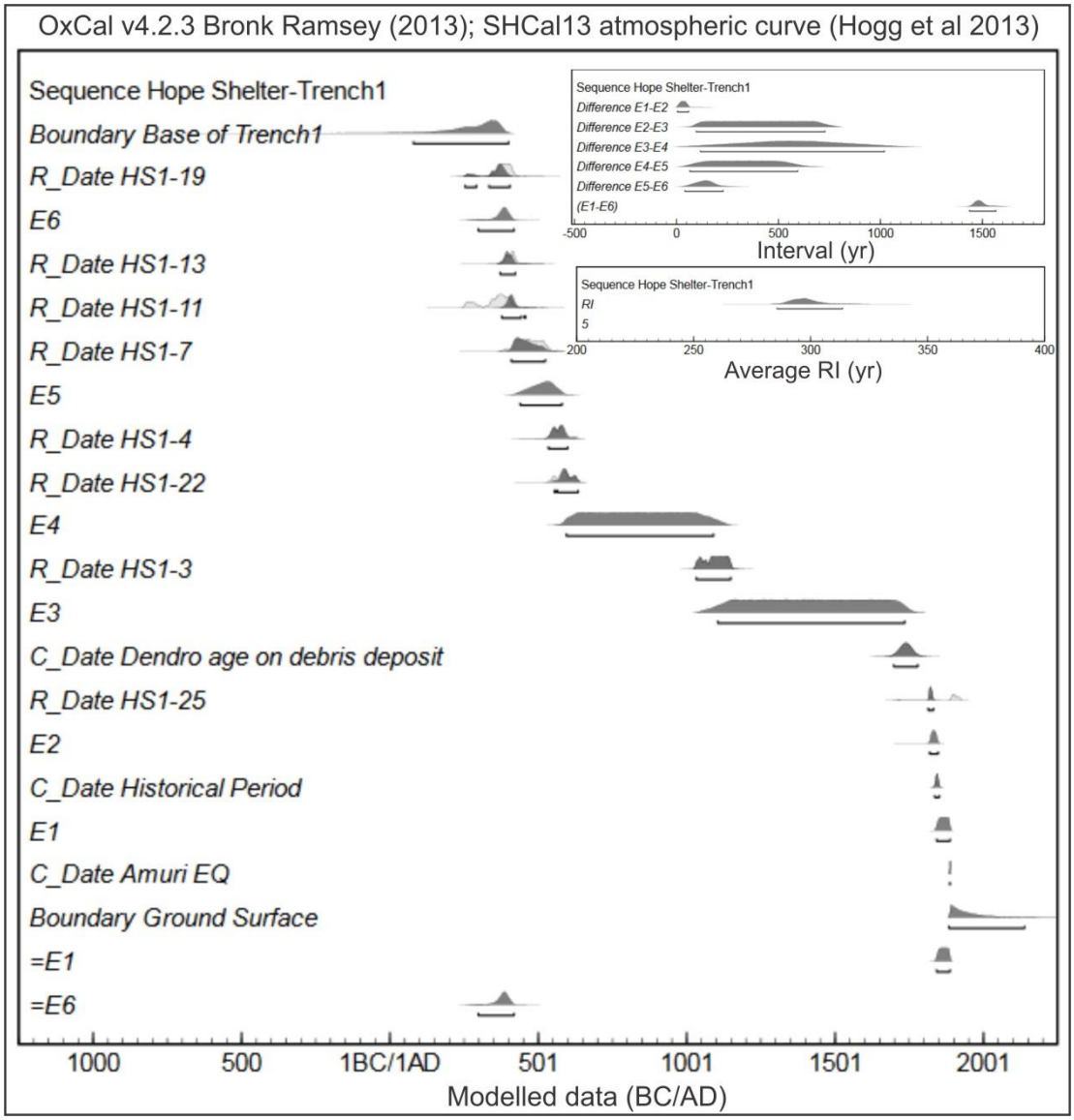


Figure 2.12. The results of OxCal modelling (Trench 1- model 1) including dates plots, plots of RI times between each two events, and average RI time are presented. Calibration curved used for this analysis is SHCal13. E1-E6 are the events.

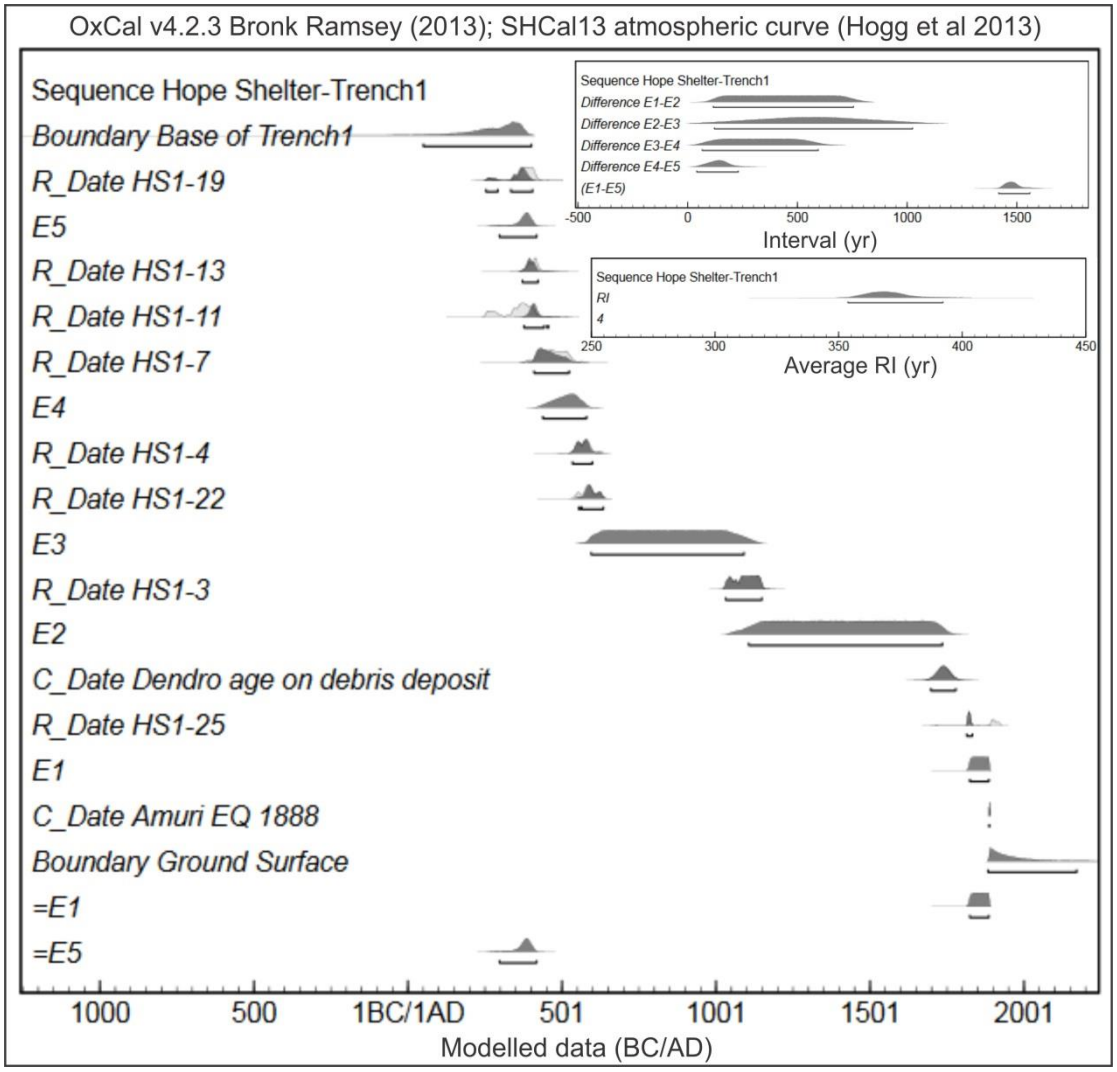


Figure 2.13. The results of OxCal modelling (Trench 1- model 2) including dates plots, plots of RI times between each two events, and average RI time are presented. Calibration curved used for this analysis is SHCal13. E1-E5 are the events.

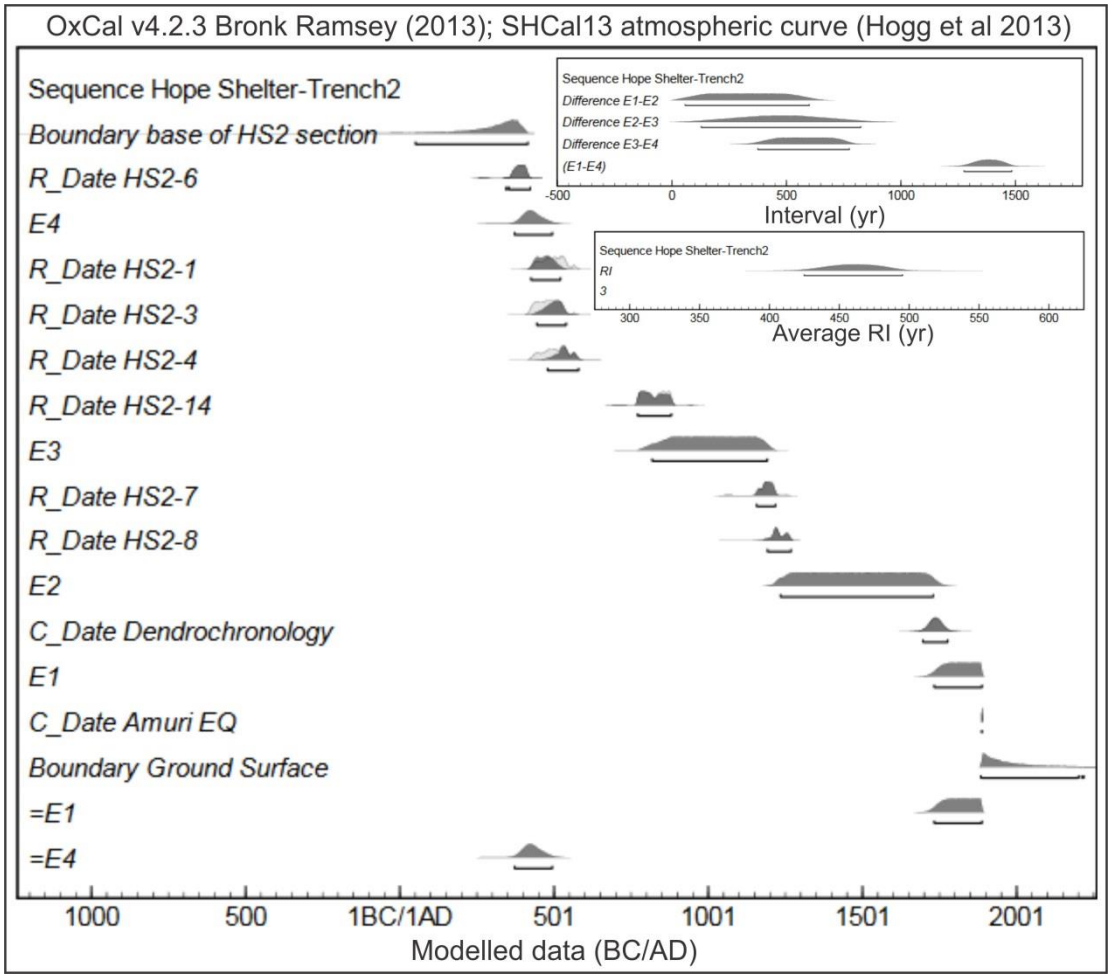


Figure 2.14. The results of OxCal modelling (Trench 2) including dates plots, plots of RI times between each two events, and average RI time are presented. Calibration curved used for this analysis is SHCal13.E1-E4 are the events.

## 2.6 **Discussion**

### 2.6.1 Paleoearthquakes on the Hurunui segment

The trench exposures at the Hope Shelter site and related data provide the longest record of paleoseismicity along the Hope Fault (see Cowan and McGlone, 1991; Langridge et al., 2003; 2013), extending back to ~300 A.D. Evidence for paleoseismic events in trenches comes from upward fault terminations, scarp-derived colluvial wedges, unconformities, and/or progressive folding of the shutter basin deposits, and for the most recent earthquakes from geomorphic and dendrochronologic data from the nearby debris deposit and trees.

The ages of the most recent events in the T-2 OxCal model and T-1 OxCal model 2 span the ages of the two youngest events in the T-1 OxCal model 1 (i.e., there likely is an extra upper event in the T-1 model 1, Figs. 2.7 and 2.15 and Table 2.5). The age of the

penultimate event in the T-2 model overlaps with the ages of the penultimate event in the T-1 model 2 and the event E3 in the T-1 model 1. The age of the event E3 in the T-2 model is nearly consistent with the ages of the events E4 in the T-1 model 1 and event E3 in the T-1 model 2. The age of the oldest event in the T-2 model also nearly spans the ages of the two oldest events in the T-1 model 1 and in the T-1 model 2 (i.e., there likely is an extra lower event in the T-1 models, Figs. 2.7 and 2.15).

Table 2.5. Paleoseismic history of trenches 1 and 2 modelled using OxCal program. All of the values are reported at 2σ level. Two models are presented for Trench 1 and compared with the Trench 2 model. Abbreviation RI: Recurrence Interval.

| **Trench 1 (Model1)** | | **The Min. and Max. times between every 2 events** | **Trench 2** | | **The Min. and Max. times between every 2 events** |
|---|---|---|---|---|---|
| **Events** | **Timing (A.D.)** | | **Events** | **Timing (A.D)** | |
| E1 | 1843-1888 | E1-E2: 5-60 | E1 | 1733-1888 | E1-E2: 58-600 |
| E2 | 1819-1848 | E2-E3: 97-729 | E2 | 1235-1730 | E2-E3: 128-825 |
| E3 | 1106-1735 | E3-E4: 118-1020 | E3 | 819-1192 | E3-E4: 375-775 |
| E4 | 596-1092 | E4-E5: 65-595 | E4 | 373-495 | |
| E5 | 439-580 | E5-E6: 41-230 | | | |
| E6 | 299-419 | | | | |
| Distribution of the average RI: 285.7- 313.7<br>Mean: 297.968<br>Median: 297.2 | | | Distribution of the average RI: 424.833- 495.333<br>Mean: 460.705<br>Median: 460.833 | | |
| **Trench 1 (Model 2)** | | **The Min. and Max. times between every 2 events** | **Trench 2** | | **The Min. and Max. times between every 2 events** |
| **Events** | **Timing (A.D.)** | | **Events** | **Timing (A.D.)** | |
| E1 | 1825-1887 | E1-E2: 117-756 | E1 | 1733-1888 | E1-E2: 58-600 |
| E2 | 1107-1736 | E2-E3:122-1025 | E2 | 1235-1730 | E2-E3: 128-825 |
| E3 | 596-1092 | E3-E4: 66-595 | E3 | 819-1192 | E3-E4: 375-775 |
| E4 | 439-580 | E4-E5: 42-231 | E4 | 373-495 | |
| E5 | 298-419 | | | | |
| Distribution of the average RI: 353.75-392.25<br>Mean: 369.872<br>Median: 368.75 | | | Distribution of the average RI: 424.833-495.333<br>Mean: 460.705<br>Median: 460.833 | | |

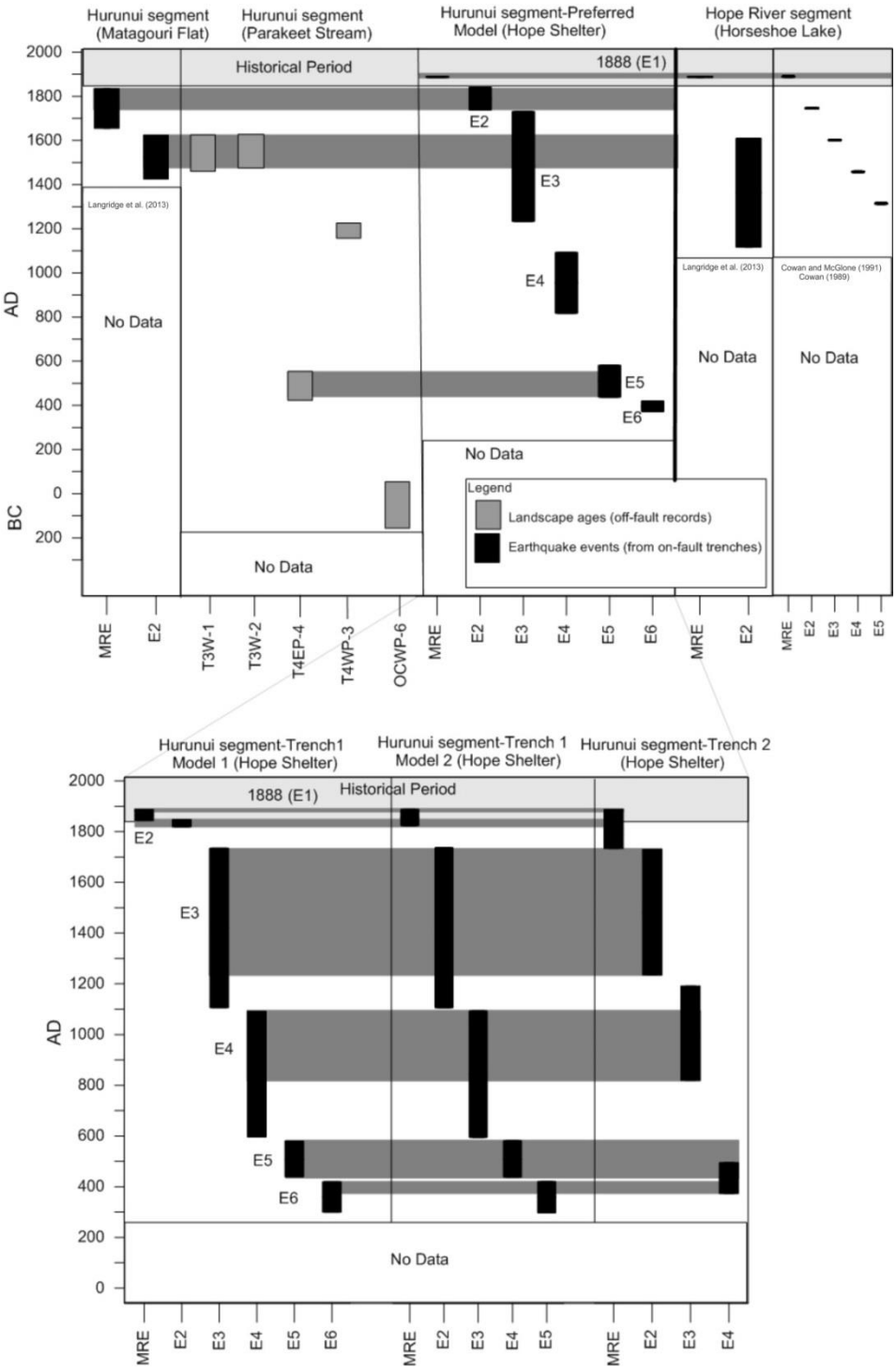


Figure 2.15. The timing of late Holocene paleoearthquake histories for the Hurunui and Hope River segments of the Hope Fault including the 1888 Amuri earthquake. The events timings calculated by the models for the Hope Shelter site are presented and compared. My preferred model for the Hope Shelter site represents six events which are identified considering time overlaps between all of the available data for the two segments of the Hope Fault. I compare two sets of data: (1) the on-fault trenching data which are interpreted as direct evidence for surface faulting events (Cowan, 1989; Cowan and McGlone, (1991); Langridge et al., 2013; this study), and (2) the off-fault data (from pits on the swampy areas adjacent and south of the fault scarp near Parakeet Stream) which are not direct evidence for surface rupturing events. The bold vertical line on the top figure separates the Hope River segment data from the Hurunui segment data.

The existence of the extra upper event in the T-1 model 1 (i.e., if I interpret the deposition and faulting of unit 2 as 2 events) suggests that I am missing evidence for an event in T-2. I argue that fault F3 in T-2 could have ruptured twice recently, meaning that 2 events faulted unit 12. The reason for this argument is that unit 12 could have been derived from the reworking of (i.e., postdates) the debris deposit on the surface. If this interpretation is valid, and the debris deposit has been faulted twice on the surface, the missing event in T-2 must have occurred on fault F3. Therefore, the two recent events in T-2 should be younger than ~800 B.P., i.e., younger than the maximum age estimation of the faulted debris deposit using the age of sample HS2-8 in T-2.

A critical stratigraphic relationship within T-1 is whether unit 2 is a scarp-derived colluvium and if it is, whether it has been subsequently faulted. According to the similarity between the ages of the penultimate events in the T-1 model 2 and T-2 model, it could be inferred that unit 2 in T-1 is unfaulted and only draped across the fault scarp free-faces immediately after the most recent event. If this interpretation is valid, I am not missing an event in T-2, but the age scenario of the debris deposit could remain valid. At this stage, both interpretations are possible; however, based on the age of unit 2 in T-1 and the only known historic event on the fault (the 1888 event) I favour the interpretation that unit 2 in T1 is faulted colluvium.

The existence of the extra lower event in the T-1 models suggests that I am missing evidence for another event in T-2. According to the stratigraphy of the trenches (Figs. 2.7-2.9), event E6 in the T-1 model 1 correlates well with the oldest event in the T-2 model. Therefore, I am missing an event between E3 and E4 in T-2. I argue that the missing event possibly occurred between units 4 and 5. This argument is supported by: (1) the chronology and position (Fig. 2.7) of the peat unit 4, (2) changes in the depositional environment, that is to say changes from a quiet (unit 4; peat) to a more energetic alluvial environment (unit 5; sand), and (3) the unconformity between units 4 and 5 to the north of T-2. Unfortunately, due to the more alluvial nature of T-2 with respect to T-1, I do not have enough dates between units to estimate a higher resolution age range for the event. My interpretation, which relies on the changes in depositional environment as earthquake proxies, is consistent with the work of other researchers (e.g., Cowan and McGlone, 1991, Berryman et al, 2012b; Clark et al., 2013).

From the above, it can be inferred that two events in T-2 are missing and my preferred record comprises six events that occurred during the last ~1700 yr at the site. Therefore, I

give more credit to the T-1 model 1 than other models in terms of the number of the events. To construct my preferred model (i.e., the best possible unified model in terms of the timing of the events), I examined the overlapping time between the events in the three models and the results of dendrochronology (see the events timings in my preferred model, Fig. 2.15). To examine the chronology of the events along the two segments of the Hope Fault, I shaved the timing of the events in my preferred model considering all of the modelled events along the Hurunui and Hope River segments (Cowan and McGlone, 1991; Langridge and Berryman, 2005; Langridge et al., 2013) and the ages of the off-fault samples from augers and pits near Parakeet Stream (Figs. S2.9-S2.10 in Supplementary file). Taking that into account, the preferred and shaved timing of these six events are calculated as follows. The most recent faulting event correlates with the 1888 Amuri earthquake (A.D. 1888) (Figs. 2.7, 2.11 and 2.15 and Table 2.5). The penultimate faulting event (E2) likely occurred between ~A.D. 1740 and 1840. An important constraint that I modelled for this event was that it had to have occurred before A.D. 1840 as there is no historical record of another large earthquake in the area between A.D. 1840 and 1888. The pre-penultimate faulting event (E3) possibly occurred between ~A.D. 1479 and 1623. The faulting events E4, E5 and E6 likely occurred between A.D. 819 and 1092, between A.D. 439 and 551, and between A.D. 373 and 419, respectively. Using the Monte Carlo statistical approach a mean recurrence interval of 298 ± 88 yr is calculated from these event ages (see Part 7 in Supplementary file).

### 2.6.2 Most recent faulting event: the 1888 Amuri earthquake

The combination of McKay's observations, the trench results, and other dating techniques provide strong evidence that the 1888 Amuri earthquake ruptured through the Hope Shelter site. Data from trenches provide support for at least one faulting event (E1) during the 19th century (A.D. 1817-1921, see age of the sample HS1-25) with an OxCal modelled age of A.D. 1843-1888. It appears that the most recent event faulted colluvial unit 2 in T-1, and is consistent with evidence at T-2 (Figs. 2.7 and 2.9). I estimate a surface rupture length of 44-70 km for the 1888 Amuri earthquake. The minimum surface rupture length of 44 km is estimated from the Hope-Kiwi confluence (McKay, 1890) approximately 5 km west of my trench site to the western margin of the Hanmer Basin (Cowan, 1991) (Fig. 2.2B). The western extent of the 1888 rupture could have passed through the Parakeet Stream area; although, no clear evidence for this was identified in my preliminary investigations. The maximum surface rupture length of 70 km is limited to the west by the trench site of

Langridge et al. (2013) where dating appears to preclude the possibility that the 1888 Amuri earthquake ruptured this far to the west, with an easternmost trace location consistent with the maximum eastward position of rents and fissures observed east of the Hanmer Basin (Hossack Station; Fig. 2.2B) (McKay, 1890). Conversion of surface rupture lengths to earthquake magnitudes using the scaling equation of Wesnousky (2008) yields an estimated magnitude $M_w$ of 7.1 ± 0.1 for the Amuri earthquake.

The dendrochronology results (Fig. 2.11) provide several important insights applicable to the paleoseismic record: (1) the oldest tree sampled on the deposit had grown up to corer height by A.D. 1737 confirming that the emplacement of the debris deposit was not the result of the 1888 event, (2) the existence of the distinct period of non-colonisation (A.D. 1815-1737) followed by the older major tree age peak at ~130 ± 10 yr, clearly predates the 1888 event and could likely represent an earthquake that knocked down a group of trees before the European settlement of New Zealand (A.D. 1840), (3) the forest re-colonisation immediately post-1888 (Fig. 2.11, second peak at ~110 ± 10 yr) suggests that some trees could have been damaged or knocked down by the 1888 event, allowing younger trees to shoot up immediately following the 1888 event as implied by McKay's observations of tree damage. Taken together, these results of dendrochronology collectively indicate that the debris deposit probably experienced two events in the last 275 yr (since A.D. 1737) with some certainty that one of these events was the 1888 Amuri earthquake.

The results of this study confirm that the horizontal displacement of 2.6 ± 0.3 m measured at the western edge of the debris deposit at the Hope Shelter site is the result of one or two displacement events. Although a maximum coseismic displacement of 2.6 m in the 1888 Amuri earthquake was documented on the Hope River segment (McKay, 1890), the location of my study site closer to the end of the 1888 rupture extent, and on a different rupture segment, suggests that a smaller coseismic slip in this event is likely, which is consistent with the observation of decreasing surface rupture displacements towards rupture tips (e.g., Lin et al., 2012; Quigley et al., 2012). The base of the colluvial wedge (unit 2; Fig. 2.8) is interpreted as stepped, but appears to be stratigraphically coherent across the fault zone; if larger (e.g., ≥ 0.5-1m) coseismic displacement occurred it is likely that this relatively thin (< 20 cm) unit would have been structurally dismembered or juxtaposed against a different lithology.

### 2.6.3 Relationship between surface and subsurface data and slip rate estimation

From the relationship between the geomorphic features and their estimated ages at the Hope Shelter site, a horizontal slip rate can be computed. This study estimates the age of the shutter ridge fan to be between ~1700 yr (based on the development of the shutter basin) and ~3300 yr (based on the estimated age of the Hope Shelter terrace according to the downcutting rate of the Hope River). With the estimated mean RI of ~298 ± 88 yr in this study, I expect 4-16 events to rupture the Hope Shelter site during this time. Earthquake records from the trenches are consistent with the lower range of the expected events on the shutter ridge fan. The Hope Shelter fan has preserved a cumulative dextral displacement of 14 ± 3 m at the Hope Shelter site. This fan should probably have an equivalent age to the minimum age of the Hope Shelter terrace because, like the shutter ridge fan, it also gently grades to the Hope Shelter terrace and has been entrenched by the shutter basin (Fig. 2.4). Therefore, using the minimum age of the shutter ridge fan (~1700 yr) and the 14 ± 3 m of cumulative displacement on the surface, I estimate a preliminary maximum horizontal slip rate of 6.5-10 mm/yr at the Hope Shelter site. This estimated slip rate is consistent with the estimated minimum horizontal slip rate of 8-11 mm/yr calculated for a site at the western part of the Hurunui segment (see Langridge and Berryman, 2005).

### 2.6.4 Periodic versus Episodic Earthquake Recurrence

The faulted stratigraphy at the Hope Shelter site provides the longest and potentially most complete record of paleoearthquakes along the Hope Fault, allowing for a critical assessment of late Holocene earthquake recurrence times. Figure 2.15 shows a summary of event chronologies along the two segments of the Hope Fault, from which inter-event times are extracted. Based on the data from this study (Figs. 2.2 and 2.15), event E1 (1888) ruptured the Hope River segment and parts of the Hurunui segment indicating that the western extent of the 1888 Amuri earthquake rupture is somewhere between the Hope-Kiwi confluence and Parakeet Stream, but not as far west as the Langridge et al. (2013) trench site. The most recent event of Langridge et al. (2013) provides support for the occurrence of an event (i.e., E2) in A.D. ~1740-1840 on the Hurunui segment, which coincides with a strong shaking event along the Hope River segment (Langridge et al., 2013, Table 2.1). Based on the correlation between the Parakeet Stream dataset and earthquake events, it appears that the stratigraphy in the Parakeet Stream sections represents seismically-driven clastic pulses into a

largely stable peat-forming setting associated with Hope Fault earthquakes. This interpretation is strengthened by the radiocarbon dates, which are all of late Holocene age and typically separated by 300-500 years across the Parakeet Stream area. The youngest dates at this site, which is located halfway between the Matagouri Flat and Hope Shelter trench sites (Langridge et al., 2013; this study), align with those at Hope Shelter, Matagouri Flat, and Horseshoe Lake (Cowan and McGlone, 1991). This provides support for the occurrence of an event (or events) between ~A.D. 1400 and 1600 (i.e., E3) on both the Hope River and Hurunui segments (Fig. 2.15). One of the older dates (T4EP-4) at Parakeet Stream Site provides support for the occurrence of an event (i.e., E5) in the ~A.D. 400-600 timeframe on the Hurunui segment (Fig. 2.15).

The calculated MRI of 298 ± 88 years overlaps with both the previous estimates of RI = 310-490 yr for the Hurunui segment (Langridge and Berryman, 2005; Langridge et al., 2013) and the previous estimates of the RI = 81-200 yr for the Hope River segment (Cowan and McGlone, 1991). The mean RI of 298 ± 88 years using inter-event times from the preferred ages of the events is consistent with the mean RI times calculated by the three individual OxCal models in this study (i.e., ~300, ~370 and ~460 yrs) (Table 2.5). Cowan and McGlone (1991) proposed a periodic earthquake model for the Hope River segment (earthquake surface ruptures every ~81-200 yrs); however, Langridge et al. (2013) interpreted that only two of the five events identified by Cowan and McGlone (1991) can be directly attributed to surface rupturing events and the rest could be attributed to shaking events that generated subsequent silt deposition in their trench on the Hope River segment (Table 2.1). Resolving this debate is beyond the scope of this thesis.

Median inter-event times between successive events identified from the Hope Shelter trenches range from 98 to 595 yrs. Inter-event times between E1 and E2, E2 and E3, and E5 and E6 are shorter than the mean RI, and median inter-event time between events E3 and E4 and E4 and E5 are longer than the mean RI. There is a long average inter-event time between events E4 and E3 (595 yr). It is my preferred hypothesis that E3 involved rupture of both the Hurunui and Hope River segments of the fault, either coseismically (and thus somewhat similar to the multi-segment rupture in the 1888 Amuri earthquake) or in separate events spaced closely enough in time to be unresolvable from dating resolution. A moderate average inter-event time of ~239 yr exists between events E3 and E2, and a shorter average inter-event time exists between events E2 and E1 (98 yr); the youngest event (E1, 1888) having ruptured the entire Hope River segment and part of the Hurunui segment. There is a long

inter-event time of 460 yr between events E4 and E5 and a shorter average inter-event time between events E5 and E6 (99 yr).

Inter-event times that are significantly shorter than the mean recurrence interval can be explained by: (1) coalescing rupture overlap from the adjacent Hope River fault segment on to the Hurunui segment at the study site (e.g., E1 and possibly E3), which could create apparent earthquake clustering irrespective of whether the individual segments exhibit periodic or episodic rupture behaviour, and/or (2) earthquake temporal clustering (i.e., episodic temporal behaviour) on the Hurunui and/or Hope River segments. Inter-event times that are significantly longer than the mean recurrence interval can be explained by earthquake temporal clustering (episodic behaviour), and/or 'missing' or otherwise unresolved events (option 3). The final possibility (option 4) is that the apparently variable inter-event times simply reflect limited chronologic resolution due to some large age ranges of radiocarbon samples. However, the large number of samples, use of OxCal modelling and different recurrence scenarios, and inability to fit periodic recurrence to the age data even with full consideration of age ranges, suggests that the latter possibility is the least likely reason for the observed variability.

Given the conclusion that the 1888 Amuri earthquake involved coeval rupture of both the Hope River and part of the Hurunui segment, I consider rupture overlap (option 1) to provide a reasonable explanation for some of the temporal distribution of earthquakes at the study site, irrespective of whether individual segments exhibit periodic or episodic behaviour. However, this scenario alone is unlikely to explain all of the observed variability, because some of the inter-event times (i.e., E3-E4-E5) greatly exceed the proposed ranges of average inter-event times on adjacent segments, particularly for the proposed periodic RI for the Hope River segment (Cowan and McGlone, 1991). Episodic rupture behaviour on the Hurunui segment, Hope River segment, or both, could account for both the comparably short and long inter-event times with respect to the mean RI. I cannot dismiss the possibility that I may be missing events from the trench record, despite the closely spaced and detailed nature of my investigations (option 3). 'Missing events' could include earthquake ruptures that did not rupture through the trench site (i.e., ruptured other strands, or terminated beneath or outside of the trench extent), or that did not leave a stratigraphic and structural record in the trench that was distinguishable from other events. Missing events could account for inter-event times longer than expected from periodic recurrence intervals from the Hurunui and Hope River segments. With the current state of knowledge I cannot easily assess the possibility that

one or more events could have occurred but were not recognized during the time period encompassed by the trench stratigraphy. Future paleoseismic studies along the Hurunui and Hope River segments of the Hope Fault should continue to refine the extent, timing, and rupture behaviour of past earthquakes in this region.

### 2.6.5 Rupture segmentation: evidence for a geometric barrier between the two segments?

The preferred earthquake model for the Hope Shelter site indicates two events within the last ~250 yr and/or three events within the last 400-500 yr (Fig. 2.15). In contrast, the paleoseismic records from other segments along the Hope Fault (Table 1) show evidence for two or three events within the last ~600-900 yr (Langridge et al., 2013). The discrepancy here can be explained by the location of the trenches as they were excavated near a segment boundary; where the ruptures of the Hope River and Hurunui segments could overlap (e.g., events E1 and E3?, Fig. 2.15). The boundary between the two segments is characterized by a ~850-m-wide right stepover in the fault associated with a 9º-14° fault bend (Fig. 2.3).

Several studies show that stepovers or bends separating fault segments can arrest or ease rupture propagation under certain circumstances (e.g., Barka and Kadinsky-Cade, 1988; Wesnousky, 2006, 2008; Oglesby, 2005; Elliot et al., 2009; Wesnousky and Biasi, 2011). In particular studies on the historical strike-slip surface ruptures (e.g., Wesnousky, 2006; Wesnousky and Biasi, 2011) showed that stepovers ≥ 1 km are about 50% effective in stopping rupture propagation while stepovers ≥ 3-4 km appear to arrest rupture propagation. Barka and Kadinsky-Cade (1988) also indicated that bend angles > 30º may stop large rupture propagation. Other factors such as the existence of structural complexity or changes in the dynamic behaviour of the rupture near the stepover, the existence of fault segments separated by bends or stepovers with favourable orientations to rupture with respect to the regional stress field can influence the rupture dynamics and propagation (Elliot et al., 2009).

According to the criteria explained by the above studies, it seems that the conditions at the study site, between the two fault segments, are more favourable for rupture propagation than arrest. The width and bend angle of the right stepover between the Hope River and Hurunui segments are narrower and smaller compared to the rupture-limiting thresholds mentioned by the above studies. In the overlapping area of the two segments just west of the bend, dextral slip has dropped dramatically, but transferred into vertical slip represented by a suite of en echelon structures (Khajavi et al., 2014) (Fig. 2.3). Characteristics such as the

more favourable orientation of the Hurunui segment to rupture with respect to the regional stress field (Khajavi et al., 2014), the < 1 km width of the local releasing stepover (e.g., Elliot et al, 2009; Wesnousky and Biasi, 2011), the rapid changes in the slip mode (dextral to vertical), and the comparable paleoseismic histories obtained from the trenches along both segments, it is likely that some of the ruptures can propagate through the bend and stepover and continue some distance along the adjacent segment (e.g., events E1 and E3, Fig. 2.15). Regarding event E3, I cannot confirm whether this event was a Hope River rupture that propagated towards the Hurunui segment, or vice versa, or a bilateral rupture. It appears that event E3 did not stop at the stepover and involved rupture on both segments, with a rupture length consistent with (or longer than?) the historical event E1 (the 1888 Amuri earthquake). Based on an oral account in MacKay (1890), the 1888 rupture likely propagated from the west toward the east of Glynn Wye station (Fig. 2.2B) (McKay, 1890; Cowan, 1991). Based on the results of this study there are two possibilities: (1) the rupture could have nucleated on the Hurunui segment and propagated to the Hope River segment, via the bend and stepover, with a unilateral directivity towards the east, or (2) the rupture could have propagated bilaterally from Glynn Wye station (see Fig. 2.2 and Appendix 2.1: 17) or from an unknown point west of the Glynn Wye station. Because the Hurunui segment is better oriented for slip (Khajavi et al., 2014), it can be inferred that larger multi-segment ruptures may be more likely to initiate on the Hurunui segment than on the Hope River segment. The possibility that rupture directivity and/or rupture velocity may have influenced whether Holocene ruptures propagated through or arrested near the study site remains a focus of future research. By demonstrating that the 1888 Amuri earthquake propagated through a proposed segment boundary, I provide first evidence for coseismic multi-segment ruptures on the Hope Fault. In combination with the paleoearthquake chronology, I conclude that paleoearthquake records near geometrically complex segment structural boundaries on major strike-slip faults may show temporal recurrence distributions resulting from earthquake ruptures that variably arrest or propagate through proposed segment boundaries. I posit that earthquake recurrence along major strike-slip plate boundary faults may vary between more periodic and more episodic end-members, even on adjacent, geometrically-defined segments.

## 2.7 **Conclusions**

Paleoseismic investigations of the Hurunui segment of the Hope Fault coupled with reanalysis of historical observations (McKay, 1890) provide first evidence for the surface

rupturing on this fault segment during the 1888 Amuri earthquake. The results of trenching, combined with defining the slip gradient curve, show that the 1888 rupture could have a surface rupture length of 44-70 km, and a magnitude of $M_w$ = 7.1 ± 0.1. A preliminary maximum horizontal slip rate of 6.5-10 mm/yr is estimated at the Hope Shelter site on the Hurunui segment. The results from two closely spaced paleoseismic trenches excavated at the Hope Shelter site indicate that 6 earthquake events likely occurred in the past ~1700 yr. The timing (~A.D. 1888, 1740-1840, 1479-1623, 819-1092, 439-551, and 373-419) of these events were estimated using OxCal modelling and overlapping event times using data from trenches in this study, and other trenches along the Hurunui and Hope River segments and the data from the Parakeet Stream site. A mean RI of 298 ± 88 yr is estimated for the identified events. Earthquake records on the Hurunui segment of the Hope Fault contain evidence for short inter-event times (as short as ~98 yr) resulting from (1) rupture overlap and multi-segment ruptures, and/or (2) earthquake temporal clustering. The geometrically-defined segment boundary between the Hurunui and Hope River segments does not always act as barrier to rupture propagation, and analogous geometric discontinuities may not limit rupture dimensions elsewhere along the Hope Fault, implying that the magnitude of future earthquakes may in some instances exceed estimates based on lengths of individual fault segments.

## Acknowledgements

I wish to thank NZ Natural Hazards Research Platform for funding the LiDAR project. I thank the department of Geological Sciences, University of Canterbury, GHZ Paleoseismicity (GNS Science), and the New Zealand Earthquake Commission (EQC) for funding this research. I thank the Department of Conservation and the owner of the Poplars Station, Kevin Henderson for site access. I acknowledge Stefan Winkler for providing a Schmidt hammer and related academic discussions. I thank Sam McColl for reviewing this work and giving constructive comments. I acknowledge the reviewers (Glen Biasi and Nic Barth) and editors for their constructive comments to improve the manuscript. I also thank David Norton and Jarg Pettinga for their advice on dendrochronology and fault behaviour.

# CHAPTER 3. POST-LAST GLACIAL SLIP RATE ALONG THE WESTERN HOPE FAULT, SOUTH ISLAND, NEW ZEALAND

# Post-last glacial slip rate along the western Hope Fault, South Island, New Zealand

**Narges Khajavi**[1, *], **Robert M. Langridge**[2], **Mark C. Quigley**[1, 3]

[1]Department of Geological Sciences, University of Canterbury, New Zealand
[2]GNS Science, Lower Hut, Wellington, New Zealand
[3]Now at School of Earth Sciences, The University of Melbourne, Australia
[*]Corresponding author. Email: narges.khajavi@pg.canterbury.ac.nz

Article history:
Intended for submission to: Tectonophysics
Proposed submission date: 2016

## 3.1 Abstract

The Hope Fault is a major active strike-slip fault in the northern South Island, New Zealand. The fault comprises five geometric segments and is the fastest slipping fault in the Marlborough Fault System (MFS). High resolution airborne LiDAR are used to measure 477 dextral displacements and scarp heights from the principal slip zone (PSZ) and the structures within the total fault deformation zone along the Hurunui segment of the Hope Fault. Qualitative indices (QIs) are assigned to the measured horizontal (QIs: 1 to 5) and vertical (QIs: 1 to 2) displacements. Geomorphic analysis of features with large horizontal displacements shows that the scarp heights are only ~1% of the horizontal displacements and confirms that the fault is predominantly strike-slip. Dextral displacements with QIs 1 to 3 preserved along 59 geomorphic features including alluvial fans, debris deposits, terrace risers, and active or abandoned channels are in the range of 2.6 to 189 m. The general correlation between the dextral displacements and elevations (565-950 m a.s.l.) of the geomorphic features suggests the possibility of age correlation between the geomorphic features at different sites. Radiocarbon ages ranging from ~16000 to 500 yr B.P. obtained from previous studies from 7 sites along the Hurunui segment are used to calculate a dextral slip rate. Calculated average slip rates using on-site ages (i.e., Matagouri Flat, McKenzie Fan, Macs Knob and Hope River sites) range from 9.3 to 14.9 mm/yr with a mean of 12.2 ± 2.4 mm/yr. Calculated average slip rates using on-site and sites with correlative ages (i.e., sites: Landslip Stream, McMillan Stream, West and East of McMillan Stream, Three Mile Stream, Parakeet Stream and Lodge Stream) range from 6.3 to 15.5 mm/yr with a mean of 11.8 ± 2 mm/yr. These two mean values are quite similar and suggest that the application of age correlations

to derive slip rates is a feasible approach in this environment. The linear relationship between the slip rates from different sites along this segment suggests a constant spatiotemporal slip rate since the late Pleistocene. A mean single event displacement (SED) of 3.6 ± 0.7 m for the Hurunui segment is estimated from interpretation of "grouped" displacements of ≤ 25 m. Using the preferred mean slip rate and mean SED, a mean recurrence interval of ~200 to 440 yr is estimated. This recurrence interval is consistent with the mean recurrence interval (i.e., ~210-386) obtained from previous paleoseismic studies. Comparing the results of this study with the slip rate estimates from previous studies for the western Hope Fault (i.e., the Hope River and Hurunui segments), it is inferred that both adjacent segments of the fault follow a constant slip rate (12.5 ± 2.1 mm/yr) with earthquake rupture of ≥ $M_w$ ~7.

## 3.2 **Introduction**

Seismic hazard parameters for faults capable of surface rupturing earthquakes are investigated by evaluating the spatiotemporal accumulation of slip preserved along geomorphic features and surficial deposits (Weldon and Sieh, 1985; Langridge and Berryman, 2005; Kozaci et al., 2007; Langridge et al., 2010; Rizza et al., 2011; Ninis et al., 2013; Barth et al., 2014; Khajavi et al., 2014; Rittase et al., 2014; Manighetti et al., 2015; Zielke et al., 2015) and paleoseismologic trenching (Hartleb et al., 2006; Scharer et al., 2007; McCalpin, 2009; Berryman et al., 2012; Langridge et al., 2013; Hornblow et al., 2014; Khajavi et al., accepted manuscript). Typically, there are discrepancies between slip rates estimated from paleoseismic, geodetic and geomorphic data, especially at regions where: (1) wide deformation zones are associated with structurally immature faults, (2) faults have long recurrence intervals (RIs), (3) there are regional changes in strain rates, (4) there are fault interactions, and (5) strike-slip faults have significant dip slip (Cowie and Roberts, 2001; Polonia et al., 2004; Oskin et al., 2008; Cowie et al., 2012; Dolan and Haravitch, 2014). Paleoseismic trenches often provide short ($10^3$-$10^4$yr) or incomplete records of seismic activity due to their limited depths, site selection, erosion or sedimentation, lack of datable materials or dating problems, and the complicated nature of faulting especially where strike-slip movement transfers laterally heterogeneous units along the fault (Hartleb et al., 2003; 2006; Mason et al., 2006; Scharer et al., 2007; Cowie et al., 2012; Quigley et al., 2012; Langridge et al., 2013; Ninis et al., 2013; Hornblow et al., 2014; Khajavi et al., accepted manuscript). In comparison, geodetic slip rates rely on GPS or satellite data which are limited to the last few decades (Cowie and Roberts, 2001; Wallace et al., 2012). For this reason, slip

rates and fault parameters estimated from displaced geomorphic features are likely to be more reliable where landforms display long geologic time spans over which they are displaced by mature faults with average RIs of ≤ 4 kyr (Cowie et al., 2012; Ninis et al., 2013; Nicol et al., (in review)). Such cumulative displacements provide information on temporal variability (Knuepfer, 1992; Ninis et al., 2013; Rittase et al., 2014; Kendrick et al., 2015) or consistency (Der Woerd et al., 2002; Cowgill et al., 2009; Gold et al., 2011; Rizza et al., 2011; Barth et al., 2014) of slip rate through geological time and help to better understand fault behaviour. Particularly, slip rate data for active faults with a lack of historical seismic release are required for evaluating long-term seismic hazards.

The Marlborough Fault System (MFS) in the northern South Island of New Zealand is a strike-slip plate boundary transfer zone which links the Hikurangi subduction zone to its north with the dextral strike-slip Alpine Fault to its south (Van Dissen and Yeats, 1991; Berryman et al., 1992; Knuepfer, 1992; Nicol and Van Dissen, 2002) (Fig. 3.1). Nearly pure strike-slip deformation occurs across the MFS at rates of ~39-48 mm/yr (DeMets et al., 1994, 2010; Beavan et al., 2002; Yeats and Berryman, 1987; Berryman and Beanland, 1991; Van Dissen and Yeats, 1991; Pettinga et al., 2001; Wallace et al., 2007, 2012). The MFS comprises four major dextral strike-slip faults: the Wairau, Awatere, Clarence, and Hope faults (Lensen, 1962; Van Dissen and Yeats, 1991). The ENE-striking Hope Fault (~230 km long) is the youngest and southernmost fault in the MFS and has a history spanning the last ~1-2 Myr (Freund, 1971; Van Dissen, 1989; Cowan, 1990; Wood et al., 1994; Langridge and Berryman, 2005). Field, aerial phototographic, and light detection and ranging (LiDAR) mapping (McKay, 1890; Freund, 1971; Cowan, 1989; Langridge et al., 2003; Langridge and Berryman, 2005; Langridge et al., 2013; Beauprêtre et al., 2012; Khajavi et al., 2014) indicate that the Hope Fault is highly segmented (Fig. 3.1). The Hope Fault consists of five geometrically-defined segments (from west to east: Taramakau, Hurunui, Hope River, Conway, and Seaward) of ~20 to 70 km length. The Kelly Fault is effectively a sixth geometric segment of the Hope Fault (R. Langridge pers. comm. 2015) (Fig. 3.1). Measured slip rates along the Hope Fault indicate that it accommodates nearly half of the plate-tectonic motion across the MFS, i.e., it is the second fastest slipping fault in New Zealand after the Alpine Fault (Cowan, 1990; Cowan and McGlone, 1991; McMorran, 1991; Van Dissen and Yeats, 1991, Knuepfer, 1992; Langridge et al., 2003; Langridge and Berryman, 2005) (Fig. 3.1). Previous studies (Clayton, 1965, 1968; Freund, 1971; Suggate et al., 1978; Hardy and Wellman, 1984; Wellman, 1985; Knuepfer, 1984, 1988; Cowan, 1989, 1990; Van Dissen,

1989; McMorran, 1991; Van Dissen and Yeats, 1991; Langridge et al., 2003; Langridge and Berryman, 2005; Kahajavi et al., accepted manuscript) examined slip rates of the Hope Fault from three sites along the Hurunui segment, two sites along the Hope River segment, and four sites along the Conway segment using cumulative slip measurements on the surface and ages of faulted landforms.

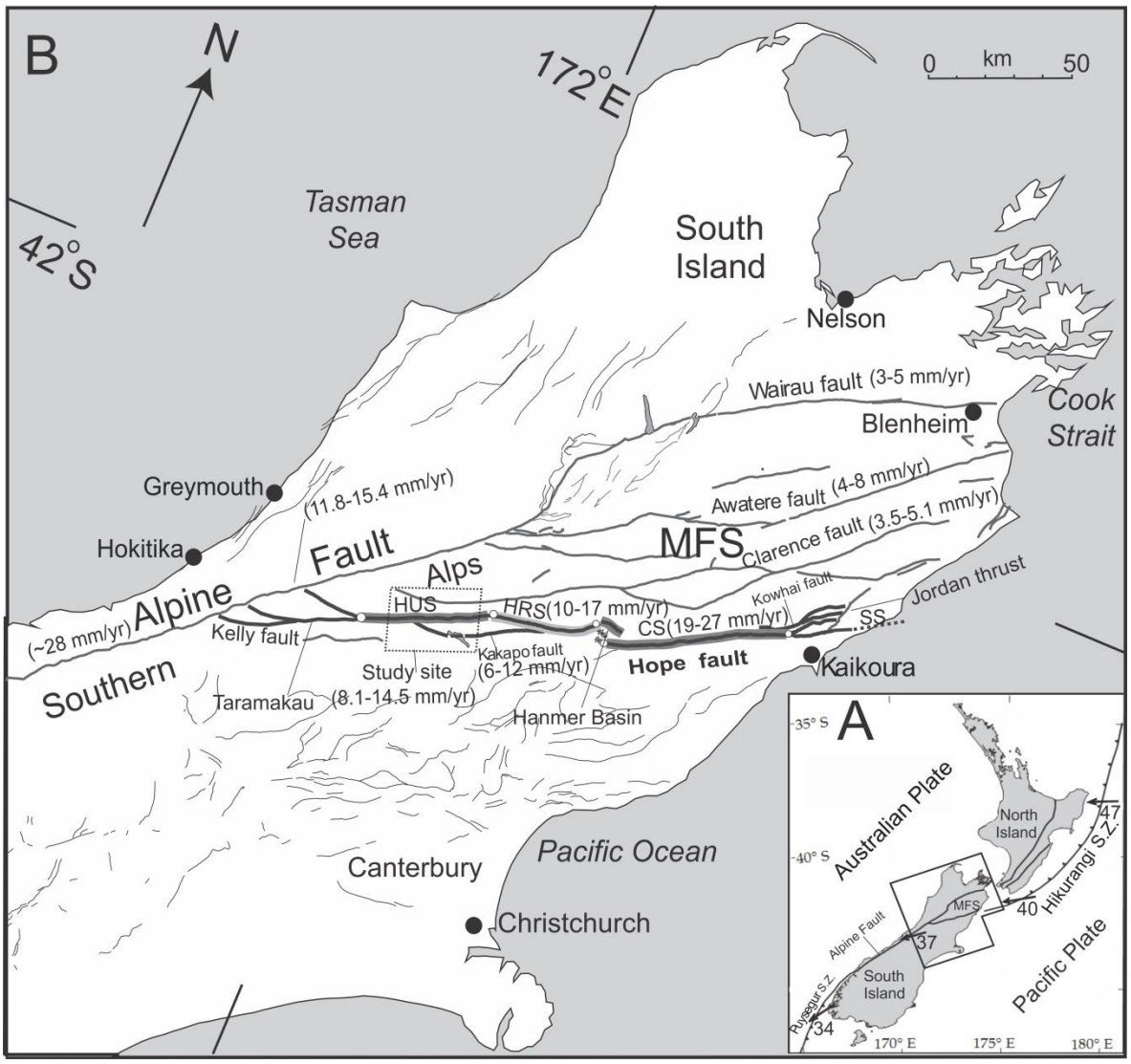


Figure 3.1. Geological setting of New Zealand and active faults in the northern South Island. (A), New Zealand plate boundary including subduction zones and major faults. Nuvel-1 plate rates (mm/yr) and orientations are after DeMets et al. (1994). (B), Location of active faults within the northern South Island are shown; Marlborough Fault System (MFS) and the Alpine Fault are highlighted; and the Hope Fault is heavily highlighted; modified from Langridge et al. (2003). The late Pleistocene-Holocene slip rate estimates (values in brackets) for the Hurunui (HUS), Hope River (HRS) and Conway (CS) segments are presented in mm/yr (Cowan, 1990; Cowan and McGlone, 1991; Langridge et al., 2003; Langridge and Berryman, 2005) and their related segments are colored in gray bold (with historic event) and black bold (with known event). The late Pleistocene-Holocene slip rate estimates for other faults within the MFS, at the junction of the Hope Fault with the Alpine Fault, and for south of the junction of the Hope and Alpine faults are also presented (Mason et al., 2006; Zachariasen et al., 2006; van Dissen and Nicol, 2009; Langridge et al., 2010; Barth et al., 2014). The box on the Hope Fault shows the study area.

In this study, airborne light detection and ranging (LiDAR) data is used to investigate dextral displacements along a 29 km-long section of the Hurunui segment of the Hope Fault concealed beneath beech forest. Qualitative indices (QIs) from 1 to 5 are assigned to measured dextral displacements in order to show the degree of confidence in measuring a displacement depending on the landform preservation. Reconstruction of two faulted geomorphic features is used as a proxy to constrain the vertical component of slip on the fault. The relationship between dextral displacements and elevations of the features that preserved those displacements is assessed to see if age correlation is possible. Radiocarbon data from previous studies (Langridge and Berryman, 2005; Langridge et al., 2013, Khajavi et al., accepted manuscript) from 7 sites along the Hurunui segment are used to better estimate slip rates in time and space. The variability of single event displacement (SED) is examined and combined with the mean slip rate to calculate the mean recurrence interval (RI) for the Hurunui segment of the Hope Fault. The slip rate and RI estimates from this work are compared with the slip rates and RIs determined from other methods (i.e., paleoseismological, geomorphological, and geodetic) for the Hurunui segment and the Hope River segment which is adjacent to the Hurunui segment and a possible slip model is discussed.

## 3.3 **Review of the Hope Fault slip rates and regional offsets**

The earliest slip rate estimates for the Hope Fault were derived from the central part of the Hope River segment (Clayton, 1965, 1968; Freund, 1971; Suggate et al., 1978; Hardy and Wellman, 1984; Wellman, 1985; Knuepfer, 1984, 1988), the western part of the Conway segment (Van Dissen, 1989; McMorran, 1991) and the eastern part of the Conway segment (Knuepfer, 1984, 1988; Van Dissen, 1989; Van Dissen and Yeats, 1991). Late Pleistocene-Holocene slip rates from the above studies for the Hope River and Conway segments varied from 7.5 to 26 mm/yr and 10 to 48 mm/yr, respectively. The most recent estimates of the slip rates for the central part of the Hope River segment come from reassessing previous estimates (i.e., reassessing dextral displacements and their ages) by Cowan (1989, 1990) (14-18 mm/yr and 11-17 mm/yr since late Pleistocene), Cowan and McGlone (1991) (10-11 mm/yr since late Holocene) and (Knuepfer, 1992) (15.2-23.8 mm/yr since late Pleistocene, and 6.1-23.3 mm/yr since late Holocene). The most recent estimate of the slip rate for the Conway segment was obtained from a site at the eastern part of the segment by Langridge et al.,

(2003) (≤ 19-27 mm/yr since mid-Holocene). Langridge and Berryman (2005) provided slip rate estimates from the western (8.1-11 mm/yr since late Holocene) and central (11.5-14.5 mm/yr since late Pleistocene) parts of the Hurunui segment of the Hope Fault. Khajavi et al. (accepted manuscript) presented a preliminary slip rate (6.5-10 mm/yr since late Holocene) from the eastern part of the Hurunui segment of the Hope Fault. The best slip rate estimates for the Hope Fault are the 11-17 mm/yr (Cowan, 1990) and 10-11 mm/yr (Cowan and McGlone, 1991) which incorporate both good displacement and age data along the Hope River segment. All of the above studies, measured the displacements along the geomorphic features at a few sites in the field and estimated the age of the displaced features using different techniques including radiocarbon dating from paleoseismic trenches or surfaces, weathering rinds and soils development, and/or relative dating. The late Pleistocene-Holocene geomorphic slip rates increase from west to east along the Hope Fault. The lower slip rates along the Hurunui and Hope River segments are explained by the existence of the Kakapo branch fault of the Hope Fault in the west (Langridge and Berryman, 2005) (Fig. 3.1) because the late Pleistocene and Holocene slip rates of the Kakapo Fault have been determined to be 8.1-12.1 mm/yr and 6-6.8 mm/yr, respectively (Yang, 1991).

Geodetic data (GPS) indicate decadal slip rates of 13.9 mm/yr (Hurunui segment), 15.5-16.7 mm/yr (Hope River segment) and 18.4 mm/yr (Conway segment) from the west to the east along the Hope Fault (Wallace et al., 2012). These geodetic slip rates also increase from west to east, consistent with the pattern observed from geomorphic slip rates; however, there are small discrepancies between the values from both methods.

The most recent trench data along the Hope Fault also provide paleoseismic slip rate estimates. Table 3.1 shows a summary of these data. Although there are similarities between some of the calculated rates from trench, geomorphic and geodetic data, some discrepancies are observed. Examples of that are: (1) the paleoseismic slip rate of 15 ± 2 mm/yr is higher than the geomorphic slip rate of 8.1-11 mm/yr for the western Hurunui segment, (2) the paleoseismic slip rate of 5.7 ± 1.4 mm/yr is nearly half of the geomorphic slip rate of 10-11 mm/yr and one third of the geodetic slip rate of 15.5-16.7 mm/yr for the central Hope River segment, and (3) the paleoseismic slip rate of 20.6 ± 1.9 mm/yr is consistent with the lower range of the geomorphic slip rate of 19-27 mm/yr for the eastern Conway segment.

Regional dextral offsets along the Hope Fault increase from west to east, consistent with the increased gradient in the slip rates. The bedrock dextral offset along the Hurunui segment of the Hope Fault increases eastward (Langridge and Berryman, 2005), i.e., bedrock

offsets of 8.5-13 km (Nathan et al., 2002) and 19 km (Freund, 1971) were measured at the western and eastern parts of the Hurunui segment, respectively. Greater dextral offsets were reported along the Conway segment. For example, a bedrock dextral offset of 60 miles (96 km) was suggested by Mason (1958), and a bedrock dextral offset of ~30-40 km is indicated on the regional geological maps produced by Rattenbury et al. (2006). The observed regional offsets and estimated slip rates indicate that the Hope Fault has been active throughout the Pleistocene.

Table 3.1. The most recent paleoseismic data for the Hope Fault. Abbreviations: SED; Single event displacement, and RI; Recurrence interval. This study estimates the slip rates for the presented data (see the last column).

| **Segments** | **Events** | **Estimated SED** | **Reference** | **Slip rate (SED/RI)** |
|---|---|---|---|---|
| Hurunui (West) | 2 events in the last ~600 yr (RI: ~300yr) | 4.5 ± 0.6 | Langridge et al. 2013 | 15 ± 2 mm/yr |
| Hurunui (East) | 6 events in the last ~1700 yr (RI: ~283) | 2.6 ± 0.3 (?) (considering the smallest offset near the trench) or it includes 2 events? | Khajavi et al. (accepted manuscript) | 9.2 ± 1 mm/yr<br>4.6 ± 0.5 mm/yr |
| Hope River (Centre) | 5 events in the last ~700 yr (RI: ~140)<br>2 events in the last ~700 yr (RI: ~350) | 2 ± 0.5 (considering the average of the 4 reported slip measurements)<br>2 ± 0.5 | Cowan and McGlone (1991), McKay (1890)<br>Langridge et al. (2013) reinterpreted the Trench data from Cowan and McGlone (1991) | 14.3 ± 3.6 mm/yr<br>5.7 ± 1.4 mm/yr |
| Conway (East) | 3 events in the last ~800 yr (RI: ~267) | 5.5 ± 0.5 | Langridge et al. (2003) | 20.6 ± 1.9 mm/yr |

## 3.4 **Methodology**

### 3.4.1 Geomorphic features and measuring displacements

Numerous geomorphic features of Late Pleistocene to Holocene age (Nathan et al., 2002; Langridge and Berryman, 2005; Khajavi et al., 2014; Khajavi et al., accepted manuscript) have been preserved along the Hurunui segment of the Hope Fault. The geomorphic features and surfaces at higher elevations (i.e., ~≥ 700 m a.s.l.) were mainly formed during and following the Last Glacial Maximum (LGM-Otira glaciation; ~28-18 ky. B.P) (Nathan et al., 2002; Alloway et al., 2007). The Holocene features (Barrel and Townsend, 2012) at the lower elevations (i.e., ~≤ 700 m a.s.l.) such as alluvial fans, debris

deposits, terrace risers, and landslides were created as the result of interaction between eroding rivers that incised into higher-elevation features and alluvial deposition modified by the fast-slipping Hope Fault (Khajavi et al., 2014). Along the beech-covered Hurunui segment, the principal slip zone of the fault (PSZ), the subsidiary traces within the fault deformation zone, and the displaced geomorphic features (e.g., active and abandoned alluvial fans, active and abandoned channels, terraces risers, vegetated and unconsolidated landslides/debris deposits, gravitational failure scarps, cut banks/cliffs) were mapped on the 2 m hillshade model generated from LiDAR data and some of the tectonic and geomorphic features were field-validated (see Khajavi et al., 2014).

This study provides maps that show the location of measured displacements and assesses the vertical and dextral displacements preserved by geomorphic features along a 29 km-long section of the Hurunui segment of the Hope Fault; where LiDAR data is available (see Langridge et al., 2014 and Khajavi et al., 2014). Displacements are measured both from the fault PSZ and from the structures within the fault deformation zone. To measure a vertical displacement at a certain point on the fault, an elevation profile perpendicular to the fault trace passing that point was produced on the LiDAR digital elevation model (DEM) using ArcMap (GIS) software (Amos et al., 2010). On the profile, the near-field vertical separation (i.e., scarp height) between both sides of the fault was measured and a measurement uncertainty was assigned to the vertical displacement. To measure the horizontal displacements, two general rules were applied: (1) where displaced feature approached the fault at low angle on both sides or one side, the linear (straight) sections of that feature, farther away from the fault, were projected to the fault trace and then the horizontal separation between the projected lines was measured (Quigley et al, 2012; Zielke et al., 2015) and (2) where displaced feature approached the fault at relatively high angle on both sides providing piercing lines, the horizontal separation between the piercing lines was measured (Langridge et al., 2010; Zielke et al., 2012; Langridge et al., 2013). To evaluate the uncertainty, the possible variability of projection line locations was considered. In this way, the maximum and minimum horizontal displacements of a certain feature were measured. The average of the differences between the horizontal separation (between the piercing lines) and the accepted maximum and minimum displacements was used as the uncertainty. Using the above methods, uncertainties associated with the vertical displacements were lower than those associated with the horizontal displacement.

The epistemic uncertainty in correlating features from both sides of the fault can be classified qualitatively (McCalpin, 2009; Zielke et al., 2010; Zielke et al., 2012; Scharer et al., 2014; Manighetti et al., 2015). In this study, QIs from 1 to 5 were assigned to the measured dextral displacements. The methodology used follows that of Manighetti et al. 2015 and Zielke et al. 2012. Table 3.2 shows a summary of this classification. In comparison, qualitative indices from 1 to 2 were assigned to the measured vertical displacements. As those were measured using elevation profiles perpendicular to the fault scarps, they were less likely to have high epistemic uncertainties. Therefore, qualitative indices of 1 and 2 were assigned to well-preserved and less-preserved fault scarps, respectively.

Table 3.2. Criteria to assign quality indices to the dextral displacements observed along the Hurunui segment of the Hope Fault.

| Quality Index (QI) | Description |
|---|---|
| 1 | The geomorphic feature is well preserved, it approaches the fault at a high angle, it is clearly visible on the LiDAR hillshade model, it can be reconstructed very well |
| 2 | The geomorphic feature is well preserved, it approaches the fault at a high to moderate angle, sections of the feature might have gone under erosion, it is clearly visible on LiDAR, it can be reconstructed well |
| 3 | The geomorphic feature is generally preserved, it approaches the fault at a moderate to low angle, sections of the feature have undergone some erosion specifically where it approaches the fault, it is visible on LiDAR, it can be reconstructed |
| 4 | The geomorphic feature is generally preserved, it approaches the fault at a moderate to low angle, it has undergone some erosion generally, it is visible on LiDAR, it is hard to reconstruct the feature, sometimes it is hard to believe that the feature has been displaced because displacement only appears on one side of the feature or it is much greater/smaller on one side of the feature, the displacement looks apparent |
| 5 | The geomorphic feature is generally or poorly preserved, it approaches the fault at a moderate or low angle, it has undergone moderate to severe erosion, it is visible on LiDAR, it has a high degree of sinuosity which makes the displacement measurement hard or impossible, sometimes it is hard to believe that the feature has been displaced because it is along the inferred PSZ, it is hard to reconstruct the feature, the displacement looks apparent, it could or could not be a displacement so it is reported as X ± X (e.g., 10 ± 10) |

### 3.4.2 Horizontal versus vertical displacements

The strike-slip Hope Fault is a structurally mature (Cowan et al., 1996; Khajavi et al., 2014), well-established and fast slipping fault (Cowan 1989, 1990; Cowan and McGlone, 1991; Langridge et al., 2003; Langridge and Berryman, 2005). The Hurunui segment of the Hope Fault strikes between 070° and 075° and is optimally oriented for dextral strike-slip within the regional stress field (Khajavi et al., 2014). In a general view, this segment of the fault is remarkably straight with a gentle curve in its middle. Dextral displacements along its PSZ are well preserved (Khajavi et al., 2014) and the ratio of horizontal to vertical displacements indicates primarily strike-slip (~7 ± 2:1, Langridge and Berryman, 2005).

Khajavi et al. (2014) argued that the Hurunui segment is dominantly strike-slip with a dip angle of ~85° NW at depth (along much of its length) or SE at a shallower depth (in its middle), but can appear as a dextral-reverse or dextral–normal fault with dip angle of 60°-65° near the surface depending on the existence of high topography south or north of the fault or thickness of deposits.

To assess vertical and horizontal displacements along the Hurunui segment of the Hope Fault, two sites (Macs Knob and Parakeet Stream sites) that show high dextral displacements along relatively simple geomorphic features (Figs. 3.2-3.3) were investigated. In the Macs Knob area (the middle section of the Hurunui segment) (Fig. 3.2A), a fan has been displaced horizontally in association with an apparent maximum scarp height of ~22 m. The fault strike at this location is 071°. On the surface, horizontal displacements of 120 ± 10 m and 128 ± 13 m were measured from the faulted western and eastern margins of the fan, respectively. To capture the near-field vertical changes in elevation along the fan surface, I extended fault-parallel elevation profiles along the fan surface on both sides of the fault at the close proximity to the fault (Fig. 3.2A and C). The highest points on these profiles have been separated 4m vertically and 114 m horizontally, providing the approximate horizontal and vertical displacements of the fan apex (Fig. 3.2C). An uncertainty of 11 m, which was the average of the uncertainties associated with the horizontal displacements of the eastern and western fan margins, was added to the horizontal displacement of 114 m. Khajavi et al. (2014) mapped a thrust flake associated with the PSZ in this area (the orange line on Fig. 3.2). To differentiate the vertical displacement on the thrust flake from that on the PSZ, I extended an elevation profile across the thrust flake passing through the PSZ (Fig. 3.2A-B). Subsequent to this, a back-slipping approach (e.g., Manighetti et al., 2015; Zielke et al., 2015) was used and the thrust flake was removed to reconstruct the original shape of the fan (Fig. 3.2D-E) and assess the measured displacements on the surface. At the Parakeet Stream area (the middle section of the Hurunui segment to the east of Macs Knob), the toe of a debris deposit has been displaced horizontally and the apparent scarp height is up to ~2 m. The fault strike at this location is 071°. On the surface, the maximum and minimum horizontal displacements of 81 ± 5 m and 56 ± 4 m are measurable from the western and eastern margins of the debris deposit, respectively. The same methodology as that described for Macs Knob was used to capture the near-field vertical changes in elevation along the debris deposit surface (Fig. 3.3A-B). The elevation profiles from both sides of the fault were compared to assess the measured displacements on the surface.

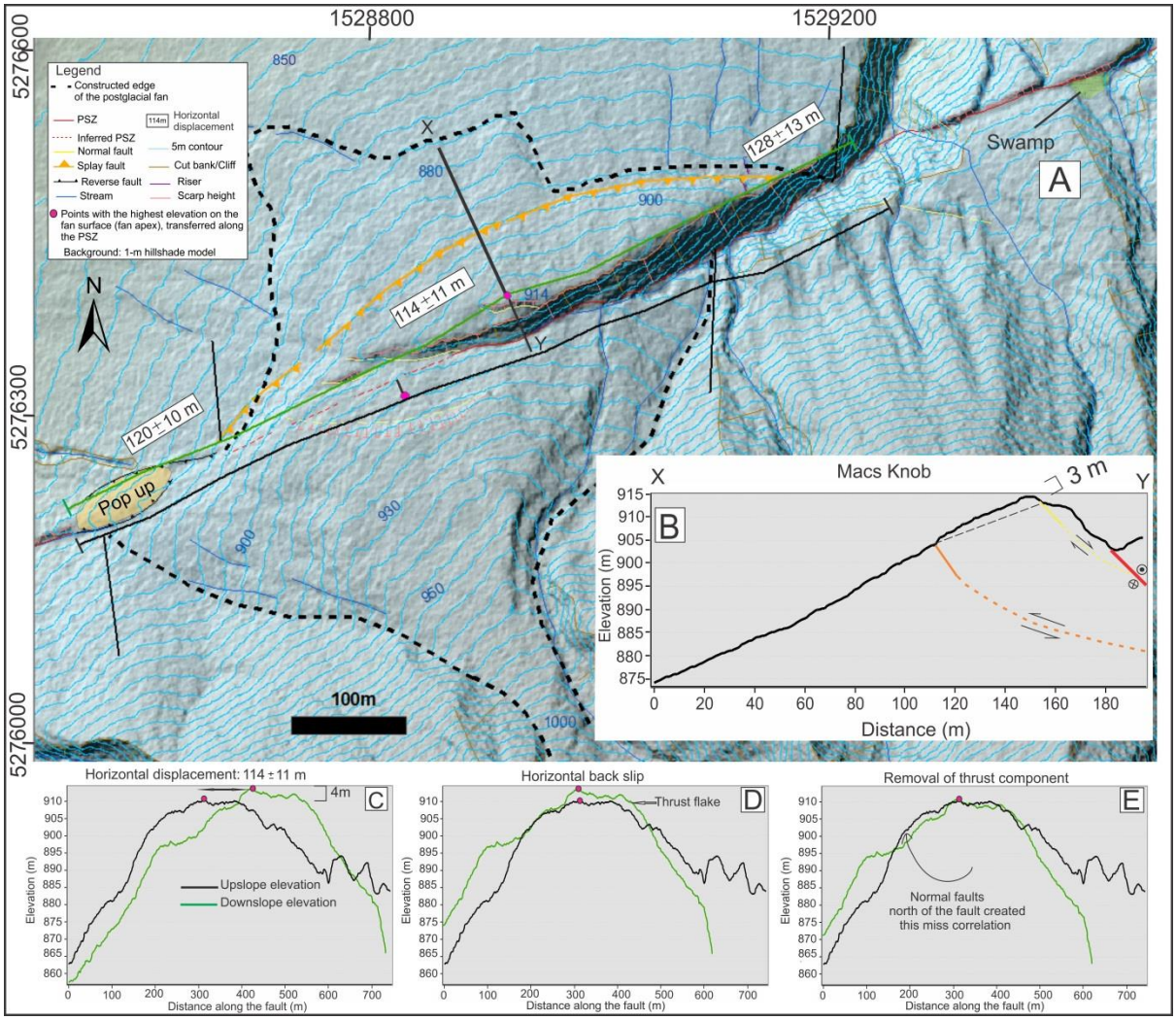


Figure 3.2. Macs Knob area (the middle section of the Hurunui segment). (A), 2-m hillshade model of Macs Knob showing a displaced fan. 5-m topographic contours are overlain on the hillshade model. Upslope and downslope elevation profiles (black and green lines) are extended along the fan on both sides of the fault. Profile XY is extended across the thrust flake and the PSZ on the fan surface. Dextral displacements of the fan are measured from its margins and its apex (the highest part of the fan). (B), Cross-section XY showing fault model at depth (fault dips and orientations are used from Khajavi et al. (2014)) and the actual vertical displacement on the thrust flake. (C), Upslope and downslope elevation profiles showing the horizontal and vertical displacements of the fan. (D), Back-slipping the upslope elevation profile to correlate the apex of the fan. The thrust flake is captured following back-slipping. (E), Removal of thrust component. Not only the apex, but also the middle section of the fan is matched.

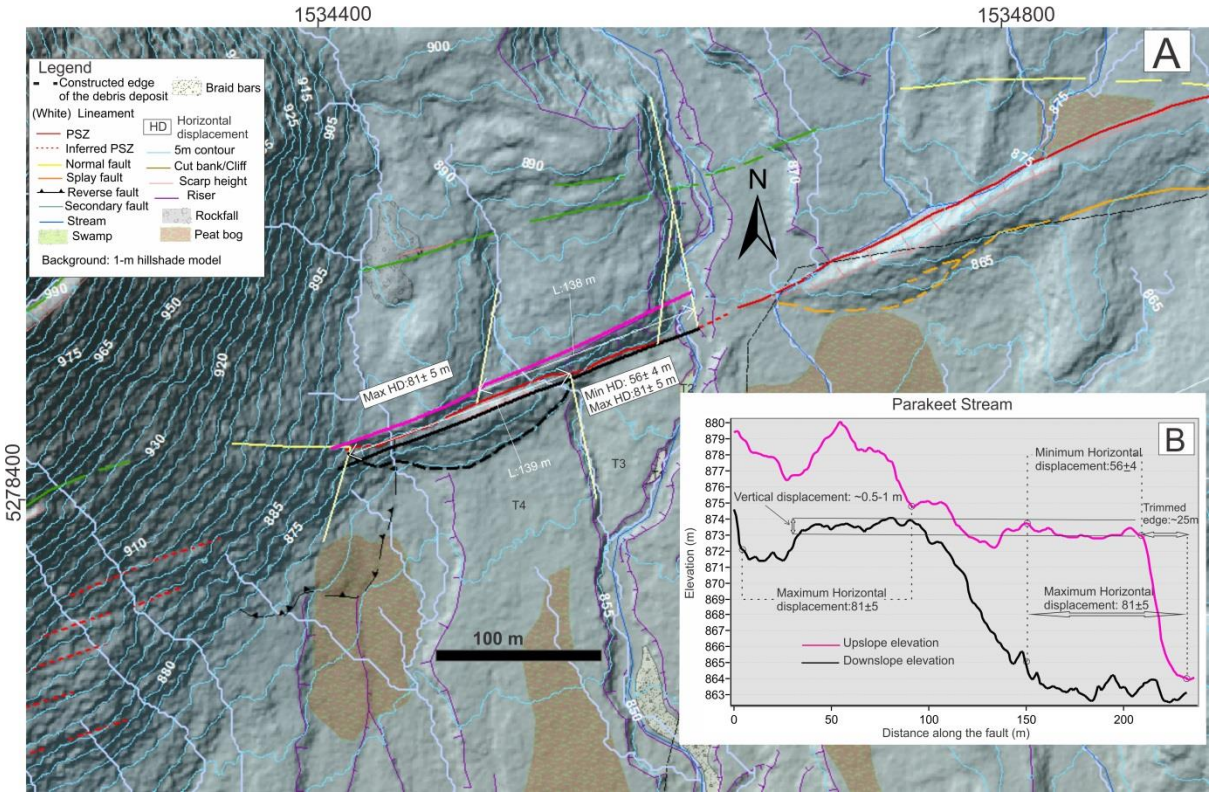


Figure 3.3. Parakeet Stream area (the middle section of the Hurunui segment to the east of Macs Knob). (A), 2-m hillshade model of Parakeet Stream site showing a displaced debris deposit. 5-m topographic contours are overlain on the hillshade model. Upslope and downslope elevation profiles (pink and black lines) are extended along the toe of the debris deposit on both sides of the fault. The surface length of the displaced feature is equal north and south of the fault (i.e., L:138 m and L: 139 m, shown in white). The minimum and maximum dextral displacements of the debris deposit are measured from its margins. (B), Upslope and downslope elevation profiles showing the horizontal and vertical displacements of the debris deposits. Profiles show that the north-eastern margin of the debris deposit was trimmed by ~25 m, note the sharp termination of the pink profile compared with its counterpart on the black profile (see the gentle part of the black profile at distance ~100-150 m).

### 3.4.3 Radiocarbon data

This study utilizes the radiocarbon data published by Langridge and Berryman (2005), Langridge et al. (2013) and Khajavi et al. (accepted manuscript) alongside the LiDAR-derived cumulative strike-slip displacements (measured in this study) to estimate slip rates for the Hurunui segment. Those radiocarbon data obtained from excavated paleoseismic trenches, hand-dug pits, rift zone (fault trough), and outcrops of post-LGM deposits (Table 3.3). The paleoseismic trenches and pits excavated in previous studies (were of ~1-1.5 m depth, therefore only the ages of the radiocarbon samples which were collected from the lowest horizons within those trenches or pits are used in this study and considered as minimum surface ages. In addition, as described by Langridge and Berryman (2005) and

Langridge et al. (2013), the radiocarbon data from outcrops, pits and fault zones are also minimum ages.

Table 3.3. A summary of the published radiocarbon data by previous studies along the Hurunui segment of the Hope fault.

| Location Reference | Sample ID | Lab number | Calibrated age 2σ rage (cal. yr B.P.) | Description |
|---|---|---|---|---|
| Matagouri Flat Langridge et al. (2013) | MF1E | NZA 18592 | 515-653 | Plant fragment collected from paleoseismic trench (minimum surface age) |
| McKenzie Stream Langridge and Berryman (2005) | MKS | NZA13360 | 2179-2467 | Woody twigs collected from aggradation gravels in McKenzie Stream catchment , 2 km upstream of fault |
| The Park Langridge and Berryman (2005) | FP | NZA13358 | 3476-3826 | Fresh peat collected from open fissure on the Park (minimum surface age) |
| Macs Knob (Mc Millan Stream) Langridge and Berryman (2005) | MMS | NZA13361 | 14489-15979 | Compact postglacial peat collected from an outcrop including a section of silt and peat sequences northwest of Macs Knob |
| Macs Knob (Three Mile Stream) Langridge and Berryman (2005) | 3MS | NZA13362 | 6738-7149 | Compact faulted peat collected from a rift zone (fault trough) (minimum surface age) |
| Hope-Kiwi Lodge Langridge and Berryman (2005) | HKL | NZA13357 | 12634-13060 | Compact postglacial peat collected from an outcrop of postglacial deposit (minimum surface age) |
| Parakeet Stream Khajavi et al. (accepted manuscript) | T3W-1<br>T4WP-3<br>T4EP-4<br>OCWP-6 | NZA53427<br>NZA53430<br>NZA54174<br>NZA54154 | 327-490<br>729-794<br>1399-1525<br>1900-2105 | All peat samples collected from 4 pits on the surfaces of the terrace risers produced by the Parakeet Stream (minimum surface ages) |
| Hope River (Hope Shelter) Khajavi et al. (accepted manuscript) | HS1-19 | NZA40317 | 1418-1688 | Peat sample collected from paleoseismic trench (minimum surface age) |

## 3.5 **Results**

### 3.5.1 Location and characteristics of the displacements measured along the Hurunui segment

Locations of the measured vertical and horizontal displacements from the PSZ and subsidiary structures forming the fault deformation zone are identified on the maps (Figs. 3.4-3.7, see the yellow and black data points). The basemaps are 2-m LiDAR hillshade models. Appendix 3.1 provides a LiDAR-derived fault database including site names, data point identities, fault characteristics, measured displacements and their uncertainties and assigned QIs at each data point. Table 3.4 shows a summary of the number and mean percentage of uncertainties associated with the dextral displacements measured from the PSZ. In total, only

one third of the measured dextral displacements (those with QIs of 1 to 3) from the PSZ are considered as good data and used for further analysis. I observe larger dextral displacements along the PSZ than subsidiary fault traces as expected. For simplicity, I do not include the displacement data collected from the subsidiary fault traces within the fault deformation zone except if I observe displacement of a geomorphic feature along several fault strands, which makes it the highest cumulative slip for a specific site (see Table 3.5 for such examples).

### 3.5.2 Vertical displacements of the fault at Macs Knob and Parakeet Stream sites

The results of horizontal versus vertical slip analysis from the Macs Knob and Parakeet Stream sites show that the vertical displacements are negligible with respect to the horizontal displacements. This is consistent with the results of Khajavi et al. (2014) which showed that the Hurunui segment is optimally oriented for dextral strike-slip within the regional stress field. The fault-parallel elevation profiles on the fan surface at Macs Knob area suggest that: (1) the best estimate of the horizontal displacement of the fan surface is 121 ± 11 m consistent with the average of the displacements measured at the margins of the fan and (2) it is most likely that the fan has only been displaced horizontally because the vertical displacement on the thrust flake measured from cross-section XY is 3 m and the vertical displacement on the PSZ (including the thrust flake) measured from the fault-parallel profiles is 4 m (Fig. 3.2B-C). The difference between these two values is ~1 m which could well be related to the measurement uncertainty. The ~1 m difference in elevation is nearly 5% of the observed apparent scarp height on the surface, and is ~1% of the dextral displacement at this site. Khajavi et al. (2014) also noted that the scarp heights in the Macs Knob area are not direct proxies of oblique motion associated with the strike-slip Hurunui segment. They mentioned that the scarp heights are inevitably overestimated at areas where streams have actively been incising at the base of the scarps, or where the fault has cut through a fan surface and dextrally juxtaposed surfaces of pre-existing differential elevations. In comparison, the fault-parallel elevation profiles on the debris deposit at Parakeet Stream area suggest that: (1) the eastern margin of the debris deposit north of the fault trace has been trimmed by ~25 m, (2) the southern surface of the debris deposit is ~0.5-1 m higher in elevation than the northern surface of it, and (3) the best estimate of the horizontal displacement of the debris deposit is 81 ± 5 m (Fig. 3.3B). The ~0.5-1 m difference in elevation is nearly 25-50% of the observed apparent scarp height on the surface and is ~1% of the dextral displacement at this site. According to

the results of this analysis, only horizontal displacements and horizontal slip rates were evaluated and vertical displacements were eliminated from further analysis or discussion.

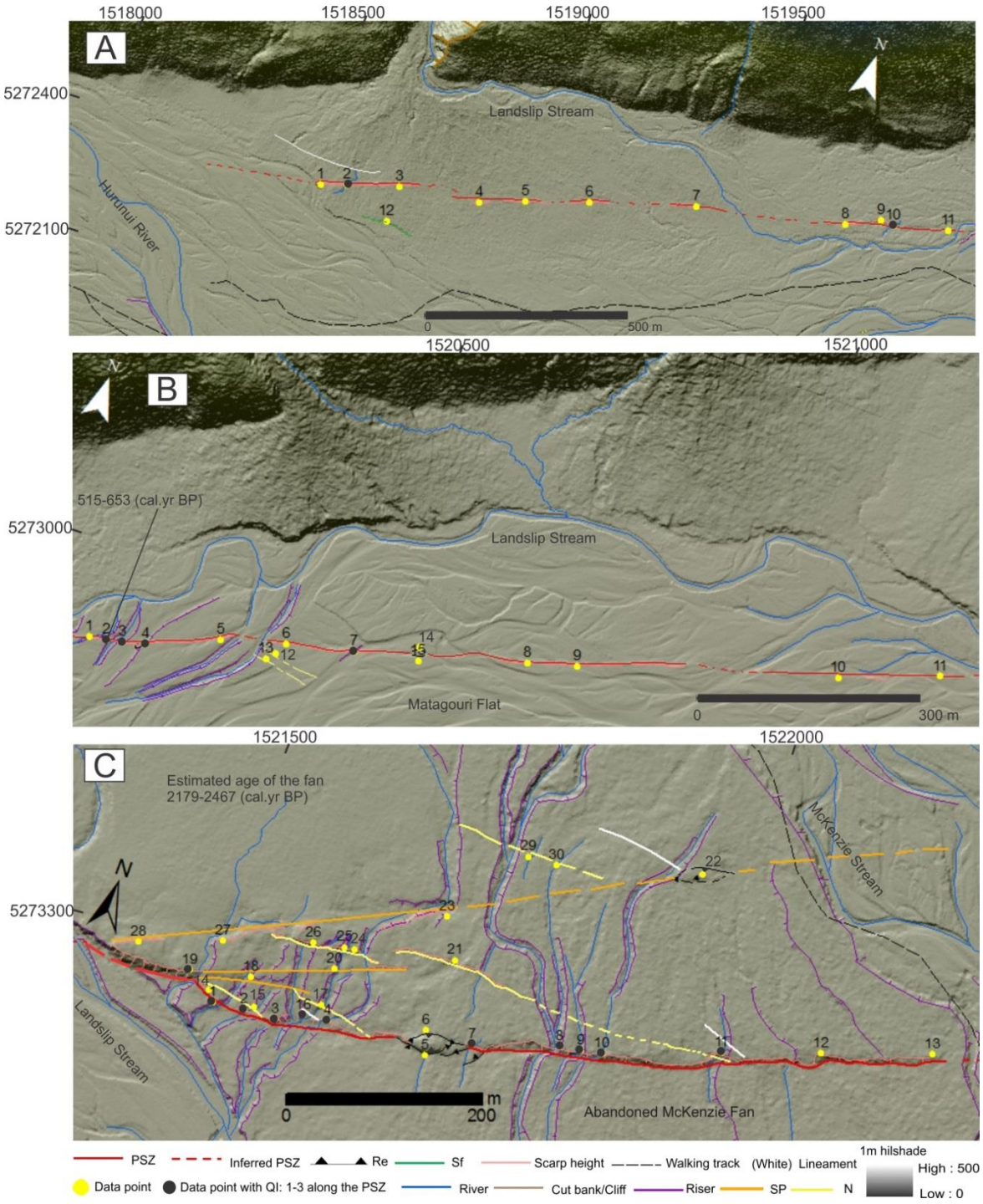


Figure 3.4. Continuous structurally-interpreted LiDAR hillshade strips from the western limit of LiDAR swath toward the east (see Khajavi et al., 2014). Abbreviations in the figure caption: PSZ; Principal slip zone, Re; Dextral-reverse fault, Sf; Secondary fault, SP; Splay fault, and N; Normal fault. Location of the measured displacements (yellow points) are shown. Each data point has an identity number that can be followed in Table1 from Appendix 3.1 for the complete characteristics of the fault and displaced feature at that location (A), Landslip Stream site. (B), Matagouri Flat site. (C), McKenzie Fan site. Radiocarbon surface ages are presented in cal. yr B.P. (See Langridge and Berryman, 2005 and Langridge et al., 2013).

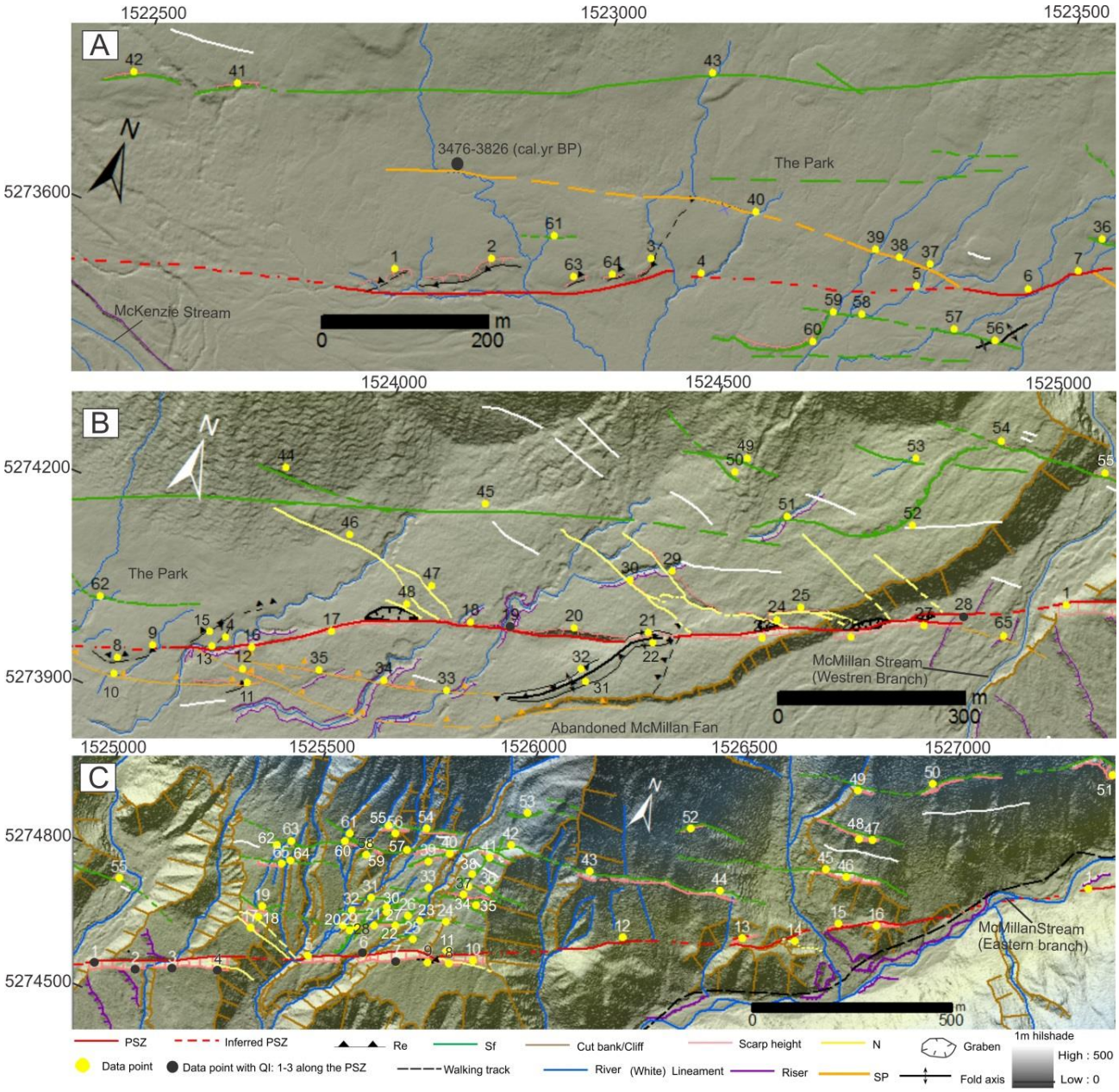


Figure 3.5. Continuous structurally-interpreted LiDAR hillshade strips from east of McKenzie Fan toward the east (see Khajavi et al., 2014). Abbreviations in the figure caption: PSZ; Principal slip zone, Re; Dextral-reverse fault, Sf; Secondary fault, SP; Splay fault, and N; Normal fault. Location of the measured displacements (yellow points) are shown. Each data point has an identity number that can be followed in Table1 from Appendix 3.1 for the complete characteristics of the fault and displaced feature at that location. (A) and (B), The Park and west of McMillan stream site. (C), East of McMillan Stream site. Radiocarbon surface ages are presented in cal. yr B.P. (See Langridge et al., 2013).

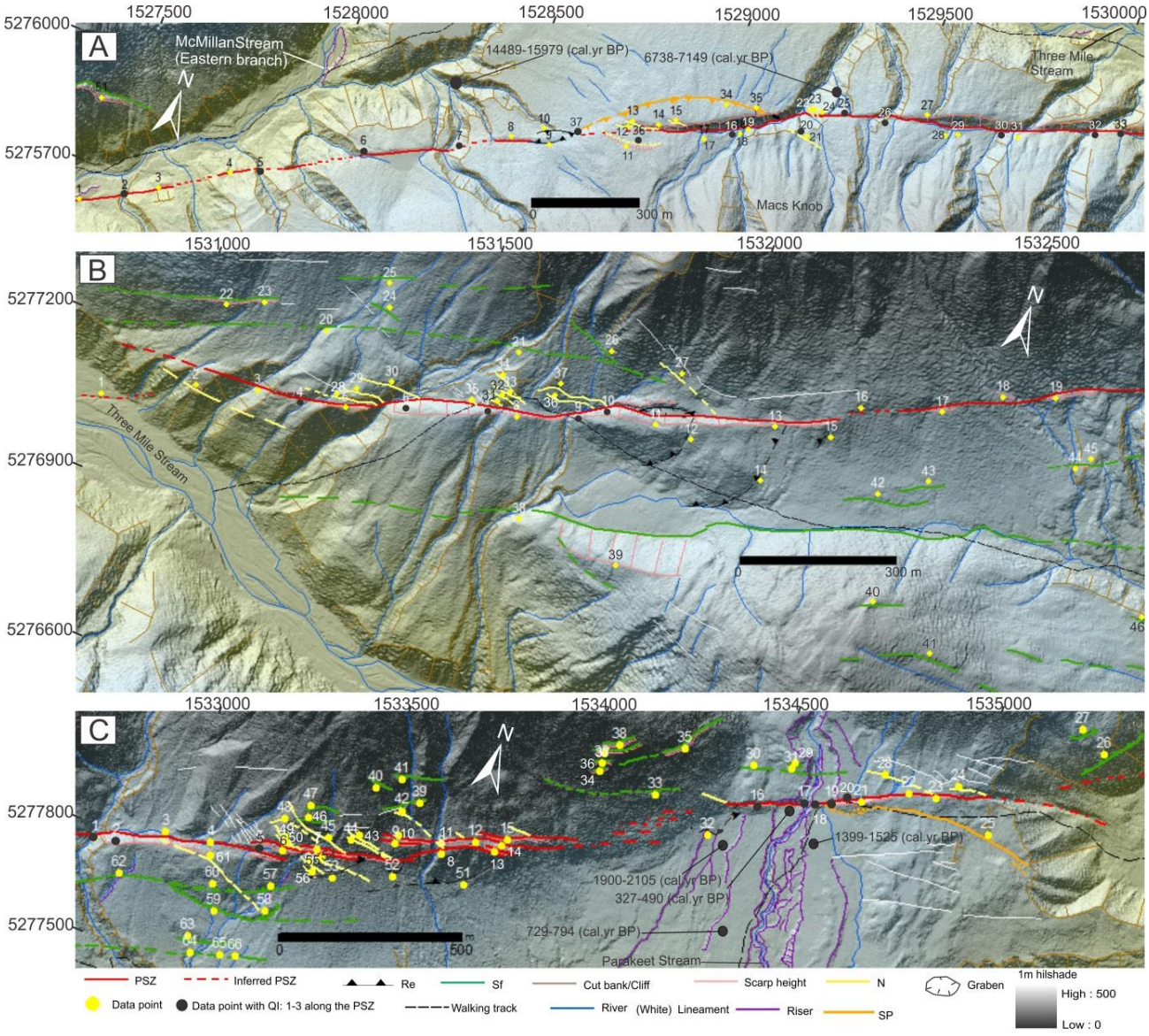


Figure 3.6. Continuous structurally-interpreted LiDAR hillshade strips from east of the eastern branch of McMillan Stream toward the east (see Khajavi et al., 2014). Abbreviations in the figure caption: PSZ; Principal slip zone, Re; Dextral-reverse fault, Sf; Secondary fault, SP; Splay fault, and N; Normal fault. Location of the measured displacements (yellow points) are shown. Each data point has an identity number that can be followed in Table1 from Appendix 3.1 for the complete characteristics of the fault and displaced feature at that location. (A), Macs Knob site. (B), Three Mile Stream site. (C), Parakeet Stream site. Radiocarbon surface ages are presented in cal. yr B.P. (See Langridge and Berryman, 2005 and Khajavi et al., accepted manuscript).

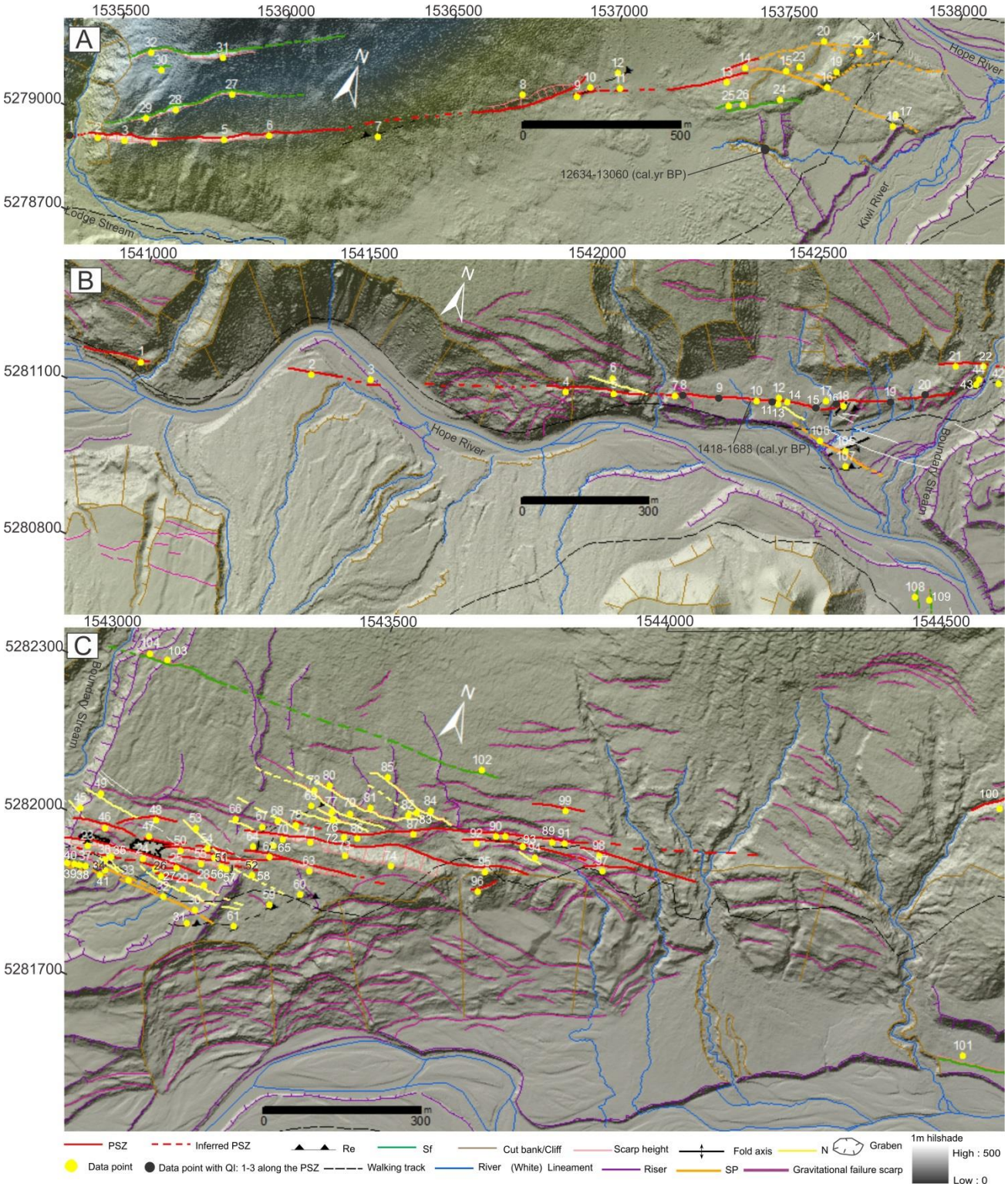


Figure 3.7. Continuous structurally-interpreted LiDAR hillshade strips from east of the Parakeet Stream toward the eastern end of the LiDAR swath (see Khajavi et al., 2014). Abbreviations in the figure caption: PSZ; Principal slip zone, Re; Dextral-reverse fault, Sf; Secondary fault, SP; Splay fault, and N; Normal fault. Location of the measured displacements (yellow points) are shown. Each data point has an identity number that can be followed in Table1 from Appendix 3.1 for the complete characteristics of the fault and displaced feature at that location. (A), Lodge Stream and Hope Kiwi confluence site. (B) and (C), Hope River site. Radiocarbon surface ages are presented in cal. yr B.P. (See Langridge and Berryman, 2005 and Khajavi et al., accepted manuscript).

Table 3.4. The number of measured dextral displacements, and the mean percentage of uncertainty/dextral displacement are reported for each qualitative index category. Abbreviations: X; shows the number of measurements from the fault deformation zone excluding the PSZ, and Y; shows the number of measurements from the PSZ.

| Quality Index (QI) | Number (X,Y) | Mean percentage (%) of uncertainty/dextral displacement |
|---|---|---|
| 1 | 18, 21 | 8 |
| 2 | 19, 25 | 14 |
| 3 | 6, 13 | 25 |
| 4 | 6, 9 | 36 |
| 5 | 28,15 | 100 or not assessable |
| Total number of dextral displacements (measured from the PSZ and from the structures within the fault deformation zone): 160<br>Total number of dextral displacements measured from the PSZ: 83<br>Total number of dextral displacements measured from the fault deformation zone excluding the PSZ:77<br>Total number of measured displacements from PSZ with QI of 1 to 3: 59 | | |

### 3.5.3 Relationship between elevation and dextral displacements of the geomorphic features

The elevations and dextral displacements of the geomorphic features within the study site are examined to see whether a general age correlation is possible. Field observations, LiDAR hillshade models, surface dating and geological maps suggest that the higher-altitude fans, scree, terrace risers, and other geomorphic features are of late Pleistocene to early Holocene ages (i.e., post-LGM) (Knuepfer, 1992; Nathan et al., 2002; Langridge and Berryman, 2005; Barrell and Townsend, 2012; Khajavi et al., 2014; Khajavi et al., accepted manuscript, (Figs. 3.4-3.7, see also Figs. 1.7-1.10 in Chapter 1). These surfaces cover the bedrock and are composed of clastic sediments (mainly gravel). In comparison, lower-altitude smaller geomorphic features are of late Holocene age (Langridge and Berryman 2005, Langridge et al., 2013, Khajavi et al., accepted manuscript). Larger cumulative displacements along older, higher elevation features cut by the fault are thus expected. To measure the elevation of a displaced feature, the elevations of the right and left sides of that feature where they reach the fault trace were measured on the LiDAR DEM and then an average was made. The elevations of the geomorphic features at the Hope River, Matagouri Flat, and McKenzie Fan sites were corrected according to the gradient of the Hurunui and Hope rivers which are parallel to the fault at those locations. In this way, 59 displaced features with QIs of 1 to 3 were compared in terms of their elevation (Fig. 3.8). The results of this analysis suggest that there is a good correlation between elevation and displacement data of geomorphic features. However, there are 3 clusters of displacement data at elevations of

~625, ~700, and ~850 m a.s.l. The lowest-elevation cluster includes those displacements which have been measured along the geomorphic features at the valley sides/floors of the Hurunui and Hope rivers (Fig. 3.4 and Fig. 3.7). In both valleys, the Hope Fault cut through young deposits (i.e., young fans or flood plain). In comparison, the highest-elevation cluster includes those displacements which have been measured along geomorphic features in the mountainous areas. Here, post-LGM fans, terrace risers, debris deposits and bedrock features have been displaced by the Hope Fault (Fig. 3.6).

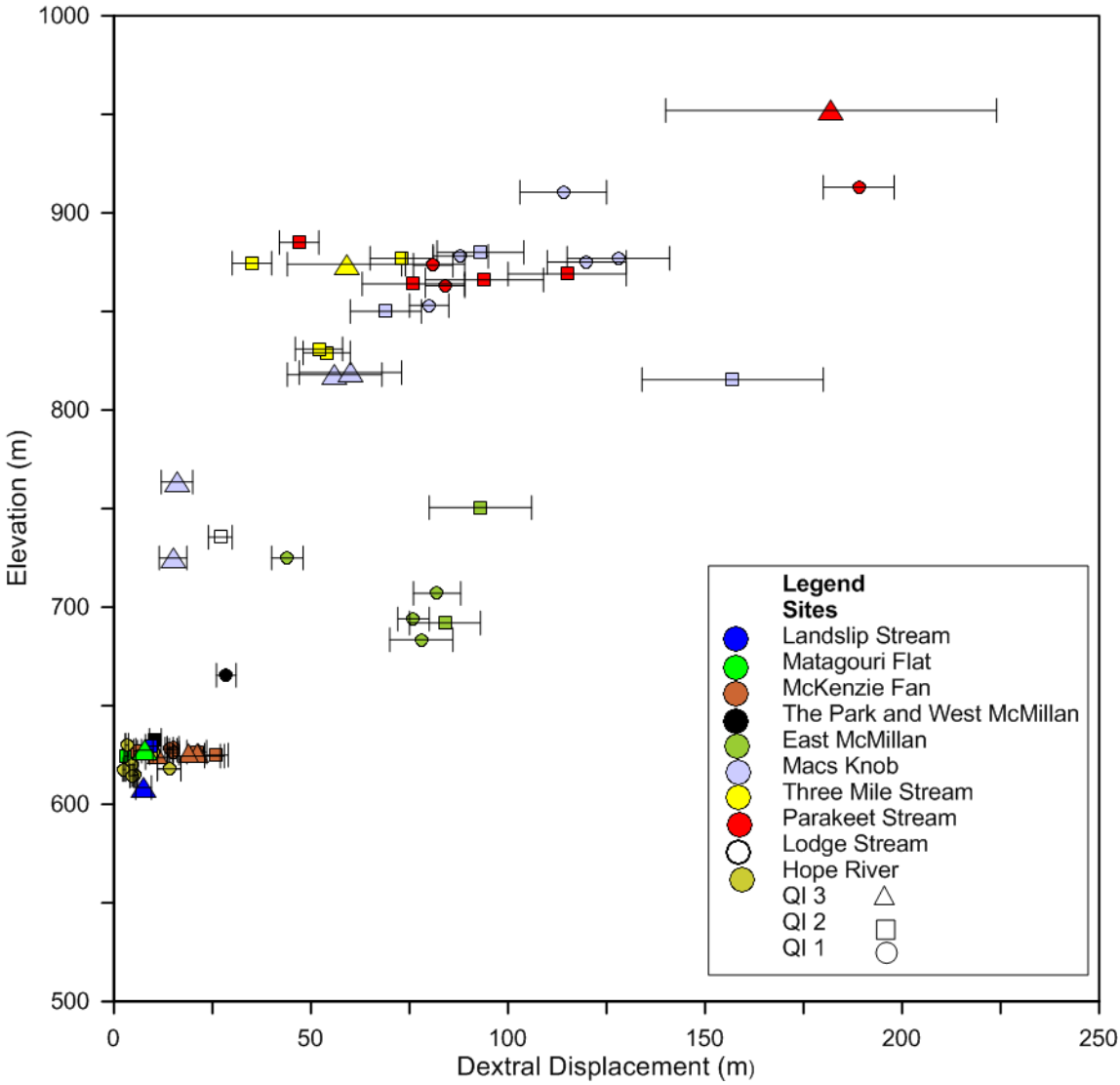


Figure 3.8. Plot of dextral displacements versus elevations of 59 displaced features of QIs 1-3. The dextral displacements have been colour-coded according to the site names and ranked according to the QIs.

### 3.5.4 Distribution of dextral displacements and available surface ages

The spatial distribution of dextral displacements measured along the Hurunui segment of the Hope Fault is examined alongside the available surface age data (Fig. 3.9, Table 3.3) to see whether age contours can be produced for the entire fault segment that could be useful for slip rate estimates and understanding slip rate variations over time. Surface age data along the Hurunui segment of the Hope Fault are available for 7 sites by Langridge and Berryman (2005), Langridge et al. (2013) and Khajavi et al. (accepted manuscript) (see Figs 3.4-3.7 for locations and ages). All of the available age data are radiocarbon dates and presented in cal. yr B.P. Among the surface age data, two were located at sites where it was hard to assess dextral displacements and/or preserved displacements were of low quality (at The Park and near Hope-Kiwi confluence, Fig. 3.4A and Fig.3.7A). However, for completeness, I prefer to show their location along the fault on the graph (see the black bold ages on the Fig. 3.9; arrows point to their locations/distance on the fault, see also Figs. 3.4A and 3.6A). Six age contours are produced to correlate displacements at sites with available age data to their equivalent displacements at other sites which lack age data (Fig. 3.9). I compare the age and distribution of 59 displaced features with QIs of 1 to 3 along the fault. This analysis shows that dextral slip decreases from the central part of the fault towards the east and west, but the surface age increases from the east and west to the central part of the fault. However, the slip pattern towards the west is better expressed than that towards the east. This is mainly due to the existence of the Hope River at the eastern part of the study site (Fig. 3.7A-B), which has eroded the fault trace. In addition, the fault east of the Hope-Kiwi confluence (Fig. 3.7A) becomes a rangefront feature with no preserved dextral displacement. Age contours at the lower elevations have approximately spaced equally (i.e., there is a constant slip rate gradient; ~10 m increase in the dextral slip every ~900 year). There is no age data available between the ~2300 yr and ~7000 yr contours, but still the slip gradient remains constant (i.e., there is ~50 m increase in the dextral slip over ~4700 yr). In comparison, a decreased slip gradient appears between the ~7000 yr and 13000 yr contours (i.e., there is only ~40 m increase in the dextral slip over ~6000 yr). The same slip gradient as that for the lower-elevation data appears again between the ~13000 yr and ~15000 yr contours (i.e., ~20 m increase in the dextral slip over ~2000 yr).

### 3.5.5 Estimates of slip rate

This study presents two suites of slip rate estimates: (1) slip rate estimates for the sites that include quality cumulative dextral slip and surface ages, and (2) slip rate estimates for the sites that include quality cumulative slip, but lack surface ages. In the latter, correlative surface ages were used meaning that the ages of other similar features or surfaces that have more or less equivalent displacements (Figs. 3.8-3.9) and similar altitude were applied or geomorphically-interpreted ages were assigned to the displacements. Cumulative dextral slip measurements and on-site radiocarbon ages were available for 4 sites including Matagouri Flat, Mckenzie Fan, Macs Knob and Hope River sites (Figs 3.4-3.7 and Table 3.3). Slip rate estimates for Landslip Stream, west and east of McMillan Stream, Three Mile Stream, Parakeet Stream and Lodge Stream sites are based on correlative ages (see notes in Table 3.3 and Table 3.5).

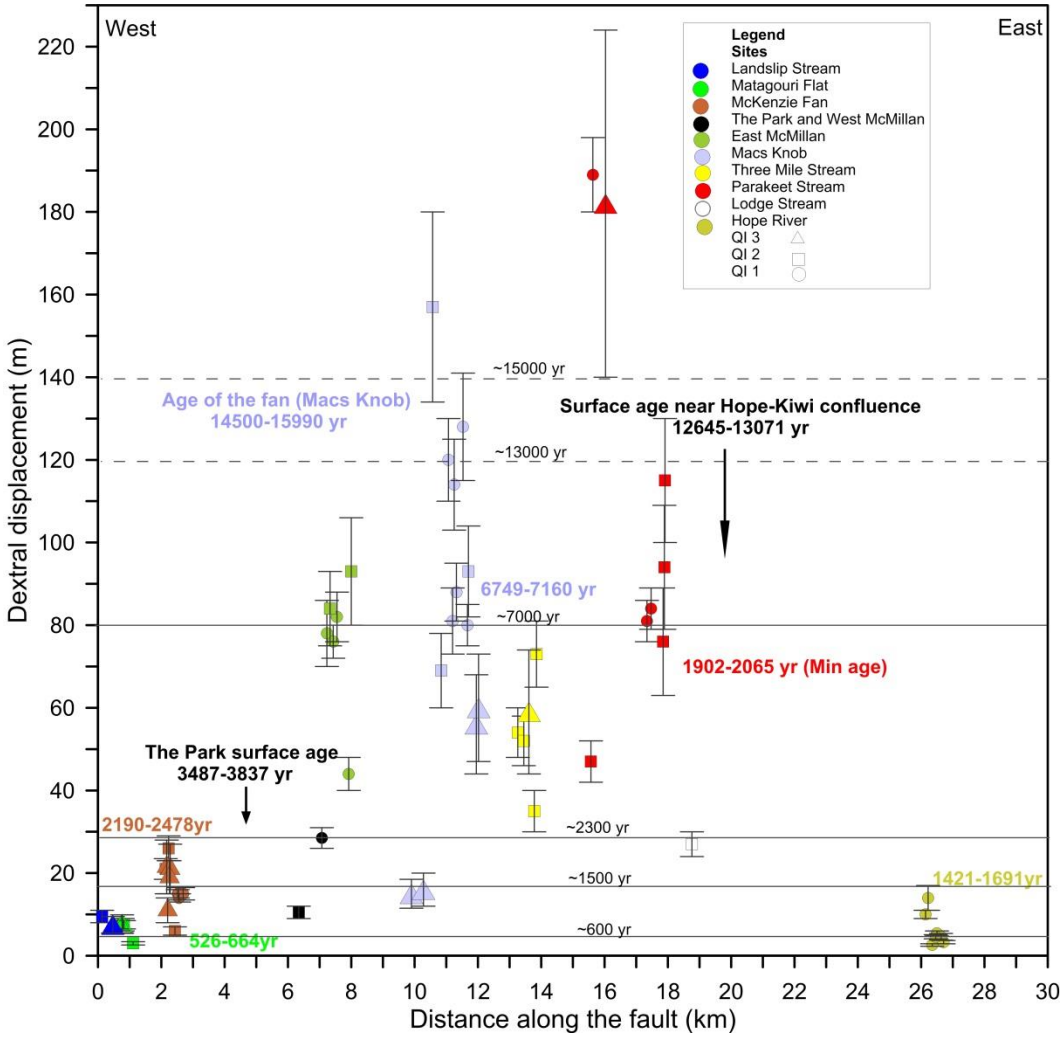


Figure 3.9. Dextral slip distribution along the PSZ of the Hurunui segment of the Hope Fault. Dextral displacements have been colour-coded according to the site names and ranked according to the QIs. Dashed contour lines are used where correlative ages were allocated to displacements (see Langridge and Berryman (2005)). Radiocarbon ages are in cal. yr B.P.

The strategy in using correlative ages for the above sites is explained here in detail. At the Landslip Stream site, a quality dextral displacement of 9.5 ± 1.5 m (Table 3.5) is recorded along a channel on a young alluvial fan surface which has been cut by the Hurunui River (Fig. 3.4A, data point 2). The displaced channel is located at an altitude of ~630 m a.s.l. The slip value and altitude of this displaced feature is comparable to the slip values and altitudes (10 ± 1 and 14 ± 3 m, ~620 m a.s.l., Figs 3.8-3.9) of two displaced features on another young alluvial fan surface which has been cut by the Hope River (Fig 3.7B, data points 8 and 9). These fans are geomorphically comparable as both are of the same size, at very similar elevations, cut by the Hope Fault, truncated by the active Hope and Hurunui rivers, and were abandoned and later overgrown by forest. The displaced fan at the Landslip Stream site grades onto a terrace which is ~3 m a above the modern Hurunui River whereas the displaced fan at the Hope River site grades onto a terrace which is ~17 m above the modern Hope River. According to the above comparison, the surface age presented at the Hope River site can be used as the maximum correlative age (see Fig. 3.9). At the McMillan Stream site, a high quality dextral displacement of 28 ± 2.5 m (Table 3.5) has been preserved along an abandoned terrace riser on the alluvial fan of McMillan Stream (Fig. 3.5B, data point 28). The displaced terrace riser is located at an altitude of ~665 m and in a close proximity (~100 m distance) to the active channel of McMillan Stream meaning that it has to be a young feature. Probably the fan and terrace riser at this site are younger than The Park surface as it seems that McMillan Stream cut through The Park surface and rangefront. In addition, the McMillan Stream fan appears to be older (?) than the McKenzie Fan as it has a wider mouth and deeply incised cut banks, is bigger in size and located at higher elevation (altitude: ~675 m a.s.l). However the slip value of the displaced terrace riser is comparable to the cumulative displacements of the McKenzie Fan. According to this interpretation, I prefer to assign the correlative age range of 2179-2467 cal. yr B.P (as a minimum age), which is the surface age of the McKenzie Fan (Langridge and Berryman, 2005) to the displacement measured at the McMillan site. The McMillan and McKenzie fans have probably formed at the same time along the Hurunui Valley. Langridge et al. (2013) mentioned that the radiocarbon age for The Park surface is the minimum age. Therefore, if my geomorphic interpretation is valid, the displacement age at the McMillan site has to be younger than ~3000 cal. yr B.P. Towards the east of McMillan Stream, where a quality dextral displacement of 107 ± 15 m (Table 3.5) has been preserved along a channel cut bank on a fan surface (Fig.3.5C, data points 7 and 24). The displaced feature is located at an altitude of

~750 m a.s.l. The slip value of this displaced feature is comparable to some of the slip values measured at the Parakeet Stream and Macs Knob sites (see data points 25, 26 and 30 on Fig. 3.6A and data point 16 on Fig. 3.6C, and Fig. 3.9). However, the displaced feature at this site is at lower altitude than the displaced features at both Parakeet and Macs Knob sites (~870 m a.s.l). The late Holocene surface age at the Parakeet site is considered to be the minimum age (Khajavi et al., accepted manuscript). In comparison, the mid Holocene surface age from Macs Knob, which is also considered to be the minimum surface age (Langridge and Berryman, 2005), is more realistic in the context of displacements at these three sites. The reason for this is that the high-altitude fans within the Hope and Hurunui valleys must have formed following the Aranuian interglacial period (~14500 years ago) in New Zealand (Langridge and Berryman, 2005). At Macs Knob site, high quality dextral displacements (121 ± 11 m and 83 ± 7 m, Table 3.5) were measured along two adjacent fans (Fig 3.2 and Fig 3.6A). Two radiocarbon dates are available from both fans, but one shows an age range of 14500 to 15990 cal. yr B.P which most likely predates the fan age based on the glacial history of the study area because the latest Otiran (Lewis) advance (i.e., the latest glacial period) has been inferred to have a minimum age of 14000 ± 220 cal. yr B.P (Suggate, 1965; Cowan 1989). In addition, Clayton (1968) and Burrows (1988) reported radiocarbon dates of 13309 ± 203 cal. yr B.P. and 10800 ± 150 cal. yr B.P. respectively from the lowest beds of the late-Otiran to early-Aranuian age lake in the lower Hope and Boyle valleys (Cowan, 1989). Langridge and Berryman (2005) also assigned the radiocarbon age obtained from a terrace riser near the Hope-Kiwi confluence to the displaced fans at Macs Knob site. Therefore, in this study I also use the same correlative age as that was used by Langridge and Berryman (2005) for the fan with the highest offset (Fig. 3.6, data points 16, 36, 37, and Table 3.5). At the Three Mile Stream site, a high quality dextral displacement of 73 ± 8 m (Table 3.3) was measured along a channel (Fig. 3.6B, data point 10). The displaced feature is located at an altitude of ~877 m a.s.l. The slip value and altitude of this displaced channel is comparable to those (~80 m, and ~870 m a.s.l.) from a fan and a channel at Macs Knob site and from a debris deposit and a channel at Parakeet Stream site (Figs. 3.8-3.9). All of these displaced channels are well-established tributaries of Three Mile and Parakeet streams that cut through post-LGM alluvial surfaces (either fans or debris deposits) (Fig. 3.6A-C). Therefore, I assign the mid Holocene surface age from Macs Knob to all of these displacements. At the western part of the Parakeet site, a high quality displacement of 189 ± 9 m was measured at along a lozenge-shaped feature which most likely is a bedrock feature (Fig. 3.6C, data point 2). If my

geomorphic interpretation is valid, the displacement associated with this feature has to be older than the post-LGM fans within the study site. Therefore, I assign the older radiocarbon age from Langridge and Berryman (2005) (i.e., 14489-15979 cal. yr B.P) to this displacement as the minimum surface age. At the Lodge Stream site, a quality dextral displacement of 27 ± 3 m (Table 3.5) was measured along a terrace tread (Fig. 3.7A, data point 1). The displaced feature is located at an altitude of ~740 m a.s.l. This site is adjacent (~1 km distance) to the Parakeet Stream site, but located at lower elevation. The Lodge Stream has a well-established channel that has produced a flight of terrace risers by cutting through the post-LGM surfaces at higher elevations and deposited a wide Holocene alluvial fan near the Hope-Kiwi confluence. The displacement here is similar to the cumulative displacement at the McKenzie site (Fig. 3.9). According to this, I prefer to assign the correlative age range of 2179-2467 cal. yr B.P (as a minimum age) (Langridge and Berryman, 2005) to the displacement measured at this site.

From the results of slip rate calculations, two mean slip rates of 12.2 ± 2.4 mm/yr and 11.5 ± 1.7 mm/yr are estimated for the Hurunui segment of the Hope Fault (Fig. 3.10). The former mean slip rate is the average of slip rate estimates that incorporated on-site ages (i.e., Matagouri Flat, McKenzie Fan, Macs Knob, and Hope River sites, the purple line), and the latter mean slip rate is the average of slip rate estimates that incorporated correlative ages (i.e., Landslip Stream, West and East of McMillan Stream, Three Mile Stream, Parakeet Stream and Lodge Stream). In comparison, the mean slip rate of all of the sites with on-site and correlative ages is 11.8 ± 2 mm/yr. The age and offset data (yellow and green data on Fig. 3.10) estimated from previous studies on the Hurunui and Hope River segments have also been presented alongside with the results of this study. As observed on the Fig. 3.9 and described in the previous section, a decreased slip rate appears between ~7000 yr and 13000 yr in the quality dataset from this study (i.e., the purple data points on Fig. 3.10). The purple data point with the highest displacement and surface age data is slightly off the lower bound of the mean slip rate of 12.2 ± 2.4 mm/yr providing a slip rate of ~5.9-6.4 mm/yr from the period between ~7000 yr and ~13000 yr.

### 3.5.6 Estimate of single event displacement and recurrence interval

Average single event displacement is one of the useful components in estimating the magnitude of earthquakes (Hanks and Kanamori, 1979; Wells and Coppersmith 1994; Stirling et al., 2013). There is one historical earthquake record (the 1888 Amuri earthquake)

Table 3.5. Slip rate estimates from different sites along the Hurunui segment of the Hope Fault. Sites with available age data are marked with asterisks.

| Sites | Cumulative dextral displacement (m) | Uncertainty (m) | Min age (Cal. yr B.P.) | Max age (Cal. yr B.P.) | Min slip rate (mm/yr) | Max slip rate (mm/yr) | Average slip rate (mm/yr) | Uncertainty (mm/yr) |
|---|---|---|---|---|---|---|---|---|
| Landslip Stream | 9.5 | 1.5 | 1418 | 1688 | 4.7 | 7.8 | 6.3 | 1.5 |
| Note: Estimated equivalent age from Khajavi et al. (accepted manuscript) (age presented at the Hope River site, Fig. 3.7B) was used. This yields a minimum slip rate (the cumulative displacement here is lower than the age contour of ~1500 yr, see text and Fig. 3.9). | | | | | | | | |
| Matagouri Flat* | 7.5 | 1 | 515 | 653 | 10 | 16.5 | 13.3 | 3.2 |
| Note: Surface age from Langridge et al. (2013) was used. Slip value of data point 4 was used as the best estimate. This yields a maximum slip rate using a minimum (Langridge et al., 2013) surface age. This slip rate incorporates slip along most of the entire fault deformation zone. | | | | | | | | |
| McKenzie Fan* | 32.6 | 5.6 | 2179 | 2467 | 10.9 | 17.5 | 14.2 | 3.3 |
| Note: Surface age from Langridge and Berryman (2005) was used. Slip values of data points 16, 17, 20 and 25 were summed and used as cumulative slip. | | | | | | | | |
| McKenzie Fan* | 34 | 5 | 2179 | 2467 | 11.8 | 17.9 | 14.9 | 3 |
| Note: Surface age from Langridge and Berryman (2005) was used. Slip values of data points 19 and 27 were summed and used as cumulative slip. This slip rate incorporates slip along the entire fault deformation zone. | | | | | | | | |
| The Park, and West of McMillan Stream | 28.5 | 2.5 | 2179 | 2467 | 10.5 | 14.2 | 12.4 | 1.8 |
| Note: Estimated equivalent age (age presented at the McKenzie Fan by Langridge and Berryman (2005)) was used. Using this correlative age is more relevant than the age presented for The Park surface because it is likely that both McKenzie and McMillan rivers generated fans at around similar time along the Hurunui Valley. The cumulative displacement here falls on the ~2300 yr age contour. | | | | | | | | |
| East of McMillan Stream | 107 | 15 | 6738 | 7149 | 12.9 | 18.1 | 15.5 | 2.6 |
| Note: Estimated equivalent age (the younger age presented at the Macs Knob by Langridge and Berryman (2005)) was used. Slip values of data points 7 and 24 were summed and used as cumulative slip. This yields a maximum slip rate using a minimum (Langridge and Berryman, 2005) surface age. This slip rate incorporates slip along part of the entire fault deformation zone. | | | | | | | | |
| Macs Knob* | 121 | 11 | 12634 | 13060 | 8.4 | 10.4 | 9.4 | 1 |
| Note: Surface age from Langridge and Berryman (2005) near the Hope-Kiwi confluence was used. They also used the same age when estimated a slip rate for Macs Knob site. However, this age seems to be old as the fans in Macs Knob area must be post-LGM features. The mean slip value of data points 16, 36, and 37 was used. This probably yields a minimum slip rate. | | | | | | | | |
| Macs Knob* | 83 | 7 | 6738 | 7149 | 10.6 | 13.4 | 12 | 1.4 |
| Note: Surface age from Langridge and Berryman (2005) (the younger age presented at the Macs Knob) was used. The mean slip value of data points 25, 26 and 30 was used. This yields a maximum slip rate using a minimum (Langridge and Berryman, 2005) surface age. | | | | | | | | |
| Three Mile Stream | 73 | 8 | 6738 | 7149 | 9.1 | 11.9 | 10.5 | 1.4 |

| | | | | | | | | |
|---|---|---|---|---|---|---|---|---|
| Note: Estimated equivalent age (the younger age presented at the Macs Knob by Langridge and Berryman (2005)) was used. This yields a maximum slip rate using a minimum (Langridge and Berryman, 2005) surface age. | | | | | | | | |
| Parakeet Stream | 81 | 5 | 6738 | 7149 | 10.6 | 12.8 | 11.7 | 1.1 |
| Note: Estimated equivalent age (the younger age presented at the Macs Knob by Langridge and Berryman (2005)) was used. This yields a maximum slip rate using a minimum (Langridge and Berryman, 2005) surface age. | | | | | | | | |
| Parakeet Stream | 189 | 9 | 14489 | 15979 | 11.3 | 13.7 | 12.5 | 1.2 |
| Note: Estimated equivalent age (the older age presented at the Macs Knob by Langridge and Berryman (2005)) was used because the displaced feature looks be a bedrock feature. If so, it has to be older than all of the post-LGM features within the study site. If this feature is bedrock feature, the slip rate is probably a maximum slip rate using a minimum surface age. | | | | | | | | |
| Lodge Stream | 27 | 3 | 2179 | 2467 | 9.7 | 13.8 | 11.8 | 2 |
| Note: Estimated equivalent age (age presented at the McKenzie Fan by Langridge and Berryman, 2005) was used. | | | | | | | | |
| Hope River* | 14 | 3 | 1418 | 1688 | 6.5 | 12 | 9.3 | 2.7 |
| Note: Surface age from Khajavi et al. (accepted manuscript) was used. This yields a maximum slip rate using a minimum surface age. | | | | | | | | |

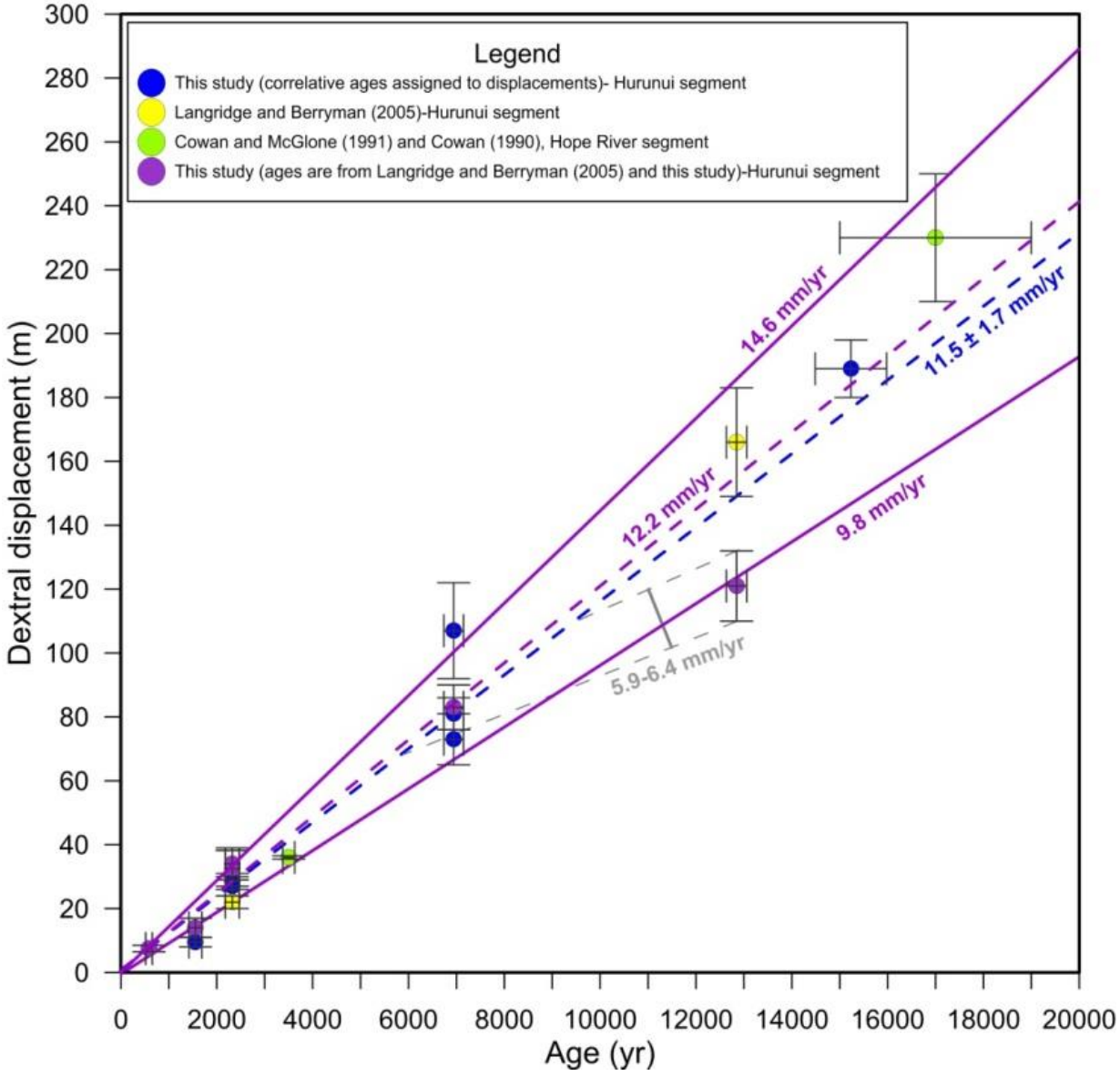


Figure 3.10. Slip rate estimates for the Hurunui segment of the Hope Fault. Data from this study (blue and purple data points) is compared to the data from previous studies for the Hurunui and Hope River segments (yellow and green data points).

of the Hope Fault, which is considered to involve rupture of the Hope River segment and parts of the Hurunui segment (Khajavi et al., accepted manuscript). Therefore, it is important to constrain the slip history of the Hurunui segment and assess it with regards to the coseismic slip during the 1888 earthquake. To constrain the slip history, and characterize the mean single event displacement and the recurrence interval for the Hurunui segment of the Hope Fault, dextral displacements of ≤ 25 m (Langridge and Berryman, 2005) measured along the geomorphic features were plotted in ascending order of size (Fig. 3.11). It is assumed that the steps in the plot represent displacements in surface rupturing events (Nicol et al., 2011). I obtained 26 dextral displacements that are ≤ 25 m along the Hurunui segment.

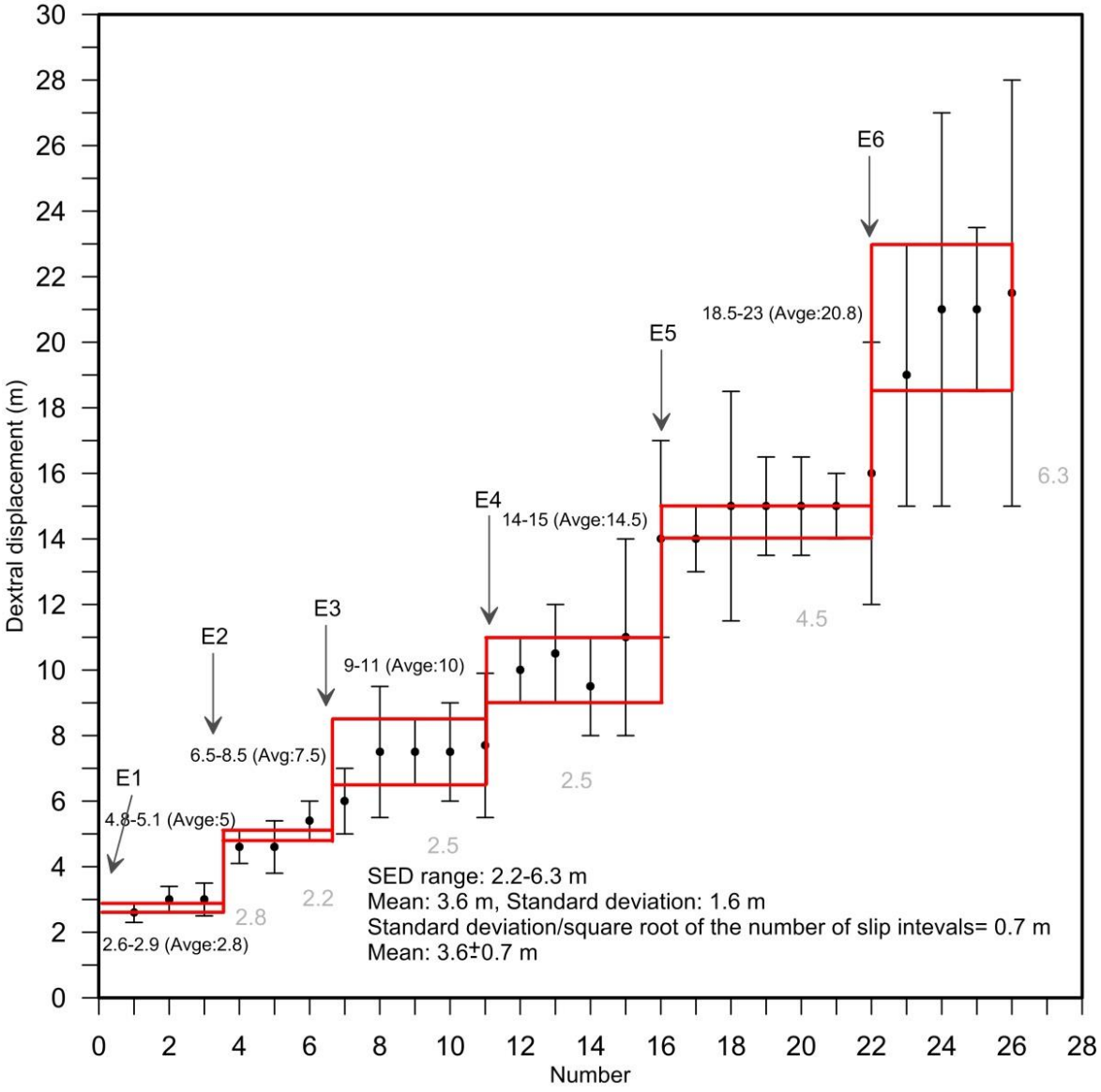


Figure 3.11. Displacement plot for the Hurunui segment. The stepped red line shows the number of paleoearthquakes at the vertical segments of the line. Red boxes are drawn based on the communality between all displacemnet data at each step. Pale grey numbers at the bottom of the red line represent SEDS per events.

As some displacements have large uncertainties, the steps are shown in boxes (instead of lines) to cover the communality between all cumulative displacements at each step. Subsequently, averages were made at steps and differences between the averages were calculated as the SEDs. To calculate the mean SED and its uncertainty, the Monte Carlo procedure was applied using the 6 SEDs input data. The mean SED of 3.6 m and Standard deviation of 1.6 m were calculated. The uncertainty in the mean SED is the Standard deviation divided by the square root of the number of SED intervals (G. Biasi pers. comm. 2015, also see Khajavi et al., accepted manuscript). Based on this analysis, the mean SED is reported 3.6 ± 0.7 m with a range of 2.2 m to 6.3 m. The SEDs estimated for the 4 younger

events are all in the same range, but there is a big change in SED from event 4 to 5 and 5 to 6 as the averages of measured displacements increase from 14.5 m to 20.8 m. In general, the uncertainties in the slip measurements increase towards the older events.

The earthquake recurrence interval was examined at each site using two methods (Table 3.6): (1) from dividing the mean SED by the slip rate estimate for each site, and (2) from dividing the site age (on-site or correlative) by the estimated number of the events at each site (Langridge et al., 2003; Langridge and Berryman, 2005). The number of events at each site was computed from dividing the cumulative dextral slip measured at each site by the mean SED. The recurrence interval estimates from the sites with age data varies between ~160 yr and ~500 yr. A mean recurrence interval of ~200-440 yr for the Hurunui segment is estimated using the mean slip rate and SED.

Table 3.6. Estimates of recurrence intervals from different sites along the Hurunui segment of the Hope Fault. Sites with available age data are marked with asterisks. Abbreviation: NoE: Number of events.

| No | Site name | Cumulative slip | NoE (SED: 3.6±0.7) | Age (yr) | Slip rate | RI (SED/Slip rate) | RI (age/NoE) |
|---|---|---|---|---|---|---|---|
| 1 | Landslip Stream | 9.5±1.5 | 2-4 | 1418-1688 | 6.3±1.5 | 372-915 | 355-844 |
| 2 | Matagouri Flat* | 7.5±1 | 2-3 | 515-653 | 13.3±3.2 | 176-430 | 172-327 |
| 3 | McKenzie Fan* | 32.6±5.6 | 6-13 | 2179-2467 | 14.2±3.3 | 166-394 | 168-412 |
| 4 | McKenzie Fan* | 34±5 | 7-13 | 2179-2467 | 14.9±3 | 162-364 | 168-352 |
| 5 | The Park and West of McMillan Stream | 28.5±2.5 | 6-11 | 2179-2467 | 12.4±1.8 | 204-410 | 199-412 |
| 6 | East of McMillan Stream | 107±15 | 21-42 | 6738-7149 | 15.5±2.6 | 160-333 | 160-340 |
| 7 | Macs Knob* | 121±11 | 26-46 | 12634-13060 | 9.4±1 | 279-512 | 275-502 |
| 8 | Macs Knob* | 83±7 | 18-31 | 6738-7149 | 12±1.4 | 216-406 | 217-397 |
| 9 | Three Mile Stream | 73±8 | 15-28 | 6738-7149 | 10.5±1.4 | 244-473 | 241-477 |
| 10 | Parakeet Stream | 81±5 | 18-30 | 6738-7149 | 11.7±1.1 | 227-406 | 225-397 |
| 11 | Parakeet Stream | 189±9 | 42-68 | 14489-15979 | 12.5±1.2 | 212-381 | 213-380 |
| 12 | Lodge Stream | 27±3 | 6-10 | 2179-2467 | 11.8±2 | 210-443 | 218-412 |
| 13 | Hope River* | 14±3 | 3-6 | 1418-1688 | 9.3±2.7 | 242-662 | 236-563 |
| Mean RI range using the preferred mean slip rate of 12.2±2.4 and mean SED of 3.6±0.7: ~200-440 yr | | | | | | | |

## 3.6 **Discussion**

### 3.6.1 Slip rate of the Hurunui segment

Taking the uncertainty in slip measurements and age data (which are maximum or minimum surface ages) and correlating ages into account, this study favours the mean dextral slip rate of 12.2 ± 2.4 mm/yr for the Hurunui segment of the Hope Fault (Fig. 3.10, Table 3.5). The preferred mean slip rate is the mean of slip rate estimates for the Matagouri Flat (13.3 ± 3.2 mm/yr), McKenzie Fan (14.2 ± 3.3 mm/yr and 14.9 ± 3 mm/yr), Macs Knob (9.4 ± 1 mm/yr and 12 ± 1.4 cmm/yr), and Hope River (9.3 ± 2.7 mm/yr) sites. In comparison, the mean slip rate estimate of 11.5±1.7 mm/yr from sites with correlative ages and the mean slip rate estimate of 11.8 ± 2 mm/yr from all sites are statistically indistinguishable from the preferred slip rate suggesting that the application of age correlations to derive slip rates is a feasible approach in this environment.

I cannot exclude the possibility that apparent variation in slip rates from different sites could be related to the uncertainty in surface ages and assigned ages rather than being related to the slip measurements. This study only used those LiDAR-derived slip data which were of QIs of 1 to 3. Most of the surface age data used in this study (Table 3.5 and Table 3.3) are the minimum ages and some are interpreted to be good enough for being used in slip rate calculations. The decreased slip gradient observed between ~7000 yr and ~13000 yr with respect to the preferred mean slip rate (Figs. 3.9-3.10) is most likely apparent due to quality of the surface age data. This can be explained by the age of ~13000 yr assigned to the post-LGM fan that has preserved a quality displacement of 121 ± 11 m (Fig. 3.2) in Macs Knob area. This fan is slightly higher (~20 m) in elevation than its adjacent fan which has recorded an average dextral displacement of 83 ± 7 m (measured in this study) and has a minimum surface age of ~7000 (Langridge and Berryman, 2005) (Fig. 3.6A). Therefore, I speculate that the fan with the higher elevation should have an age between ~7000 and ~13000 years and maybe more close to the lower range. If this is valid, then a constant mean slip rate of 12.2 ± 2.4 mm/yr of the western Hope Fault is plausible.

The preferred mean slip rate is higher than the slip rate estimate from Langridge and Berryman (2005) for the McKenzie Fan site. This is explained by measuring larger cumulative dextral slip revealed on the LiDAR hillshade model of the McKenzie fan site (i.e., more fault structures were observed and geomorphic features that have been displaced along multiple fault strands were mapped). From this, it can be inferred that the average slip rate of

~14.5 ± 3 from McKenzie Fan site is the only slip rate along the Hurunui segment that incorporates the maximum dextral slip occurred within the fault deformation zone. This slip rate is comparable to the contemporary geodetic slip rate of 13.9 mm/yr (Wallace et al., 2012) for the Hurunui segment of the Hope Fault. The upper bound of the preferred mean slip rate also correlates with the geodetic slip rate. Slip rate estimates from paleoseismic trench data (15 ± 2 mm/yr and 9.2 ± 1 mm/yr, Table 3.1) along the Hurunui segment (Langridge et al., 2013; Khajavi et al., accepted manuscript) match with the geomorphic slip rates (13.3 ± 3.2 mm/yr, and 9.3 ± 2.7 mm/yr, Table 3.5) estimated for the same sites (i.e., Matagouri Flat and Hope River sites). However, these paleoseismic slip rates are closer to the lower and upper bounds of the preferred mean slip rate. Possible reasons for this could be related to the resolution of the trench data or trench locations. The trench excavated by Langridge et al. (2013) is across a single trace of the fault which has cut through the flood plain of the Hurunui River. At this site, a SED of 3 ± 0.4 m was measured on the LiDAR hillshade model (this study) (see Appendix 3.1). Considering the slip measurements from this study and the RI estimate from trench data by Langridge et al. (2013), a paleoseismic slip rate of 10 ± 1.3 mm/yr is calculated which is now fit in the lower bound of the preferred mean slip rate. Therefore, it can be inferred that the observed discrepancy here is related to the resolution of the trench data rather than being related to the different SEDs measured on the surface. At the Hope Rive site, in comparison, the geomorphic slip rate being lower than the preferred mean slip rate can be related to the trench location. Because the Hope River site is near the geomorphic segment boundary (Khajavi et al., accepted manuscript) there is possibility of surface rupture slip deficits when computed over short intervals of time.

### 3.6.2 Single event displacement and recurrence interval of the Hurunui segment

The results of this study suggest a mean SED of 3.6 ± 0.7 m with a range of 2.2 m to 6.3 m for the Hurunui segment of the Hope Fault. The considerable change in SED from event 4 to 5 and 5 to 6 may be explained by: (1) epistemic error in slip measurement (Fig. 3.11); I measured larger uncertainties with larger displacements on the LiDAR hillshade model and in the field, and/or (2) missing events; each of the older SEDs could represent more than one displacement event when compared with the younger SEDs. According to the pattern observed from the smaller measured displacements, I favour option 2 and suggest that between 6 to 8 earthquakes are required to create ~21 m of slip on the surface. The results of paleoseismic trenches on the eastern part (called “Hope River” site in this study) of the

Hurunui segment by Khajavi et al. (accepted manuscript) suggested that 6 events ruptured this site since ~300 A.D., and produced a cumulative slip of 14 ± 3 m on the surface of a fan near the trench site. The mean SED resulted from this study suggest that 4 events are required to create such cumulative slip on the surface. The observed discrepancy in the event numbers required to produce 14 ± 3 m slip on the surface can be explained by two options: (1) missing events/epistemic error in slip measurement in this study meaning that the mean SED is overestimated or (2) slip deficits near the geomorphic segment boundary (trench location) or both options. At this stage, I cannot fully resolve this, but it is more likely to be resulted from a combination of both options. However, using the 298 ± 88 mean recurrence interval determined from paleoseismic trench data by Khajavi et al. (accepted manuscript) and my preferred slip rate of 12.2 ± 2.4 mm/yr, an average SED of ~3.5 m is estimated which is similar to the mean SED determined from this study.

This study provides evidence for characteristic slip at point. A SED of 3 ± 0.4 m and a cumulative slip of 7.5 ± 1 m were measured at the Matagouri Flat site on the LiDAR hillshade model (Fig. 3.4A, data points 2, 3, 4 and 7, also see Appendix 3.1). The trench data from Langridge et al. (2013) from the same site provided evidence for two surface rupturing earthquakes. These findings suggest that equivalent slip in successive events along the Hurunui segment. When I apply this SED and cumulative slip and the mean slip rate of ~12.2 mm/yr, the timing of the past two events on the Hurunui segment would be calculated as ~A.D. 1668-1809 and 1148-1570. If I apply the SED and the slip rate at the Matagouri Flat, the timing of the past two events would be calculated as ~A.D. 1675-1833 and 1215-1622. The estimated timing of the most recent event here correlates with the timing of the most recent event presented by Langridge et al. (2013) (i.e., A.D. 1655-1855) and the penultimate event presented by Khajavi et al. (accepted manuscript) (i.e., A.D. 1740-1840) from paleoseismic trenches located near the western and eastern boundaries of the Hurunui segment. This is in agreement with the argument of Khajavi et al. (accepted manuscript, Chapter 2) which suggested that the ~A.D. 1650-1850 earthquake has been the Hurunui segment earthquake with no known rupture of the Hope River segment.

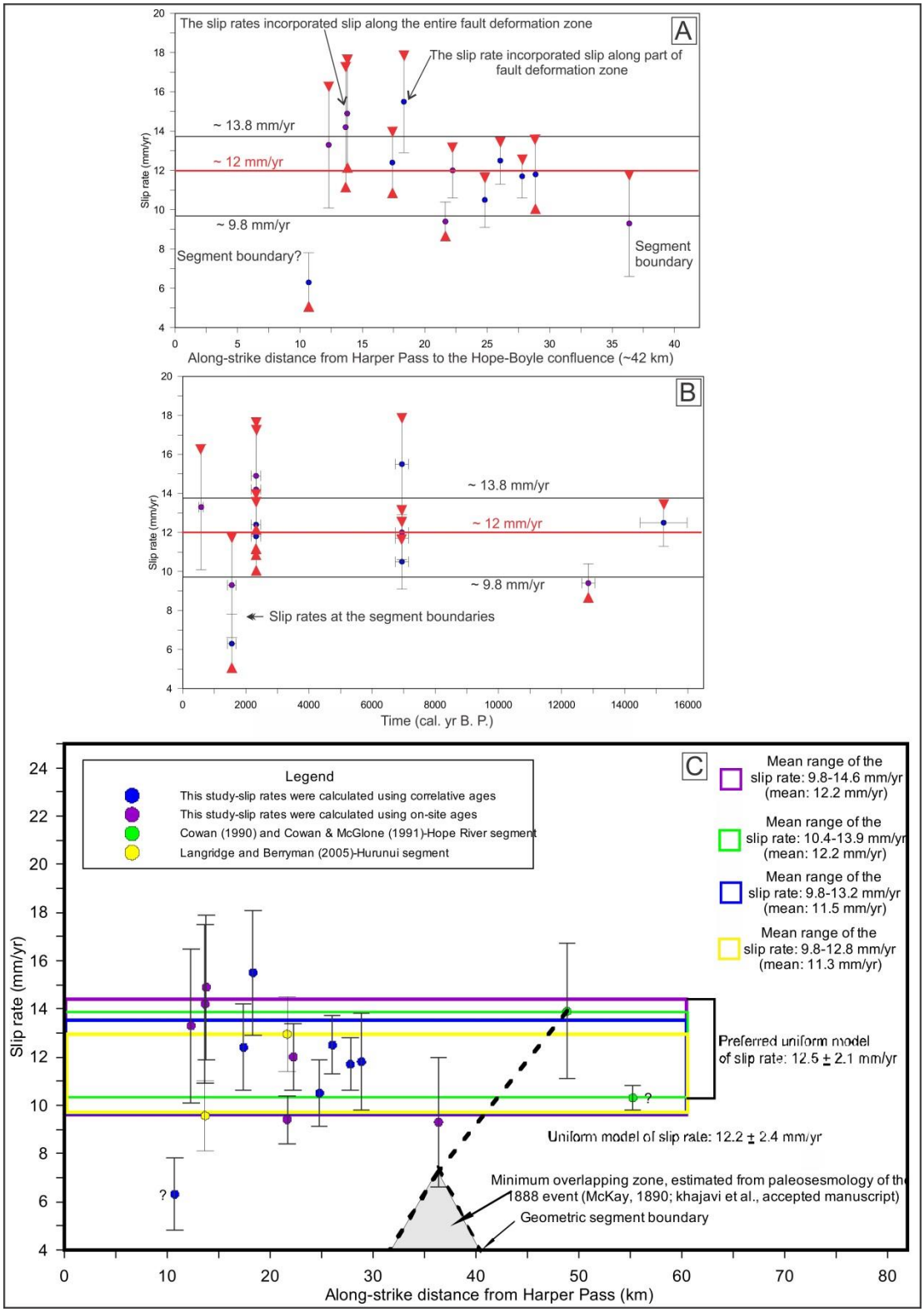


Figure 3.12. Slip rate estimates from Hurunui and Hope River segments are compared along ~40 km of the western Hope Fault. (A) and (B), show the spatiotemporal distribution of the estimated slip rates using on-site and correlative ages. The black box shows the range of the mean slip rate of 11.8 ± 2 mm/yr. Minimum and maximum slip rates are shown with an arrow at the upper and lower ends. (C), This graph is the equivalent of Fig. 3.10, which presents the spatiotemporal distribution of the slip rate data for the western Hope Fault. The preferred uniform model of slip rate is shown for the western Hope Fault. Location of the minimum overlapping zone between the two segments has been highlighted in grey on the X axis.

The results of this study suggest a mean recurrence interval of ~200-440 yr calculated from the mean SED and slip rate. This Holocene recurrence interval is consistent with the recurrence interval of 210-386 yr calculated from the paleoseimic trench data at the Hope River site (Khajavi et al., accepted manuscript) over ~1700 yr, but is shorter than the recurrence interval of 310-490 yr calculated from the slip rate estimates by Langridge and Berryman (2005) over ~550 yr.

### 3.6.3 Spatiotemporal variation in the Hope Fault slip rate

This study presents constant spatiotemporal slip rates for the Hurunui segment of the Hope Fault. Slip rate estimates incorporated both on-site and correlative ages, and show apparent spatiotemporal slip rates for the Hurunui segment of the Hope Fault that vary between 6.2 mm/yr (minimum average slip rate) and 15.5 mm/yr (maximum average slip rate) (Table 3.5). However, sites (excluding the Hope River that possibly indicate slip deficits) with quality cumulative displacements from ~7 to 80 m and on-site ages from mid to late Holocene, show constant spatiotemporal average slip rates of ~12-14 mm/yr (Table 3.5). Fig. 3.12A-B presents all of the estimated slip rates along the length of the Hurunui segment and versus time by considering those as the minimum or maximum values according to the applied surface ages. Although the mean slip rate of 11.8 ± 2 was determined from all slip rate estimates (shown on Fig. 3.12), a mean slip rate of ~12-14 mm/yr is more plausible when slip rates are presented as maximum or minimum values. Two points can be collected from Fig. 3.12 that are: (1) slip rate is constant along the strike of the Hurunui segment, and (2) slip rate is constant during Holocene.

The slip rates from this study and those from Cowan (1990) and Cowan and McGlone (1991) for the Hope River segment are consistent (Fig. 3.10 and Fig. 3.12C) suggesting a constant slip rate for both segments of the fault. Slip rates from both segments are within a range of 9.8 to 14.6 (mean 12.2 ± 2.4 mm/yr). The overlapping area between my preferred mean slip rate of 9.8-14.6 mm/yr for the Hurunui segment and the mean slip rate of 10.4-13.9 mm/yr for the Hope River segment, suggest a constant slip rate of 12.2 ± 2.4 mm/yr. However, this study prefers a constant slip rate of 12.5 ± 2.1 mm/yr (Fig. 3.12C) because of two reasons which are: (1) the mean slip rate range of 10.4-13.9 mm/yr from Cowan (1990) and Cowan and McGlone (1991) is the best slip rate estimate for the Hope River segment of the Hope Fault, and (2) the results of the slip rate analysis show that the upper bound of the preferred slip rate seems to be more realistic for the Hurunui segment of the Hope Fault. The

observed constant slip rate appears to be reasonable as these segments of the fault are structurally simple and show records of at least 6 and 5 earthquakes in the last 700 to 1700 years (Cowan and McGlone, 1991; Khajavi et al., accepted manuscript). In addition, the Hope Fault is a major and well-stablished structure in the MFS that transfers motion between the Hikurangi subduction zone and the dextral-slip Alpine Fault (Van Dissen and Yeats, 1991; Berryman et al., 1992; Knuepfer, 1992; Nicol and Van Dissen, 2002).

A constant slip rate of ~28 mm/yr has been reported by Barth et al. (2014) for the central Alpine Fault (south of the Hope Fault) which is a larger plate boundary fault. The constant slip rate of the Hurunui and Hope River segments is nearly half of the slip rate of the Conway segment (≤ 19-27 mm/yr, Langridge et al., 2003). Langridge and Berryman (2005) concluded that the Kakapo Fault, which is a branch of the Hope Fault to the south of the Hurunui and Hope River segments (Freund, 1991; Cowan, 1989), adds slip rates of 6.4 ± 0.4 mm/yr (Yang, 1991) to the Hope Fault system at this area. The summed slip rate of ~ 18-20 mm/yr for the Hope Fault system is similar to the lower bound of that for the Conway segment which shows that the slip rate of the Conway segment can well be lower than 27 mm/yr, and maybe around 19 mm/yr.

### 3.6.4 Earthquake magnitude, fault segmentation and slip model

The mean SED determined from this study is useful to evaluate the magnitude of past earthquakes and estimates magnitudes of future earthquakes on the Hurunui segment. Using the fault area of A: 13 *42 $km^2$ for the Hurunui segment and the earthquake scaling relation of Hanks and Kanamori (1979) which is based on the seismic moment ($M_o$), a moment magnitude ($M_w$) of ~7.1-7.2 is estimated for past earthquakes and hypothesized for future earthquakes of the Hurunui segment of the Hope Fault. According to Stirling et al. (2013), the best scaling relation for the strike-slip dominated fast slipping plate boundary faults with A > 537 $Km^2$, is the scaling relations of Wesnousky (2008). Based on this relation, the Hurunui segment is capable of generating a surface rupture earthquake of $M_w$ 7.

The geomorphic segmentation of the Hope Fault is supported by the younger SEDs of ~2.5 m determined from this study, which are very similar to the maximum coseismic slip displacements (2.4-2.6 m) of the 1888 historic event (McKay, 1890) on the Hope River segment of the Hope Fault. The Hope River rupture segment and the Hurunui geometric segment (Langridge et al., 2013) both have approximately the same length (~35 km and ~42 km, respectively). If these 2 segments have always ruptured together as a thoroughgoing

structure, then I would have expected to observe higher coseismic surface displacement with the combined rupture length. The results of paleoseismic trenching and slip rate estimates from the western Hope Fault (e.g., McKay, 1890; Cowan, 1989,1990; Cowan and McGlone, 1991; Khajavi et al., accepted manuscript; Langridge et al., 2013; this study), all together, suggest that the Hurunui and Hope River segments are individual segments that could have rupture overlaps for some distances along the fault. For example, the coalescing rupture overlap from the adjacent Hope River segment on to the Hurunui segment at the Hope River site (the 1888 $M_w$ 7.1 Amuri earthquake, sourced primarily from the Hope River segment) was suggested by Khajavi et al. (accepted manuscript).

## 3.7 **Conclusion**

I document 477 displacements (dextral and vertical) across the Hurunui segment of the Hope fault using LiDAR data. Reconstruction of two faulted geomorphic features with large dextral displacements at Macs Knob and Parakeet Stream sites, suggest that the scarp heights are only ~1% of the horizontal displacements on the PSZ confirming that the fault is predominantly strike-slip. Analysis of 59 quality dextral displacements shows that: (1) dextral displacement increases as a function of the elevation of the displaced feature; meaning that higher-altitude older features record higher displacements along the fault, and (2) the elevation-displacement relation alongside with the available surface age data can be used to assign correlative ages to the features that lack surface age. Using the correlative ages, available on-site ages, and cumulative dextral displacements at Landslip Stream, Matagouri Flat, McKenzie Fan, McMillan Stream, Macs Knob, Three Mile Stream, Parakeet Stream, Lodge Stream and Hope River sites, three mean slip rate estimates of 12.2 ± 2.4 mm/yr (sites including on-site ages), 11.5 ± 1.7 mm/yr (sites with correlative ages) and 11.8 ± 2 (all sites) mm/yr are determined for the Hurunui segment. My preferred slip rate is the former which seems to be relatively constant since late Pleistocene. This study estimates the mean single event displacement of 3.6 ± 0.7 m and constrains the slip history for the Hurunui segment that goes back to 6 earthquakes. The higher average surface slip of ~21 m associated with these 6 events than the cumulative surface slip of 14 ± 3 m measured at the Hope River site (where 6 events were identified in the trenches excavated by Khajavi et al., accepted manuscript) suggest deficits in slip at the Hope River site which is near the segment boundary between the Hope River and Hurunui segments of the Hope Fault. Using the preferred slip rate and mean SED, a mean recurrence interval of ~200 to 440 yr is estimated for the Hurunui segment

which is consistent with the mean recurrence interval of ~210 to 386 obtained from paleoseismic studies. The results of this study show that both adjacent segments of the fault have a constant slip rate (12.5 ± 2.1 mm/yr).

## Acknowledgements

I wish to thank NZ Natural Hazards Research Platform for funding the LiDAR project. I thank the department of Geological Sciences, University of Canterbury, GHZ Paleoseismicity (GNS Science), and the New Zealand Earthquake Commission (EQC) for funding this research. I thank the Department of Conservation and the owner of The Poplars Station, Kevin Henderson for site access. I acknowledge Jarg Pettinga and Andy Nicol for useful academic discussions. I also thank Amir Rezanejad for his assistance in the field.

# PART TWO: THE COSEISMICALLY-DISPLACED BOULDERS IN THE PORT HILLS

# CHAPTER 4. SEISMICALLY INDUCED BOULDER DISPLACEMENTS IN THE PORT HILLS, NEW ZEALAND DURING THE 2010 DARFIELD (CANTERBURY) EARTHQUAKE

# Seismically induced boulder displacement in the Port Hills, New Zealand during the 2010 Darfield (Canterbury) earthquake

**Narges Khajavi[1], Mark Quigley[1], Sam McColl[1], Amir Rezanejad[2]**

[1]Department of Geological Sciences, University of Canterbury, Christchurch, New Zealand
[2] Parsa Company, Christchurch, New Zealand

Article history:
Submitted to: New Zealand Journal of Geology and Geophysics
Received May 2012
Accepted June 2012
Version of record first published: 13 Aug 2012

## 4.1 Abstract

An analysis of boulders displaced during the September 2010 $M_w$ 7.1 Darfield (Canterbury) earthquake provides non-instrumental constraints on the variability, distribution and origin of strong ground motion during major earthquakes. Boulders ranging in mass from 10 to 5000 kg were displaced 8-970 cm laterally from hosting soil sockets of < 1 cm to 50 cm depth at several sites in the Port Hills, roughly 35 km southeast of the earthquake epicentre. Boulder displacements were observed on N-striking (000°-015°) ridges above ~400 m elevation but not on NE-, NW- and SE-striking ridges. The prevailing boulder horizontal displacement azimuth of 250° ± 20° is subparallel with the direction of instrumentally recorded transient peak ground horizontal displacements. Boulder displacement distance has no correlation with displacement azimuth, boulder mass or soil socket depth and has a partial correlation with slope angle. The lateral displacement of many boulders from low slope (< 10°) ground surfaces on ridge crests exceeds nearby instrumentally recorded peak ground displacements at lower elevations by up to an order of magnitude, implying that seismic waves were amplified at the study sites. Preliminary 2-D FLAC modelling suggests that topographic amplification may explain this observation. The co-existence of displaced and non-displaced boulders at proximal (< 1 m spacing) sites also suggests small-scale ground motion variability and/or varying boulder-ground dynamic interactions relating to shallow phenomena such as variability in soil depth, bedrock fracture density and/or microtopography on the bedrock-soil interface. Remapping of boulders following the February 2011 $M_w$ 6.2 Christchurch earthquake reveals no subsequent relocation despite locally recorded horizontal and vertical ground accelerations well in excess of the Darfield earthquake and pervasive rockfalls and landslides elsewhere. This study successfully identifies some of the major controls on spatial ground motion variability at non-instrumented locations and highlights the

complexity of ground response at different spatial scales and for different earthquake characteristics.

## 4.2 **Introduction**

Measurements of earthquake strong ground motion are important for understanding the spatial distribution, intensity and origin of seismic shaking, with relevance for the engineering of earthquake-resistant structures. In areas lacking dense seismometer arrays, it is necessary to use independent techniques to characterize earthquake ground motion. Coseismically displaced boulders may provide non-instrumental proxies of earthquake motion (Oldham, 1899; Clark, 1972; Bolt and Hansen, 1977; Umeda et al., 1987; Iio and Yoshioka, 1992; Ohmachi and Midorikawa, 1992; Bouchon et al., 2000).

Several studies have concluded that local peak vertical ground accelerations (PVAs) must have exceeded 1 g in order to cause the observed lateral boulder displacements (e.g. Umeda et al., 1987; Iio and Yoshioka, 1992; Bouchon et al., 2000). Shaking table experiments and numerical arguments based on empirical data, on the other hand, suggest that boulder 'upthrow' can be produced by strong horizontal ground motion alone, due to the impact and dynamic interactions of boulders with the sidewalls of ground sockets (e.g. Ohmachi and Midorikawa, 1992). Many other studies have similarly concluded that lateral boulder displacements used to infer the 'upthrow' of objects do not require vertical ground accelerations in excess of 1 g (e.g. Newark, 1973; Clark, 1972; Bolt and Hansen, 1977; Ohmachi and Midorikawa, 1992).

There is a general paucity of comparisons between coseismic boulder displacement data (distance and azimuth), boulder characteristics (e.g. mass), site conditions (e.g. slope, soil thickness, socket depth, elevation, hosting ridge orientation) and seismologic attributes (earthquake magnitude, peak ground acceleration data, frequency content, etc.) that are necessary for providing insights into the relationships among displaced boulders and strong ground motion characteristics.

The $M_w$ 7.1 Darfield (Canterbury, New Zealand) earthquake of September 2010 occurred on a previously unknown fault network beneath the Canterbury Plains approximately 40 km west of the Christchurch central business district (CBD) at a depth of ~11 km (Quigley et al., 2010, 2012; Gledhill et al., 2011). An $M_w$ 6.2 aftershock (Christchurch earthquake) occurred on February 2011 at depth of 5 km on a dextral-reverse fault network approximately 5 km southeast of the Christchurch CBD (Beavan et al., 2011).

The seismological attributes of these earthquakes relevant to this study are presented in Table 4.1.

The Darfield earthquake generated an array of coseismic geomorphic features in the Port Hills south of Christchurch (Fig. 4.1) including displaced boulders, shattered ridges, landslides and other forms of ground damage (Fig. 4.2, see also section S4.4 in Supplementary file). The locations, physical attributes, hosting socket geometries, displacement directions and displacement azimuths of displaced boulders were mapped at several sites starting approximately two weeks after the Darfield earthquake, and key sites were revisited from two days following the Christchurch earthquake. In this study, I present boulder displacement data, site characteristic data, seismologic data and preliminary results from finite difference models (Fast Lagrangian Analysis of Continua (FLAC) 6.0) in order to obtain non-instrument constraints on the intensity, spatial variance and origin of strong ground motion during the Darfield earthquake.

Table 4.1. Seismic characteristics of Darfield and Christcurch earthquakes. PHDs and PVDs, and P.H.G.Ds are peak horizontal displacements, peak vertical displacements, and permanent horizontal ground displacements, respectively. Station codes are CRLZ, Canterbury Ring Laser; LPCC, Lyttelton Port Company; and HVSC, Heathcote Valley Primary School.

| Earthquakes | Fault | Distance to study site (km) | PHAs and PVAs (g) | | | PHDs and PVDs(mm) | | | P.H.G.D (mm) |
|---|---|---|---|---|---|---|---|---|---|
| | | | CRLZ | LPCC | HVSC | CRLZ | LPCC | HVSC | |
| Darfield | Strike-Slip | 39 | 0.12,0.07 | 0.37, 0.15 | 0.66,0.28 | 75, 13 | 70, 41 | 87, 38 | 115-145 at study site |
| Christchurch | Dextral-Reverse | 5.6 | _ | 1,0.41 | 1.5, 1.47 | _ | 126, 59 | 149, 119 | N/A |

## 4.3 **Boulder displacement in the Darfield earthquake**

### 4.3.1 Methodology

Fifty-four displaced basaltic boulders and tens of non- displaced boulders were mapped at various locations in the Port Hills following the Darfield earthquake (Figs. 4.1-4.2). Net displacement distances were measured from the centre of the identifiable pre-earthquake boulder location (soil socket) to the centre of the present resting position of the boulder. As most boulders were relocated at small distances (< 2.5 m) on gentle (< 10°) slopes, the reported displacement distances are primarily horizontal displacements. Boulder displacement azimuths were recorded and boulder dimensions (length, width and height) were combined with a basaltic density of 2.85 g/cm$^3$ to derive boulder masses (Fig. 4.3A-B). Soil socket depths were measured in the field and estimated from field photographs, local slopes were measured using a clinometer (Fig. 4.3A-B) and soil thicknesses were derived

using a soil penetrometer. The orientations of ten linear segments of ridgeline crests in the Port Hills were measured and it was noted whether these ridges contained displaced boulders or not (Table 4.2).

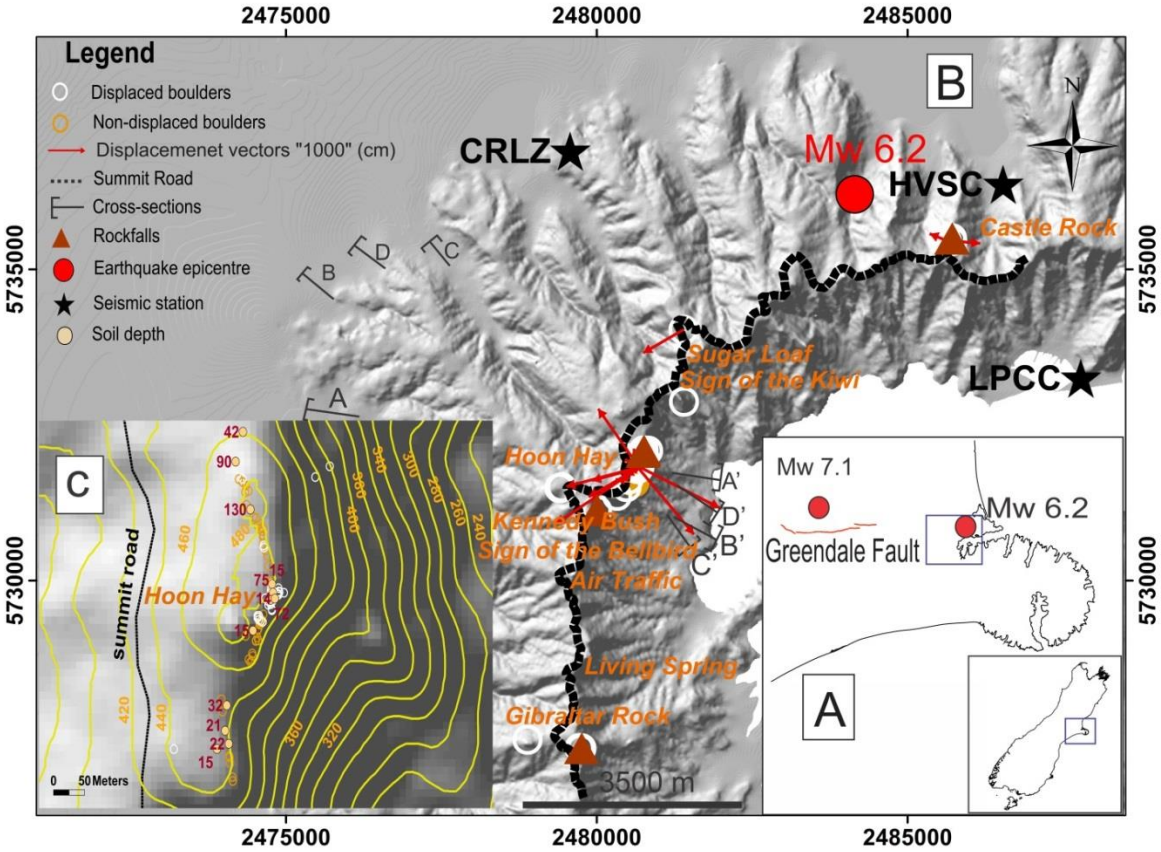


Figure 4.1. General view of the Port Hills. (A), Location of study area is shown by a blue square on map of the Canterbury region and within South Island of New Zealand. (B), 10 m hillshade model of the Port Hills showing the distribution of displaced boulders, rockfalls and seismic stations. Vectors show the 1000 x exaggerated horizontal displacement of boulders displaced from flat to gently sloping ground. (C), Ridge crests of two modelled sites have been magnified to show the details.


Figure 4.2. Displaced boulders at Hoon Hay site. (A), Displaced boulder on the Flat ground at ridge crest; turf between socket and boulder remained without damage. (B), Coseismic shattered ridge; turf was torn up and boulders and soil were thrown away.

Table 4.2. Azimuth measurements in ten places along the Port Hill ridgeline. Existence of displaced boulders or ground damage is indicated with 'Yes' or 'No'.

| Number | Location | Ridge Azimuth | Displaced Boulders |
|---|---|---|---|
| 1 | Hoon Hay | 040 | No |
| 2 | Hoon Hay | 014 | Yes |
| 3 | Kennedy Bush | 015 | Yes |
| 4 | East of Gibraltar | 000 | Yes |
| 5 | Castle Rock Ridge | 013 | Yes |
| 6 | Sign of the Kiwi | 034 | No |
| 7 | South of Castle. R | 129 | No |
| 8 | Sign of the Bellbird | 026 | No |
| 9 | Air traffic control | 028 | No |
| 10 | Living spring | 343 | No |

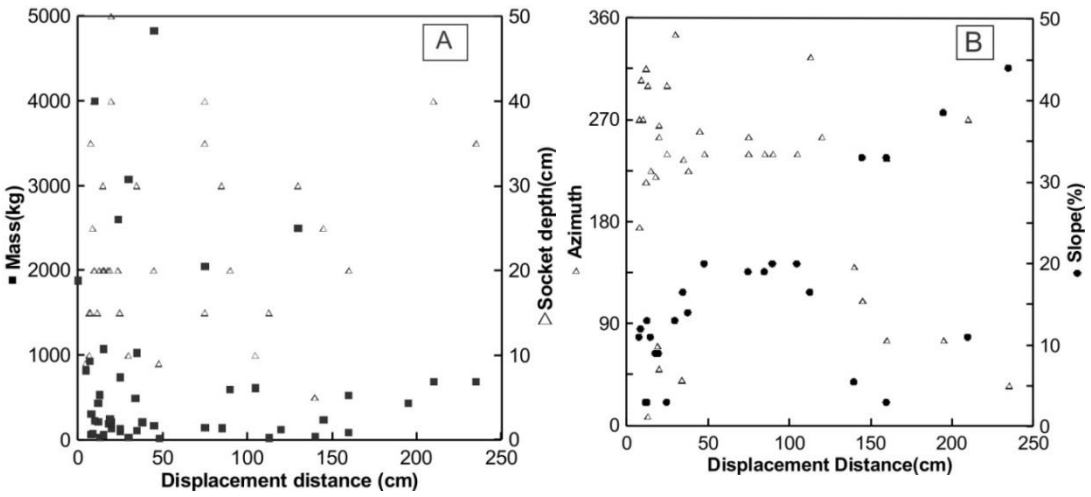


Figure 4.3. Plots of displacement distance of boulders versus (A), Mass and socket depth and (B), azimuth and slope.

### 4.3.2 Field observations

Thirty-eight (two-thirds) of the identified displaced boulders were concentrated at a prominent ridge crest ~488 m a.s.l. in Hoon Hay Scenic Reserve (Fig. 4.1). Some of these boulders were displaced 0.75-1.6 m from flat or gently sloping (0°-10°) ground with no geomorphic evidence of sliding, rolling or being overturned on the surface (Fig. 4.2A). Other evidence for strong ground shaking at this site included cracks, rockfalls, a 23 $m^2$ area of shattered and disturbed turf and soil (Fig. 4.2B) and some boulders, weakened by pre-existing

joints, that were broken and/or rotated in situ and split open. The largest crack to develop, located on the western flank 5 m below the ridge crest and oriented parallel to the topographic contour, measured 1.5 cm in width and was 3.25 m long. A rockfall and a slump occurred on the eastern flank of the ridge with volumes of ~10.7 $m^3$ and 4.8 $m^3$ respectively. On an adjacent ridge (~450 m a.s.l. and ~300 m south), only one big spheroid boulder was ejected from the ridge flank and the only ground damage at the crest was minor gaps formed between surface turf and rock outcrop.

Displaced boulders were observed, but to a limited extent, at several other sites around the Port Hills. At Kennedy Bush Scenic Reserve and Gibraltar Rock, where spurs are perpendicular to the Port Hills ridgeline (Fig. 4.1), several boulders were displaced from sloping ground. A big rockfall, sourced from a steep (~87°) NE-facing slope, caused ground damage, disturbed vegetation and crossed a walking track. Several smaller rockfalls were noted at Gibraltar Rock. At Castle Rock spur, displaced boulders were found on the flanks (Fig. 4.1). Rockfalls were also common at a steep outcrop along this spur, presumably because of the influence of well-developed columnar jointing. A rockfall sourced from the NE face of weathered and jointed basalt outcrop, with estimated volume of ~1300 $m^3$, is considered to be the biggest rockfall triggered by the Darfield earthquake in the study site.

Non-displaced boulders with similar morphologies and in close proximity to displaced boulders are observed at all sites; this indicates small-scale (~1-5 m) spatial variability in ground motion or other conditions favourable for boulder displacement. Many boulders were observed to have millimeter to centimeter scale gaps between the boulder edge and the formerly flush edge of the soil socket indicating transient, but not necessarily permanent, coseismic boulder displacement.

All previously described sites were re-inspected 2 days after the Christchurch earthquake except for Castle Rock, which was inaccessible due to numerous rockfalls and slips blocking the road. Neither previously displaced boulders nor other boulders were relocated at any of the study sites. This is despite the Christchurch earthquake producing greater damage to road cuts in the area and higher accelerations being recorded by nearby seismic stations (Table 4.1). Landslides were considerably more numerous than the Darfield earthquake but were mainly distributed in the north-northeast part of the study area, closer to the earthquake epicentre (Hancox et al., 2011).

### 4.3.3 Analysis of displacement data

Coseismically displaced boulders in the Port Hills were only observed on ridges with azimuthal orientations of 000-015° (Table 4.2). Many of these ridges comprise similar bedrock lithology and elevation, implying that ridge orientation may have played a role in generating the conditions required for boulder dislocation. Displaced boulders were only observed at elevations > 400 m a.s.l. with the exception of Castle Rock (360-420 m a.s.l.).

Boulders ranging in mass from 10 to 5000 kg were displaced 8-970 cm laterally from hosting soil sockets of < 1 cm to 50 cm depth (Fig. 4.3A). The prevailing boulder displacement azimuth is 250 ± 20°, although isolated displacement azimuths were recorded over a full 360° range. Displaced boulders at the Hoon Hay site appear to exhibit bimodal displacements of 8-50 cm and 70-160 cm along an azimuth of 215-270°. Soil thickness varies over the range 15-32 cm on the site without displaced boulders and 14-130 cm on the Hoon Hay site, which includes most of the displaced boulders (Fig. 4.1). Further investigations are required to document whether small-scale thickness variations exist beneath each boulder displacement site.

No clear relationship is observed between displacement distance and mass, socket depth and displacement azimuth (Fig. 4.3A-B). A partial correlation exists between slope and displacement distance, although significant exceptions exist with some of the largest displacements recorded on gentle (≤ 15°) slopes.

Field investigations suggest that boulders were either (a) ejected from a socket of soil (5 cm ≤ socket depth ≤ 40 cm) on sloping or relatively flat ground, with the largest travelling distances of 45-970 cm among the others or (b) were not ejected, but either slid along the local slope or became unattached within their soil sockets due to severe shaking. The displacement distance of group (b) was generally smaller (8-85 cm), but recorded as 130-160 cm where ground was steeper (slope > 30°).

The prevailing SW-directed boulder displacement azimuth range is subparallel with the NE-SW direction of instrumentally recorded transient peak horizontal ground displacements from the closest strong ground motion seismographs (Canterbury Ring Laser or CRLZ and Heathcote Valley Primary School or HVSC; Fig. 4.4, Table 4.1) and at high angles to the NW-orientated net permanent horizontal displacements interpolated for the study site from GPS and differential InSAR data (Beavan et al., 2012). Observed boulder displacements are therefore attributed to the dynamic phase of ground motion, occurring around the largest amplitude of the ground velocity (Iio and Yoshioka, 1992) rather than the permanent tectonic

deformation. Several measured boulder horizontal displacements, including boulders that show no geomorphic evidence for rolling or sliding (Fig. 4.2A), exceed the maximum instrumentally recorded horizontal displacements by an order of magnitude (Table 4.1). This implies greatly enhanced horizontal ground accelerations at the study site. Other studies on seismically induced boulder displacements have indicated that topographic amplification may have been important because of the distribution of displaced boulders being concentrated on ridge crests (e.g. Umeda et al., 1987; Iio and Yoshioka, 1992). To investigate whether the topography of the Port Hills may have amplified the shaking response in the Darfield earthquake, I used 2D FLAC modelling.

## 4.4 Possible role of topographic amplification

### 4.4.1 Methodology

To assess whether ridge shape and earthquake frequency spectra may have influenced variation in displaced boulders, a 2D explicit finite difference program (FLAC 6.0) is used to model the shaking response at two sites: one for which boulders were displaced during the Darfield earthquake only, and the other for which boulders were present but not displaced during either earthquake. The methodology used follows that of McColl et al. (2012).

Both sites are on the crest of the semi-circular ridgeline defining the western skyline of the Lyttelton Harbour. They are within close proximity to each other and have almost similar ridge-crest orientation. For each site, two cross-sections (AA'-DD'; Fig. 4.1) were made using a 10 m digital elevation model (DEM) and data were imported into the FLAC software to define the model free surface for each site. The cross-section orientations were approximately perpendicular to the ridge crest to provide a range of likely topographic amplification. Null (zero stress) zones were applied above the free surface and an isotropic elastic constitutive material model represented the volcanic rock (modelled as homogenous basalt). To account for potential deviations from generic properties for basaltic rock masses at the locations, upper and lower bounds were selected and modelled separately.

Seismic inputs used in the model were based on the horizontal ground motion data available from the GeoNet website (www.geonet.org.nz) and applied as vertically propagating horizontal shear waves. Records of the Lyttelton Port Company (LPCC) seismometer for the Darfield and Christchurch earthquakes and records of the CRLZ seismometer for Darfield earthquake (no data were available from this seismometer for the Christchurch earthquake) were applied. Each model was run for both components of

horizontal motion separately and for the upper and the lower bound rock properties to provide a range of likely ground motion amplifications. The output from the models included peak ground velocities and accelerations (vertical and horizontal) recorded at the modelled ridge crest and slope base to assess the effect of topographic amplification of seismic shaking.

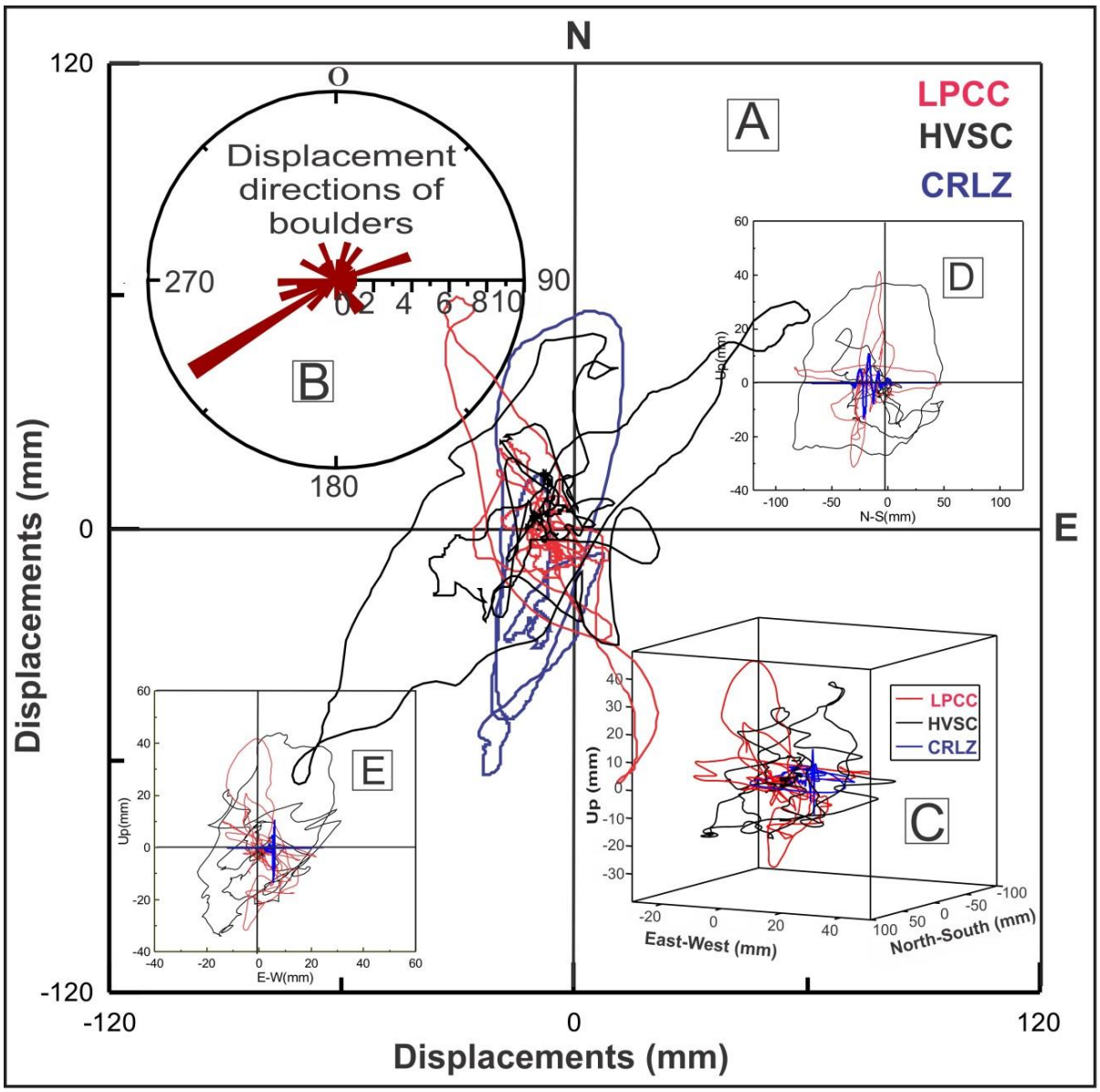


Figure 4.4. A comparison of observed and instrumentally recorded displacement directions. (A), Horizontal displacement records of three seismic stations (LPCC, HVSC and CRLZ) for Darfield earthquake. (B), rose diagram shows displacement directions of boulders measured in the field. (C), 3D diagram of displacements. (D), sectional view (up versus north-south). (E), sectional view (up versus east- west).

### 4.4.2 Results and interpretation

The results of topographic amplification analyses along profiles AA' and BB' for upper-bound rock properties have been selected as an example (Fig. 4.5). Amplification of horizontal ground velocity and acceleration at the ridge crest occurs at all sites, with a maximum amplification of around 80% of the ground motion at the base of the hill. The amplification factor varies significantly between seismic inputs, reflecting frequency-dependent response. Amplification of horizontal velocities and accelerations are higher for all seismic inputs at the site with displaced boulders (Fig. 4.5).

It is difficult to determine what specific topographic conditions caused this difference, except to note that the elevation of the site with displaced boulders was slightly higher. On the contrary, greater vertical amplifications were modelled at the site without displaced boulders for three of the seismic inputs (Fig. 4.5). However, vertical accelerations presented here are merely a secondary product of horizontal motion of the hill and not representative of the real vertical ground motion, which is a result of additional wave forms not modelled here.

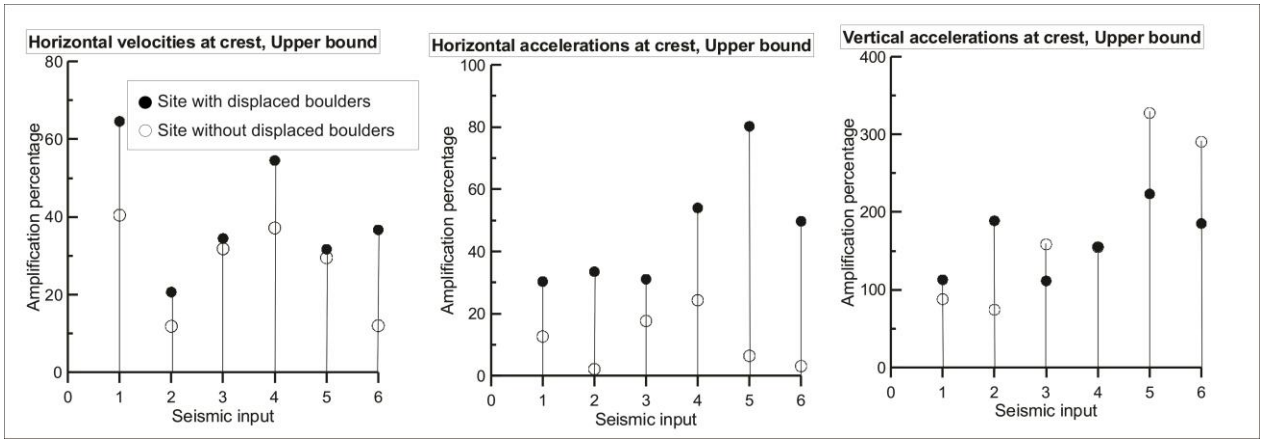


Figure 4.5. Results of topographic amplification modelling along profiles AA' and BB'. Numbers 1-6 on the x axes show the different seismic inputs. 1, 2: LPCC data of S80W and N10W components recorded for the Darfield earthquake; 3, 4: CRLZ data of east and north components for the same earthquake; 5, 6: LPCC data of similar components recorded for the Christchurch earthquake.

## 4.5 **Concluding discussion**

A comparison of field measurements with seismologic data indicates that the predominant direction of coseismic boulder displacement in the Port Hills was governed primarily by the orientation of peak transient horizontal ground displacement during the

Darfield earthquake. As variations in the timing and height of object upthrow and directions of object displacement are observed even in shaking table experiments with uniform objects, constant socket depths and purely horizontal seismic input (e.g. Ohmachi and Midorikawa, 1992), it is not surprising that some variability is observed in both the displacement and displacement direction of the boulders I describe. The overall consistency between these datasets suggests that the displacement azimuths of coseismically displaced boulders have the potential to provide insights into the prevailing direction of transient peak ground deformation during major earthquakes in some instances.

In the absence of geomorphic evidence for rolling or sliding, the lateral displacement of some boulders on low-slope (< 10°) surfaces exceeds instrumentally recorded transient peak horizontal ground displacements by more than an order of magnitude. This implies that horizontal ground displacements at the sites with displaced boulders were amplified relative to the seismometer sites. Field observations and FLAC modelling indicate that both ridge orientation and shape are likely to have amplified ground motions. The rather narrow azimuthal range in ridge orientations with displaced boulders is at a high angle to the seismic wave propagation direction from the Darfield earthquake, which is likely to have amplified incoming seismic waves at these sites.

The lack of correlation between boulder displacement, mass and socket depth is somewhat surprising, given that heavier boulders with deeper (or more cohesive) soil sockets might be expected to have smaller displacements. Beyond a threshold level, soil socket geometry and depth must play a role in influencing the ability of a boulder to be ejected and displaced; an extensively deep socket and/or an enclosing, highly concave-up socket geometry (e.g. a buried boulder) would prohibit a boulder becoming dislodged and ejected in an earthquake. In this instance; however, for boulders that were ejected from a socket, the depth of the socket does not seem be relevant in influencing the finite displacement distance.

The lack of a correlation between displacement, boulder mass and socket depth (Fig. 4.3A), together with the general lack of clearly distinguishable boulder impacts on the edges of some major sockets, suggests that some boulders may have been ejected from sockets due to PVAs ≥ 1 g (Iio and Yoshioka, 1992). Under such circumstances the mass of the boulder would be theoretically irrelevant to lateral transport distance, but shape, ground slope and transient vertical and horizontal ground motions at landing time of the boulder would be critical factors to determine the final displacement distances. At this stage I cannot resolutely prove that Darfield earthquake PVAs exceeded 1 g based on my observations. It remains

possible that amplified peak horizontal accelerations (PHAs) and ground displacements at the study sites with PVAs <1 g may have driven boulder displacement through impacts and 'ramping' of boulders against soil sockets and/or other dynamic site effects (Clark, 1972; Newmark, 1973; Bolt and Hansen, 1977; Ohmachi and Midorikawa, 1992).

The co-existence of morphologically similar displaced and non-displaced boulders in close proximity (Fig. 4.2A) suggests small-scale variability in boulder-ground dynamics and/or the frequency and intensity of strong ground motion relating to site effects. Microtremor measurements reveal that boulders on soft ground have differing vibration characteristics from the ground due to dynamic boulder-ground interactions (Ohmachi and Midorikawa, 1992), and I suspect that these complex interactions may be partially responsible for the variability in displacement I observe here. Shallow site conditions such as variability in soil depth, bedrock fracture density and/or microtopography on the bedrock-soil interface may be possible sources to explain both differential site responses. The subsequent lack of boulder displacement at these sites in the Christchurch earthquake, despite higher recorded PHAs and PVAs at the closest seismometers (Table 4.1), highlights some of the challenges in directly inferring earthquake characteristics using 'non-instrumental' techniques such as displaced boulders. The shorter shaking duration of the Christchurch event, differing frequency contents (Fig. 4.6) and different source characteristics (e.g. location, depth and focal mechanism) are all factors that may have contributed to generating circumstances less favourable to boulder displacement in this earthquake.

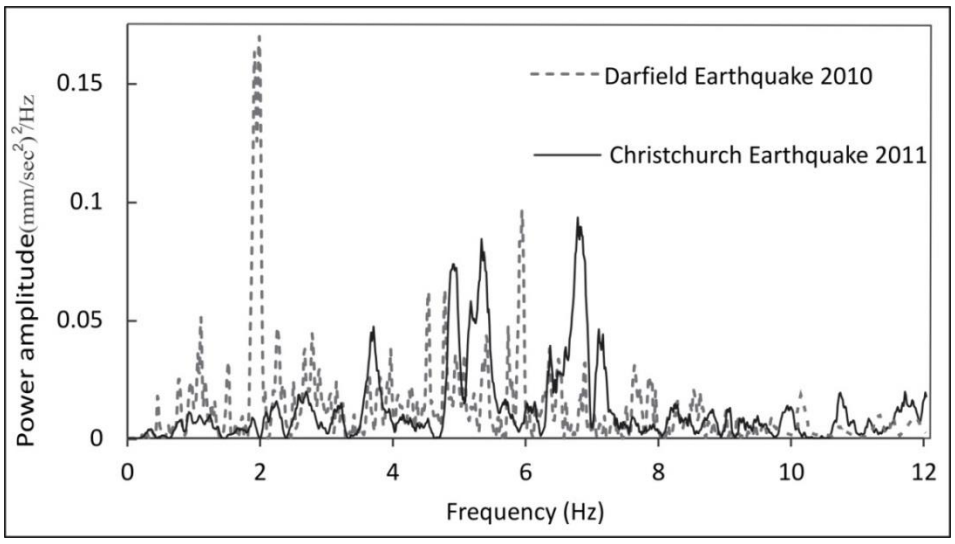


Figure 4.6. Seismograms in the frequency domain for Darfield and Christchurch earthquakes at LPCC site. This record is for the east west component of ground motion. Power spectra analyses were performed using SeismoSignal 4.3.0.

# CHAPTER 5. CONCLUSIONS

# Conclusions

## 5.1 **Introduction**

This thesis investigates the neotectonics and paleoseismology of the Hurunui segment of the Hope Fault and documents coseismically-displaced boulders and ground damage in the Port Hills in the South Island of New Zealand. LiDAR data, photogrammetry, structural and geomorphic mapping, paleoseismic trenching, dendrochronology, surface dating, and documentation of earthquake-induced ground modifications were applied to provide seismic hazard parameters for the Hurunui segment of the Hope Fault and evaluate characteristics of the strong ground motion during the Darfield earthquake in the Port Hills, south of Christchurch city. This thesis shows that a combination of field techniques and computer skills and modelling are required to study faults and produce useful dataset. The seismic hazard parameters, the structural geomorphic maps and data on the strong ground motion characteristics (documented in the Port Hills) of the Greendale Fault that I have produced are applicable to the New Zealand national seismic hazard model and provide insights into future coseismic displacements and fault rupture hazards. I summarise the key findings of this thesis and make some suggestions for future research considerations.

## 5.2 **Key findings**

The key findings of this thesis are summarised below.

Table 5.1 Research questions and outcomes of this thesis (after Table P. 1).

| Goal/Scientific contribution | Research questions | Relevant chapter |
|---|---|---|
| Defining the fault deformation zone associated with the Hurunui segment of the Hope Fault and investigating the faults' structural complexities | How accurate are the fault structures and geomorphic features mapped along the Hurunui segment using LiDAR data? | Chapter 1 |
| | How wide is the deformation zone? | |
| | What are the structures within the fault deformation zone and how are their kinematics interpreted in the context of the regional stress field? | |
| | Why has the mature Hope Fault developed a wide deformation zone instead of a simple thoroughgoing structure? What factors affect the spatial distribution of the fault deformation zone? | |
| | Are valuable sites to conduct further paleoseismic studies identified on the western Hope Fault using LiDAR data? | |
| Obtaining an earthquake chronology for the Hurunui segment using paleoseismic trenching and other Quaternary techniques and explore the fault behaviour | What is the structural configuration of the fault at the proposed segment boundary area? | Chapter 2 |
| | Did the 1888 earthquake rupture through the segment boundary? | |
| | Can the segment-to-segment rupture scenarios be resolved to provide a Holocene rupture behaviour of the western Hope Fault? | |
| Measuring dextral displacements along the Hurunui segment, obtaining slip history, single event displacement, slip rate, recurrence interval, and the magnitude potential of the Hurunui segment | How faulted geomorphic features, their displacements and surface age can be compared along the entire Hurunui segment? | Chapter 1, Chapter 2 and Chapter 3 |
| | What are the seismic hazard parameters of the fault? | |
| | Are geomorphic, geodetic and paleoseismic slip rates consistent? | |
| | Is there along-strike spatiotemporal variation in the slip rate? How does the slip rate vary from segment-to-segment? | |
| | How are estimates of seismic hazard parameters improved by integrating field and LiDAR data? | |
| Documenting the characteristics of displaced boulders and ground damage observed in the Port Hills and investigate the possible factors affecting boulder displacement | What characteristics should be mapped and what is the relationship between those? | Chapter 4 |
| | What is the relation between coseismic displacement of boulders, the transient peak ground horizontal displacement recorded at the nearby stations, and the permanent post-seismic horizontal ground displacement? | |
| | Did topography influence the boulder displacement? | |

### 5.2.1 **How accurate are the fault structures and geomorphic features mapped along the Hurunui segment using LiDAR data?**

A comparison of LiDAR fault mapping with the previous field mapping indicates that the use of LiDAR has enabled large improvements in the detection and mapping of the fault structures and geomorphic features. With LiDAR data I was able to map the precise location of the fault principal slip zone (PSZ), secondary structures forming the fault deformation zone (FDZ), geomorphic features, and to measure the horizontal and vertical displacements

along the PSZ and secondary structures; many of fault structures, geomorphic features and displacements were previously unrecognized. In particular, I identified and mapped features on the LiDAR hillshade model including: (1) ~ 20 km of the PSZ (from a 29 km-long section of the Hurunui segment), (2) 238 subsidiary fault traces, (3) a range of geomorphic features including abandoned and active fans and channels, terrace risers, landslides, debris deposits, gravitational failure features, rockfalls, basins, swamps, etc., and (4) 160 dextral displacements from the PSZ and fault deformation zone. I was able to identify all of these features either on the 1-m or 2-m LiDAR-derived hillshade models with the aid of my field observations. At some places where lacking vegetation cover, I could identify big boulders within debris deposits and measure horizontal displacements of ~3 m and vertical displacements of ~0.2 m on the 1-m LiDAR hillshade model.

### 5.2.2 **How wide is the deformation zone?**

I measured the widths of the FDZ, including all of the mapped structures on the LiDAR DEM, along the entire length of the fault section on the LiDAR swath. In total, I made 330 measurements of the FDZ width along the fault length. Where the FDZ width was highly variable along the PSZ, I increased the number of the measurements to 10 m spacing and where the FDZ was narrow and only limited to the fault scarp, I decreased the spacing of measurements. In addition, to show the spatial distribution of the FDZ width in more detail, I made 415 measurements of the FDZ width north and south of the PSZ. I assigned positive signs to those measured from north of the PSZ, and negative signs to those measured from south of the PSZ to assess the symmetry of the FDZ with respect to the PSZ along the Hurunui segment. FDZ width measurements from 415 locations reveal a spatially-variable, active FDZ up to ~ 500 m wide with an average width of 200 m, which is distributed more to the north of the PSZ.

### 5.2.3 **What are the structures within the fault deformation zone and how are their kinematics interpreted in the context of the regional stress field?**

I categorized the structures observed on the LiDAR hillshade model into three groups; (1) the PSZ strands, (2) fault strands that are connected to the PSZ on the surface, and (3) fault strands that are within the FDZ, but are farther away from the PSZ and have no physical connection to it on the surface. I named the latter “secondary faults”. Apart from 69 individual PSZ strands with a range of length between 30 and 1500 m, 70 normal, 55 dextral-

reverse, 13 splay, and 100 secondary faults were mapped. Normal and secondary faults are more common north of the PSZ, but dextral-reverse faults are more common south of the PSZ. Secondary faults are parallel to sub-parallel to the PSZ. Length-weighted Rose diagrams indicated that the longest segments of the PSZ strike between 070° and 075°, the longest segments of the normal faults strike between 095° and 100°, and the longest segments of the dextral-reverse faults strike between 055° and 065°. The orientation and kinematics of the normal faults are best explained by a vertical $\sigma_1$, and a $\sigma_3$ orientation of 005°-010° that is perpendicular to the regional $\sigma_1$ orientation (i.e., geodetic: 100°- 110° and earthquake focal mechanisms: 115° ± 16°) (Nicol and Wise, 1992; Pettinga and Wise, 1994; Sibson et al., 2011; Wallace et al., 2007, 2012). The orientation of the dextral-reverse faults is within 5°-20° of the PSZ and 35°-45° of the regional $\sigma_1$, consistent with oblique (rather than purely reverse) displacement. In particular, the $\sigma_3$ orientation derived from single-event normal faults indicates consistency between the near-fault coseismic and regional stress fields in the absence of local conditions that could perturb the stress field. From these data I conclude that the Hurunui segment of the Hope Fault is optimally oriented for dextral strike-slip within the regional stress field and that the observed fault zone complexity is thus unlikely to result from large-scale fault mis-orientation with respect to regional stresses.

### 5.2.4 **Why has the mature Hope Fault developed a wide deformation zone instead of a simple thoroughgoing structure? What factors affect the spatial distribution of the fault deformation zone?**

It has already been modelled that topographic relief creates spatial variations in gravitational loads that may perturb near-surface and regional tectonic stress fields (McTigue and Mei, 1981; McTigue and Stein, 1984; Savage et al., 1985; Savage and Swolfs, 1986; Liu and Zoback, 1992). Those studies suggested that regional horizontal compression can be modified (decreased or changed to tension) in the proximity of high topography. Norris and Cooper (1995, 1997) also discussed the effect of topographically perturbed stresses on developing serial and parallel partitioning of the central segment of the dextral-reverse Alpine Fault and suggested a depth of 1-4 km for stress perturbation around the fault. None of those studies; however, specifically explained the relationship between topographic relief and the FDZ width. The configuration of the FDZ along the Hurunui segment suggests that the zone of high shear stress on the valley sides could possibly rotate the fault plane and cause fault bifurcation into separate segments. The local valley relief (700-1100 m) adjacent to the

Hurunui segment suggests that the near-fault stress field could be perturbed to depths of ~1-2 km. The modelled cross-sections using field data show that shallower (< 85°) dip angles of the PSZ occur in cover deposits at depths generally < 100-200 m, although I cannot dismiss the possibility of additional fault rotation at depth. Field and LiDAR-derived data strongly suggest that the Hurunui segment is dominantly strike-slip, but can appear as a dextral-reverse or dextral–normal fault with shallower dip angles near the surface depending on the existence of high topography south or north of the fault or thickness of deposits. The asymmetric FDZ observed also confirms the fault should be dipping more gently near the surface especially where it enters the cover deposits. According to my modelled cross-sections in this research, the normal and dextral-reverse faults and the very small-scale faults that are connected to the secondary faults on the surface merge into a single PSZ strand or into their relevant major secondary fault at depths of ~50-200 m. In contrast, the strike-slip secondary and splay faults merge with the PSZ at greater depths beyond the cross-sectional views. This is consistent with the likely stress perturbation depth of ~1-2 km in this area. The subsurface interaction of the majority of the faults (the branching depth) in most instances seems to be close to, or at the basement-cover interface, i.e., 50-200 m depth.

In addition to topographic relief, I also illustrate that the thickness of the unconsolidated cover deposits and changes in fault strike (6°-15°) are important factors in influencing the FDZ width. However, I interpret that the changes in the strike of the fault are resulted from different responses of the fault to the existing variable topography along it. Therefore, I believe that the thickness of cover deposits is a second order control (after topography relief) on the FDZ both at the flanks of mountains and adjacent to valleys. An important first order control of topography is also illustrated by the 1888 Hope Fault rupture; the surface rupture is comparably narrow and straight where it traverses areas with minimal surface relief despite significant thicknesses of underlying unconsolidated outwash deposits, and is more complex (more fault step-overs and/or bends) in areas of higher topographic relief (Cowan, 1990; Cowan and McGlone, 1991).

Finally, I present 3D block diagrams and conclude that the FDZ associated with the Hurunui segment has locally been controlled by the oblique component of slip resulting from topographic loading on the fault plane and deflecting it from its favourable orientation for strike-slip motion, the proximity of the fault to the major river valleys and thickness of cover deposits. The surface rupture zone complexity results from shallow fault zone widening and

bifurcation at the expected penetration depth of topographically-influenced stress perturbations.

### 5.2.5 **Are valuable sites to conduct further paleoseismic studies identified on the western Hope Fault using LiDAR data?**

The answer to this question is "Yes". On the LiDAR hillshade models, many important places display value for paleoseismic investigations. In this thesis, I considered two sites to conduct paleoseismic investigation; the Hope Shelter and Parakeet Stream sites. At the Hope Shelter site, a single trace of the fault has cut a Holocene terrace and fans and a debris deposit and created a shutter scarp and basin, which made it an ideal place for paleoseismic trenching (Chapter 2 presents the details of my paleoseismic work). In addition, this site is the most accessible, least vegetated, and closest site to the proposed segment boundary between the Hurunui and the Hope River segments of the Hope Fault. According to the results of this study presented in the future sections, there is still a lot of potential at this site for paleoseismic studies. At the Parakeet Stream site, a debris deposit has been cut by a clear fault trace and has preserved a large cumulative dextral displacement of ~80 m. This site is in a ~2 km walking distance to the Hope-Kiwi confluence and includes open surfaces (i.e., peat bogs and swamps formed on the terrace surfaces of the Parakeet Stream) which were ideal places for off-fault paleoseismic studies (Chapter 2 and its appendix present the details of my work at this site). This site is a potential location for paleoseismic trenching across the fault where it has cut a young terrace just west of the Parakeet Stream; however, it is not as accessible as the Hope Shelter site. Other less accessible, more densely forested places which show decent cumulative displacements are also identified along the fault. These places will be suggested to future research considerations in the "future work" section.

### 5.2.6 **What is the structural configuration of the fault at the proposed segment boundary area?**

Prior to this study, Cowan (1989) considered a large-scale constraining bend of 8° to 13° resulted from a change in the strike (085° to 072°) of the surface trace of the Hope Fault south of the Hope-Boyle confluence, west of Dismal Flats (see Fig. 2.3 in Chapter 2 for these locations). He argued that this locality may have been the epicentre for the 1888 Amuri earthquake on the Hope River segment. Subsequently, Cowan (1991) estimated a rupture length of 30 ± 5 km for the Amuri earthquake and inferred that this earthquake ruptured the

fault between two tectonic basins (the Hope-Boyle and Hanmer) formed at releasing bends (Clayton, 1966; Freund, 1971; Cowan, 1989, 1990) in the Hope Fault zone. He discussed that the E-W trend of the fault in this area is structurally distinct from the fault traces to its southwest and northeast.

In this thesis, I produced a 5-m photogrammetrically-derived hillshade model integrated with a 2-m LiDAR hillshade model (Chapter 2) to study the structural configuration of the fault in the area west of the Dismal Flats and Hope-Boyle confluence. This area is covered by beech trees so that a high-resolution technique was required to study the fault. I found that the boundary between the two segments is characterized by a ~850-m-wide right stepover in the fault associated with a 9º-14° fault bend (see Fig. 2.3 in Chapter 2). The location and size of this structure contradict the previous studies which discussed that the 1888 surface rupture should have arrested/nucleated at the "large-sized" fault bend located to the south of the Hope River.

### 5.2.7 **Did the 1888 earthquake rupture through the segment boundary?**

In the study area, two paleoseismic trenches and 7 pits were excavated, faulted geomorphic features were mapped and displacements along them were measured. In addition, I applied dendrochronology in one site and Schmidt hammer in two sites along the study area to understand the location and surface rupture length of the 1888 Amuri earthquake. The integrated results from the above techniques, in addition to the observed characteristics of the fault bend and stepover, defining the slip gradient curve of the 1888 earthquake (measured along the Hope River segment) in relation to the measured surface slip at the Hope Shelter site, and careful reinterpretation of McKay's observations (Chapter 2) provided evidence for the 1888 rupture propagation through the segment boundary. The results of this study concluded two possibilities regarding the 1888 Amuri earthquake: (1) the rupture could have nucleated on the Hurunui segment and propagated to the Hope River segment, via the bend and stepover, with a unilateral directivity (McKay, 1890; Cowan, 1991) towards the east; and (2) the rupture could have propagated bilaterally from Glynn Wye station (see Fig. 2.2 and Appendix 2.1: 17) or from an unknown point west of the Glynn Wye station. Based on the above, I estimated a surface rupture length of 40 to 77 km for the 1888 Amuri earthquake. The minimum length was estimated from the Hope-Kiwi confluence (McKay, 1890) approximately 5 km west of the trench site (at the Hope Shelter site) to the western margin of the Hanmer Basin (Cowan, 1991) (Fig. 2.2B). The western extent of the 1888 rupture could

have passed through the Parakeet Stream area, although no clear evidence for this was identified in my preliminary investigations (see section S2.6). The maximum length was limited to the west by the trench site of Langridge et al. (2013) where their trench data appear to preclude the possibility that the 1888 Amuri earthquake ruptured this far to the west, with an easternmost trace location consistent with the maximum eastward position of rents and fissures observed east of the Hanmer Basin (Hossack Station; Fig. 2.2B) (McKay, 1890). Conversion of surface rupture lengths to earthquake magnitudes using the scaling equation of Wesnousky (2008) yielded an estimated magnitude $M_w$ of 7.1 ± 0.1 for the Amuri earthquake.

In conclusion, comparing the characteristics of the segment boundary area with the most likely criteria required for rupture arrest or propagation explained by Barka and Kadinsky-Cade (1988), Wesnousky (2006), Elliot et al. (2009), and Wesnousky and Biasi (2011), I inferred that the conditions at the study site are more favourable for rupture propagation than arrest. The width and bend angle of the right stepover between the Hope River and Hurunui segments are narrower and smaller compared to the rupture-limiting thresholds (i.e., stepovers ≥ 3-4, and bend angles > 30°) mentioned by the above studies. In addition, my field observations, LiDAR mapping, and trench data (Chapter 1 and 2 and Khajavi et al. (2014)) support the statement above as they indicate that: (1) the slip mode has rapidly changed from dextral to vertical represented by a suite of en echelon structures just at the west of the bend (Fig. 1.10 and Fig. 2.3), (2) the Hurunui segment has a more favourable orientation to rupture with respect to the regional stress field, and (3) the paleoseismic histories obtained from the trenches along both segments are comparable (e.g., events E1 and E3, Fig. 2.15).

### 5.2.8 **Can the segment-to-segment rupture scenarios be resolved to provide a Holocene rupture behaviour of the western Hope Fault?**

I used OxCal 4.2.3 programme (Bronk Ramsey, 2013) and radiocarbon ages obtained from trenches and pits to construct the paleoseismic history of trenches and compare it with other trench and pit data both along the Hurunui and Hope River segments of the Hope Fault. The resolution of data from both trenches allowed me to construct 3 models with different numbers of paleoearthquakes (i.e., 4, 5, or 6 events) and then suggest a preferred model by combining the results according to the interpretations of the entire dataset from trenches and pits and the stratigraphy observed in both trenches, and other data including structural,

geomorphic, and historic data. I include the historic 1888 Amuri earthquake, the beginning of the historical period (A.D. 1840), and the maximum age of the trees grown on the debris deposit (275 ± 20 yr) at the Hope Shelter site into OxCal models. I learned that even paleoseismic trenches excavated in close proximity (they were only 4 m apart in this study) might not necessarily provide the same stratigraphy, and express or preserve the same number of events; which highlights the challenges in paleoseismic interpretation. The results of OxCal models, overlapping event times using data from the trenches at the Hope Shelter site, and other trenches along the Hurunui and Hope River segments and the data from the Parakeet Stream site collectively indicate that 6 earthquake events likely occurred in the past ~1700 yr at A.D. 1888, 1740-1840, 1479-1623, 819-1092, 439-551, and 373-419. I used the Monte Carlo procedure to generate a recurrence interval histogram from earthquake input data (i.e., timings of the earthquakes and their uncertainties). I calculated a mean recurrence interval of ~298 ± 88 yr with successive median inter-event times ranging from 98 to 595 yrs.

The faulted stratigraphy at the Hope Shelter site provides the longest and potentially most complete record of paleoearthquakes along the Hope Fault, allowing for a critical assessment of late Holocene earthquake recurrence times (see Fig. 2.15). Based on the data from this study, the 1888 earthquake ruptured the Hope River segment and parts of the Hurunui segment indicating that the western extent of the 1888 Amuri earthquake is somewhere in between the Hope-Kiwi confluence and Parakeet Stream, but not as far west as the Langridge et al. (2013) trench site. The most recent event of Langridge et al. (2013) provides support for the occurrence of an event in A.D. ~1740-1840 on the Hurunui segment which coincides with a strong shaking event along the Hope River segment (Langridge et al., 2013, Table 2.1). The youngest dates at the Parakeet Stream site, which is located halfway between the Matagouri Flat and Hope Shelter trench sites (Langridge et al., 2013; this study), align with those at Hope Shelter, Matagouri Flat and Horseshoe Lake (Cowan and McGlone, 1991). This provides support for the occurrence of a rupture event (or events) between A.D. ~1400-1600 on both the Hope River and Hurunui segments (Fig. 2.15). According to these correlations, it is inferred that the geometrically-defined segment boundary between the Hurunui and Hope River segments does not always act as barrier to rupture propagation, and analogous geometric discontinuities may not limit rupture dimensions elsewhere along the Hope Fault, implying that the magnitude of future earthquakes may in some instances exceed estimates based on lengths of individual fault segments.

Cowan and McGlone (1991) proposed a periodic earthquake model for the Hope River segment (earthquake surface ruptures every ~81-200 yrs); however, Langridge et al. (2013) interpreted that only two of the five events identified by Cowan and McGlone (1991) could be directly attributed to surface rupturing events and the rest could be attributed to shaking events that generated subsequent silt deposition in their trench on the Hope River segment (Table 2.1). Resolving this debate was beyond the scope of this thesis. However, based on the varied inter-event times observed in this study, I proposed some options which should be considered regarding fault behaviour. The short inter-event times can be explained by (1) coalescing rupture overlap from the adjacent Hope River fault segment on to the Hurunui segment at the study site (e.g., E1 and possibly E3), which could create apparent earthquake clustering irrespective of whether the individual segments exhibit periodic or episodic rupture behaviour, and / or (2) earthquake temporal clustering (i.e. episodic temporal behaviour) on the Hurunui and/or Hope River segments. Long inter-event times can be explained by (1) earthquake temporal clustering (episodic behaviour), and / or (2) 'missing' or (3) unresolved events. In addition, the least likely reason for the apparently variable inter-event times could simply reflect limited chronologic resolution due to some large age ranges of radiocarbon samples. My preferred options are: (1) rupture overlap: like the 1888 event, event E3 involved rupture of both the Hurunui and Hope River segments of the fault, either coseismically (and thus somewhat similar to the multi-segment rupture in the 1888 Amuri earthquake) or in separate events spaced closely enough in time to be unresolvable from dating resolution, irrespective of whether individual segments exhibit periodic or episodic behaviour, (2) earthquake temporal clustering on the Hurunui segment, Hope River segment, or both. Future paleoseismic studies along the Hurunui and Hope River segments of the Hope Fault are required to refine the extent, timing, and rupture behaviour of past earthquakes in this region.

### 5.2.9 **How faulted geomorphic features, their displacements and surface age can be compared along the entire Hurunui segment?**

LiDAR hillshade model, geomorphic maps produced in Chapter 1, and Arc GIS software were used to measure vertical and horizontal displacements, preserved along faulted geomorphic features, on the PSZ and subsidiary structures forming the fault deformation zone (Figs. 3.4-3.7). I assigned qualitative indices from 1 to 5 to measured dextral displacements in order to show the degree of my confidence in measuring a displacement

depending on the landform preservation. In addition, qualitative indices 1 and 2 were assigned to well-preserved and less-preserved fault scarps, respectively. I mapped the location of the measured vertical and horizontal displacements on the LiDAR-derived structural geomorphic maps and produced a large dataset including 477 measurements and their characteristics (Appendix 3.1); some were field-validated. In total, only one third of the measured dextral displacements (those with QIs of 1 to 3) from the PSZ were considered as good data and used for further analysis. I reconstructed 2 faulted geomorphic features (a fan and a debris deposit) with large displacements (~120 m and ~80 m) to constrain the vertical component of slip on the fault. Reconstruction of those two faulted geomorphic features with high dextral displacements at Macs Knob and Parakeet Stream sites, suggested that the scarp heights are only ~1% of the horizontal displacements on the PSZ confirming that the fault is predominantly strike-slip.

Field observations, LiDAR hillshade models, surface dating and geological maps suggest that the very large higher-altitude fans, scree, terrace risers, and other geomorphic features are of late Pleistocene to early Holocene ages (i.e., post-LGM) (Knuepfer, 1992; Nathan et al., 2002; Langridge and Berryman, 2005; Barrell and Townsend, 2012; Khajavi et al., 2014; Khajavi et al., accepted manuscript) (Figs. 3.4-3.7). In comparison, lower-altitude smaller geomorphic features are of late Holocene age (Langridge and Berryman 2005, Langridge et al., 2013, Khajavi et al., accepted manuscript). I applied two analyses to see whether a general age correlation between the displaced features and their dextral displacements is possible. The analyses were based on: (1) plotting the elevations versus dextral displacements of the geomorphic features within the study site (Fig. 3.8), and (2) plotting the dextral displacements along the length of the Hurunui segment alongside with the available surface age data (Fig. 3.9, Table 3.3) to see whether age contours can be produced for the entire fault segment. The results of the first analysis suggest that there is a good correlation between elevation and displacement data of geomorphic features; however, there are 3 clusters of similar displacement data at elevations of ~600, ~700, and ~850 m a.s.l. The lowest-elevation cluster included those displacements which have been measured along the geomorphic features at the young valley sides/floors of the Hurunui and Hope rivers (Fig. 3.4 and Fig. 3.7). In comparison, the highest-elevation cluster included those displacements which have been measured along geomorphic features such as post-LGM fans, terrace risers, debris deposits and bedrock features in the mountainous areas. In the second analysis I generated 6 age contours that correlated displacements at sites with available age data to their

equivalent displacements at other sites which lack age data (Fig. 3.9). This analysis shows that the observed or preserved dextral slip decreases from the central part of the fault towards the east and west, but the surface age increases from the east and west to the central part of the fault. According to the results of these 2 analyses, I concluded that: (1) dextral displacement increases as a function of the elevation of the displaced feature; meaning that higher-altitude older features record higher displacements along the fault, and (2) the elevation-displacement relation alongside with the available surface age data can be used to assign correlative ages to the features that lack surface age.

### 5.2.10 **What are the seismic hazard parameters of the fault?**

Using the correlative ages, available on-site ages, and cumulative dextral displacements from 9 sites along the Hurunui segment, I determined three geomorphic mean slip rate estimates of 12.2 ± 2.4 mm/yr (sites including on-site ages), 11.5 ± 1.7 mm/yr (sites with correlative ages) and 11.8 ± 2 (all sites) mm/yr. The mean slip rate of 12.2 ± 2.4 is preferred which seems to be relatively constant since late Pleistocene. Using the measured displacements of ≤ 25 m, which were mainly measured on LiDAR hillshade model and some in the field), I estimated a mean SED of 3.6±0.7 m. Using the estimated mean SED and slip rate, I calculated a mean recurrence interval of ~ 320 ± 120 yr (200-440 yr) for the Hurunui segment of the Hope Fault. Using the mean SED and fault area of A: 13 *42 $km^2$ and the earthquake scaling relation of Hanks and Kanamori (1979), I calculated a moment magnitude ($M_w$) of ~7.2 for past earthquakes and hypothesized for future earthquakes of the Hurunui segment of the Hope Fault

### 5.2.11 **Are geomorphic, geodetic and paleoseismic slip rates consistent?**

The preferred mean slip rate from this study is higher than the slip rate estimate from Langridge and Berryman (2005) for the McKenzie Fan site. I explain that by measuring larger cumulative dextral slip revealed on the LiDAR hillshade model of the McKenzie fan site (i.e., more fault structures were observed and geomorphic features that have been displaced along multiple fault strands were mapped). From this, it can be inferred that the average slip rate of ~14.5 ± 3 from McKenzie Fan site is the only slip rate along the Hurunui segment that incorporates the maximum dextral slip occurred within the fault deformation zone (see Table 3.5). This slip rate is comparable to the contemporary geodetic slip rate of

13.9 mm/yr (Wallace et al., 2012) for the Hurunui segment of the Hope Fault. The upper bound of the preferred mean slip rate also correlates with the geodetic slip rate. Slip rate estimates from paleoseismic trench data along the Hurunui segment (Langridge et al. (2013) and Khajavi et al. (accepted manuscript)) match with the geomorphic slip rates estimated for the same sites (i.e., Matagouri Flat and Hope River sites). However, these paleoseismic slip rates are closer to the lower and upper bounds of the preferred mean slip rate. Possible reasons for this could be related to the resolution of the trench data or trench locations. The trench excavated by Langridge et al. (2013) is across a single trace of the fault which has cut through the flood plain of the Hurunui River. At this site, a SED of 3 ± 0.4 m was measured on the LiDAR hillshade model (this study) (see Appendix 3.1). Considering the slip measurements from this study and the RI estimate from trench data by Langridge et al. (2013), a paleoseismic slip rate of 10 ± 1.3 mm/yr is calculated which is now fit in the lower bound of the preferred mean slip rate. Therefore, it can be inferred that the observed discrepancy here is related to the resolution of the trench data rather than being related to the different SEDs measured on the surface. At the Hope River site, in comparison, the geomorphic slip rate being lower than the preferred mean slip rate can be related to the trench location. Because the Hope River site is near the geomorphic segment boundary (Khajavi et al., accepted manuscript) there is possibility of surface rupture slip deficits when computed over short intervals of time.

### 5.2.12 **Is there along-strike spatiotemporal variation in the slip rate? How the slip rate varies from segment-to-segment?**

I argued for uniform spatiotemporal slip rates since post- LGM for the Hurunui segment of the Hope Fault in spite of the fact that the range of the slip rate estimates vary between 6.2 mm/yr (minimum average slip rate) and 15.5 mm/yr (maximum average slip rate) (Table 3.5). The reason for such argument is that sites (excluding the Hope River that possibly indicate slip deficits) with quality cumulative displacements from ~7 to 80 m and on-site ages from mid to late Holocene, show uniform spatiotemporal average slip rates of ~12-14 mm/yr (Table 3.5). To clarify this point, I presented all of the estimated slip rates along the strike of the Hurunui segment and versus time by considering those as the minimum or maximum values based on the applied surface ages (Fig. 3.12A-B). According to this analysis, I concluded that: (1) although the mean slip rate of 11.8 ± 2 was determined from all slip rate estimates, a mean slip rate of ~12-14 mm/yr is more plausible when slip

rates are presented as maximum or minimum values; this highlights the resolution of surface age data used in this study, (2) slip rate is constant along the strike of the Hurunui segment, and (3) slip rate is constant during the Holocene.

The slip rates from this study and those from Cowan (1990) and Cowan and McGlone (1991) for the Hope River segment are consistent (Figs. 3.10 and 3.12C) suggesting a constant slip rate for both segments of the fault. The overlap between the mean slip rate of 9.8-14.6 mm/yr for the Hurunui segment and the mean slip rate of 10.4-13.9 mm/yr for the Hope River segment, suggest a constant slip rate of 12.2 ± 2.4 mm/yr. However, I preferred a constant slip rate of 12.5 ± 2.1 mm/yr (Fig. 3.12C) because of two reasons that are: (1) the mean slip rate range of 10.4-13.9 mm/yr from Cowan (1990) and Cowan and McGlone (1991) are the best slip rate estimates for the Hope River segment of the Hope Fault, and (2) the results of slip rate analysis in this thesis showed that the upper bound of my preferred slip rate seems to be more realistic for the Hurunui segment of the Hope Fault. The observed constant slip rate appears to be reasonable as these segments of the fault are structurally simple and show records of at least 6 and 5 earthquakes in the last 700 to 1700 years (Cowan and McGlone, 1991; Khajavi et al., accepted manuscript). In addition, the Hope Fault is a major and well-stablished structure in the MFS that transfers motion between the Hikurangi subduction zone and the dextral-slip Alpine Fault (Van Dissen and Yeats, 1991; Berryman et al., 1992; Knuepfer, 1992; Nicol and Van Dissen, 2002).

### 5.2.13 **How estimates of seismic hazard parameters are improved by integrating field and LiDAR data?**

This thesis used a variety of modern and established techniques both in the field and using computer programmes to study a particular segment of the major fast-slipping Hope Fault. However, there are still many unresolved questions regarding the Holocene and pre-Holocene rupture behaviour of the Hurunui segment, fault segmentation, rupture behaviour of the Hope Fault in relation to the fault network nearby, etc., which definitely require more consideration. Taking that into account, I believe that this thesis has significantly improved the current knowledge as using the integrated techniques and data provided: (1) the most complete record of paleoearthquakes on the Hope Fault (i.e., since 300 A.D.) (Chapter 2), (2) evidence of segment-to-segment ruptures (i.e., the 1888 event and possibly an event between A.D. ~1400 and ~1600) (Chapter 2), (3) detailed structural and geomorphic maps for the Hurunui segment and the segment boundary area between the Hurunui and Hope River

segments (Chapter 1 and 2), (4) more knowledge on the surface rupture length of the historical 1888 Amuri earthquake (i.e., rupture length: 44-70 km) (Chapter 2), (5) late Pleistocene slip rate (12.2 ± 2.4 mm/yr) and Holocene recurrence interval of the Hurunui segment (298 ± 88 yr from paleoseismic trenches and ~320 ± 120 yr from SED and slip rate) (Chapter 2 and 3), (6) estimates of SED (3.6 ± 0.7) and fault slip history which goes back to 6-8 earthquakes (Chapter 3), and (7) the potential magnitude of the future earthquakes on the Hurunui segment ( $M_w = 7.2$ ) and the magnitude of the 1888 event ($M_w = 7.1 \pm 0.1$) (Chapter 2 and 3).

LiDAR data was especially important to discover unknown displacements along the PSZ, the width of the fault deformation zone, constructing the slip history of the Hurunui segment. Once these displacement data were collected, they were integrated with paleoseismic data and slip measurements in the field to obtain more complete estimates of seismic hazard parameters of the fault. Among these data, the SED estimate was of particular importance because the resolution of LiDAR allowed measurements of numerous dextral displacements larger than 3.5 m and field investigations added some value to it by providing displacements of ≤ 3 m.

### 5.2.14 **What characteristics should be mapped and what is the relationship between those?**

The $M_w$ 7.1 Darfield (Canterbury, New Zealand) earthquake of September 2010 occurred approximately 40 km west of the central Christchurch (Quigley et al., 2010, 2012; Gledhill et al., 2011) and generated an array of coseismic geomorphic features in the Port Hills south of Christchurch including displaced boulders, shattered ridges, landslides and other forms of ground damage. In comparison, the $M_w$ 6.2 aftershock (Christchurch earthquake) of February 2011 occurred approximately 5 km southeast of the central Christchurch (Beavan et al., 2011) and under Port Hills. The latter earthquake caused severe shakes, numerous landslides in the Port Hills (Hancox et al., 2011), and led to deaths of 185 people, but did not make any modification to the sites including displaced boulders.

In order to obtain non-instrumental constraints on the intensity, spatial variance and origin of strong ground motion during the Darfield earthquake, I required data on the locations, physical attributes (length, width, and height), hosting socket geometries, displacement directions and displacement azimuths of displaced boulders immediately after the earthquake to avoid any modification. In addition, I needed data on the site characteristics

(density of the basaltic rock, local slopes, soil thickness, and orientation of the ridgeline crests) and seismology of the Darfield and Christchurch earthquake. I started collecting all the above data approximately two weeks after the Darfield earthquake, and revisited the key sites from two days following the 2011 Christchurch earthquake.

The results of field investigations showed that: (1) boulders ranging in mass from ~10 to 5000 kg were displaced 8-970 cm laterally from hosting soil sockets of < 1 cm to 50 cm depth and from flat or gently sloping (0°-10°) ground with no geomorphic evidence of sliding, rolling or being overturned on the surface at several sites in the Port Hills, (2) two-thirds of the identified displaced boulders and a 23 $m^2$ area of shattered and disturbed turf and soil were concentrated at a prominent ridge crest ~488 m a.s.l. in Hoon Hay Scenic Reserve (3) boulder displacement occurred on N-striking (000°-015°) ridges above ~400 m elevation but not on NE-, NW- and SE-striking ridges, (4) the prevailing boulder horizontal displacement azimuth was 250 ± 20°, (5) non-displaced boulders with similar morphologies and in close proximity to displaced boulders are observed at all sites, (6) boulder displacement distance has no correlation with displacement azimuth, boulder mass or soil socket depth and has a partial correlation with slope angle, and (7) the co-existence of displaced and non-displaced boulders at proximal (< 1 m spacing) sites suggested that small-scale ground motion variability and/or varying boulder-ground dynamic interactions relating to shallow phenomena such as variability in soil depth, bedrock fracture density and/or microtopography on the bedrock-soil interface. The above observation, together with the general lack of clearly distinguishable boulder impacts on the edges of some major sockets, suggests that some boulders may have been ejected from sockets due to PVAs ≥ 1 g (Iio and Yoshioka, 1992).

### 5.2.15 **What is the relation between coseismic displacement of boulders, the transient peak ground horizontal displacement recorded at the nearby stations, and the permanent post-seismic horizontal ground displacement?**

Coseismically displaced boulders in the Port Hills were only observed on ridges with azimuthal orientations of 000°-015°. These ridges have mainly similar bedrock lithology and elevation; therefore, I concluded that ridge orientation may have played a role in generating the conditions required for boulder dislocation. The prevailing boulder displacement azimuth range (i.e., 250 ± 20°) was subparallel with the NE-SW direction of instrumentally recorded transient peak horizontal ground displacements from the closest strong ground motion

seismographs (Canterbury Ring Laser or CRLZ and Heathcote Valley Primary School or HVSC; Fig. 4.4, Table 4.1). In comparison, the SW boulder displacement azimuth was at high angles to the NW-orientated net permanent horizontal displacements interpolated for the study site from GPS and differential InSAR data (Beavan et al., 2012). In addition, many boulders were observed to have millimetre to centimetre scale gaps between the boulder edge and the formerly flush edge of the soil socket indicating transient, but not necessarily permanent, coseismic boulder displacement. Therefore, I conclude that the boulder displacements should have coseismically occurred around the largest amplitude of the ground velocity (Iio and Yoshioka, 1992) rather than the permanent tectonic deformation. On the other hand, several measured boulder horizontal displacements exceed the maximum instrumentally recorded horizontal displacements by an order of magnitude. I inferred that that the horizontal ground accelerations at the study site should have been enhanced; consistent with other studies on the same phenomenon elsewhere in the world which indicated that topographic amplification may have been important because of the distribution of displaced boulders being concentrated on ridge crests (e.g. Umeda et al., 1987; Iio and Yoshioka, 1992). I suggested that the displacement azimuths of coseismically displaced boulders have the potential to provide insights into the prevailing direction of transient peak ground deformation during major earthquakes in some instances.

### 5.2.16 **Did topography influence the boulder displacement?**

From the above characteristics and the fact that displaced boulders were only observed at elevations > 400 m a.s.l. with the exception of Castle Rock (360-420 m a.s.l.), I used 2D FLAC modelling to investigate whether the topography of the Port Hills may have amplified the shaking response in the Darfield earthquake. I modelled topographic amplification along 2 nearby ridges; one recorded displaced boulders and the other did not. I applied seismic records of the Lyttelton Port Company (LPCC) seismometer for the Darfield and Christchurch earthquakes and records of the CRLZ seismometer for the Darfield earthquake (no data were available from this seismometer for the Christchurch earthquake) into models. The results showed that: (1) amplification of horizontal ground velocity and acceleration at the ridge crest occurs at both sites, with a maximum amplification of around 80% of the ground motion at the base of the hill, (2) the amplification factor varies significantly between seismic inputs, reflecting frequency-dependent response, and (3) amplification of horizontal velocities and accelerations are higher for all seismic inputs at the site with displaced

boulders (Fig. 4.5). It was difficult to determine what specific topographic conditions caused this difference, except that the site with displaced boulders had slightly higher elevation. Field observations and FLAC modelling indicate that both ridge orientation and shape are likely to have amplified ground motions. The rather narrow azimuthal range in ridge orientations with displaced boulders is at a high angle to the seismic wave propagation direction from the Darfield earthquake, which is likely to have amplified incoming seismic waves at these sites.

Based on the available data, I could not prove that the Darfield earthquake PVAs exceeded 1 g. It remains possible that amplified PHAs and ground displacements at the study sites with PVAs < 1 g may have driven boulder displacement through impacts and 'ramping' of boulders against soil sockets and/or other dynamic site effects (Clark, 1972; Newmark, 1973; Bolt and Hansen, 1977; Ohmachi and Midorikawa, 1992). Lack of boulder displacement at the study sites in the Christchurch earthquake, despite generating higher PHAs and PVAs (Table 4.1), highlights some of the challenges in directly inferring earthquake characteristics using displaced boulders. I conclude that the shorter shaking duration of the Christchurch event, differing frequency contents (Fig. 4.6) and different source characteristics were all factors that may have contributed to generating circumstances less favourable to boulder displacement in this earthquake.

### 5.2.17 **Suggestions for future work**

| Suggestions | Details |
|---|---|
| More LiDAR data are required for the areas covered by forest along the Hope Fault | The Taramakau section, and Kelly and Kakapo (its western extent) branch faults of the Hope Fault require more investigations because: (1) this thesis showed that the Kakapo Fault does not join to the Hope Fault at the Hurunui Valley, whereas it is subparallel to the trace of the Hope Fault and traverses the mountain flank to the south of the Hurunui Valley before it becomes concealed by the beech forest to the west, (2) surface slip and paleoseismic data are unavailable for those faults due to being inaccessible/hard to access and (3) those segments are all join to the major dextral-slip Alpine Fault so that they should be investigated in terms of segment-to-segment rupture propagation and earthquake triggering. |
| Origin of the features that I interpreted as coseismic normal faults, which are parallel to subparallel to the PSZ and are within $\leq$ 500 m of the PSZ, is an interesting subject to be studied | In this thesis (Chapter 2), I argued that these features are coseismic features (have tectonic origin) rather than being sackungen with earthquake origin (resulted from shaking) or other origins. I suggest paleoseismic trenching on one of those features (e.g., the lower-elevated one near Lodge stream) might provide some information on the actual origin of them. Sag ponds formed behind some of these features are good spots for dating. These off-PSZ records are useful to determine the actual FDZ, when compared with the paleoseismic records from the PSZ. |
| Dating of terraces near MacMillan Stream | This locality could provide a good slip rate estimate for the Hurunui segment. At this site, high-quality displacements were measured using LiDAR data, but surface age data are unavailable. |
| Dating of the triangular peat swamp formed at the Macs Knob area | I presume this locality can provide a good slip rate estimate for the Hurunui segment. At this site, high-quality displacements were measured using LiDAR data, but surface ages are poorly constrained |
| Paleoseismic data are required from the stepover and bend area between the Hope River and Hurunui segments | A large basin has formed behind the fault trace at this area. Paleoseismic trenching or augering into this basin could provide good information on the rupture history of the Hurunui and Hope River segment, when compared with other available paleoseismic data from this study and previous studies. |
| Paleoseismic data are required from the Parakeet Stream site | In this thesis, I provided off-fault data from this site. I suggest paleoseismic trenching across the fault on the young terrace to the west of the Parakeet Stream could supply more information on the rupture length of the 1888 earthquake. |

# REFERENCES


Alloway, B.V., Lowe, D.J., Barrell, D.J., Newnham, R.M., Almond, P.C., Augustinus, P.C., Bertler, N.A., Carter, L., Litchfield, N.J., McGlone, M.S., 2007. Towards a climate event stratigraphy for New Zealand over the past 30000 years (NZ-INTIMATE project). Journal of Quaternary Science 22, 9-35.

Amos, C.B., Kelson, K.I., Rood, D.H., Simpson, D.T., Rose, R.S., 2010. Late quaternary slip rate on the Kern Canyon fault at Soda Spring, Tulare County, California. Lithosphere 2, 411-417.

Arrowsmith, J.R., Zielke, O., 2009. Tectonic geomorphology of the San Andreas Fault zone from high resolution topography: An example from the Cholame segment. Geomorphology 113, 70-81.

Aydin, A., Schultz, R.A., 1990. Effect of mechanical interaction on the development of strike-slip faults with echelon patterns. Journal of Structural Geology 12, 123-129.

Azzaro, R., Branca, S., Gwinner, K., Coltelli, M., 2012. The volcano-tectonic map of Etna volcano, 1:100.000 scale: An integrated approach based on a morphotectonic analysis from high-resolution DEM constrained by geologic, active faulting and seismotectonic data. Italian Journal of Geosciences 131, 153-170.

Barka, A., 1996. Slip distribution along the North Anatolian fault associated with the large earthquakes of the period 1939 to 1967. Bulletin of the Seismological Society of America 86, 1238-1254.

Barka, A.A., Kadinsky-Cade, K., 1988. Strike-slip fault geometry in Turkey and its influence on earthquake activity. Tectonics 7, 663-684.

Barka, A., Akyüz, H.S., Altunel, E., Sunal, G., Çakir, Z., Dikbas, A., Yerli, B., Armijo, R., Meyer, B., De Chabalier, J.B., Rockwell, T., Dolan, J.R., Hartleb, R., Dawson, T., Christofferson, S., Tucker, A., Fumal, T., Langridge, R., Stenner, H., Lettis, W., Bachhuber, J., Page, W., 2002. The surface rupture and slip distribution of the 17 August 1999 İzmit earthquake (M 7.4), North Anatolian fault. Bulletin of the Seismological Society of America 92, 43-60.

Barrell, D.J.A., Townsend, D.B., 2012. General distribution and characteristics of active faults and folds in the Hurunui District, North Canterbury GNS Science Consultancy Report 2012/113, 45p.

Barth, N.C., 2013. A tectono-geomorphic study of the Alpine Fault, New Zealand, Geological Sciences. University of Otago, Dunedin, p. 319.

Barth, N.C., Kulhanek, D.K., Beu, A.G., Murray-Wallace, C.V., Hayward, B.W., Mildenhall, D.C., Lee, D.E., 2014. New c. 270 kyr strike-slip and uplift rates for the southern Alpine Fault and implications for the New Zealand plate boundary. Journal of Structural Geology 64, 39-52.

Barth, N.C., Toy, V.G., Langridge, R.M., Norris, R.J., 2012. Scale dependence of oblique plate-boundary partitioning: New insights from LiDAR, central Alpine fault, New Zealand. Lithosphere doi: 10.1130/L201.1.

Beauprêtre, S., Garambois, S., Manighetti, I., Malavieille, J., Sénéchal, G., Chatton, M., Davies, T., Larroque, C., Rousset, D., Cotte, N., Romano, C., 2012. Finding the buried record of past earthquakes with GPR-based palaeoseismology: a case study on the Hope fault, New Zealand. Geophysical Journal International 189, 73-100.

Beavan, J., Fielding, E., Motagh, M., Samsonov, S., Donnelly, N., 2011. Fault location and slip distribution of the 22 February 2011 Mw 6.2 Christchurch, New Zealand, earthquake from geodetic data. Seismological Research Letters 82, 789-799.

Beavan, J., Motagh, M., Fielding, E.J., Donnelly, N., Collett, D., 2012. Fault slip models of the 2010–2011 Canterbury, New Zealand, earthquakes from geodetic data and observations of postseismic ground deformation. New Zeal J Geol Geop 55, 207-221.

Beavan, J., Tregoning, P., Bevis, M., Kato, T., Meertens, C., 2002. Motion and rigidity of the Pacific Plate and implications for plate boundary deformation. Journal of Geophysical Research 107(B10).

Beck, A.C., 1968. Gravity faulting as a mechanism of topographic adjustment. New Zeal J Geol Geop 11, 191-199.

Begg, J.G., Mouslopoulou, V., 2010. Analysis of late Holocene faulting within an active rift using lidar, Taupo Rift, New Zealand. Journal of Volcanology and Geothermal Research 190, 152-167.

Benson, A.M., Little, T.A., Van Dissen, R.J., Hill, N., Townsend, D.B., 2001. Late Quaternary paleoseismic history and surface rupture characteristics of the Eastern Awatere strike-slip fault, New Zealand. Bulletin of the Geological Society of America 113, 1079-1091.

Ben-Zion, Y., Andrews, D.J., 1998, Properties and Implications of Dynamic Rupture Along a Material Interface, Bull. Seismol., Soc. Am. 88, 1085–1094.

Ben-Zion, Y., Rice, J.R., 1995. Slip patterns and earthquake populations along different classes of faults in elastic solids. Journal of Geophysical Research: Solid Earth 100, 12959-12983.

Berryman, K.R., 1984. Late Quaternary tectonics of New Zealand in: an introduction to the recent crustal movements of New Zealand. The Royal Society of New Zealand Miscellaneous series 7, 91-107.

Berryman, K., Beanland, S., 1991. Variation in fault behaviour in different tectonic provinces of New Zealand. Journal of Strutural Geology 13, 177-189.

Berryman, K.R., Beanland, S., Cooper, A.F., Cutten, H.N., Norris, R.J., Wood, P.R., 1992. The Alpine Fault, New Zealand: variation in Quaternary structural style and geomorphic expression. Annales Tectonicae 6, 126-163.

Berryman, K.R., Cochran, U.A., Clark, K.J., Biasi, G.P., Langridge, R.M., Villamor, P., 2012. Major Earthquakes Occur Regularly on an Isolated Plate Boundary Fault. Science 336, 1690-1693.

Berryman, K.R., Rattenbury, M., Isaac, M., Villamor, P., Van Dissen, R., 2003. Active faulting and strain at the junction of the Alpine and Hope faults, New Zealand Geological Society of New Zealand Miscellaneous Publication 116A, 18.

Biasi, G.P., Weldon, R.J., 1994. Quantitative Refinement of Calibrated 14C Distributions. Quaternary Research 41, 1-18.

Biasi, G.P., Weldon, R.J., 2009. San Andreas Fault Rupture Scenarios from Multiple Paleoseismic Records: Stringing Pearls. Bulletin of the Seismological Society of America 99, 471-498.

Biasi, G.P., Weldon, R.J., Fumal, T.E., Seitz, G.G., 2002. Paleoseismic Event Dating and the Conditional Probability of Large Earthquakes on the Southern San Andreas Fault, California. Bulletin of the Seismological Society of America 92, 2761-2781.

Binet, R., Bollinger, L., 2005. Horizontal coseismic deformation of the 2003 Bam (Iran) earthquake measured from SPOT-5 THR satellite imagery. Geophysical Research Letters 32, L02307.

Bolt, B.A., Hansen, R.A., 1977. The upthrow of objects in earthquakes. Bulletin of the Seismological Society of America 67, 1415-1427.

Bouchon, M., Gaffet, S., Cornou, C., Dietrich, M., Glot, J.P., Courboulex, F., Caserta, A., Cultrera, G., Marra, F., Guiguet, R., 2000. Observations of vertical ground accelerations exceeding gravity during the 1997 Umbria-Marche (central Italy) earthquakes. Journal of Seismology 4, 517-532.

Bowen, F.E., 1964. Sheet 15- Buller. Geological Map of New Zealand 1:250000, Wellington, New Zealand, Department of Scientific and Research.

Bronk Ramsey, C., 2013. OxCal Program, v. 4. 1. 7. Oxford, UK, Radiocarbon Accelerator Unit, University of Oxford, https://c14.arch.ox.ac.uk/oxcal.html. Last ac-cessed on 7/30/12.

Browne, G.H., 1987. Geological comments on the Lake Sumner-Harper Pass area, Southern Alps. Immediate Report, New Zealand Geological Survey, Christchurch.

Browne, G.H., 1992. The northeastern portion of the Clarence Fault: Tectonic implications for the late Neogene evolution of Marlborough, New Zealand. New Zeal J Geol Geop 35, 437-445.

Burbank, D.W., Anderson, R.S., 2006. Tectonic Geomorphology, in: 5 (Ed.). Blackwell Science Ltd, p. 304.

Burrows, C., 1988. Late Otiran and early Aranuian radiocarbon dates from South Island localities. New Zealand natural sciences 15.

Carne, R.C., Little, T.A., 2012. Geometry and scale of fault segmentation and deformational bulging along an active oblique-slip fault (Wairarapa fault, New Zealand). Bulletin of the Geological Society of America 124, 1365-1381.

Casas, A.M., Gapais, D., Nalpas, T., Besnard, K., Román-Berdiel, T., 2001. Analogue models of transpressive systems. Journal of Structural Geology 23, 733-743.

Chan, Y.C., Chen, Y.G., Shih, T.Y., Huang, C., 2007. Characterizing the Hsincheng active fault in northern Taiwan using airborne LiDAR data: Detailed geomorphic features and their structural implications. Journal of Asian Earth Sciences 31, 303-316.

Clark, W.K., 1972. Intensity of shaking estimated from displaced stones. USGS professional paper 787, 175-182.

Clark, K.J., Cochran, U.A., Berryman, K.R., Biasi, G., Langridge, R., Villamor, P., Bartholomew, T., Litchfield, N., Pantosti, D., Marco, S., Van Dissen, R., Turner, G., Hemphill-Haley, M., 2013. Deriving a long paleoseismic record from a shallow-water Holocene basin next to the Alpine fault, New Zealand. Bulletin of the Geological Society of America 125, 811-832.

Clayton, L.S., 1965. Late Pleistocene Geology of the Waiau Valley, North Canterbury, New Zealand. University of Illinois, Urbann, p. 91.

Clayton, L.S., 1966. Tectonic depressions along the hope fault, a transcurrent fault in North Canterbury, New Zealand. New Zeal J Geol Geop 9, 95-104.

Clayton, L., 1968. Late Pleistocene glaciations of the Waiau valleys, north Canterbury. New Zeal J Geol Geop 11, 753-767.

Cowan, H.A., 1989. An evaluation of the late Quaternary displacements and seismic hazard assocciated with the Hope and Kakapou faults, Amuri District, North canterbury, Geological Sciences. University of Canterbury, Christchurch, p. 239.

Cowan, H.A., 1990. Late Quaternary displacements on the Hope Fault at Glynn Wye, North Canterbury. New Zealand Journal of Geology & Geophysics 33, 285-293.

Cowan, H.A., 1991. The North Canterbury earthquake of September 1, 1888. Journal of the Royal Society of New Zealand 21, 1-12.

Cowan, H.A., McGlone, M.S., 1991. Late Holocene displacements and characteristic earthquakes on the Hope River segment of the Hope Fault, New Zealand. Journal of the Royal Society of New Zealand 21, 373-384.

Cowan, H., Nicol, A., Tonkin, P., 1996. A comparison of historical and paleoseismicity in a newly formed fault zone and a mature fault zone, North Canterbury, New Zealand. Journal of Geophysical Research B: Solid Earth 101, 6021-6036.

Cowgill, E., Gold, R.D., Xuanhua, C., Xiao-Feng, W., Arrowsmith, J.R., Southon, J., 2009. Low Quaternary slip rate reconciles geodetic and geologic rates along the Altyn Tagh fault, northwestern Tibet. Geology 37, 647-650.

Cowie, P.A., Roberts, G.P., 2001. Constraining slip rates and spacings for active normal faults. Journal of Structural Geology 23, 1901-1915.

Cowie, P.A., Roberts, G.P., Bull, J.M., Visini, F., 2012. Relationships between fault geometry, slip rate variability and earthquake recurrence in extensional settings. Geophysical Journal International 189, 143-160.

Cunningham, W.D., Mann, P., 2007. Tectonics of strike-slip restraining and releasing bends. Geological society, London, Special publications 290, 1-12.

DeMets, C., Gordon, R.G., Argus, D.F., Stein, S., 1994. Effect of recent revisions to the geomagnetic reversal time scale on estimates of current plate motions. Geophysical Research Letters 21, 2191-2194.

DeMets, C., Gordon, R.G., Argus, D.F., 2010. Geologically current plate motions. Geophysical Journal International 181, 1-80.

Der Woerd, J.V., Tapponnier, P., J. Ryerson, F., Meriaux, A.-S., Meyer, B., Gaudemer, Y., Finkel, R.C., Caffee, M.W., Guoguan, Z., Zhiqin, X., 2002. Uniform postglacial slip-rate along the central 600 km of the Kunlun Fault (Tibet), from 26Al, 10Be, and 14C dating of riser offsets, and climatic origin of the regional morphology. Geophysical Journal International 148, 356-388.

Dolan, J.F., Haravitch, B.D., 2014. How well do surface slip measurements track slip at depth in large strike-slip earthquakes? The importance of fault structural maturity in controlling on-fault slip versus off-fault surface deformation. Earth and Planetary Science Letters 388, 38-47.

Dor, O., Rockwell, T., Ben-Zion, Y., 2006. Geological Observations of Damage Asymmetry in the Structure of the San Jacinto, San Andreas and Punchbowl Faults in Southern California: A Possible Indicator for Preferred Rupture Propagation Direction. Pure and Applied Geophysics 163, 301-349.

Dor, O., Yildirim, C., Rockwell, T.K., Ben-Zion, Y., Emre, O., Sisk, M., Duman, T.Y., 2008. Geological and geomorphologic asymmetry across the rupture zones of the 1943 and 1944 earthquakes on the North Anatolian Fault: possible signals for preferred earthquake propagation direction. Geophysical Journal International 173, 483-504.

Dorsey, R.J., 2002. Stratigraphic record of Pleistocene initiation and slip on the Coyote Creek fault, Lower Coyote Creek, southern California. Geological Society of America Special Paper 365, 251-269.

Duffy, B., Quigley, M., Barrell, D.J.A., Van Dissen, R., Stahl, T., Leprince, S., McInnes, C., Bilderback, E., 2013. Fault kinematics and surface deformation across a releasing bend during the 2010 MW 7.1 Darfield, New Zealand, earthquake revealed by differential LiDAR and cadastral surveying. Bulletin of the Geological Society of America 125, 420-431.

Elliott, A.J., Dolan, J.F., Oglesby, D.D., 2009. Evidence from coseismic slip gradients for dynamic control on rupture propagation and arrest through stepovers. Journal of Geophysical Research: Solid Earth 114, B02313.

Eusden, J.D., Pettinga, J.R., Campbell, J.K., 2000. Structural evolution and landscape development of a collapsed transpressive duplex on the Hope Fault, North Canterbury, New Zealand. New Zeal J Geol Geop 43, 391-404.

Eusden, J.D., Pettinga, J.R., Campbell, J.K., 2005. Structural collapse of a transpressive hanging-wall fault wedge, Charwell region of the Hope Fault, South Island, New Zealand. New Zeal J Geol Geop 48, 295-309.

Freund, R., 1971. The Hope Fault: A strike-slip fault in New Zealand. New Zealand Geological Survey Bulletin 86, 49p.

Fumal, T.E., Weldon, R.J., Biasi, G.P., Dawson, T.E., Seitz, G.G., Frost, W.T., Schwartz, D.P., 2002. Evidence for large earthquakes on the San Andreas fault at the Wrightwood, California paleoseismic site: A.D. 500 to present. Bulletin of the Seismological Society of America 92, 2726-2760.

Gledhill, K., Ristau, J., Reyners, M., Fry, B., Holden, C., 2011. The Darfield (Canterbury, New Zealand) MW 7.1 earthquake of September 2010: A preliminary seismological report. Seismological Research Letters 82, 378-386.

Gold, R.D., Cowgill, E., Arrowsmith, J.R., Chen, X., Sharp, W.D., Cooper, K.M., Wang, X.-F., 2011. Faulted terrace risers place new constraints on the late Quaternary slip rate for the central Altyn Tagh fault, northwest Tibet. Geological Society of America Bulletin 123, 958-978.

Gold, R.D., Stephenson, W.J., Odum, J.K., Briggs, R.W., Crone, A.J., Angster, S.J., 2013. Concealed Quaternary strike-slip fault resolved with airborne lidar and seismic reflection: The Grizzly Valley fault system, northern Walker Lane, California. Journal of Geophysical Research: Solid Earth 118, 3753-3766.

Grant, L.B., Sieh, K., 1994. Paleoseismic evidence of clustered earthquakes on the San Andreas Fault in the Carrizo Plain, California. Journal of Geophysical Research: Solid Earth 99, 6819-6841.

Graymer, R. W., Langenheim, V. E., Simpson, R. W., Jachens, R. C., & Ponce, D. A., 2007. Relatively simple through-going fault planes at large-earthquake depth may be concealed by the surface complexity of strike-slip faults. Geological Society, London, Special Publications, 290(1), 189-201.

Gregg, D.R., 1964. Sheet 18- Hurunui. Geological Map of New Zealand 1:250000, Wellington, New Zealand, Department of Scientific and Industrial Research.

Haddad, D.E., Akçiz, S.O., Arrowsmith, J.R., Rhodes, D.D., Oldow, J.S., Zielke, O., Toké, N.A., Haddad, A.G., Mauer, J., Shilpakar, P., 2012. Applications of airborne and terrestrial laser scanning to paleoseismology. Geosphere 8, 771-786.

Haeussler, P.J., Schwartz, D.P., Dawson, T.E., Stenner, H.D., Lienkaemper, J.J., Sherrod, B., Cinti, F.R., Montone, P., Craw, P.A., Crone, A.J., Personius, S.F., 2004. Surface Rupture and Slip Distribution of the Denali and Totschunda Faults in the 3 November 2002 M 7.9 Earthquake, Alaska. Bulletin of the Seismological Society of America 94, S23-S52.

Hancox, G., Massey, C., Perrin, N.D., 2011. Landslides and related ground damage caused by the Mw 6.3 Christchurch earthquake of 22 February 2011. New Zealand Geomechanics News 81, 53-65.

Hanks, T.C., Kanamori, H., 1979. Fault mechanics. Journal of Geophysical Research B: Solid Earth 84, 2145.

Hardy, E.F., Wellman, H.W., 1984. The Alpine, Wairau, and Hope Faults. University of Wellington Geology Department Publication 27.

Harris, R.A., Simpson, R.W., 1998. Suppression of large earthquakes by stress shadows: A comparison of Coulomb and rate-and-state failure. Journal of Geophysical Research: Solid Earth 103, 24439-24451.

Hartleb, R.D., Dolan, J.F., Akyüz, H.S., Dawson, T.E., Tucker, A.Z., Yerli, B., Rockwell, T.K., Toraman, E., Çakir, Z., Dikbaş, A., Altunel, E., 2002. Surface Rupture and Slip Distribution along the Karadere Segment of the 17 August 1999 İzmit and the Western Section of the 12 November 1999 Düzce, Turkey, Earthquakes. Bulletin of the Seismological Society of America 92, 67-78.

Hartleb, R.D., Dolan, J.F., Akyüz, H.S., Yerli, B., 2003. A 2000-Year-Long Paleoseismologic Record of Earthquakes along the Central North Anatolian Fault, from Trenches at Alayurt, Turkey: Bulletin of the Seismological Society of America 93, 1935-1954.

Hartleb, R.D., Dolan, J.F., Kozaci, Ö., Akyüz, H.S., Seitz, G.G., 2006. A 2500-yr-long paleoseismologic record of large, infrequent earthquakes on the North Anatolian fault at Çukurçimen, Turkey. Geological Society of America Bulletin 118, 823-840.

Holt, R.A., Savage, M.K., Townend, J., Syracuse, E.M., Thurber, C.H., 2013. Crustal stress and fault strength in the Canterbury Plains, New Zealand. Earth and Planetary Science Letters 383, 173-181.

Honegger, D.G., Nyman, D.J., Johnson, E.R., Cluff, L.S., Sorensen, S.P., 2004. Trans-Alaska Pipeline System Performance in the 2002 Denali Fault, Alaska, Earthquake. Earthquake Spectra 20, 707-738.

Hornblow, S., Quigley, M., Nicol, A., Van Dissen, R., Wang, N., 2014. Paleoseismology of the 2010 Mw 7.1 Darfield (Canterbury) earthquake source, Greendale Fault, New Zealand. Tectonophysics 637, 178-190.

Howarth, J.D., Fitzsimons, S.J., Norris, R.J., Jacobsen, G.E., 2014. Lake sediments record high intensity shaking that provides insight into the location and rupture length of large

earthquakes on the Alpine Fault, New Zealand. Earth and Planetary Science Letters 403, 340-351.

Hreinsdóttir, S., Freymueller, J.T., Bürgmann, R., Mitchell, J., 2006. Coseismic deformation of the 2002 Denali Fault earthquake: Insights from GPS measurements. Journal of Geophysical Research: Solid Earth 111, B03308.

Iio, Y., Yoshioka, K.B., 1992. Strong Ground Motion in the Source Region of the 1984 Western Nagano Prefecture Earthquake-Inferred from Displaced Boulders. Journal of Physical Earth 40, 407-419.

Jackson, J., Bouchon, M., Fielding, E., Funning, G., Ghorashi, M., Hatzfeld, D., Nazari, H., Parsons, B., Priestley, K., Talebian, M., Tatar, M., Walker, R., Wright, T., 2006. Seismotectonic, rupture process, and earthquake-hazard aspects of the 2003 December 26 Bam, Iran, earthquake. Geophysical Journal International 166, 1270-1292.

Jones, E., 1933. Autobiography of an early setteler in New Zealand. Coulls Somerville Wilkie Ltd, Wellington.

Joussineau, G., Aydin, A., 2009. Segmentation along Strike-Slip Faults Revisited. Pure and Applied Geophysics 166, 1575-1594.

Kendrick, K.J., Matti, J.C., Mahan, S.A., 2015. Late Quaternary slip history of the Mill Creek strand of the San Andreas fault in San Gorgonio Pass, southern California: The role of a subsidiary left-lateral fault in strand switching. Geological Society of America Bulletin 127, 825-849.

Khajavi, N., 2015. Surface rupture morphology and paleoseismology of the western Hope Fault and characteristics of seismically-displaced boulders in the Port Hills, South Island, New Zealand, Geological Sciences. University of Canterbury, Christchurch.

Khajavi, N., Quigley, M., Langridge, R.M., 2014. Influence of topography and basement depth on surface rupture morphology revealed from LiDAR and field mapping, Hope Fault, New Zealand. Tectonophysics 630, 265-284.

Khajavi, N., Langridge, R., Quigley, M., Smart, C., Rezanejad, A., Martín-González, F., (accepted manuscript). Late Holocene rupture behaviour and earthquake chronology on the Hope Fault, New Zealand. Geological Society of America Bulletin.

Khajavi, N., Langridge, R., Quigley, M., 2012. New insights into the rupture history of the Hope fault, New Zealand, AGU Fall Meeting Abstracts, p. 03.

Kim, Y.S., Peacock, D.C.P., Sanderson, D.J., 2004. Fault damage zones. Journal of Structural Geology 26, 503-517.

Knuepfer, P.L.K., 1984. Tectonic Geomorphology and present-day tectonics of the Alpine shear system, South Island, New Zealand (Neotectonics, Faults).

Knuepfer, P.L.K., 1988. Estimating ages of late Quaternary stream terraces from analysis of weathering rinds and soils. Geological Society of America Bulletin 100, 1224-1236.

Knuepfer, P.L.K., 1992. Temporal variations in latest Quaternary slip across the Australian-Pacific plate boundary, northeastern South Island, New Zealand. Tectonics 11, 449-464.

Kozaci, Ö., Dolan, J., Finkel, R., Hartleb, R., 2007. Late Holocene slip rate for the North Anatolian fault, Turkey, from cosmogenic 36Cl geochronology: Implications for the constancy of fault loading and strain release rates. Geology 35, 867-870.

Langridge, R., 2004. How is tectonic slip partitioned from the Alpine Fault to the Marlborough Fault System?-Results from the Hope Fault. Institute of Geological & Nuclear Sciences Science Report 2004/32, 18 p.

Langridge, R.M., Berryman, K.R., 2005. Morphology and slip rate of the Hurunui section of the Hope Fault, South Island, New Zealand. New Zeal J Geol Geop 48, 43-57.

Langridge, R., Campbell, J., Hill, N., Pere, V., Pope, J., Pettinga, J., Estrada, B., Berryman, K., 2003. Paleoseismology and slip rate of the Conway Segment of the Hope Fault at Greenburn Stream, South Island, New Zealand. Ann Geophys-Italy 46, 1119-1140.

Langridge, R., Duncan, R., Almond, P., 2007. Indicators of recent paleoseismic activity along the western Hope Fault GNS Science Consultancy Report 2006/151, 99p.+appendices.

Langridge, R.M., Almond, P.C., Duncan, R.P., 2013. Timing of late Holocene paleoearthquakes on the Hurunui segment of the Hope fault: Implications for plate boundary strain release through South Island, New Zealand. Geological Society of America Bulletin 125, 756-775.

Langridge, R.M., Ries, W.F., Farrier, T., Barth, N.C., Khajavi, N., De Pascale, G.D., 2014. Developing sub 5-m LiDAR DEMs for forested sections of the Alpine and Hope faults, South Island, New Zealand: Implications for structural interpretations Journal of Structural geology 64, 53-66.

Langridge, R.M., Stenner, H.D., Fumal, T.E., Christofferson, S.A., Rockwell, T.K., Hartleb, R.D., Bachhuber, J., Barka, A.A., 2002. Geometry, Slip Distribution, and Kinematics of Surface Rupture on the Sakarya Fault Segment during the 17 August 1999 İzmit, Turkey, Earthquake. Bulletin of the Seismological Society of America 92, 107-125.

Langridge, R.M., Villamor, P., Basili, R., Almond, P., Martinez-Diaz, J.J., Canora, C., 2010. Revised slip rates for the Alpine fault at Inchbonnie: Implications for plate boundary kinematics of South Island, New Zealand. Lithosphere 2, 139-152.

Lensen, G.J., 1962. Sheet 16- Kaikoura. Geological Map of New Zealand 1:250000, Wellington, New Zealand, Department of Scientific and Indestrial Research.

Leonard, M., (2010). Earthquake fault scaling: Self-consistent relating of rupture length, width, average displacement, and moment release. Bulletin of the Seismological Society of America100, 1971-1988.

Li, Y.-G., Vidale, J.E., Day, S.M., Oglesby, D.D., Cochran, E., 2003. Postseismic Fault Healing on the Rupture Zone of the 1999 M 7.1 Hector Mine, California, Earthquake. Bulletin of the Seismological Society of America 93, 854-869.

Li, Z., Bruhn, R.L., Pavlis, T.L., Vorkink, M., Zeng, Z., 2010. Origin of sackung uphill-facing scarps in the Saint Elias orogen, Alaska: LIDAR data visualization and stress modeling. Bulletin of the Geological Society of America 122, 1585-1589.

Lienkaemper, J.J., 2001. 1857 slip on the San Andreas fault Southeast of Cholame, California. Bulletin of the Seismological Society of America 91, 1659-1672.

Lienkaemper, J.J., Ramsey, C.B., 2009. OxCal: Versatile Tool for Developing Paleoearthquake Chronologies- A Primer. Seismological Research letters 80, 431-434.

Lin, A., Kikuchi, M., Fu, B., 2003. Rupture Segmentation and Process of the 2001 Mw 7.8 Central Kunlun, China, Earthquake. Bulletin of the Seismological Society of America 93, 2477-2492.

Lin, A., Ren, Z., Jia, D., Wu, X., 2009. Co-seismic thrusting rupture and slip distribution produced by the 2008 Mw 7.9 Wenchuan earthquake, China. Tectonophysics 471, 203-215.

Lin, A., Rao, G., Yan, B., 2012. Field evidence of rupture of the Qingchuan Fault during the 2008 Mw7.9 Wenchuan earthquake, northeastern segment of the Longmen Shan Thrust Belt, China. Tectonophysics 522–523, 243-252.

Little, T.A., 1996. Faulting-related displacement gradients and strain adjacent to the Awatere strike-slip fault in New Zealand. Journal of Structural Geology 18, 321-340.

Little, T.A., Jones, A., 1998. Seven million years of strike-slip and related off-fault deformation, northeastern Marlborough fault system, South Island, New Zealand. Tectonics 17, 285-302.

Liu, L., Zoback, M.D., 1992. The effect of topography on the state of stress in the crust: Application to the site of the Cajon Pass Scientific Drilling Project. Journal of Geophysical Research: Solid Earth 97, 5095-5108.

Lunina, O.V., Gladkov, A.S., Novikov, I.S., Agatova, A.R., Vysotskii, E.M., Emanov, A.A., 2008. Geometry of the fault zone of the 2003 Ms=7.5 Chuya earthquake and associated stress fields, Gorny Altai. Tectonophysics 453, 276-294.

Manighetti, I., Perrin, C., Dominguez, S., Garambois, S., Gaudemer, Y., Malavieille, J., Matteo, L., Delor, E., Vitard, C., Beauprêtre, S., 2015. Recovering paleoearthquake slip record in a highly dynamic alluvial and tectonic region (Hope fault, New Zealand) from airborne LiDAR. Journal of Geophysical Research: Solid Earth 120, 4484-4509.

Mason, B., 1958. The intrusive rocks of the Kaikoura Mountains, Marlborough, New Zealand, Transactions of the Royal Society of New Zealand, pp. 247-262.

Mason, D.P., Little, T.A., Van Dissen, R.J., 2006. Rates of active faulting during late Quaternary fluvial terrace formation at Saxton River, Awatere fault, New Zealand. Geological Society of America Bulletin 118, 1431-1446.

Martel, S.J., Pollard, D.D., Segall, P., 1988. Development of simple strike-slip fault zones, Mount Abbot quadrangle, Sierra Nevada, California. Bulletin of the Geological Society of America 100, 1451-1465.

McCalpin, J.P., 2003. Criteria for determining the seismic significance of sackungen and other scarplike landforms in mountainous regions, in: Hart, E.W. (Ed.), Ridge-Top Spreading in California: California Geological Survey, Open-File Report, 1CD-ROM.

McCalpin, J. P., 2009. Paleoseismology, 2ed. Elsevier Science, Burlington.

McColl, S.T., Davies, T.R.H., McSaveney, M.J., 2012. The effect of glaciation on the intensity of seismic ground motion. Earth Surface Processes and Landforms 37, 1290-1301.

McKay, A., 1890. On the earthquakes of September 1888 in the Amuri and Marlborough Districts of the South Island. New Zealand Geological Survey Report of Geological Explorations 20, 1-16.

McKay, A., 1902. Report on the recent seismic disturbances within Cheviot County in northern Canterbury and the Amuri District of Nelson, New Zealand (November and December, 1901). Govt. Printer, Wellington [N.Z.].

McMorran, T.J., 1991. The Hope Fault at Hossack Station east of Hanmer Basin, North Canterbury, Geological Sciences. University of Canterbury, Christchrch, p. 93.

McTigue, D.F., Mei, C.C., 1981. Gravity-induced stresses near topography of small slope. Journal of Geophysical Research 86, 9268-9278.

McTigue, D.F., Stein, R.S., 1984. Topographic amplification of tectonic displacement: implications for geodetic measurement of strain changes. Journal of Geophysical Research 89, 1123-1131.

Murata, A., Takemura, K., Miyata, T., Lin, A., 2001. Quaternary vertical offset and average slip rate of the Nojima Fault on Awaji Island, Japan. Island Arc 10, 360-367.

Nathan, S., Rattenbury, M.R., Suggate, R.P., 2002. Geology of the Greymouth area: scale 1:250,000. Lower Hutt: Institute of Geological & Nuclear Sciences. Institute of Geological & Nuclear Sciences 1:250,000 geological map 12. 58 p. + 1 folded map + 65 p.

Newmark, N.M., 1973. Interpretation of apparent upthrow of objects in earthquakes. Proceedings of the fifth world conference on earthquake engineering, paper no. 294, 2338-2343.

Nicol, A., Langridge, R., Van Dissen, R. 2011. Wairau Fault Late Quaternary displacements and paleoearthquakes. In: Lee, J.M. (ed). Field Trip Guides, Geosciences 2011

Conference, Nelson, New Zealand. Geoscience Society of New Zealand Miscellaneous Publication 130B. 33 p.

Nicol, A., Robinson, R., Van Dissen, R., Harvison, A., (in review). variability of recurrence interval and single-event slip for surface-rupturing earthquakes in New Zealand. Bulletin of the Seismological Society of America.

Nicol, A., Van Dissen, R., 2002. Up-dip partitioning of displacement components on the oblique-slip Clarence Fault, New Zealand. Journal of Structural Geology 24, 1521-1535.

Nicol, A., Wise, D.U., 1992. Paleostress adjacent to the Alpine Fault of New Zealand: fault, vein, and styolite data from the Doctors Dome area. Journal of Geophysical Research 97, 17,685-617,692.

Nicol, A., VanDissen, R., Vella, P., Alloway, B., Melhuish, A., 2002. Growth of contractional structures during the last 10 m.y. at the southern end of the emergent Hikurangi forearc basin, New Zealand. New Zeal J Geol Geop 45, 365-385.

Ninis, D., Little, T.A., Van Dissen, R.J., Litchfield, N.J., Smith, E.G., Wang, N., Rieser, U., Henderson, C.M., 2013. Slip rate on the Wellington fault, New Zealand, during the late Quaternary: Evidence for variable slip during the Holocene. Bulletin of the Seismological Society of America 103, 559-579.

Nissen, E., Krishnan, A.K., Arrowsmith, J.R., Saripalli, S., 2012. Three-dimensional surface displacements and rotations from differencing pre-and post-earthquake LiDAR point clouds. Geophysical Research Letters 39.

Norris, R.J., Cooper, A.F., 1995. Origin of small-scale segmentation and transpressional thrusting along the Alpine fault, New Zealand. Geological Society of America Bulletin 107, 231-240.

Norris, R.J., Cooper, A.F., 1997. Erosional control on the structural evolution of a transpressional thrust complex on the Alpine Fault, New Zealand. Journal of Structural Geology 19, 1323-1342.

Norris, R.J., Cooper, A.F., 2001. Late Quaternary slip rates and slip partitioning on the Alpine Fault, New Zealand. Journal of Structural Geology 23, 507-520.

Oglesby, D.D., 2005. The Dynamics of Strike-Slip Step-Overs with Linking Dip-Slip Faults. Bulletin of the Seismological Society of America 95, 1604-1622.

Ohmachi, T., Midorikawa, S., 1992. Ground-motion intensity inferred from upthrow of boulders during the 1984 Western Nagano Prefecture, Japan, earthquake. Bulletin of the Seismological Society of America 82, 44-60.

Oldham, R.D., 1899. Report on the great earthquake of 12 June 1897, Memories of the Geological Survey of India, Report No. 29, 1379 p.

Oskin, M.E., Arrowsmith, J.R., Corona, A.H., Elliott, A.J., Fletcher, J.M., Fielding, E.J., Gold, P.O., Garcia, J.J.G., Hudnut, K.W., Liu-Zeng, J., Teran, O.J., 2012. Near-Field Deformation from the El Mayor–Cucapah Earthquake Revealed by Differential LIDAR. Science 335, 702-705.

Oskin, M., Perg, L., Shelef, E., Strane, M., Gurney, E., Singer, B., Zhang, X., 2008. Elevated shear zone loading rate during an earthquake cluster in eastern California. Geology 36, 507-510.

Petersen, M.D., Wesnousky, S.G., 1994. Fault slip rates and earthquake histories for active faults in southern California. Bulletin of the Seismological Society of America 84, 1608-1649.

Petersen, M.D., Dawson, T.E., Chen, R., Cao, T., Wills, C.J., Schwartz, D.P., Frankel, A.D., 2011. Fault Displacement Hazard for Strike-Slip Faults. Bulletin of the Seismological Society of America 101, 805-825.

Pettinga, J.R., Wise, D.U., 1994. Paleostress adjacent to the Alpine Fault: broader implications from fault analysis near Nelson, South Island, New Zealand. Journal of Geophysical Research 99, 2727-2736.

Pettinga, J.R., Yetton, M.D., Van Dissen, R.J., Downes, G., 2001. Earthquake source identification and characterisation for the Canterbury region, South Island, New Zealand. Bulletin of the New Zealand Society for Earthquake Engineering 34, 282-317.

Polonia, A., Gasperini, L., Amorosi, A., Bonatti, E., Bortoluzzi, G., Çagatay, N., Capotondi, L., Cormier, M.H., Gorur, N., McHugh, C., Seeber, L., 2004. Holocene slip rate of the North Anatolian Fault beneath the Sea of Marmara. Earth and Planetary Science Letters 227, 411-426.

Pucci, S., De Martini, P.M., Pantosti, D., 2008. Preliminary slip rate estimates for the Düzce segment of the North Anatolian Fault Zone from offset geomorphic markers. Geomorphology 97, 538-554.

Quigley, M., Dissen, R.V., Villamor, P., Litchfield, N., Barrell, D., Furlong, K., Stahl, T., Duffy, B., Bilderback, E., Noble, D., Townsend, D., Begg, J., Jongens, R., Ries, W., Claridge, J., Klahn, A., McKenzie, H., Smith, A., Hornblow, S., Nicol, R., Cox, S., Larngridge, R., Pedley, K., 2010. Bulletin of the New Zealand Society for Earthquake Engineering 43, 1-7.

Quigley, M., Litchfield, N., Stahl, T., Noble, D., Jongens, R., Klahn, A., Cox, S., 2010. Surface rupture of the Greendale fault during the Darfield (Canterbury) earthquake, New Zealand: initial findings. Bulletin of the New Zealand Society for Earthquake Engineering, 43(4), 236.

Quigley, M., Van Dissen, R., Litchfield, N., Villamor, P., Duffy, B., Barrell, D., Furlong, K., Stahl, T., Bilderback, E., Noble, D., 2012. Surface rupture during the 2010 Mw 7.1 Darfield (Canterbury) earthquake: Implications for fault rupture dynamics and seismic-hazard analysis. Geology 40, 55-58.

Rattenbury, M.S., Townsend, D., Johnston, M.R., 2006. Geology of the Kaikoura area: scale 1:250,000 geological map. Lower Hutt: GNS Science. Institute of Geological & Nuclear Sciences 1:250,000 geological map 13. 70 p. + 1 folded map

Richard, P., 1991. Experiments on faulting in a two-layer cover sequence overlying a reactivated basement fault with oblique-slip. Journal of Structural Geology 13, 459-469.

Richard, P., Mocquet, B., Cobbold, P.R., 1991. Experiments on simultaneous faulting and folding above a basement wrench fault. Tectonophysics 188, 133-141.

Richard, P.D., Naylor, M.A., Koopman, A., 1995. Experimental models of strike-slip tectonics. Petroleum Geoscience 1, 71-80.

Riedel, W., 1929. Zur mechanik geologischer Brucherscheinungen: Centralbl. Mineral. Geol. u. Pal 1929B, 354-368.

Rittase, W.M., Kirby, E., McDonald, E., Walker, J.D., Gosse, J., Spencer, J.Q., Herrs, A., 2014. Temporal variations in Holocene slip rate along the central Garlock fault, Pilot Knob Valley, California. Lithosphere 6, 48-58.

Rizza, M., Ritz, J.-F., Braucher, R., Vassallo, R., Prentice, C., Mahan, S., McGill, S., Chauvet, A., Marco, S., Todbileg, M., 2011. Slip rate and slip magnitudes of past earthquakes along the Bogd left-lateral strike-slip fault (Mongolia). Geophysical Journal International 186, 897-927.

Rockwell, T.K., Ben-Zion, Y., 2007. High localization of primary slip zones in large earthquakes from paleoseismic trenches: Observations and implications for earthquake physics. Journal of Geophysical Research 112.

Rockwell, T.K., Lindvall, S., Herzberg, M., Murbach, D., Dawson, T., Berger, G., 2000. Paleoseismology of the Johnson Valley, Kickapoo, and Homestead Valley Faults: Clustering of Earthquakes in the Eastern California Shear Zone. Bulletin of the Seismological Society of America 90, 1200-1236.

Sagy, A., Brodsky, E.E., Axen, G.J., 2007. Evolution of fault-surface roughness with slip. Geology 35, 283-286.

Savage, W.Z., Swolfs, H.S., 1986. Tectonic and Gravitational Stress in Long Symmetric Ridges and Valleys. Journal of Geophysical Research 91, 3677-3685.

Savage, W.Z., Swolfs, H.S., Powers, P.S., 1985. Gravitational stresses in long symmetric ridges and valleys. International Journal of Rock Mechanics and Mining Sciences and 22, 291-302.

Scharer, K.M., Salisbury, J.B., Arrowsmith, J.R., Rockwell, T.K., 2014. Southern San Andreas Fault Evaluation Field Activity: Approaches to Measuring Small Geomorphic Offsets—Challenges and Recommendations for Active Fault Studies. Seismological Research Letters 85, 68-76.

Scharer, K.M., Weldon Ii, R.J., Fumal, T.E., Biasi, G.P., 2007. Paleoearthquakes on the southern San Andreas Fault, Wrightwood, California, 3000 to 1500 B.C.: A new method for evaluating paleoseismic evidence and earthquake horizons. Bulletin of the Seismological Society of America 97, 1054-1093.

Scholz, C.H., 1977. Transform fault systems of California and New Zealand: Similarities in their tectonic and seismic styles. Journal of the Geological Society 133, 215-228.

Scholz, C.H., Ando, R., Shaw, B.E., 2010. The mechanics of first order splay faulting: The strike-slip case. Journal of Structural Geology 32, 118-126.

Schulz, S.E., Evans, J.P., 2000. Mesoscopic structure of the Punchbowl Fault, Southern California and the geologic and geophysical structure of active strike-slip faults. Journal of Structural Geology 22, 913-930.

Schwartz, D.P., Haeussler, P.J., Seitz, G.G., Dawson, T.E., 2012. Why the 2002 Denali fault rupture propagated onto the Totschunda fault: Implications for fault branching and seismic hazards. Journal of Geophysical Research: Solid Earth 117, B11304.

Seitz, G., Weldon Ii, R., Biasi, G.P., 1997. The pitman canyon paleoseismic record: A re-evaluation of Southern San Andreas fault segmentation. Journal of Geodynamics 24, 129-138.

Seitz, G.G., Biasi, G.P., Weldon, R.J., 2013. An Improved Paleoseismic Record of the San Andreas Fault at Pitman Canyon, Quaternary Geochronology. American Geophysical Union, pp. 563-566.

Shipton, Z.K., Cowie, P.A., 2001. Damage zone and slip-surface evolution over μm to km scales in high-porosity Navajo sandstone, Utah. Journal of Structural Geology 23, 1825-1844.

Shipton, Z.K., Cowie, P.A., 2003. A conceptual model for the origin of fault damage zone structures in high-porosity sandstone. Journal of Structural Geology 25, 333-344.

Sibson, R.H., 1985. Stopping of earthquake ruptures ar dilational fault jogs. Nature 316, 248-251.

Sibson, R., Ghisetti, F., Ristau, J., 2011. Stress Control of an Evolving Strike-Slip Fault System during the 2010–2011 Canterbury, New Zealand, Earthquake Sequence. Seismological Research Letters 82, 824-832.

Sieh, K.E., 1978. Slip along the San Andreas fault associated with the great 1857 earthquake. Bulletin of the Seismological Society of America 68, 1421-1434,IN1421,1435-1448.

Sieh, K.E., Jahns, R.H., 1984. Holocene activity of the San Andreas fault at Wallace Creek, California. Bulletin of the Geological Society of America 95, 883-896.

Sieh, K., Jones, L., Hauksson, E., Hudnut, K., Eberhart-Phillips, D., Heaton, T., Hough, S., Hutton, K., Kanamori, H., Lilje, A., Lindvall, S., McGill, S.F., Mori, J., Rubin, C., Spotila, J.A., Stock, J., Thio, H.K., Treiman, J., Wernicke, B., Zachariasen, J., 1993.

Near-field investigations of the Landers earthquake sequence, April to July 1992. Science 260, 171-176.

Stahl, T., Winkler, S., Quigley, M., Bebbington, M., Duffy, B., Duke, D., 2013. Schmidt hammer exposure-age dating (SHD) of late Quaternary fluvial terraces in New Zealand. Earth Surface Processes and Landforms 38, 1838-1850.

Stirling, M., Gerstenberger, M., Litchfield, N., McVerry, G., Smith, W., Pettinga, J., Barnes, P., 2008. Seismic hazard of the Canterbury Region, New Zealand: New earthquake source model and methodology. Bulletin of the New Zealand Society for Earthquake Engineering 41, 51-67.

Stirling, M., Goded, T., Berryman, K., Litchfield, N., 2013. Selection of earthquake scaling relationships for seismic-hazard analysis. Bulletin of the Seismological Society of America.

Stirling, M., McVerry, G., Gerstenberger, M., Litchfield, N., Van Dissen, R., Berryman, K., Barnes, P., Wallace, L., Villamor, P., Langridge, R., Lamarche, G., Nodder, S., Reyners, M., Bradley, B., Rhoades, D., Smith, W., Nicol, A., Pettinga, J., Clark, K., Jacobs, K., 2012. National seismic hazard model for New Zealand: 2010 update. Bulletin of the Seismological Society of America 102, 1514-1542.

Stirling, M., Rhoades, D., Berryman, K., 2002. Comparison of earthquake scaling relations derived from data of the instrumental and preinstrumental era. Bulletin of the Seismological Society of America 92, 812-830.

Stirling, M.W., Wesnousky, S.G., Shimazaki, K., 1996. Fault trace complexity, cumulative slip, and the shape of the magnitude-frequency distribution for strike-slip faults: a global survey. Geophysical Journal International 124, 833-868.

Suggate, R.P., 1965. Late Pleistocene geology of the northern part of the South Island, New Zealand. New Zealand Dept. of Scientific and Industrial Research.

Suggate, R.P., Stevens, G.R., Te Punga, M.T., 1978. The Geology of New Zealand. Government Printer, Wellington, 2 vols., 820 pp.

Sylvester, A.G., 1988. Strike-slip faults. Bulletin of the Geological Society of America 100, 1666-1703.

Tchalenko, J.S., 1970. Similarities between shear zones of different magnitudes. Bulletin of the Geological Society of America 81, 1625-1640.

Tchalenko, J.S., Ambraseys, N.N., 1970. Structural Analysis of the Dasht-e Bayaz (Iran) Earthquake Fractures. Bulletin of the Geological Society of America 81, 41-60.

Treiman, J.A., Kendrick, K.J., Bryant, W.A., Rockwell, T.K., McGill, S.F., 2002. Primary Surface Rupture Associated with the Mw 7.1 16 October 1999 Hector Mine Earthquake, San Bernardino County, California. Bulletin of the Seismological Society of America 92, 1171-1191.

Umeda, Y., Kuroiso, A., Ito, K., Muramatu, I., 1987. High accelerations produced by the Western Nagano Prefecture, Japan, earthquake of 1984. Tectonophysics 141, 335-343.

Vallée, M., Satriano, C., 2014. Ten year recurrence time between two major earthquakes affecting the same fault segment. Geophysical Research Letters 41, 2312-2318.

Van Dissen, R., 1989. Late Quaternary faulting in the Kaikoura region, southeastern Marlborough, New Zealand. Unpublished MS thesis, Oregon State University, USA, 72p.

Van Dissen, R., Barrell, D., Litchfield, N., Villamor, P., Quigley, M., King, A., Mote, T., 2011. Surface rupture displacement on the Greendale Fault during the Mw 7.1 Darfield (Canterbury) earthquake, New Zealand, and its impact on man-madestructures.

Van Dissen, R., Hornblow, S., Quigley, M., Litchfield, N., Villamor, P., Nicol, A., Barrell, D.J.A., Sasnett, P., Newton, K., 2013. Towards the development of design curves for characterising distributed strike-slip surface fault rupture displacement: an example from the 4 September, 2010, Greendale Fault rupture, NZ. NZGS Geotechnical Symposium. Ed. CY Chin, Queenstown Proc. 19.

Van Dissen, R., Nicol, A., 2009. Mid-late Holocene paleoseismicity of the eastern Clarence Fault, Marlborough, New Zealand. New Zeal J Geol Geop 52, 195-208.

Van Dissen, R., Yeats, R.S., 1991. Hope Fault, Jordan Thrust, and uplift of the Seaward Kaikoura Range, New Zealand. Geology 19, 393-396.

Villamor, P., Litchfield, N., Barrell, D., Van Dissen, R., Hornblow, S., Quigley, M., Levick, S., Ries, W., Duffy, B., Begg, J., Townsend, D., Stahl, T., Bilderback, E., Noble, D., Furlong, K., Grant, H., 2012. Map of the 2010 Greendale Fault surface rupture, Canterbury, New Zealand: application to land use planning. New Zeal J Geol Geop 55, 223-230.

Wallace, L.M., Beavan, J., McCaffrey, R., Berryman, K., Denys, P., 2007. Balancing the plate motion budget in the South Island, New Zealand using GPS, geological and seismological datas. Geophysical Journal International 168, 332-352.

Wallace, L.M., Barnes, P., Beavan, J., Van Dissen, R., Litchfield, N., Mountjoy, J., Langridge, R., Lamarche, G., Pondard, N., 2012. The kinematics of a transition from subduction to strike-slip: An example from the central New Zealand plate boundary. Journal of Geophysical Research B: Solid Earth 117.

Ward, S.J., 2000. The physical, chemical and mineralogical properties of a fault zone, Geological Sciences. University of Canterbury, Christchurch, p. 169.

Warren, G., 1967. Sheet 17- Hokitika. Geological Map of New Zealand 1: 250000, Wellington, New Zealand, Department of Scientific and Industrial Research.

Weldon, R.J., Fumal, T.E., Biasi, G.P., Scharer, K.M., 2005. Past and Future Earthquakes on the San Andreas Fault. Science 308, 966-967.

Weldon, R.J., Sieh, K.E., 1985. Holocene rate of slip and tentative recurrence interval for large earthquakes on the San Andreas fault, Cajon Pass, southern California. Geological Society of America Bulletin 96, 793-812.

Wellman, H.W., 1985. Rate of dextral faulting in the central part of New Zealand from weathering rind ages. Unpublished draft report, Dept. of Geology, Research School of earth Sciences, V.U.W., Wellington.

Wells, D.L., Coppersmith, K.J., 1994. New empirical relationships among magnitude, rupture length, rupture width, rupture area, and surface displacement. Bulletin of the Seismological Society of America 84, 974-1002.

Wesnousky, S.G., 1988. Seismological and structural evolution of strike-slip faults. Nature 335, 340-343.

Wesnousky, S.G., 2006. Predicting the endpoints of earthquake ruptures. Nature 444, 358-360.

Wesnousky, S.G., 2008. Displacement and Geometrical Characteristics of Earthquake Surface Ruptures: Issues and Implications for Seismic-Hazard Analysis and the Process of Earthquake Rupture. Bulletin of the Seismological Society of America 98, 1609-1632.

Williams, P.L., Magistrale, H.W., 1989. Slip along the Superstition Hills fault associated with the 24 November 1987 Superstition Hills, California, earthquake. Bulletin of the Seismological Society of America 79, 390-410.

Wood, R.A., Pettinga, J.R., Bannister, S., Lamarche, G., McMorran, T.J., 1994. Structure of the Hanmer strike-slip basin, Hope Fault, New Zealand. Bulletin of the Geological Society of America 106, 1459-1473.

Woodcock, N.H., Fischer, M., 1986. Strike-slip duplexes. Journal of Structural Geology 8, 725-735.

Yang, J.S., 1991. The Kakapo Fault — a major active dextral fault in the central North Canterbury - Buller regions of New Zealand. New Zeal J Geol Geop 34, 137-143.

Yeats, R.S., Berryman, K.R., 1987. South Island, New Zealand, and Transverse Ranges, California: a seismotectonic comparison ( USA). Tectonics 6, 363-376.

Zachariasen, J., Prentice, C.S., 2008. Detailed Mapping of the Northern San Andreas Fault Using LiDAR Imagery. Final Technical Report. U.S. Geological Survey, 47p.

Zachariasen, J., Berryman, K., Langridge, R., Prentice, C., Rymer, M., Stirling, M., Villamor, P., 2006. Timing of late Holocene surface rupture of the Wairau Fault, Marlborough, New Zealand. New Zeal J Geol Geop 49, 159-174.

Zachariasen, J., Sieh, K., 1995. The transfer of slip between two en echelon strike-slip faults: A case study from the 1992 Landers earthquake, southern California. Journal of Geophysical Research: Solid Earth 100, 15281-15301.

Zhou, Q., Xu, X., Yu, G., Chen, X., He, H., Yin, G., 2010. Width Distribution of the Surface Ruptures Associated with the Wenchuan Earthquake: Implication for the Setback Zone of the Seismogenic Faults in Postquake Reconstruction. Bulletin of the Seismological Society of America 100, 2660-2668.

Zielke, O., Arrowsmith, J.R., Ludwig, L.G., Akciz, S.O., 2012. High-resolution topography-derived offsets along the 1857 Fort Tejon earthquake rupture trace, San Andreas fault. Bulletin of the Seismological Society of America 102, 1135-1154.

Zielke, O., Arrowsmith, J.R., Ludwig, L.G., Akçiz, S.O., 2010. Slip in the 1857 and Earlier Large Earthquakes Along the Carrizo Plain, San Andreas Fault. Science 327, 1119-1122.

Zielke, O., Klinger, Y., Arrowsmith, J.R., 2015. Fault slip and earthquake recurrence along strike-slip faults — Contributions of high-resolution geomorphic data. Tectonophysics 638, 43-62.

Zischinsky, U., 1966. On the deformation of high slopes, Proceedings of the First Congress of the International Society of Rock Mechanics, Lisbon, Portugal, pp. 179–185.

Zischinsky, U., 1969. Über Sackungen. Rock Mechanics 1, 30-52.

# APPENDIXES

# APPENDIX TO CHAPTER 2: LATE HOLOCENE RUPTURE BEHAVIOUR AND EARTHQUAKE CHRONOLOGY ON THE HOPE FAULT, NEW ZEALAND

## Appendix 2.1: Key observations of Mckay (1890) and Jones (1933) regarding the 1888 North Canterbury (Amuri) earthquake

*1-" The distance of the Clarence accommodation-house* (top right side of Fig. 2.2) *from the line of greatest disturbance where it passes along the south side of the eastern part of the Hanmer Plain is some fourteen miles in a north-north-easterly direction, but at a right angle from the eastern prolongation of the line it is not more than ten miles."* (McKay, 1890: p. 2)

*2-" lake Sumner is about 6 miles south of the earthquake-fracture at the junction of Kiwi Creek with the Hope River, and the lower part of the Otairo Gorge not more than then miles south of the line as traced if continued westward."* (McKay, 1890: p. 2)

*3-" Of the ground-rents said to have opened along the bed of the Percival River, these appear for the most part to have closed or been filled by the falling-in of the sides, although Mr. Low of St. Helen's , informed me that he could still find one special rent open which was said to be nearly 10 in. in width. This, however, I did not see and in riding along the plain to the junction of the Hanmer with the Waiau-ua* (Waiau River) *I saw no fissures nor rents of any kind."* (McKay, 1890: p. 4)

*4-" On our way through the Waiau-ua* (Waiau) *gorge Mr. Rutherford pointed out two slips on the east side of the gorge and stated that these had been caused by the earthquake of the 1st September.....true fissures must be attendant, but they have not been observed."* (McKay, 1890: p. 5)

*5-" At the bridge at the upper end of the gorge there were no visible signs of an earthquake having occurred, but I was told that some rocks had fallen on the Leslie Hills side of the river."* (McKay, 1890: p. 5)

*6-" In following up the south bank of the Waiau-ua* (Waiau River) *not a trace of the effects of the earthquake was observed for the first four miles west of the upper end of the gorge. At this distance, however, the track passes over a spur of the range on the south side of the plain..... on the western face of the spur earth-rents that, when formed, might have been 4in. or 5in. wide, crossed the track in a westerly direction....."* (McKay, 1890: p. 5)

*7-" Before reaching the crossing of the Waiau-ua* (Waiau River) *to Hopefield Station* (Glenhope) *the long cutting descending to the river-bed had been rendered almost impossible to horsemen..... rents were everywhere on this cutting, some of them being more than 12in. wide, and these, with the slipped outer edge of the road and fallen banks from the upper side,*

*showed clearly that what the violence and force of the earthquake had been."* (McKay, 1890: p. 6)

*8-"On the dray-road crossing from Hopefield* (Glenhope) *to the south bank of the river, just below the junction of the Hope, the road, going to Glenwye* (Glynn Wye), *crossing the broad low-sloping fan of Shingle Creek and on this rents and openings 4in. to 6in. in width began to appear and became more numerous as we proceeded westward. There were true fissures on a flat surface, unlike many that appeared on the edge of the terraces, where the ground rent was not equally supported on both sides."* (McKay, 1890: p. 7)

*9-" about half a mile east of Horse-shoe Lake a cubical mass of rock some 6 ft. square encumbers the road. Seemingly it has fallen or rolled down from the heights above, but it had left no track in its passage to the lower ground....."* (McKay, 1890: p. 7)

*10-" ....the higher terrace is 350 ft. above the station flat* (Glynn Wye Station), *or nearly 500ft. above the river at the junction of Kakapo Brook.....an old line of dislocation, caused by former earthquakes, runs along the middle of this higher terrace, and the recently-formed earth-rents follow the same course, or nearly so. At the back of the Glenwye* (Glynn Wye) *Station, the recently-formed fractures are on the face and brow of the high terrace, and a little to the west on the upper flat itself, where over nearly a quarter of a mile the whole surface is a network of fractures, fissures, slips, and dislocations . At one place, an area of about 4 chains in width and 10 chains or more in length has subsided 2ft.....the middle part of this may have subsided even more than that. From Glenwye* (Glynn Wye) *Station, a wire fence.....was shifted 5ft. out of the true line. About a mile and a half beyond Glenwye* (Glynn Wye) *the fence.....crosses the old earthquake-rent.....has been sundered and thrown to the east a distance of 8 ft. 6 in. Less than a mile and a half further west another fence..... Has been broken and shifted to the east 8 ft."* (McKay, 1890: p. 9&10)

*11-" In the Hope Valley, above the junction of the Boyle River, the rents and fissures begin to be less abundant than they are in the vicinity of Glenwye* (Glynn Wye)*....."* (McKay, 1890: p. 10)

*12-" A mile below the junction of Kiwi we crossed from the south to the north side of the middle Hope Valley, we skirted the edge of the bush on the side, nothing that very many of the dry birch-trees* (beech trees) *in the bush had been broken and thrown down by the earthquake, and that these were generally broken off 10ft. to 15ft. from the ground, the timber, though dry, being sound for the most part, and the roots holding firm in the ground.....in other cases, green trees 25ft. To 30 ft. in height have been torn up by the roots*

*and are now in the prostrate position. This has happened both on shingly and on rocky soil."* (McKay, 1890: p. 11&12)

*13-" We proceeded along the upper Hope Valley to Jones hut, which was reported to have been wrecked by the earthquakes of the 1st September, and near which report had it that a fissure had opened and again closed with such violence that a ridge of some height was thus formed and was traceable for a mile along the river flat. Before reaching the hut most of the signs of earthquake action had died away.....and we were now certainly beyond (to the north of) the line and belt of country most violently affected by the earthquakes.....passing thus beyond the region visibly bearing traces of earthquake-action, we did not deem it necessary to proceed further in the direction of the Hope Saddle, and from the hut we returned to the junction of the Kiwi Creek with the Hope. We might have followed the earth-fractures, old and new, about a mile farther, to the edge of the bush on the east side of the low saddle already mentioned, but the day was passing and it was necessary to return to Glenwye* (Glynn Wye) *before dark...."* (McKay, 1890: p. 12)

*14-" The mountain range lying between the low saddle mentioned and the source of the Hope River and Hope Saddle had on eastern spur one notably large slip and some of lesser size. The large slip looked to me as though it had been there before the earthquakes; but Mr. Rutherford, not having noted it previously, was of the opinion that it not only was caused by the earthquakes, but also that is happened right in the line of greater dislocation which we had followed more or less closely from Glenwye* (Glynn Wye). *In the Hope Valley.....the mountains on both sides are marked by a great number of landslips that have taken place recently, and these were not observed previous to the beginning of September 1st....."* (McKay, 1890: p. 11&13)

*15-" The facts that I noted, in my opinion, tend to show that the great shock of the morning of the 1st September commenced at some point to the west of Glenwye* (Glynn Wye), *perhaps further west than the junction of the Kiwi with the Hope, and that is travelled east-ward with increasing force to Glenwye* (Glynn Wye) *and Hopefield* (Glenhope), *beyond which places, by what appears at the surface, its destructive character began to be less; and, although as far as the eastern end of the Hanmer Plain its violence was great, if rents and fissures are to be taken as a measure of its force, it was here mild and tame compared with what it was at the Hopefield* (Glenhope) *and Glenwye* (Glynn Wye)..... *and though a number of small rents were formed along the bed of Percival River, clearly in this direction the power of the movement and force of its shock was being rapidly lessened, and not more than 10*

*miles further to the east, between the Hanmer River and Lottery Creek, there is not the least indication of fresh disturbance along the old line of earthquake -rent."* (McKay, 1890:p. 13)

*16- "After the earthquake we all learned that the earth fissure which commences at the Hanmer Plains, runs through my old place, and several miles of Glynn Wye, was an old earthquake crack. One side of this crack seemed to remain firm, while the other side shifted about five feet (1.5 m) further north. I knew this because I had a wire fence running from the hills in a straight line to the River Waiau"* (Jones, 1933: p. 123) and *"At Jones's station, the old earthquake-rent passed on to a terrace of lower level, and we had less opportunity for observing it closely....."* (McKay, 1890: p. 6)

*17-" ... Mr. Thompson, of Glenwye, informed me that…though he cannot say that the great shock came from the west of Glenwye, it certainly passed down the valley eastward from that place at a measurable rate, and was accompanied by a terrific roaring noise, which died away in the distance, while things were momentarily quiet at the place where he stood"* (McKay, 1890, p. 14)

# Appendix 2.2: Trench unit descriptions

Table 1. Trench unit descriptions, Hope Shelter-Trench 1 (February 2012), W Wall

| Unit | Description | ID |
|---|---|---|
| 1 | Top soil | [soil] |
| 1a | Light brown nutty silt, abundant fine roots, massive | [light grey brown soil/subsoil] |
| 1p | Light brown peaty silt, abundant fine roots and grass | [peaty soil] |
| 2 | Medium grey, moderately-poorly sorted, pebbly silty sand, Max. clast size: 4 cm, moderately firm | [colluvial wedge] |
| 3 | Dark grey brown, moderately-poorly sorted, sandy to pebbly peat, Max. clast size: 1.5 cm, common plant fragments and stones | [stony peat/ colluvium?] |
| 4 | Dark brown gritty peat, common root traces, Max. clast size: 5mm, moist, massive, spongy, silt texture peat | [peat] |
| 5 | Dark grey, moderately-poorly sorted, gravely sandy silt, wet, Max. clast size: 4cm, Ave. clast size: 1-2 cm, matrix: sandy silt | [alluvium/colluvium] |
| 6 | Medium grey gritty silty sand, Max.clast size: 8mm, include root fragments, soft, moist, sticky | [fine sand] |
| 6p | Light grey brown peat, abundant root fibers, soft, moist | [peat] |
| 7a | Medium grey most silt, soft | [fine sandy silt] |
| 7p1&7p2 | Thin rooty fibers | [thin peat stringers] |
| 7b | Reverse grading sequence of 4 subunits (b1: fine sandy silt, b2: medium to fine sand, b3: fine sand silt, b4: pebbly coarse sand (each layer is 2-3 cm thick) | [silty alluvium] |
| 8 | Light reddish grey silt with abundant peaty root fibers, moist soft and spongy, organic silt | [silt] |
| 8p | Red brown fibrous peat | [peat] |
| 9 | Reverse grading pair of subunits, (9a: medium-brown grey organic silt (2 cm thick), moist, spongy, 9b: silty fine sand, light grey, well sorted (2 cm thick)) | [alluvium] |
| 9p | Red fine fibrous peat | [peat] |
| 10 | Medium grey fine sandy silt, abundant peaty root traces, occasional plant fragments (leaf), moist | [silt] |
| 10p | Red brown spongy fibrous peat | [peat] |
| 11 | Normal grading sequence, package of light grey stony silt at base (moderately-sorted) to light grey silt at top, top has some peaty root fibers (very well sorted), moist , soft | [silty alluvium] |
| 11p & 11p2 | Light reddish brown fine fibrous peat | [peat] |
| 12p | Thick red-brown peat | [peat] |
| 12a | Medium grey coarse sand, Max. clast size:5 mm, well sorted, loose | [alluvial sand] |
| 13p | Red fine hairy peat | [peat] |
| 13 | Light grey clayey silt, moist | [silt] |
| 14 | Light grey clayey silt, moist | [silt] |
| 15 | Medium grey silty gravel, Max. clast size: 15 cm, moderately-poorly sorted, Ave. clast size: 2-3 cm, matrix: sandy silt | [alluvial gravel] |
| 18 | Medium grey stony fine sandy silt, Max. clast size: 3 cm, Ave. clast size:1 cm, moist, slightly peaty with common peaty root fibrous | [sand, channel deposit] |
| 20 | Light brown grey gravelly silt, Max. clast size: 7cm, Ave. clast size: 2-3cm, matrix: fine sandy silt with abundant fine roots, slight iron staining on clasts and roots | [colluvium] |
| 21 | Medium grey firm massive fine sandy silt, well sorted | [alluvial silt] |
| 22 | Medium- brown grey clayey silt, massive, firm, clast orientation along a line | [alluvial silt] |
| 23 | Light brown grey stony silt, Max. clast size: 2 cm, moist, slightly firm, matrix: fine sandy silt | [faulted colluviums] |
| 25 | Light brown grey sandy pebbly gravel, Max. clast size: 10cm, sub angular, matrix: clayey silty sand, vertically oriented clasts | [faulted colluvium/shear zone] |
| 26 | Light grey silty gravel, wet, Max. clast size:12 cm, matrix: sandy silt | [shear zone] |
| 27 | Light reddish grey sandy gravel, M. clast size: 12cm, oxidized greywacke clast, sub angular to sub rounded, matrix: medium to coarse sand | [faulted edge of fan deposits] |
| 28 | Light reddish grey pebbly silty sand, Max. clast size: 7cm, Ave. clast size: 1cm, moderately loose, matrix: loamy sand, some iron oxidation along root traces, gravely loamy(clay, silt, sand) sand | [fan alluvium] |
| 28a | Gravely silt, light brown grey, Max. clast size: 11cm, Ave. clast size: 2-3cm, matrix: fine sandy silt with abundant fine roots | [fan alluvium] |
| 29a | Light olive grey medium sand, well sorted, occasional pebbles up to 2 cm | [sand, channel deposit] |
| 29 | Medium olive grey gravely sand, Max. clast size:3cm, Ave. clast size: 8mm, matrix: moderately loose | [sand, channel deposit] |
| 30a | Light olive grey sandy gravel, Max. clast size: 18cm, Ave. clast size:3cm, matrix: medium-coarse sand, moderately loose, large clast iron stained | [fan alluvium] |
| 30b | Light reddish grey gravely sand, loose, moist, Max. clast size: 15cm,varies from poorly sorted to moderately sorted | [fan alluvium] |
| 30c | Dark grey medium-coarse sand, very well sorted, moist | [fan alluvium] |

Table 2. Trench unit descriptions, Hope Shelter-Trench 2 (February 2013), E wall

| Unit | Description | ID |
|---|---|---|
| 1 | Light grey clayey silt | [alluvial silt] |
| 2 | Peat | [peat] |
| 2a | Peaty silt | [alluvial silt] |
| 3 | Gritty fine sand | [alluvial sand] |
| 4 | Peat | [peat] |
| 5 | Moderately well-sorted fine to medium sand with occasional root pieces, it grades toward fault to fine muddy sand | [alluvial sand] |
| 6 | Sandy pebble gravel, subangular to angular | [channel deposits] |
| 7 | Medium grey clayey fine sandy silt, common peaty roots | [alluvial silt] |
| 7pa | Peat | [peat] |
| 7pb | Peat stringer | [peat] |
| 8 | Silty sandy pebble gravel, Ave. clast size: 2 cm, Max. clast size: 4cm | [channel deposits] |
| 9 | Medium grey clayey silt, slightly gritty, abundant peaty roots | [alluvial silt] |
| 10 | Light reddish gray brown spongy silty peat, contains wood and plant fragments | [peat] |
| 11 | Light grey brown stony sandy silt, common fine roots | [stony swamp soil] |
| 12 | Light grey coarse sandy pebble gravel, firm, thins toward scarp | [channel gravel] |
| 13 | Light brown grey organic silt, slightly stony, spongy, abundant fine roots | [peaty soil] |
| 20 | Undifferentiated sandy gravel, Ave. clast size: 5-7 cm, Max. clast size: 20 cm, subangular to subrounded clasts, matrix: medium to coarse sand, matrix supported | [fan alluvium] |
| 21 | Medium grey silty clay | [faulted alluvium] |
| 21p | Peat stringer showing fault | [peat] |
| 22 | Firm light grey sandy silty clay with occasional pebbles | [marginal deposits/faulted colluviums?] |
| 23 | Medium grey clayey silt | [faulted alluvium] |
| 24 | Zone of medium grey gritty silty clay with vertical fabric | [shear zone] |

# Appendix 2.3: Details of OxCal Modelling

## Modelling Trench 1 Data

For modelling T-1, I used ages from samples HS1-25, HS1-3, HS1-22, HS1-4, HS1-7, HS1-11, HS1-13, and HS1-19 (Table 2.2). Nine samples were eliminated from the model because their ages were out of stratigraphic order, reversed, or considered to be modern or too young. Samples HS1-1, HS1-1/2, HS1-2, HS1-3 and HS1-23 are in a reverse order of age with respect to each other. Among these, I preferred to use sample HS1-3 because its age is concordant with the age of the upper peat (unit 10) in T-2. Samples HS1-20 and HS1-5 were considered to be out of stratigraphic order with the sequence in T-1 and on closer inspection these samples were probably rooty materials. Sample HS1-16 comprised several different fragments indicating a younger age than sample HS1-13 which is in a higher stratigraphic position. Therefore, this sample was also not used.

Event horizons are identified between the dated samples based on our description in the section “Trench 1-faulting”. Because faulting of unit 2 was unclear, I constructed two models: 1- using six events (T-1 model 1) and 2- using five events (T-1 model 2). The command “Boundary” was applied to the top and bottom of the model to assume that all events are equally likely to come anywhere within the sequence and to force OxCal to sample

the sequence for the entire age range used within the sequence (Lienkaemper and Bronk Ramsey, 2009). The 1888 Amuri earthquake was placed in the OxCal model above E1 in T-1 model 1 in order to better constrain the timing of that event. The command "Difference" was used to calculate the inter-event intervals and the command "RI" was used to calculate the distribution of the average recurrence between E1 and E6. The results are presented in Figs. 2.12 and 2.13.

**Modelling Trench 2 Data**

For modelling T-2, I used ages from samples HS2-8, HS2-7, HS2-14, HS2-4, HS2-3, HS2-6 and HS2-1 (Table 2.2). Four samples were not used in the model. Samples HS2-11 has a modern age and sample HS2-13 has an old age compared with other samples taken from below it. Sample HS2-9 comes from a very compact peat with no distinguishable organic macrofossils. This part of the stratigraphy at the northern end of T-2 appears to be interfingered and unconformable with the main sequence in the trench. Therefore, I suspect it is out of stratigraphic order and did not use it in the OxCal model. Samples HS2-1, HS2-2 and HS2-3 are at the bottom, middle and top of unit 2 respectively. Sample HS2-2 is not in order with the other two samples. Therefore, my preference is to use sample HS2-1 and HS2-3 because they come from stalky plant materials and seeds which are more reliable, i.e. delicate, non-reworked fragments compared to other datable materials.

Event horizons are identified as specific stratigraphic levels between the dated samples based on the description in the section "Trench 2-faulting". As with the T-1 models, the commands "Boundary", "Difference" and "RI" were applied. The results are presented in Fig. 2.14.

# APPENDIX TO CHAPTER 3: POST-LAST GLACIAL SLIP RATE ALONG THE WESTERN HOPE FAULT, SOUTH ISLAND, NEW ZEALAND

## Appendix 3.1: Measured Displacements along the fault

Table 1. Characteristics of the fault structures and vertical and horizontal displacements. These data were collected from 2- and 1-m LiDAR hillshade models (depending on the vegetation cover, see Langridge et al. (2013)) and some in the field. Qualitative index shows the accuracy of measured displacement. Where a displacement was not assessable, qualitative index (5) was used. Where two measurements are reported in this study (i.e., using LiDAR and in the field), two indices are assigned and qualitative index (1) was used for the field data. Abbreviations are: PSZ, Principal slip zone; IPSZ, Inferred PSZ; N, Normal faults; Re, Thrust/Reverse faults; Sf, Secondary fault; SP, Splay fault (see section 1.5.2 in chapter 1 for fault mapping and classification). Symbols: ^, Khajavi (2015) measured the displacement in the field, *, Langridge and Berryman (2005) measured the displacement in the field, +, Langridge et al. (2013) measured the displacement using RTK, #, Freund (1971) measured the displacement. No symbol: this study measured displacement on LiDAR hillshade model. Dextral measurements from the PSZ are shown in red. Qualitative indices from 1 to 5 and from 1-2 are assigned to dextral displacement and scarp heights, respectively. Projected coordinate system for X and Y: NZGD_2000_TM.

| **Hope Fault- Hurunui segment- Landslip Stream (see Fig. 3.4A in Chapter 3)** | | | | | | | | | | | | | |
|---|---|---|---|---|---|---|---|---|---|---|---|---|---|
| **No** | **Fault type** | **Strike** | **Downthrown Quadrant** | **Offset feature** | **Fault dominant Sense** | **Fault sub sense** | **Strike-slip displacement (m)** | **Uncertainty (m)** | **Scarp height (m)** | **Uncertainty (m)** | **QI** | **X** | **Y** |
| 1 | PSZ | 71 | NW | Outwash Fan | Dextral | Normal | | | 0.8 | 0.1 | 1 | 1518554 | 5272408 |
| 2 | **PSZ** | 71 | NW | Channel | Dextral | Normal | **9.5** | **1.5** | **0.5** | | **2-1** | 1518616 | 5272429 |
| 3 | PSZ | 71 | NW | Outwash Fan | Dextral | Normal | | | 0.2 | | 1 | 1518738 | 5272470 |
| 4 | PSZ | 72 | NW | Outwash Fan | Dextral | Normal | | | 0.35 | | 1 | 1518938 | 5272499 |
| 5 | PSZ | 72 | NW | Outwash Fan | Dextral | Normal | | | 0.3 | | 1 | 1519043 | 5272540 |
| 6 | PSZ | 69 | NW | Outwash Fan | Dextral | Normal | | | 0.5 | | 1 | 1519192 | 5272593 |

| | | | | | | | | | | | | | | |
|---|---|---|---|---|---|---|---|---|---|---|---|---|---|---|
| 7 | PSZ | 78 | NW | Outwash Fan | Dextral | Normal | | | 0.2 | | 1 | 1519442 | 5272672 |
| 8 | PSZ | 72 | NW | Outwash Fan | Dextral | Normal | | | 0.8 | 0.2 | 1 | 1519800 | 5272756 |
| 9 | PSZ | 72 | SE | Outwash Fan | Dextral | Reverse? | | | 0.8 | 0.2 | 1 | 1519881 | 5272796 |
| 10 | **PSZ** | 72 | SE | Channel | Dextral | Reverse? | **7.5** | **2** | | | **3** | 1519914 | 5272796 |
| 11 | PSZ | 72 | NW | Outwash Fan | Dextral | Normal | | | 0.4 | | 1 | 1520043 | 5272829 |
| 12 | Sf | 93 | S | Outwash Fan | Normal? | | | | 1 | 0.2 | 1 | 1518739 | 5272379 |
| **Hope Fault- Hurunui segment- Matagouri Flat (see Fig. 3.4B in Chapter 3)** | | | | | | | | | | | | | |
| 1 | **PSZ** | 70 | NW | Channel | Dextral | Normal | **14, *16.7** | **5** | **0.6,*0.7** | **0.1** | **4-1** | 1520171 | 5272866 |
| 2 | **PSZ** | 70 | NW | Channel Riser | Dextral | Normal | **7.7,*9.2,+5.5** | **2.2** | **0.7,*0.5** | **0.1** | **3-1** | 1520195 | 5272869 |
| 3 | **PSZ** | 70 | NW | Channel Riser | Dextral | Normal | **7.5,+4-5** | **1.5** | **0.7, *0.8** | **0.1** | **2-1** | 1520215 | 5272875 |
| 4 | **PSZ** | 70 | NW | Channel Riser (best estimate) | Dextral | Normal | **7.5,*4.8-5.4, +4-4.4** | **1** | **0.8,*0.6** | **0.2** | **2-1** | 1520246 | 5272883 |
| 5 | PSZ | 70 | NW | Hurunui Flood Plain | Dextral | Normal | | | 0.3 | | 1 | 1520342 | 5272924 |
| 6 | PSZ | 73 | NW | Hurunui Flood Plain | Dextral | Normal | | | 0.25 | | 1 | 1520428 | 5272948 |
| 7 | **PSZ** | 73 | NW | Channel Riser | Dextral | Normal | **3** | **0.4** | **0.4** | **0.2** | **2-1** | 1520519 | 5272971 |
| 8 | PSZ | 73 | NW | Hurunui Flood Plain | Dextral | Normal | | | 0.6 | 0.1 | 1 | 1520748 | 5273037 |
| 9 | PSZ | 73 | NW | Hurunui Flood Plain | Dextral | Normal | | | 0.3 | | 1 | 1520812 | 5273056 |
| 10 | PSZ | 71 | NW | Hurunui Flood Plain | Dextral | Normal | | | 0.2 | | 1 | 1521155 | 5273164 |
| 11 | PSZ | 71 | NW | Hurunui Flood Plain | Dextral | Normal | | | 0.2 | | 1 | 1521285 | 5273213 |
| 12 | N | 99 | SW | Hurunui Flood Plain | Normal | | | | 0.3 | | 1 | 1520418 | 5272932 |
| 13 | N | 281 | NE | Hurunui Flood Plain | Normal | | | | 0.5 | | 1 | 1520409 | 5272920 |
| 14 | Re | 81 | NW | Hurunui Flood Plain | Reverse | | | | 0.2 | | 1 | 1520600 | 5273007 |
| 15 | Re | 253 | SE | Hurunui Flood Plain | Reverse | | | | 0.2 | | 1 | 1520606 | 5272988 |
| **Hope Fault- Hurunui segment- McKenzie Stream (see Fig. 3.4C in Chapter 3)** | | | | | | | | | | | | | |
| 1 | **PSZ** | 74 | S | Channel Riser | Dextral | Reverse | **21.5,*16** | **6.5,*1.5** | **1.4, *2** | **0.4** | **3-2** | 1521540 | 5273244 |
| 2 | **PSZ** | 74 | S | Channel Riser | Dextral | Reverse | **11,*9.2** | **3, *1** | **1** | **0.2** | **3-2** | 1521572 | 5273247 |
| 3 | **PSZ** | 74 | S | Channel Riser | Dextral | Reverse | **26, *not assessable** | **3** | **1.6, *1.2** | **0.2** | **2-2** | 1521605 | 5273250 |
| 4 | **PSZ** | 74 | SE | Channel Riser | Dextral | Reverse | **21, *not assessable** | **6** | **1.5,*1.2** | **0.2** | **3-2** | 1521656 | 5273267 |
| 5 | Re | 261 | SE | Outwash Fan | Reverse | | | | 1.8, ***2.5** | 0.2 | 1 | 1521761 | 5273267 |
| 6 | Re | 76 | NW | Outwash Fan | Reverse | | | | 1.8, ***2.5** | 0.2 | 1 | 1521754 | 5273291 |

| | | | | | | | | | | | | | |
|---|---|---|---|---|---|---|---|---|---|---|---|---|---|
| 7 | **PSZ** | 74 | SE | Channel | Dextral | Reverse | **6,*10.9** | **1, *1.2** | **1.5, *2.5** | | **2-1** | 1521803 | 5273294 |
| 8 | **PSZ** | 74 | SE | Channel Riser | Dextral | Reverse | **15, *6.8** | **1, *0.8** | **2, *1.85** | **0.2** | **1-1** | 1521887 | 5273322 |
| 9 | **PSZ** | 74 | SE | Channel Riser | Dextral | Reverse | **15, *16.1** | **1.5, *1.5** | **1.7, *1.85** | **0.2** | **1-1** | 1521909 | 5273326 |
| 10 | **PSZ** | 74 | SE | Channel | Dextral | Reverse | **14, *16** | **1, *1.5** | **2, *1.95** | **0.1** | **1-1** | 1521930 | 5273330 |
| 11 | **PSZ** | 74 | SE | Channel | Dextral | Reverse | **15** | **1.5** | **2.5, *2.5** | **0.5** | **1-1** | 1522045 | 5273373 |
| 12 | PSZ | 74 | SE | Outwash Fan | Dextral | Reverse | | | 3 | 0.2 | 1 | 1522141 | 5273407 |
| 13 | PSZ | 74 | SE | Outwash Fan | Dextral | Reverse | | | 1.6 | 0.1 | 1 | 1522248 | 5273445 |
| 14 | PSZ | 110 | SW | Outwash Fan | Dextral | Reverse | | | 1.1 | 0.2 | 1 | 1521531 | 5273254 |
| 15 | N | 101 | SW | Outwash Fan | Normal | | | | 0.8 | 0.2 | 1 | 1521581 | 5273253 |
| 16 | **PSZ** | 74 | SE | Channel | Dextral | Reverse | **19,*not assessable** | **4** | **2.5** | **0.2** | **3-2** | 1521631 | 5273262 |
| 17 | N | 103 | SW | Channel | Dextral | Normal | 4.7 | 0.8 | 1.5 | | 2-2 | 1521644 | 5273279 |
| 18 | SP | 76 | SW | Outwash Fan | Dextral | Reverse | | | 0.6 | 0.1 | 2 | 1521568 | 5273281 |
| 19 | **SP/PSZ?** | 86 | S | Channel | Dextral | Reverse | **21, *22** | **2.5, *2** | **4.5, *4-5** | **0.5** | **2-2** | 1521506 | 5273267 |
| 20 | SP | 68 | SE | Channel Riser | Dextral | Reverse | 4.7 | 0.5 | 0.4 | 0.1 | 2-2 | 1521645 | 5273318 |
| 21 | N | 88 | S | Outwash Fan | Normal | | | | 1.4 | 0.2 | 1 | 1521757 | 5273369 |
| 22 | SP | 74 | NW | Outwash Fan | Dextral | Reverse | | | 0.1 | | 2 | 1521962 | 5273536 |
| 23 | SP | 74 | NW | Channel Riser | Dextral | Normal | 9 | 3 | 0.4 | 0.1 | 4-2 | 1521734 | 5273408 |
| 24 | N | 85 | S | Channel | Dextral | Normal | 14 | 6 | 1.1 | 0.2 | 5-2 | 1521657 | 5273344 |
| 25 | N | 85 | S | Channel | Dextral | Normal | 4.2 | 0.3 | 1.5 | 0.2 | 1-2 | 1521647 | 5273342 |
| 26 | N | 85 | S | Channel/Outwash Fan | Dextral | Normal | ? | | 2.2 | 0.2 | 1-2 | 1521615 | 5273336 |
| 27 | SP | 74 | NW | Channel | Dextral | Normal | 13 | 2.5 | 0.8 | 0.2 | 2-2 | 1521527 | 5273306 |
| 28 | SP | 74 | NW | Outwash Fan | Dextral | Normal | ? | | 1 | 0.1 | 1 | 1521446 | 5273275 |
| 29 | N | 91 | S | Channel | Dextral | Normal | 3 | 3 | 0.1 | | 5-2 | 1521792 | 5273494 |
| 30 | N | 91 | S | Channel | Dextral | Normal | 6.5 | 2.5 | 0.1 | | 4-2 | 1521821 | 5273495 |
| **Hope Fault- Hurunui segment- The Park & West of McMillan Stream (see Fig. 3.5A-B in Chapter 3)** | | | | | | | | | | | | | |
| 1 | Re | 223 | SE | Surface of the Park | Reverse | | | | 1.6 | 0.2 | 1 | 1522873 | 5273657 |
| 2 | Re | 239 | SE | Surface of the Park | Reverse | | | | 1.6 | 0.1 | 1 | 1522977 | 5273709 |
| 3 | Re | 193 | E-SE | Surface of the Park | Reverse | | | | 1.2 | 0.1 | 1 | 1523157 | 5273774 |
| 4 | **IPSZ** | 76 | | Channel | Dextral? | | **6** | **6** | | | **5** | 1523221 | 5273779 |

| | | | | | | | | | | | | | |
|---|---|---|---|---|---|---|---|---|---|---|---|---|---|
| 5 | **I PSZ** | 66 | | Channel | Dextral? | | **4.5** | **4.5** | | | **5** | 1523469 | 5273852 |
| 6 | **PSZ** | 52 | SE | Channel | Dextral | Reverse? | **14.5** | **14.5** | **0.1?** | | **5-2** | 1523596 | 5273895 |
| 7 | **PSZ** | 62 | NW | Channel | Dextral | Normal? | **12.5** | **12.5** | **0.1?** | | **5-2** | 1523645 | 5273936 |
| 8 | Re | 72 | S-SE | Surface of the Park | Reverse | | | | 2 | 0.2 | 2 | 1523756 | 5273959 |
| 9 | **I PSZ** | 71 | | Channel | Dextral? | | **13** | **5** | | | **4** | 1523803 | 5273998 |
| 10 | SP | 79 | | Channel | Dextral? | | 22 | 2.7 | | | 4 | 1523761 | 5273935 |
| 11 | SP | 71 | SE | Alluvial/Debris Fan | Dextral? | Reverse | | | 0.8 | 0.2 | 1 | 1523966 | 5273995 |
| 12 | SP | 94 | S | Alluvial/Debris Fan | Dextral? | Reverse | | | 1 | 0.2 | 1 | 1523951 | 5274012 |
| 13 | **PSZ** | 68 | NW | Channel | Dextral | Normal | **60** | **24** | **0.2** | | **4-2** | 1523892 | 5274029 |
| 14 | Re | 199 | SE-E | Alluvium/Colluvium | Reverse | | | | 0.7 | 0.1 | 1 | 1523908 | 5274051 |
| 15 | Re | 216 | SE | Alluvium/Colluvium | Reverse | | | | 1.4 | 0.2 | 1 | 1523882 | 5274051 |
| 16 | **PSZ** | 61 | NW | Channel Riser | Dextral | Normal | **11** | **4** | **1.5** | **0.5** | **4-1** | 1523954 | 5274049 |
| 17 | PSZ | 56 | NW | Alluvial/Debris Fan | Dextral | Normal | | | 2.3 | 0.1 | 1 | 1524064 | 5274116 |
| 18 | **PSZ** | 75 | SE | Channel Riser | Dextral | Reverse | **9** | **9** | **4.5** | **0.5** | **5-1** | 1524269 | 5274207 |
| 19 | **PSZ** | 78 | SE | Channel Riser | Dextral | Reverse | **10.5** | **1.5** | **5** | **0.5** | **2-1** | 1524332 | 5274222 |
| 20 | PSZ | 76 | SE | Alluvium/Colluvium | Dextral | Reverse | | | 7.5 | 0.5 | 1 | 1524428 | 5274255 |
| 21 | Re | 70 | SE | Alluvium/Colluvium | Reverse | | | | 2.5 | 0.5 | 1 | 1524542 | 5274288 |
| 22 | Re | 247 | NW | Alluvium/Colluvium | Reverse | | | | 2.5 | 0.5 | 1 | 1524555 | 5274275 |
| 23 | PSZ | 67 | NW | Alluvium/Colluvium | Dextral | Normal | | | 4.2 | 0.2 | 1 | 1524717 | 5274343 |
| 24 | N | 88 | S | Alluvium/Colluvium | Normal | | | | 3.5 | 0.5 | 1 | 1524728 | 5274379 |
| 25 | N | 76 | SE | Alluvium/Colluvium | Normal | | | | 3.5 | 0.5 | 1 | 1524759 | 5274410 |
| 26 | PSZ | 62 | NW | Alluvium | Dextral | Normal | | | 1.8 | 0.2 | 1 | 1524850 | 5274392 |
| 27 | PSZ | 72 | NW | Alluvium | Dextral | Normal | | | 2.8 | 0.2 | 1 | 1524954 | 5274451 |
| 28 | **PSZ** | 66 | SE | Ridge/Channel Riser | Dextral | Reverse | **28.5** | **2.5** | **1** | **0.2** | **1-1** | 1525009 | 5274485 |
| 29 | N | 110 | SW | Channel | Dextral | Normal | 7.5 | 0.5 | 2.5 | | 1-1 | 1524546 | 5274394 |
| 30 | N | 108 | SW | Channel Riser | Dextral | Normal | 4.5 | 1.5 | 2.5 | | 4-4 | 1524486 | 5274358 |
| 31 | Re | 227 | SE | Alluvium/Colluvium | Reverse | | | | 1.5 | 0.2 | 1 | 1524475 | 5274180 |
| 32 | Re | 52 | NW | Alluvium/Colluvium | Reverse | | | | 1.5 | 0.2 | 1 | 1524462 | 5274196 |
| 33 | SP | 78 | SE | Channel Riser | Dextral | Reverse | 23.5 | 4.5 | 0.4 | | 2-2 | 1524270 | 5274092 |
| 34 | SP | 78 | SE | Channel Riser | Dextral | Reverse | 14 | 8 | 1 | | 5-2 | 1524172 | 5274072 |

| | | | | | | | | | | | | | |
|---|---|---|---|---|---|---|---|---|---|---|---|---|---|
| 35 | SP | 81 | SE | Channel Riser | Dextral | Reverse | 10.5 | 1.5 | 0.9 | 0.1 | 2-2 | 1524067 | 5274051 |
| 36 | Sf | 87 | S | Channel | Dextral | Reverse? | 6 | 6 | 1.2 | 0.2 | 5-2 | 1523659 | 5273981 |
| 37 | SP | 82 | NW | Channel | Dextral | Normal? | 9 | 1 | 0.1 | | 2-2 | 1523475 | 5273883 |
| 38 | SP | 82 | NW | Channel | Dextral | Normal? | 15.5 | 2.5 | 0.1 | | 2-2 | 1523437 | 5273877 |
| 39 | SP | 82 | NW | Channel | Dextral | Normal? | 6 | 0.5 | 0.1 | | 1-2 | 1523407 | 5273877 |
| 40 | SP | 82 | NW | Channel | Dextral | Normal? | 3 | 3 | 0.1 | | 5-2 | 1523256 | 5273870 |
| 41 | Sf | 244 | SE | Channel | Dextral | Normal? | 11 | 11 | 1 | | 1 | 1522619 | 5273803 |
| 42 | Sf | 71 | SE | Furrow across surface | Normal? | | | | 0.6 | 0.1 | 4 | 1522496 | 5273773 |
| 43 | Sf | 68 | | Channel | Dextral? | | 10.5 | 1.5 | | | 4 | 1523151 | 5274010 |
| 44 | Sf | 89 | S | Alluvial Fan | Normal | | | | 4 | 0.5 | 4 | 1523906 | 5274339 |
| 45 | Sf | 74 | NW | Alluvial Fan | Dextral | Normal? | | | 0.3 | | 2 | 1524226 | 5274392 |
| 46 | N | 104 | SW | Alluvial Fan | Normal | | | | 2 | 0.2 | 2 | 1524040 | 5274273 |
| 47 | N | 114 | SW | Alluvium/Colluvium | Normal | | | | 1.5 | | 2 | 1524190 | 5274240 |
| 48 | N | 72 | SW | Alluvium/Colluvium | Normal | | | | 1 | 0.1 | 2 | 1524163 | 5274199 |
| 49 | Sf | 85 | SE | Alluvial fan | Normal? | | | | 2.5 | 0.5 | 2 | 1524595 | 5274606 |
| 50 | Sf | 115 | SW | Alluvial fan | Normal | | | | 2.8 | 0.2 | 2 | 1524584 | 5274579 |
| 51 | Sf | 68 | NW | Channel | Dextral | Normal | 8.5 | 0.5 | 0.3 | 0.1 | 1-2 | 1524688 | 5274540 |
| 52 | Sf | 213 | SE | Alluvial Fan | Reverse | | | | 3 | 0.5 | 2 | 1524882 | 5274595 |
| 53 | Sf | 86 | N | Alluvial Fan | Dextral | Normal? | 3 | 3 | 0.2 | | 5-2 | 1524850 | 5274698 |
| 54 | Sf | 88 | S | Alluvial Fan | Dextral? | Normal | | | 3.5 | 0.5 | 2 | 1524969 | 5274771 |
| 55 | Sf | 88 | S | Fluvial deposits | Dextral? | Normal | | | 0.9 | 0.1 | 2 | 1525144 | 5274779 |
| 56 | Sf | 81 | NW | Little Ridge | Dextral | Normal? | 8.5 | 0.5 | 0.2 | | 1-2 | 1523580 | 5273823 |
| 57 | Sf | 81 | NW | Channel | Dextral | Normal? | 17.5 | 17.5 | 0.1 | | 5-2 | 1523529 | 5273819 |
| 58 | Sf | 81 | NW | Channel | Dextral | Normal? | 10.5 | 10.5 | 0.1 | | 5-2 | 1523419 | 5273798 |
| 59 | Sf | 81 | NW | Channel | Dextral | Normal? | 8.5 | 0.5 | 0.1 | | 1-2 | 1523386 | 5273790 |
| 60 | Sf | 215 | E-SE | Surface of the Park | Reverse | | | | 0.5 | 0.1 | 2 | 1523374 | 5273747 |
| 61 | Sf | 71 | NW | Surface of the Park | Normal? | | | | 0.2 | | 2 | 1523039 | 5273761 |
| 62 | Sf | 82 | SE | Channel | Dextral | Reverse? | 10.5 | 10.5 | 1.2 | 0.2 | 5-1 | 1523697 | 5274044 |
| 63 | Re | 229 | SE | Surface of the Park | Reverse | | | | 1.4 | 0.2 | 2 | 1523078 | 5273722 |
| 64 | Re | 226 | SE | Surface of the Park | Reverse | | | | 1.8 | 0.2 | 2 | 1523121 | 5273741 |

| | | | | | | | | | | | | | |
|---|---|---|---|---|---|---|---|---|---|---|---|---|---|
| 65 | SP | 89 | SE-S | Channel Riser | Normal | | 12.5 | 2 | 1.3 | 0.2 | 2-1 | 1525080 | 5274480 |
| **Hope fault- Hurunui segment- East of McMillan Stream (see Fig. 3.5C in Chapter 3)** | | | | | | | | | | | | | |
| 1 | **PSZ** | 68 | NW | Fluvial Terrace T3 | Dextral | Normal | **78** | **8** | **0.5** | **0.1** | **1-2** | 1525156 | 5274558 |
| 2 | **PSZ** | 68 | NW | Fluvial Terrace T4 | Dextral | Normal | **84** | **9** | **2.3** | **0.3** | **2-1** | 1525259 | 5274578 |
| 3 | **PSZ** | 68 | NW | Channel near T5 | Dextral | Normal | **76** | **4** | **5.5** | **0.5** | **1-1** | 1525345 | 5274612 |
| 4 | **PSZ** | 68 | NW | Alluvial Fan/T5 | Dextral | Normal | **82** | **6** | **13** | **1** | **1-1** | 1525452 | 5274647 |
| 5 | **PSZ** | 68 | NW | Channel Riser | Dextral | Normal | **76** | **24** | **2** | **0.1** | **4-1** | 1525653 | 5274758 |
| 6 | **PSZ** | 68 | NW | Channel | Dextral | Normal | **44** | **4** | **?** | | **1** | 1525782 | 5274810 |
| 7 | **PSZ** | 68 | NW | Channel Riser | Dextral | Normal | **93** | **13** | **8** | **1** | **2-1** | 1525868 | 5274817 |
| 8 | N | 263 | N-NW | Alluvial Fan | Normal | | | | 0.5 | 0.1 | 2 | 1525993 | 5274860 |
| 9 | Re | 253 | S-SE | Alluvial Fan | Reverse | | | | 0.5 | | 2 | 1525940 | 5274845 |
| 10 | PSZ | 65 | NW | Alluvial Fan | Dextral | Normal | | | 3.5 | 0.5 | 2 | 1526046 | 5274889 |
| 11 | N | 97 | SW | Alluvial Fan | Normal | | | | 1.5 | | 1 | 1525978 | 5274889 |
| 12 | PSZ | 64 | SE | Bedrock? | Dextral | Reverse? | | | 2 | 0.2 | 2 | 1526380 | 5275072 |
| 13 | I PSZ | 56 | NW | Bedrock? | Dextral | Normal | | | 0.5 | | 2 | 1526661 | 5275171 |
| 14 | N | 88 | S-SE | Bedrock? | Normal | | | | 1.5 | 0.2 | 2 | 1526788 | 5275211 |
| 15 | PSZ | 62 | SE | Bedrock? | Dextral | Reverse | | | 8 | 0.5 | 1 | 1526875 | 5275289 |
| 16 | PSZ | 62 | NW | Bedrock? | Dextral | Normal | | | 4.5 | 0.5 | 2 | 1526966 | 5275316 |
| 17 | N | 107 | SW | Alluvial Fan | Normal? | | | | 6.5 | 0.5 | 2 | 1525495 | 5274775 |
| 18 | N | 110 | SW | Alluvial Fan | Normal? | | | | 1.7 | 0.2 | 2 | 1525503 | 5274806 |
| 19 | Sf | 275 | N-NE | Alluvial Fan | Normal? | | | | 5 | 0.5 | 2 | 1525504 | 5274836 |
| 20 | Sf | 68 | NW | Channel Riser | Dextral | Normal | 13 | 1 | 1.5 | 0.1 | 1-1 | 1525710 | 5274859 |
| 21 | Sf | 68 | NW | Channel Riser | Dextral | Normal | 15 | 5 | 1 | 0.1 | 4-1 | 1525783 | 5274885 |
| 22 | Sf | 210 | SE | Alluvial Fan | Reverse | Normal | | | 3 | 0.5 | 2 | 1525833 | 5274905 |
| 23 | Sf | 68 | NW | Channel Riser | Dextral | Normal | 13 | 1 | | | 1 | 1525886 | 5274936 |
| 24 | Sf | 68 | NW | Channel Riser? | Dextral | Normal | 14 | 2 | 0.2 | | 2-2 | 1525949 | 5274958 |
| 25 | Sf | 73 | NW | Alluvial Fan | Dextral? | Normal | | | 0.1 | | 2 | 1525886 | 5274887 |
| 26 | Sf | 204 | SE | Alluvial Fan | Reverse | | | | 1.8 | 0.2 | 2 | 1525856 | 5274938 |
| 27 | Sf | 207 | SE | Alluvial Fan | Reverse | | | | 3 | 0.5 | 2 | 1525802 | 5274929 |
| 28 | Sf | 68 | NW | Displaced Reverse Fault? | Dextral | Normal | 14 | 1 | 0.3 | | 1-2 | 1525743 | 5274868 |

| | | | | | | | | | | | | | |
|---|---|---|---|---|---|---|---|---|---|---|---|---|---|
| 29 | Sf | 199 | SE | Alluvial Fan | Reverse | | | | 1 | 0.1 | 2 | 1525731 | 5274853 |
| 30 | Sf | 59 | NW | Channel | Dextral | Normal | 11.5 | 2.5 | 0.2 | | 3-2 | 1525796 | 5274939 |
| 31 | Sf | 72 | SE | Alluvial Fan | Dextral? | Normal? | | | 3 | 0.5 | 2 | 1525752 | 5274950 |
| 32 | Sf | 59 | NW | Channel | Dextral | Normal | 14 | 3 | | | 3 | 1525717 | 5274903 |
| 33 | Sf | 82 | SE | Channel Riser | Dextral | Reverse? | ? | | 3.5 | 0.5 | 2 | 1525880 | 5275021 |
| 34 | Sf | 82 | SE | Alluvial Fan | Dextral | Reverse? | | | 9 | 1 | 2 | 1525967 | 5275036 |
| 35 | Sf | 106 | SW | Alluvial Fan | Reverse? | | | | 8.5 | 0.5 | 2 | 1526007 | 5275021 |
| 36 | Sf | 277 | NE | Alluvial Fan | Normal | | | | 0.5 | | 2 | 1526023 | 5275069 |
| 37 | Sf | 279 | NE | Alluvial Fan | Normal | | | | 0.5 | 0.1 | 2 | 1525972 | 5275058 |
| 38 | Sf | 46 | SE | Alluvial Fan | Reverse | | | | 1.2 | | 2 | 1525971 | 5275092 |
| 39 | Sf | 51 | NW | Alluvial Fan | Reverse? | | | | 1.7 | 0.2 | 2 | 1525856 | 5275084 |
| 40 | Sf | 76 | NW | Alluvial Fan | Dextral | Normal | | | 4 | 0.5 | 2 | 1525899 | 5275120 |
| 41 | Sf | 89 | N | Displaced Reverse Fault? | Dextral | Normal | 9.5 | 9.5 | 5 | 0.5 | 5-1 | 1525998 | 5275146 |
| 42 | Sf | 51-91 | NW-N | Alluvial Fan | Dextral? | Normal | | | 9 | 1 | 2 | 1526037 | 5275192 |
| 43 | Sf | 79 | NW | Bedrock? | Dextral? | Normal | | | 4.5 | 0.5 | 2 | 1526244 | 5275200 |
| 44 | Sf | 79 | NW | Bedrock? | Dextral? | Normal | | | 2.5 | 0.2 | 2 | 1526568 | 5275266 |
| 45 | Sf | 76 | NW | Fluvial Terrace | Dextral | Normal | 20 | 2.5 | 2.2 | 0.1 | 2-2 | 1526799 | 5275406 |
| 46 | Sf | 76 | NW | Bedrock? | Dextral | Normal | | | 4.5 | 0.5 | 2 | 1526854 | 5275405 |
| 47 | Sf | 89 | N | Ridge Line? | Dextral | Normal | | | 2.5 | 0.2 | 2 | 1526884 | 5275514 |
| 48 | Sf | 89 | N | Ridge Line? | Dextral | Normal | 22 | 22 | 0.9 | 0.1 | 5-2 | 1526851 | 5275504 |
| 49 | Sf | 82 | NW | Stream Riser | Dextral | Normal | 9 | 2 | 0.8 | 0.2 | 3-2 | 1526807 | 5275619 |
| 50 | Sf | 58 | NW | Bedrock | Dextral | Normal | | | 1.3 | 0.3 | 2 | 1526976 | 5275699 |
| 51 | Sf | 58-93 | NW-N | Bedrock | Dextral? | Normal | | | 10.5 | 0.5 | 2 | 1527394 | 5275874 |
| 52 | Sf | 260 | NW | Bedrock | Normal | | | | 1 | | 2 | 1526446 | 5275387 |
| 53 | Sf | 247 | SE | Alluvial Fan | Reverse | | | | 5 | 0.5 | 2 | 1526049 | 5275283 |
| 54 | Sf | 75 | NW | Stream Riser | Dextral | Normal | | | 2 | 0.2 | 2 | 1525824 | 5275160 |
| 55 | Sf | 75 | NW | Stream Riser | Dextral | Normal | | | 0.5 | | 2 | 1525732 | 5275135 |
| 56 | Sf | 201 | SE | Alluvial Fan | Reverse | | | | 6 | 0.5 | 2 | 1525754 | 5275120 |
| 57 | Sf | 68 | NW | Channel Riser | Dextral | Normal | 20 | 20 | 1.2 | 0.2 | 5-2 | 1525797 | 5275094 |
| 58 | Sf | 84 | NW | Channel Riser | Dextral | Normal | 12 | 2 | 0.5 | | 2-2 | 1525700 | 5275073 |

| | | | | | | | | | | | | | |
|---|---|---|---|---|---|---|---|---|---|---|---|---|---|
| 59 | Sf | 222 | SE | Alluvial Fan | Reverse | | | | 5 | 0.5 | 2 | 1525705 | 5275046 |
| 60 | Sf | 70 | NW | Channel | Dextral | Normal | 6.5 | 1 | 0.5 | | 2-2 | 1525642 | 5275060 |
| 61 | Sf | 99 | SW | Alluvial Fan | Normal | | | | 6.5 | 0.5 | 2 | 1525648 | 5275083 |
| 62 | Sf | 254 | SE | Alluvial Fan | Reverse | | | | 2.5 | 0.5 | 2 | 1525486 | 5274993 |
| 63 | Sf | 84 | SE | Alluvial Fan | Dextral | Reverse | | | 2 | 0.2 | 2 | 1525516 | 5275015 |
| 64 | Sf | 76 | NW | Channel | Dextral | Normal | 7.5 | 2 | 0.4 | | 3-2 | 1525532 | 5274967 |
| 65 | Sf | 76 | NW | Channel | Dextral | Normal | 10.5 | 2.5 | 0.8 | | 3-2 | 1525512 | 5274952 |
| **Hope Fault- Hurunui segment- Macs Knob (see Fig. 3.6A in Chapter 3)** | | | | | | | | | | | | | |
| 1 | PSZ | 62 | SE | Fluvial deposits | Dextral | Reverse | | | 1.8 | 0.2 | 2 | 1527433 | 5275585 |
| 2 | **PSZ** | 62 | Unclear | Channel Riser | Dextral | ? | **15** | **3.5** | | | **3** | 1527550 | 5275642 |
| 3 | PSZ | 62 | SE | Alluvial Fan | Dextral | Reverse | | | 1 | | 1 | 1527630 | 5275691 |
| 4 | PSZ | 61 | SE | Alluvial Fan | Dextral | Reverse | | | 1.2 | 0.1 | 1 | 1527805 | 5275799 |
| 5 | **IPSZ** | 69 | Unclear | Channel | Dextral | ? | **16, *42** | **4, *12** | | | **3** | 1527886 | 5275832 |
| 6 | **PSZ** | 64 | SE | Postglacial fan | Dextral | Reverse | **157, *62** | **23, *10** | **2.5** | **0.5** | **2-1** | 1528137 | 5275986 |
| 7 | **IPSZ** | 65 | Unclear | Channel Riser | Dextral | | **69, *60** | **9, *20** | | | **2** | 1528385 | 5276092 |
| 8 | PSZ | 71 | SE | Postglacial Fan | Dextral | Reverse | | | 1.8 | 0.2 | 1 | 1528512 | 5276165 |
| 9 | Re | 241 | SE | Postglacial fan | Reverse | | | | 0.5 | | 1 | 1528622 | 5276181 |
| 10 | Re | 71 | NW | Postglacial Fan | Reverse | | | | 0.5 | | 1 | 1528592 | 5276218 |
| 11 | N | 262 | NE | Postglacial Fan | Normal | | | | 8 | 1 | 2 | 1528825 | 5276250 |
| 12 | N | 76 | SE | Postglacial Fan | Normal | | | | 1.4 | 0.1 | 2 | 1528812 | 5276303 |
| 13 | N | 86 | SE | Postglacial Fan | Normal | | | | 2.5 | 0.2 | 2 | 1528816 | 5276323 |
| **14** | **PSZ** | 69 | SE | Postglacial Fan | Dextral | Reverse | | | 6 | 0.5 | 1 | 1528890 | 5276338 |
| 15 | N | 89 | S | Postglacial Fan | Normal | | | | 2 | | 1 | 1528932 | 5276366 |
| 16 | **PSZ** | 62 | SE | Postglacial Fan (eastern edge) | Dextral | Reverse | **128** | **13** | **20** | **2** | **1-1** | 1529096 | 5276384 |
| 17 | **PSZ** | 62 | SE | Channel | Dextral | Reverse | **not assessable, *390** | ***20** | **14** | **1** | **5-1** | 1529025 | 5276342 |
| 18 | **PSZ** | 62 | SE | Channel | Dextral | Reverse | **not assessable, *166** | ***17** | **20** | **2** | **5-1** | 1529115 | 5276392 |
| 19 | **PSZ** | 64 | SW | Channel | Dextral | Reverse | **not assessable** | | **20** | **2** | **5-1** | 1529130 | 5276412 |
| 20 | **PSZ** | 64 | SW | Channel | Dextral | Reverse | **93** | **11** | **22** | **2** | **2-1** | 1529272 | 5276455 |
| 21 | N | 101 | SW | Postglacial Fan | Normal | | | | 3.5 | 0.3 | 2 | 1529293 | 5276450 |

| | | | | | | | | | | | | | | |
|---|---|---|---|---|---|---|---|---|---|---|---|---|---|---|
| 22 | N | 133 | SW | Postglacial Fan | Normal | | | | | 4. | | 2 | 1529277 | 5276521 |
| 23 | N | 129 | SW | Postglacial Fan | Normal | | | | | 5.5 | 0.5 | 2 | 1529287 | 5276530 |
| 24 | PSZ | 71 | SE | Postglacial Fan | Dextral | Reverse | | | | 4.5 | 0.5 | 2 | 1529310 | 5276527 |
| 25 | **PSZ** | 71 | SE | Postglacial Fan | Dextral | Reverse | **81** | **8** | | **3.2** | **0.2** | **1-2** | 1529368 | 5276547 |
| 26 | **PSZ** | 71 | SE | Channel | Dextral | Reverse | **88, *120, #137** | **7, *10** | | **2.5** | **0.5** | **1-2** | 1529487 | 5276561 |
| 27 | **PSZ** | 74 | SE | Channel | Dextral | Reverse | **126** | **45** | | **9** | **1** | **4-1** | 1529590 | 5276622 |
| 28 | **PSZ** | 74 | SE | Channel | Dextral | Reverse | **not assessable** | | | **15** | **1.5** | **5-1** | 1529657 | 5276584 |
| 29 | **PSZ** | 74 | SE | Postglacial Fan | Dextral | Reverse | **not assessable, *197** | ***19** | | **19** | **1.5** | **5-1** | 1529690 | 5276598 |
| 30 | **PSZ** | 74 | SE | Channel | Dextral | Reverse | **80, *90** | **5, *17** | | **14** | **1** | **1-1** | 1529805 | 5276637 |
| 31 | **PSZ** | 74 | SE | Channel | Dextral | Reverse | **19** | **19** | | **14** | **1** | **5-1** | 1529850 | 5276650 |
| 32 | **PSZ** | 73 | SE | Channel Riser | Dextral | Reverse | **56, *56** | **12, *17** | | **12.5** | **1.5** | **3-1** | 1530053 | 5276731 |
| 33 | **PSZ** | 73 | SE | Postglacial Fan | Dextral | Reverse | **60** | **13** | | **7.5** | **1** | **3-1** | 1530119 | 5276758 |
| 34 | SP | 65 | SE | Postglacial Fan | Dextral | Reverse | | | | 3.5 | 0.5 | 2 | 1529051 | 5276456 |
| 35 | SP | 65 | SE | Postglacial Fan | Dextral | Reverse | 9 | 0.5 | | 0.5 | | 1-2 | 1529132 | 5276477 |
| 36 | **PSZ** | 62 | SE | Postglacial Fan (apex/middle point) | Dextral | Reverse | **114** | **11** | | **0-1?** | | **1-2** | 1528852 | 5276277 |
| 37 | **IPSZ** | 62 | Unclear | Postglacial Fan (western edge) | Dextral | Reverse? | **120** | **10** | | | | **1** | 1528683 | 5276242 |
| **Hope Fault- Hurunui segment- Three Mile Stream (see Fig. 3.6B in Chapter 3)** | | | | | | | | | | | | | | |
| 1 | I PSZ | 64 | SE | Alluvium | Dextral | Reverse | | | | 0.9 | 0.1 | 2 | 1530898 | 5277058 |
| 2 | N | 96 | SW | Slope Deposits | Normal | | | | | 6 | 0.5 | 2 | 1531067 | 5277136 |
| 3 | **PSZ** | 87 | SE | Channel | Dextral | Reverse | **26** | **26** | | **1.5** | **0.5** | **5-2** | 1531181 | 5277167 |
| 4 | **PSZ** | 80 | SE | Channel | Dextral | Reverse | **54** | **6** | | **8** | **1** | **2-1** | 1531269 | 5277174 |
| 5 | PSZ | 80 | NW | Bedrock? | Dextral | Normal | | | | 2 | 0.3 | 2 | 1531354 | 5277194 |
| 6 | **PSZ** | 71 | NW | Channel | Dextral | Normal | **52** | **6** | | **9** | **1** | **2-1** | 1531466 | 5277234 |
| 7 | **PSZ** | 78 | NW | Channel | Dextral | Normal | **59** | **15** | | **2** | | **3-1** | 1531618 | 5277283 |
| 8 | **PSZ** | 78 | NW | Channel Riser | Dextral | Normal | **30.5** | **10.5** | | **2** | | **4-1** | 1531674 | 5277292 |
| 9 | **PSZ** | 62 | NW | Channel | Dextral | Normal | **35** | **5** | | **2** | **0.5** | **2-1** | 1531787 | 5277329 |
| 10 | **PSZ** | 62 | NW | Channel | Dextral | Normal | **73** | **8** | | **10** | **1** | **2-1** | 1531837 | 5277361 |
| 11 | PSZ | 73 | NW | Bedrock? | Dextral | Normal | | | | 5.5 | 0.5 | 2 | 1531933 | 5277368 |
| 12 | Re | 207 | SE | Bedrock? | Reverse | | | | | 2.5 | | 2 | 1532008 | 5277365 |

| | | | | | | | | | | | | | |
|---|---|---|---|---|---|---|---|---|---|---|---|---|---|
| 13 | PSZ | 73 | NW | Bedrock? | Dextral | Normal | | | 1.5 | 0.1 | 2 | 1532153 | 5277445 |
| 14 | Re | 210 | SE | Bedrock | Reverse | | | | 1 | 0.2 | 2 | 1532162 | 5277337 |
| 15 | Re | 192 | SE | Slope Deposits | Reverse | | | | 3.5 | 0.2 | 2 | 1532262 | 5277463 |
| 16 | IPSZ | 66 | SE | Slope Deposits | Dextral | Reverse | | | 4 | | 2 | 1532299 | 5277538 |
| 17 | PSZ | 64 | NW | Slope Deposits | Dextral | Normal | | | 0.2 | | 1 | 1532449 | 5277583 |
| 18 | PSZ | 66 | SE | Slope Deposits | Dextral | Reverse? | | | 2 | 0.2 | 2 | 1532551 | 5277651 |
| 19 | PSZ | 66 | NW | Slope Deposits | Dextral | Normal | | | 0.8 | | 1 | 1532647 | 5277684 |
| 20 | Sf | 71 | Unclear | Channel | Dextral | Normal? | 18 | 18 | | | 5 | 1531268 | 5277322 |
| 21 | Sf | 78 | Unclear | Channel Riser | Dextral | Normal? | 10.5 | 10.5 | | | 5 | 1531635 | 5277411 |
| 22 | Sf | 78 | NW? | Alluvial Fan | Dextral | Normal? | | | 1 | | 2 | 1531067 | 5277303 |
| 23 | Sf | 74 | NW? | Ridge Line | Dextral | Normal? | 8 | 8 | 0.2 | | 5-2 | 1531136 | 5277333 |
| 24 | Sf | 103 | SW | Slope Deposits | Normal | | | | 2 | 0.2 | 2 | 1531368 | 5277408 |
| 25 | Sf | 71 | NW | Slope Deposits | Dextral | Normal | 4 | 4 | 0.2 | | 5-2 | 1531352 | 5277451 |
| 26 | Sf | 114 | SE | Slope Deposits | Normal | | | | 4 | 1 | 2 | 1531804 | 5277475 |
| 27 | N | 113 | SE | Slope Deposits | Normal | | | | 1.8 | 0.2 | 2 | 1531948 | 5277481 |
| 28 | N | 84 | SE | Bedrock? | Normal | | | | 2.2 | 0.2 | 2 | 1531328 | 5277213 |
| 29 | N | 88 | SE | Bedrock? | Normal | | | | 2.5 | 0.5 | 2 | 1531362 | 5277236 |
| 30 | N | 88 | SE | Bedrock? | Normal | | | | 5 | 1 | 2 | 1531421 | 5277271 |
| 31 | N | 100 | SE | Bedrock? | Normal | | | | 2.5 | 0.5 | 2 | 1531627 | 5277307 |
| 32 | N | 98 | SE | Bedrock? | Normal | | | | 2.5 | 0.5 | 2 | 1531632 | 5277321 |
| 33 | N | 102 | SE | Bedrock? | Normal | | | | 1.5 | 0.5 | 2 | 1531645 | 5277331 |
| 34 | N | 117 | SE | Bedrock? | Normal | | | | 2 | | 2 | 1531620 | 5277359 |
| 35 | N | 89 | SW | Bedrock? | Normal | | | | 2 | | 2 | 1531581 | 5277293 |
| 36 | N | 87 | SW | Slope Deposits | Normal | | | | 3.5 | 0.5 | 2 | 1531730 | 5277357 |
| 37 | N | 82 | SW | Slope Deposits | Normal | | | | 6.5 | 0.5 | 2 | 1531733 | 5277381 |
| 38 | Sf | 78 | NW | Channel | Dextral? | Normal? | 32 | 32 | 7.5 | 0.2 | 5-2 | 1531746 | 5277106 |
| 39 | Sf | 80 | NW | Moraine? | Dextral? | Normal? | | | 30 | 2 | 2 | 1531955 | 5277085 |
| 40 | Sf | 69 | SE | Moraine? | Normal? | | | | 1 | | 2 | 1532448 | 5277190 |
| 41 | Sf | 81 | SE | Moraine? | Normal? | | | | 1.5 | 0.5 | 2 | 1532587 | 5277133 |
| 42 | Sf | 71 | SE | Slope Deposits | Normal? | | | | 1.2 | 0.2 | 2 | 1532386 | 5277391 |
| 43 | Sf | 63 | SE | Slope Deposits | Normal? | | | | 1.7 | 0.3 | 2 | 1532471 | 5277447 |

| | | | | | | | | | | | | | | |
|---|---|---|---|---|---|---|---|---|---|---|---|---|---|---|
| 44 | Sf | 65 | NW | Channel Riser | Dextral | Normal | 12.5 | 2 | 1.3 | 0.1 | 2-2 | 1532731 | 5277569 |
| 45 | Sf | 65 | NW | Channel Riser | Dextral | Normal | 13 | 2 | 1.2 | 0.2 | 2-2 | 1532753 | 5277596 |
| 46 | Sf | 91 | SW | Moraine? | Normal? | | | | 2.5 | 0.2 | 2 | 1532950 | 5277340 |
| **Hope Fault- Hurunui segment- Parakeet Stream (see Fig. 3.6C in Chapter 3)** | | | | | | | | | | | | | |
| 1 | **PSZ** | 69 | NW | Channel Riser | Dextral | Normal | **47** | **5** | **12** | **1** | **2-2** | 1532821 | 5277749 |
| 2 | **PSZ** | 76 | NW | Bedrock Feature? | Dextral | Normal | **189** | **9** | **18** | **1** | **1-2** | 1532879 | 5277760 |
| 3 | **PSZ** | 76 | NW | Channel | Dextral | Normal | **not assessable** | | **9** | **1** | **5-2** | 1532997 | 5277831 |
| 4 | **PSZ** | 76 | NW | Channel | Dextral | Normal | **not assessable** | | **1.5** | **0.5** | **5-2** | 1533123 | 5277848 |
| 5 | **PSZ** | 82 | NW | Channel | Dextral | Normal | **182 (best possible)** | **42** | **5** | | **3-2** | 1533254 | 5277876 |
| 6 | **PSZ** | 78 | NW | Bedrock Features? | Dextral | Normal | **150** | **50** | **1** | | **4-2** | 1533317 | 5277894 |
| 7 | **PSZ** | 77 | NW | Channel | Dextral | Normal | **34 (minimum)** | **4.5** | **2.5** | **0.5** | **2-2** | 1533405 | 5277927 |
| 8 | PSZ | 69 | NW | Alluvial Fan | Dextral | Normal | | | 0.5 | | 1 | 1533731 | 5278035 |
| 9 | PSZ | 77 | NW | Alluvial Fan | Dextral | Normal | | | 0.5 | | 1 | 1533603 | 5278016 |
| 10 | PSZ | 81 | NW | Alluvial Fan | Dextral | Normal | | | 2.5 | 0.5 | 1 | 1533600 | 5278043 |
| 11 | PSZ | 69 | NW | Channel Riser | Dextral | Normal | | | 2.7 | 0.3 | 2 | 1533720 | 5278060 |
| 12 | PSZ | 69 | NW | Alluvial Fan | Dextral | Normal | | | 0.5 | | 2 | 1533806 | 5278096 |
| 13 | PSZ | 89 | NW-N | Alluvial Fan | Dextral | Normal | | | 0.2 | | 2 | 1533864 | 5278087 |
| 14 | PSZ | 87 | NW | Alluvial Fan | Dextral | Normal | | | 3 | | 2 | 1533879 | 5278110 |
| 15 | PSZ | 76 | NW | Alluvial Fan | Dextral | Normal | | | 0.5 | | 2 | 1533889 | 5278132 |
| 16 | **PSZ** | 70 | NW? | Debris Flow Toe | Dextral | Normal | **56: min, 81:best** | **4,5** | **1.7** | **0.3** | **1-1** | 1534501 | 5278452 |
| 17 | **PSZ** | 70 | Unclear | Parakeet Stream | Dextral | Normal? | **84** | **5** | | | **1** | 1534618 | 5278504 |
| 18 | **PSZ** | 70 | Unclear | Channel Riser | Dextral | Normal? | **76** | **13** | | | **2** | 1534648 | 5278512 |
| 19 | **PSZ** | 63 | NW | Channel | Dextral | Normal | **94** | **15** | **1** | **0.2** | **2-1** | 1534690 | 5278529 |
| 20 | **PSZ** | 63 | NW | Shutter Scarp | Dextral | Normal | **115** | **15** | **3.3** | **0.2** | **2-1** | 1534722 | 5278559 |
| 21 | **PSZ** | 63 | NW | Channel | Dextral | Normal | **not assessable** | | **6** | **0.5** | **5-2** | 1534765 | 5278562 |
| 22 | PSZ | 69 | NW | Debris Flow Deposits | Dextral | Normal | | | 0.2 | | 2 | 1534878 | 5278625 |
| 23 | PSZ | 73 | NW | Debris Flow Deposits | Dextral | Normal | | | 1.6 | | 2 | 1534951 | 5278639 |
| 24 | N | 79 | SE | Debris Flow Deposits | Normal | | | | 5 | 1 | 2 | 1535000 | 5278690 |
| 25 | SP | 92 | SW | Debris Flow Deposits | Dextral | Reverse | 55 | 6 | 2.2 | 0.2 | 2-2 | 1535121 | 5278596 |
| 26 | Sf | 215 | SE | Bedrock | Reverse? | | | | 7 | 1 | 2 | 1535345 | 5278910 |

| | | | | | | | | | | | | | |
|---|---|---|---|---|---|---|---|---|---|---|---|---|---|
| 27 | Sf | 231 | SE | Bedrock | Reverse | | | | 6 | | 2 | 1535267 | 5278956 |
| 28 | N | 90 | S | Ridge | Dextral | Normal | 5.5, ^**2.3** | 0.5, ^**0.5** | 0.5, ^**0.3** | 0.1, ^**0.1** | 1,1-2,1 | 1534799 | 5278653 |
| 29 | Sf | 82 | SE | Debris Flow Deposits | Normal | | | | 2.2 | 0.2 | 2 | 1534557 | 5278599 |
| 30 | Sf | 73 | SE | Ridge Edge | Normal | | 12, ^**15** | 1, ^**2** | 0.6, ^**0.5** | 0.1, ^**0.5** | 1,1-2,2 | 1534451 | 5278553 |
| 31 | Sf | 73 | SE | Debris Flow Deposits | Normal | | | | 3.5 | 0.5 | 2 | 1534551 | 5278582 |
| 32 | Re | 221 | SE | Slope Deposits | Reverse | | | | 2.3 | 0.2 | 2 | 1534399 | 5278333 |
| 33 | Sf | 255 | NW | Bedrock | Normal | | | | 0.5 | | 2 | 1534225 | 5278387 |
| 34 | Sf | 237 | NW | Bedrock | Normal | | | | 0.5 | | 2 | 1534060 | 5278393 |
| 35 | Sf | 219 | NW | Bedrock | Normal | | | | 2.9 | 0.1 | 2 | 1534261 | 5278533 |
| 36 | Sf | 247 | NW | Bedrock | Normal | | | | 0.2 | | 2 | 1534059 | 5278419 |
| 37 | Sf | 241 | NW | Bedrock | Normal | | | | 0.2 | | 2 | 1534056 | 5278445 |
| 38 | Sf | 237 | NW | Bedrock | Normal | | | | 0.3 | 0.1 | 2 | 1534087 | 5278481 |
| 39 | Sf | 237 | NW | Bedrock? | Normal | | | | 0.5 | | 2 | 1533628 | 5278144 |
| 40 | Sf | 276 | NE | Bedrock? | Normal | | | | 0.5 | | 2 | 1533500 | 5278144 |
| 41 | Sf | 256 | NW | Bedrock? | Normal | | | | 1.3 | 0.2 | 2 | 1533558 | 5278186 |
| 42 | N | 106 | SW | Bedrock? | Normal | | | | 1.5 | 0.2 | 2 | 1533589 | 5278108 |
| 43 | N | 101 | SW | Alluvial Fan | Normal | | | | 3.5 | 0.5 | 2 | 1533501 | 5278004 |
| 44 | N | 98 | SW | Alluvial Fan | Normal | | | | 2 | 0.2 | 2 | 1533484 | 5277984 |
| 45 | N | 112 | SW | Alluvial Fan | Normal | | | | 7 | 1 | 2 | 1533426 | 5277969 |
| 46 | Sf | 71 | SE | Bedrock? | Normal | | | | 5 | 0.5 | 2 | 1533353 | 5278003 |
| 47 | Sf | 76 | SE | Bedrock? | Normal | | | | 2.5 | | 2 | 1533348 | 5278035 |
| 48 | N | 93 | S-SW | Bedrock? | Normal | | | | 3.5 | 0.5 | 2 | 1533294 | 5277979 |
| 49 | N | 113 | SW | Bedrock? | Normal | | | | 2.5 | 0.5 | 2 | 1533309 | 5277932 |
| 50 | N | 102 | SW | Bedrock? | Normal | | | | 3.5 | 0.5 | 2 | 1533318 | 5277917 |
| 51 | Re | 237 | SE | Alluvial Fan | Reverse | | | | 3 | | 2 | 1533816 | 5277974 |
| 52 | Re | 229 | SE | Alluvial Fan | Reverse | | | | 3 | | 2 | 1533626 | 5277930 |
| 53 | Re | 233 | SE | Alluvial Fan | Reverse | | | | 2 | | 2 | 1533470 | 5277869 |
| 54 | N | 93 | SW | Alluvial Fan | Normal | | | | 4.2 | 0.2 | 2 | 1533426 | 5277912 |
| 55 | N | 107 | SW | Alluvial Fan | Normal | | | | 4 | 0.2 | 2 | 1533399 | 5277893 |
| 56 | N | 110 | SW | Alluvial Fan | Normal | | | | 3 | 0.5 | 2 | 1533413 | 5277867 |
| 57 | Sf | 252 | SE | Channel | Dextral | Reverse? | 26.5 | 2.5 | | | 1 | 1533321 | 5277792 |

| | | | | | | | | | | | | | |
|---|---|---|---|---|---|---|---|---|---|---|---|---|---|
| 58 | Sf | 231 | SE | Alluvial Fan | Dextral? | Reverse | | | 7.5 | 0.5 | 2 | 1533329 | 5277721 |
| 59 | Sf | 275 | SW-S | Alluvial Fan | Reverse | | | | 2 | | 2 | 1533197 | 5277674 |
| 60 | Sf | 252 | SE | Alluvial Fan | Reverse | | | | 4 | 0.5 | 2 | 1533170 | 5277743 |
| 61 | N | 106 | SW | Alluvial Fan | Normal | | | | 2 | | 2 | 1533137 | 5277814 |
| 62 | Sf | 72 | NW | Channel Riser | Dextral | Normal? | 12 | 2 | 0.5 | | 2-2 | 1532918 | 5277681 |
| 63 | Sf | 254 | SE | Alluvial Fan | Dextral? | Reverse | | | 2.2 | 0.2 | 2 | 1533153 | 5277584 |
| 64 | Sf | 71 | SE? | Channel | Dextral | Reverse? | 12 | 12 | | | 5 | 1533175 | 5277544 |
| 65 | Sf | 71 | SE ? | Channel | Dextral | Reverse? | 3 | 3 | | | 5 | 1533252 | 5277566 |
| 66 | Sf | 71 | SE? | Channel | Dextral | Reverse? | 9 | 9 | | | 5 | 1533294 | 5277578 |
| **Hope Fault- Hurunui segment- Lodge, Hope and Kiwi Streams (see Fig. 3.7A in Chapter 3)** | | | | | | | | | | | | | |
| 1 | **PSZ** | 58 | ? | Fluvial Terrace | Dextral | ? | **27** | **3** | | | **2** | 1535496 | 5278917 |
| 2 | PSZ | 72 | NW | Bedrock | Dextral | Normal | | | 3.5 | 0.5 | 2 | 1535582 | 5278941 |
| 3 | PSZ | 72 | NW | Bedrock | Dextral | Normal | | | 9.5 | 0.5 | 2 | 1535664 | 5278960 |
| 4 | PSZ | 71 | NW | Bedrock | Dextral | Normal | | | 1 | 0.1 | 2 | 1535756 | 5278988 |
| 5 | PSZ | 66 | NW | Bedrock | Dextral | Normal | | | 5.5 | | 2 | 1535961 | 5279071 |
| 6 | PSZ | 67 | NW | Bedrock | Dextral | Normal | | | 0.5 | | 2 | 1536088 | 5279131 |
| 7 | Re | 231 | SE | Bedrock | Reverse | | | | 5.5 | 0.5 | 2 | 1536412 | 5279246 |
| 8 | PSZ | 53 | SE | Hillslope Deposits | Dextral | Reverse | | | 13 | 1 | 2 | 1536797 | 5279528 |
| 9 | PSZ | 61 | SE | Hillslope Deposits | Dextral | Reverse | | | 1.8 | 0.2 | 2 | 1536962 | 5279583 |
| 10 | Re | 230 | SE | Hillslope Deposits | Reverse | | | | 2 | 0.2 | 2 | 1536993 | 5279624 |
| 11 | PSZ | 65 | SE | Landslide Deposits | Dextral | Reverse | | | 2 | 0.5 | 2 | 1537080 | 5279651 |
| 12 | Re | 230 | SE | Landslide Deposits | Reverse | | | | 1 | 0.2 | 1 | 1537058 | 5279695 |
| 13 | PSZ | 58 | NW | Landslide Deposits | Dextral | Normal | | | 3.5 | 0.5 | 1 | 1537390 | 5279786 |
| 14 | PSZ | 50 | NW | Landslide Deposits | Dextral | Normal | | | 2.5 | 0.2 | 1 | 1537432 | 5279848 |
| 15 | SP | 84 | SE | Landslide Deposits | Dextral | Normal? | 34 | 34 | 2.5 | 0.5 | 5-2 | 1537556 | 5279883 |
| 16 | SP | 91 | SE | Moraine Toe? | Dextral | Normal? | 7.5 | 7.5 | 4.5 | 0.5 | 5-2 | 1537695 | 5279879 |
| 17 | Re | 86 | NW | Moraine Outwash? | Reverse | | | | 2.8 | 0.2 | 2 | 1537931 | 5279873 |
| 18 | Re | 265 | SE | Moraine Outwash? | Reverse | | | | 2.8 | 0.2 | 2 | 1537934 | 5279834 |
| 19 | SP | 71 | SE | Moraine Toe? | Dextral | Normal? | 9.5 | 9.5 | 2 | | 5-2 | 1537708 | 5279935 |
| 20 | SP | 66 | SE | Moraine back basin? | Dextral | Normal? | 14 | 14 | 0.5 | | 5-2 | 1537637 | 5280013 |

| | | | | | | | | | | | | | |
|---|---|---|---|---|---|---|---|---|---|---|---|---|---|
| 21 | SP | 74 | SE | Moraine Toe? | Dextral | Normal? | 14 | 14 | 2 | | 5-2 | 1537761 | 5280055 |
| 22 | SP | 89 | SE-S | Moraine Toe? | Dextral | Normal? | 10 | 10 | 0.8 | | 5-2 | 1537752 | 5280020 |
| 23 | SP | 90 | S | Landslide Deposits | Dextral | Normal? | 7.5 | 7.5 | 1.5 | | 5-2 | 1537592 | 5279912 |
| 24 | Sf | 60 | SE | Furrow across surface | Normal? | | | | 2.5 | 0.5 | 2 | 1537568 | 5279792 |
| 25 | Sf | 54 | NW | Landslide Deposits? | Normal? | | | | 1.1 | 0.1 | 2 | 1537423 | 5279719 |
| 26 | Sf | 60 | SE | Landslide Deposits? | Normal? | | | | 1.6 | 0.2 | 2 | 1537463 | 5279736 |
| 27 | Sf | 73 | NW | Bedrock | Normal | | | | 3.8 | 0.2 | 1 | 1535935 | 5279213 |
| 28 | Sf | 56 | NW | Bedrock | Normal | | | | 5.5 | 0.5 | 1 | 1535783 | 5279108 |
| 29 | Sf | 57 | NW | Bedrock | Normal | | | | 4.7 | 0.3 | 1 | 1535704 | 5279051 |
| 30 | Sf | 66 | NW | Bedrock | Normal | | | | 1.3 | 0.2 | 1 | 1535699 | 5279211 |
| 31 | Sf | 63 | NW | Bedrock | Normal | | | | 4.5 | 0.2 | 1 | 1535867 | 5279314 |
| 32 | Sf | 58 | NW | Bedrock | Normal | | | | 2.7 | 0.3 | 1 | 1535647 | 5279251 |
| **Hope fault- Hurunui segment- Hope River (see Fig. 3.7B-C in Chapter 3)** | | | | | | | | | | | | | |
| 1 | PSZ | 83 | NW | Postglacial Fan | Dextral | Normal | | | 0.8 | 0.1 | 1 | 1541093 | 5281252 |
| 2 | PSZ | 79 | NW | Alluvial Fan | Dextral | Normal | | | 1.5 | 0.1 | 1 | 1541486 | 5281362 |
| 3 | PSZ | 76 | NW | Fluvial Terrace | Dextral | Reverse? | | | 0.8 | 0.1 | 1 | 1541622 | 5281400 |
| 4 | PSZ | 73 | NW | Postglacial Fan | Dextral | Normal | | | 1.6 | 0.1 | 1 | 1542069 | 5281531 |
| 5 | PSZ | 77 | NW | Postglacial Fan | Dextral | Normal | | | 3.2 | 0.2 | 1 | 1542179 | 5281565 |
| 6 | N | 268 | NE-N | Postglacial Fan | Normal | | | | 1.6 | | 1 | 1542164 | 5281600 |
| 7 | **PSZ** | 68 | NW | Alluvial Fan | Dextral | Normal | | | 1.5 | 0.1 | 1 | 1542318 | 5281611 |
| 8 | **PSZ** | 68 | NW | Gravity Failure Feature | Dextral | Normal | **10.5, ^10** | **0.5, ^1** | **0.6** | **0.1** | **1,1-1** | 1542335 | 5281619 |
| 9 | **PSZ** | 73 | NW | Alluvial Fan | Dextral | Normal | **13 , ^14** | **3, ^3** | **0.4** | **0.1** | **3, 1-1** | 1542417 | 5281641 |
| 10 | PSZ | 74 | NW | Alluvial Fan | Dextral | Normal | | | 1.2 | 0.2 | 1 | 1542504 | 5281666 |
| 11 | **PSZ** | 74 | NW | Debris Deposit | Dextral | Normal | **^2.6** | **^0.3** | **0.5, ^0.85** | **0.1, ^0.05** | **1** | 1542540 | 5281676 |
| 12 | PSZ | 81 | SE | Debris Deposit | Dextral | Reverse | | | 1.7 | 0.3 | 2 | 1542554 | 5281691 |
| 13 | N | 100 | SW | Debris Deposit | Normal | | | | 1.7 | 0.3 | 2 | 1542555 | 5281676 |
| 14 | PSZ | 81 | NW | Furrow across surface | Dextral | Normal | | | 0.2 | | 2 | 1542573 | 5281690 |
| 15 | **PSZ** | 81 | SE | Alluvial Fan/Channel | Dextral | Reverse | **6.5, ^4.6** | **1, ^0.5** | **1.1** | **0.1** | **2,1-1** | 1542644 | 5281700 |
| 16 | **PSZ** | 57 | NW? | Channel Riser | Dextral | Normal? | **6.2, ^5.4** | **2.3, ^0.6** | **2.5** | **0.5** | **4,1-2** | 1542686 | 5281723 |
| 17 | Re | 30 | NW | Alluvial Fan | Reverse | | | | 0.5 | 0.1 | 2 | 1542661 | 5281722 |

| | | | | | | | | | | | | | |
|---|---|---|---|---|---|---|---|---|---|---|---|---|---|
| 18 | Re | 222 | SE | Alluvial Fan | Reverse | | | | 0.5 | | 2 | 1542703 | 5281725 |
| 19 | **PSZ** | 67 | NW | Channel Riser | Dextral | Normal | **6, ^4.6** | **1, ^0.8** | **1.8, ^1.45** | **0.2, ^0.3** | **2,1-2-1** | 1542805 | 5281773 |
| 20 | **PSZ** | 63 | NW | Ridge | Dextral | Normal | **5, ^3** | **0.5, ^0.5** | **0.2, ^0.6** | **^0.2** | **1,1-2,2** | 1542876 | 5281817 |
| 21 | PSZ | 68 | NW | Alluvial Fan | Dextral? | Normal | | | 1.3 | 0.2 | 2 | 1542922 | 5281907 |
| 22 | PSZ | 73 | NW | Alluvial Fan | Dextral? | Normal | | | 1 | 0.1 | 2 | 1542983 | 5281929 |
| 23 | PSZ | 86 | NW | Postglacial Fan | Dextral? | Normal | | | 6.5 | 0.5 | 2 | 1543112 | 5281950 |
| 24 | PSZ | 86 | NW | Postglacial Fan | Dextral? | Normal | | | 6.5 | 0.5 | 2 | 1543219 | 5281962 |
| 25 | PSZ | 86 | NW | Postglacial Fan | Dextral? | Normal | | | 1.6 | 0.1 | 2 | 1543286 | 5281968 |
| 26 | PSZ | 81 | NW | Postglacial Fan | Dextral? | Normal | | | 1.4 | 0.1 | 2 | 1543248 | 5281952 |
| 27 | PSZ | 83 | NW | Postglacial Fan | Dextral? | Normal | | | 0.6 | 0.1 | 2 | 1543264 | 5281942 |
| 28 | N | 93 | SW | Paleochannel Bed | Normal | | | | 2 | 0.2 | 2 | 1543346 | 5281955 |
| 29 | N | 94 | SW | Paleochannel Bed | Normal | | | | 2.7 | 0.3 | 2 | 1543310 | 5281933 |
| 30 | SP | 95 | NE? | Paleochannel Riser | Dextral | Normal? | 14.5 | 2.5 | | | 2 | 1543346 | 5281904 |
| 31 | Re | 247 | SE | Terrace Tread | Reverse | | | | 1.3 | 0.2 | 2 | 1543339 | 5281874 |
| 32 | SP | 95 | NE | Channel | Dextral | Normal | 7.5 | 0.5 | 0.2 | | 1-2 | 1543280 | 5281907 |
| 33 | SP | 95 | NE | Channel | Dextral | Normal | 8 | 1 | 0.5 | 0.1 | 2-2 | 1543208 | 5281914 |
| 34 | SP | 92 | NE | Channel Riser | Dextral | Normal | 9 | 2 | 0.8 | 0.2 | 3-2 | 1543158 | 5281917 |
| 35 | N | 116 | SW | Postglacial Fan | Normal | | | | 0.8 | 0.2 | 2 | 1543160 | 5281945 |
| 36 | N | 107 | SW | Postglacial Fan | Normal | | | | 1.1 | 0.1 | 2 | 1543152 | 5281936 |
| 37 | Re | 215 | SE | Postglacial Fan | Reverse | | | | 0.6 | 0.1 | 2 | 1543122 | 5281912 |
| 38 | Re | 213 | SE | Postglacial Fan | Reverse | | | | 0.4 | | 2 | 1543110 | 5281909 |
| 39 | Re | 220 | SE | Postglacial Fan | Reverse | | | | 0.5 | | 2 | 1543100 | 5281908 |
| 40 | Re | 212 | SE | Postglacial Fan | Reverse | | | | 0.3 | | 2 | 1543087 | 5281905 |
| 41 | SP | 92 | NE | Paleochannel Bed | Dextral | Normal | 4 | 0.5 | 0.2 | | 2-2 | 1543154 | 5281905 |
| 42 | Re | 239 | SE | Alluvium | Reverse | | | | 0.2 | | 2 | 1543032 | 5281902 |
| 43 | Re | 233 | SE | Terrace Tread | Reverse | | | | 0.8 | 0.1 | 2 | 1542984 | 5281881 |
| 44 | Re | 238 | SE | Terrace Tread | Reverse | | | | 0.6 | 0.1 | 2 | 1542987 | 5281896 |
| 45 | N | 122 | SW | Postglacial Fan | Normal | | | | 2.5 | 0.5 | 2 | 1543075 | 5282013 |
| 46 | PSZ | 86 | NW | Postglacial Fan | Dextral? | Normal | | | 1.7 | 0.1 | 2 | 1543132 | 5281993 |
| 47 | PSZ | 77 | SE | Postglacial Fan | Dextral? | Normal | | | 1.8 | 0.1 | 2 | 1543216 | 5282006 |
| 48 | PSZ | 69 | NW | Postglacial Fan | Dextral? | Normal | | | 1.3 | 0.1 | 2 | 1543218 | 5282040 |

| | | | | | | | | | | | | | |
|---|---|---|---|---|---|---|---|---|---|---|---|---|---|
| 49 | N | 100 | SW | Postglacial Fan | Normal | | | | 2.2 | 0.2 | 2 | 1543101 | 5282051 |
| 50 | PSZ | 74 | NW | Postglacial Fan | Dextral? | Normal | | | 3.5 | | 2 | 1543282 | 5282000 |
| 51 | PSZ | 86 | NW | Postglacial Fan | Dextral? | Normal | | | 1.4 | 0.2 | 2 | 1543346 | 5282010 |
| 52 | PSZ | 71 | NW | Postglacial Fan | Dextral? | Normal | | | 2 | 0.2 | 2 | 1543417 | 5282023 |
| 53 | N | 114 | SW | Postglacial Fan | Normal | | | | 1 | 0.1 | 2 | 1543295 | 5282052 |
| 54 | PSZ | 83 | NW | Postglacial Fan | Dextral? | Normal | | | 0.6 | | 2 | 1543328 | 5282022 |
| 55 | PSZ | 80 | NW | Postglacial Fan | Dextral? | Normal | | | 2.5 | 0.5 | 2 | 1543326 | 5281990 |
| 56 | PSZ | 80 | NW | Postglacial Fan | Dextral? | Normal | | | 4.5 | 0.5 | 2 | 1543366 | 5281999 |
| 57 | Re | 175 | SW-S | Postglacial Fan | Reverse | | | | 1 | 0.1 | 2 | 1543375 | 5281997 |
| 58 | N | 97 | SW | Paleochannel Bed | Normal | | | | 1.7 | 0.3 | 2 | 1543426 | 5282003 |
| 59 | Re | 233 | SE | Paleochannel Bed | Reverse | | | | 1.7 | 0.3 | 2 | 1543476 | 5281962 |
| 60 | Re | 233 | SE | Paleochannel Bed | Reverse | | | | 2.3 | 0.2 | 2 | 1543525 | 5282000 |
| 61 | Re | 232 | SE | Paleochannel Bed | Reverse | | | | 1.1 | 0.1 | 2 | 1543427 | 5281900 |
| 62 | PSZ | 83 | NW | Postglacial Fan | Dextral | Normal | | | 1.1 | 0.1 | 2 | 1543445 | 5282048 |
| 63 | PSZ | 83 | NW | Postglacial Fan | Dextral | Normal | | | 2.4 | 0.2 | 2 | 1543525 | 5282049 |
| 64 | Re | 165 | NE | Postglacial Fan | Reverse | | | | 4.5 | 0.5 | 2 | 1543409 | 5282056 |
| 65 | Re | 359 | SW-W | Postglacial Fan | Reverse | | | | 0.4 | | 2 | 1543445 | 5282071 |
| 66 | N | 90 | S | Postglacial Fan | Normal | | | | 1.5 | 0.2 | 2 | 1543360 | 5282093 |
| 67 | Re | 208 | SE | Postglacial Fan | Reverse | | | | 1.5 | | 2 | 1543412 | 5282097 |
| 68 | Re | 213 | SE | Postglacial Fan | Reverse | | | | 1.3 | | 2 | 1543437 | 5282117 |
| 69 | Re | 226 | SE | Postglacial Fan | Reverse | | | | 1 | | 2 | 1543488 | 5282166 |
| 70 | PSZ | 78 | NW | Postglacial Fan | Dextral? | Normal | | | 3.5 | 0.5 | 2 | 1543458 | 5282088 |
| 71 | PSZ | 78 | NW | Postglacial Fan | Dextral? | Normal | | | 5.2 | 0.2 | 2 | 1543509 | 5282101 |
| 72 | Re | 210 | SE | Postglacial Fan | Reverse | | | | 0.8 | | 2 | 1543566 | 5282130 |
| 73 | PSZ | 80 | NW | Postglacial Fan | Dextral? | Normal | | | 8 | 0.5 | 2 | 1543580 | 5282099 |
| 74 | PSZ | 80 | NW | Postglacial Fan | Dextral? | Normal | | | 14 | 1 | 2 | 1543668 | 5282110 |
| 75 | N | 97 | SW | Postglacial Fan | Normal | | | | 2 | 0.1 | 2 | 1543473 | 5282121 |
| 76 | N | 83 | SE | Postglacial Fan | Normal | | | | 2.2 | 0.2 | 2 | 1543534 | 5282156 |
| 77 | N | 94 | SW | Postglacial Fan | Normal | | | | 1.5 | 0.2 | 2 | 1543528 | 5282168 |
| 78 | N | 96 | SW | Postglacial Fan | Normal | | | | 1.3 | 0.1 | 2 | 1543482 | 5282197 |
| 79 | N | 96 | SE | Postglacial Fan | Normal | | | | 3 | 0.2 | 2 | 1543561 | 5282178 |

| | | | | | | | | | | | | | |
|---|---|---|---|---|---|---|---|---|---|---|---|---|---|
| 80 | N | 92 | S-SW | Postglacial Fan | Normal | | | | 2 | 0.2 | 2 | 1543507 | 5282216 |
| 81 | N | 92 | S-SW | Postglacial Fan | Normal | | | | 2.2 | 0.2 | 2 | 1543594 | 5282202 |
| 82 | N | 92 | S-SW | Postglacial Fan | Normal | | | | 2.2 | 0.2 | 2 | 1543666 | 5282213 |
| 83 | N | 101 | SW | Postglacial Fan | Normal | | | | 1.2 | 0.2 | 2 | 1543680 | 5282223 |
| 84 | N | 105 | SW | Postglacial Fan | Normal | | | | 3 | 0.3 | 2 | 1543705 | 5282235 |
| 85 | N | 105 | SW | Postglacial Fan | Normal | | | | 1.3 | 0.3 | 2 | 1543606 | 5282268 |
| 86 | PSZ | 69 | NW | Postglacial Fan | Dextral? | Normal | | | 1.4 | 0.1 | 2 | 1543590 | 5282139 |
| 87 | PSZ | 69 | NW | Postglacial Fan | Dextral? | Normal | | | 1.3 | 0.2 | 2 | 1543688 | 5282182 |
| 88 | PSZ | 76 | NW | Postglacial Fan | Dextral? | | | | 2.7 | 0.3 | 2 | 1543854 | 5282237 |
| 89 | PSZ | 76 | NW | Postglacial Fan | Dextral? | | | | 2 | 0.2 | 2 | 1543942 | 5282258 |
| 90 | Re | 245 | SE | Postglacial Fan | Reverse | | | | 1.5 | | 2 | 1543839 | 5282232 |
| 91 | Re | 246 | SE | Postglacial Fan | Reverse | | | | 2 | | 2 | 1543966 | 5282264 |
| 92 | PSZ | 79 | NW | Postglacial Fan | Dextral? | Normal | | | 3.7 | 0.3 | 2 | 1543807 | 5282207 |
| 93 | PSZ | 79 | NW | Postglacial Fan | Dextral? | Normal | | | 2.5 | 0.5 | 2 | 1543892 | 5282231 |
| 94 | N | 102 | SW | Postglacial Fan | Normal | | | | 0.5 | | 2 | 1543922 | 5282219 |
| 95 | PSZ | 78 | NW | Postglacial Fan | Dextral? | Normal | | | 5 | 0.5 | 2 | 1543841 | 5282161 |
| 96 | PSZ | 51 | NW | Postglacial Fan | Dextral? | Normal? | | | 1 | | 2 | 1543842 | 5282122 |
| 97 | PSZ | 73 | NW | Postglacial Fan | Dextral? | Normal | | | 2.7 | 0.3 | 2 | 1544050 | 5282239 |
| 98 | PSZ | 87 | NW | Postglacial Fan | Dextral? | Normal | | | 0.8 | | 2 | 1544036 | 5282266 |
| 99 | PSZ | 78 | NW | Postglacial Fan | Dextral? | Normal | | | 1.2 | 0.2 | 2 | 1543946 | 5282323 |
| 100 | PSZ | 50 | NW | Postglacial Fan | Dextral? | Normal | | | 8 | 1 | 2 | 1544722 | 5282611 |
| 101 | Sf | 80 | SE | Fluvial Terrace | Normal? | | | | 1.7 | | 2 | 1544818 | 5282143 |
| 102 | Sf | 83 | SE | Postglacial Fan | Normal? | | | | 1.6 | 0.2 | 2 | 1543769 | 5282341 |
| 103 | Sf | 89 | SE-S | Terrace Riser | Dextral | Normal? | 14 | 1 | 1.2 | 0.2 | 1-1 | 1543134 | 5282335 |
| 104 | Sf | 8 | SE-S | Terrace Tread | Dextral? | Normal? | | | 2.5 | 0.5 | 2 | 1543097 | 5282335 |
| 105 | SP | 101 | S-SW | Ridge Line | Dextral | Normal? | 8.5 | 0.5 | 4.5 | 0.5 | 1-2 | 1542745 | 5281626 |
| 106 | SP | 101 | S-SW | Channel Riser | Dextral | ? | 9.5 | 0.5 | 1.7 | 0.2 | 5-1 | 1542680 | 5281629 |
| 107 | Re | 249 | SE | Alluvial Terrace | Reverse | | | | 1 | 0.1 | 2 | 1542757 | 5281591 |
| 108 | Sf | 151 | NE | Fluvial Terrace | Normal? | | | | 0.5 | 0.1 | 2 | 1543019 | 5281356 |
| 109 | Sf | 157 | NE | Fluvial Terrace | Normal? | | | | 0.5 | 0.1 | 2 | 1543054 | 5281360 |

# SUPPLEMENTS

# SUPPLEMENT TO CHAPTER 1: INFLUENCE OF TOPOGRAPHY AND BASEMENT DEPTH ON SURFACE RUPTURE MORPHOLOGY REVEALED FROM LIDAR AND FIELD MAPPING, HOPE FAULT, NEW ZEALAND

**Supplementary data associated with this article can be found in the online version, at http://dx.doi.org/10.1016/j.tecto.2014.05.032. These data include Google map (Kml file) of the most important areas described in this article.**

This file is composed of four main parts: (1) two supplementary figures that show continuous uninterpreted and structurally-interpreted orthophotos strips (1-4); Orthophotos strips are equivalents of the LiDAR hillshade strips in Figs. 1.7-1.10. They are provided as they show natural setting of the terrain excluding and including structures derived from LiDAR. Therefore, one can easily compare them with the bare LiDAR imagery, and the geomorphic maps produced in this study. (2) Relationship between fault scarps and kinematics. (3) Secondary structures associated with the Alpine Fault and the Conway segment of the Hope Fault. (4) detailed structural investigations of McKenzie site and eastern extent of the LiDAR swath (near Boundary Stream).

## S1.1 Supplementary figures

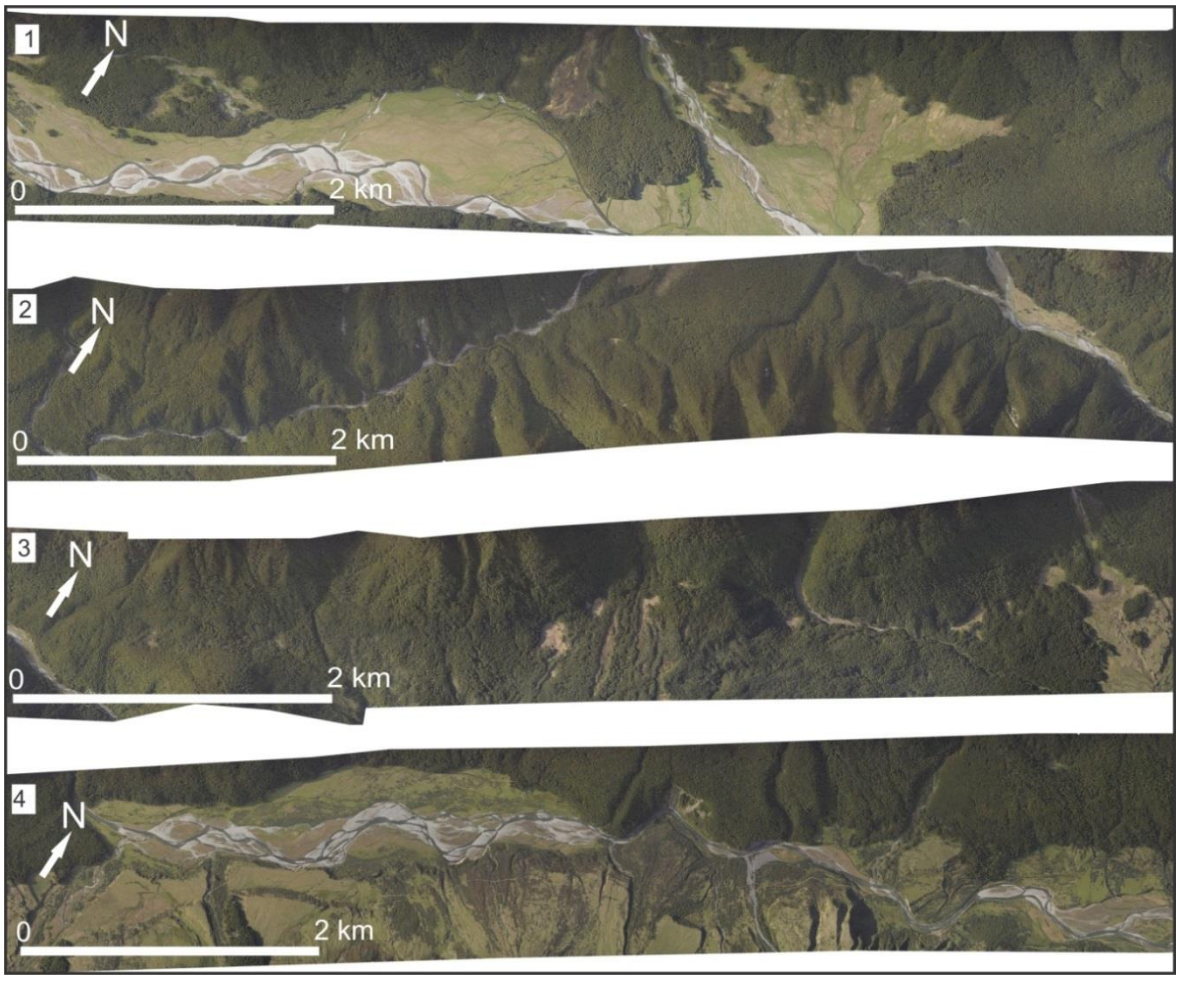


Figure S1.1. Natural setting of the terrain along the LiDAR swath from west to east (1-4).

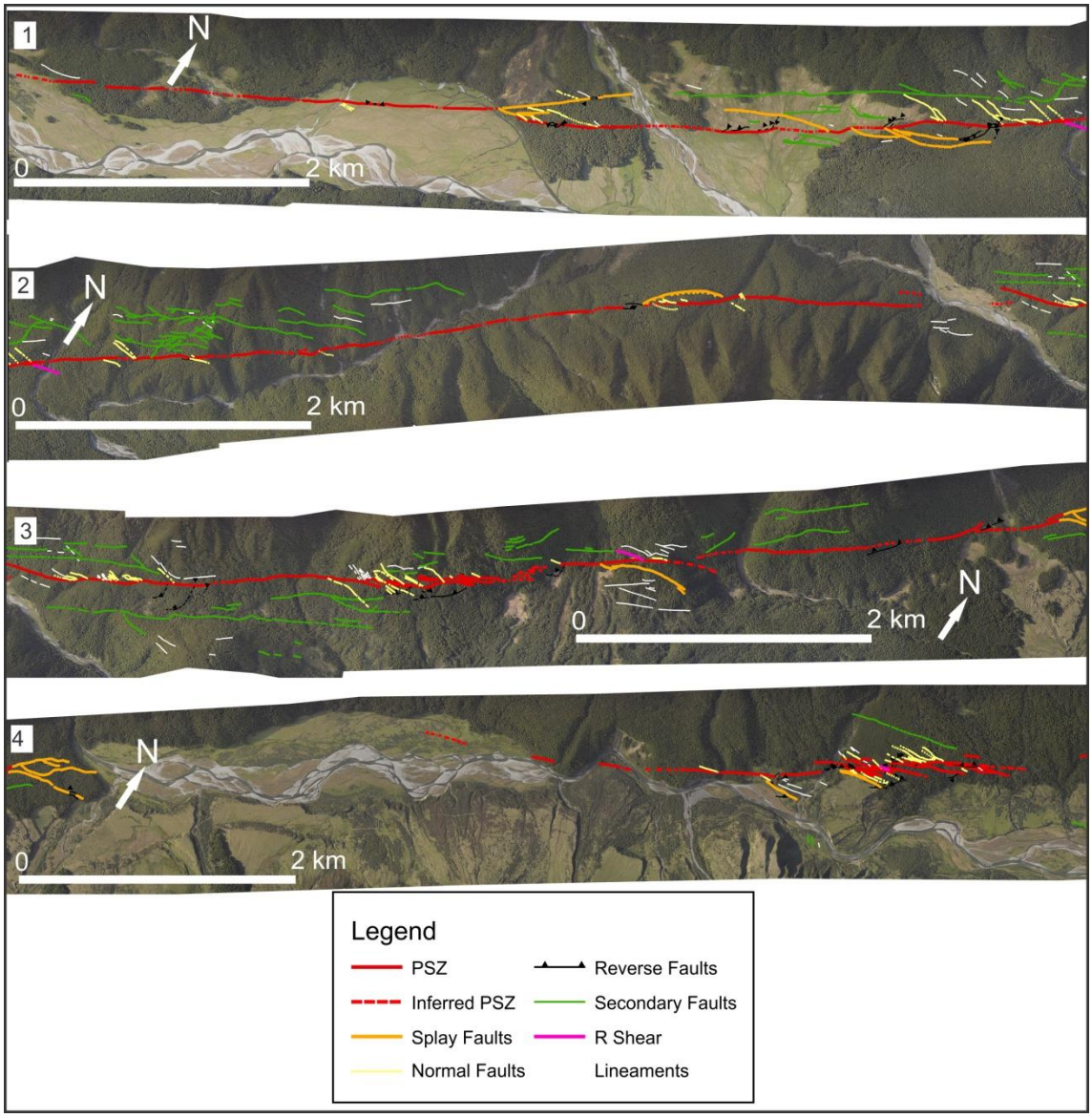


Figure S1.2. Natural setting of the terrain including interpreted structures along the LiDAR swath from west to east (1-4).

## S1.2 Relationship between fault scarps and kinematics

According to the PSZ characteristics and the FDZ appearance, two alternative hypotheses can be made. Since scarps are mostly uphill-facing with apparent heights varying from 0-19 m, one might assume that the Hurunui segment is a dextral-normal fault with a shallow dip angle toward NW. On the other hand, since the fault has a gentle curve in its middle (concave side to the south) with a south-facing scarp, one might assume that the Hurunui segment is a dextral-reverse fault with a shallow dip angle toward the SE.

Here, I note that Scarp heights in this area are not direct proxies of oblique motion associated with the strike-slip Hurunui segment. Scarp heights are inevitably overestimated at areas where streams have actively been incising base of the scarps, or where the fault has cut

through a fan surface and dextrally juxtaposed surfaces of pre-existing differential elevations. In the latter, the offset apex of a fan on one side of the fault can easily be misjudged as the vertical component of slip. Therefore, care must be taken in cases where landscape, erosional or depositional processes influence the fault appearance on the surface.

## S1.3 A comparison of secondary structures associated with faults

### S1.3.1 Secondary structures associated with the Alpine Fault

Similarly-sized ($10^0$-$10^3$ m; called "third order faults") dextral-normal faults, resulting from parallel partitioning of the Alpine Fault, were reported on the HW of the transpressive Alpine Fault by Barth et al. (2012). Asymmetric positive flower structures (fault wedges) were formed between these faults and frontal dextral- reverse faults (both dipping SE) (Barth et al., 2012). They suggested that the frontal and rear faults should be merging together at shallow depths (< 600 m) to form the dextral-reverse PSZ of the Alpine Fault. The wedges in their study have widths of ~200-600 m. Their fault kinematic analysis indicated that the dextral-normal faults could easily form rearward on the HW because the strike-slip component of the Alpine Fault cannot be accommodate on high-friction and low angle surfaces near the frontal dextral reverse fault. Therefore, they suggested that the formation of the dextral-normal faults on the HW is independent of topography, but depends on the thickness of the FW sediments and width of the fault damage zone. However, they mentioned that the second order ($10^3$-$10^4$ m) dextral-normal faults, also documented in their study, are the result of serial partitioning of the Alpine Fault due to being in proximity to large valleys and mountain ranges.

### S1.3.2 Secondary structures associated with the Conway segment of the Hope Fault

Similar secondary structures, but more curvilinear, were reported along the Conway segment (eastern Hope Fault) by Eusden et al. (2000, 2005). The strike and dip of the Conway segment at their study sites is 052°-068°/59-70° NW; its strike is at a higher angle (10°-26°) to the Pacific plate slip vector in comparison to the Hurunui segment (3°-8°). The Conway segment of the Hope Fault has been described as transpressive and forming duplexes of up to 2 km wide near Charwell and Lottery Rivers (Eusden et al., 2002, 2005). Eusden et al. (2005) observed a crosscutting relationship between the normal faults on the fault HW near the Charwell River. Near the Lottery site, Eusden et al. (2002) observed many normal

faults on the fault FW with strikes between 045°-050° which is the expected orientation for the reverse faults associated with the strike-slip system. For the Charwell site, they proposed that there has been an early transpressive fault wedge (length 5 km and width 0.2-1 km) between the frontal thrust (main trace of the fault) and the rear normal fault, but then, by development of the wedge, the HW remained unsupported, and the wedge had undergone gravitational collapse. Their model shows that early normal faults developed due to this collapse, and then a secondary fault wedge (length 7 km and width 2 km at its widest point) was initiated and developed towards the fault FW until the second collapse occurred and late normal faults formed crossing the early normal faults. For the Lottery site, as there was one set of normal faults, they proposed a transpressive wedge model (length 13 km and width 0.1-1.3 km) and its collapse that explains reversal of slip on the reverse faults to become normal faults. In both studies, they concluded that topographic loading resulted in near-surface reversal of fault motion and wedge evolution.

## S1.4 Detailed site investigations

### S1.4.1 McKenzie Fan

Two main generations of late Holocene alluvial fan building have been attributed to McKenzie Stream; a side valley of the Hurunui River (Langridge et al., 2013). The older is an abandoned and bush-covered fan which is cut by traces of the Hope Fault (Fig. 1.7A). The current channel of McKenzie Stream now incises the eastern side of its old fan. The older McKenzie fan had undergone a detailed investigation to assess the single event displacement and slip rate by Langridge and Berryman (2005).

In terms of fault structures and evolution in this area, two dextral fault strands with lengths of ~750 m (splay fault) and ~1 km (PSZ strand) clearly traverse the old McKenzie fan before becoming concealed under alluvium of the current McKenzie Stream toward the east (Figs. 1.7A and 1.11). These two strands are opposed in terms of their upthrown side. This can be verified by the incised behavior of channels that are crossing the fan in between these two strands. Normal and splay faults were formed between the two major strands. Scarp heights vary from 0.4 to 4.5 m. The strike of the well-preserved PSZ strand is 074°, which is nearly similar to the strike of the PSZ strand (071º) at the western end of the McKenzie fan. In contrast, the strike of the less-preserved northern fault strand (i.e., the splay fault) is 064º, which is different than the strikes of the southern and western PSZ strands. Therefore, an

oblique component should be associated with the strike-slip motion. It appears that the southern PSZ strand and asymmetric anticline (cross-sections AA' and BB') accommodated this oblique motion. Here, I argue for a small internal fault wedge located between the PSZ and splay strands. The width of this wedge is ~200 m at its widest point and it tapers toward the west. To some extent, this geometry is consistent with the fault-wedge model of Eusden et al. (2000, 2005) for the Conway segment of the Hope Fault. In their models, wedges formed in older part of the landscape on higher elevations and evolved at different time stages. However, I have only mapped a few preserved normal faults on the western part of the wedge surface, which could possibly be co-seismic features formed during the wedge extrusion from unconsolidated late Holocene fan deposits. Therefore, this wedge is a young tectonic feature preserved in the Hurunui Valley at ~600 m a.s.l. near the rangefront. The valley form, beneath the cross- section, looks quite complex because the cross- section is at low angle to the McKenzie Valley even though it is perpendicular to the Hurunui Valley. Formation of such a small and shallow wedge in this site is attributed to an oblique fault component (changes in fault strike) and considerable thickness of cover deposits as first and second order controls.

### S1.4.2 Boundary Stream

This site is located in the eastern extent of the LiDAR strip (Fig. 1.10). To the east of Boundary Stream, the fault splays across postglacial fan deposits (late Pleistocene) and a series of en echelon uphill-facing scarps delineate the PSZ. The most eastern PSZ strand also shows splays of normal faults toward its western tip. Scarp heights are up to 14 m. No dextral displacement is observed in this zone. It appears that a negative flower structure has formed here (cross-sections JJ' and KK'). A complex pattern of faults appear to form a "linking damage zone" with a length of ~740 m and a width of up to ~300 m. These characteristics may represent a slight change in the strike of the master fault at depth (Kim et al., 2004). Therefore, I suggest that this area displays features indicative of earthquake termination or initiation and needs further investigation. On the other hand, this complex pattern of faults could be controlled by a subsurface bend or offset since both strike-slip experimental models and natural examples (Crowell, 1974; Royden, 1985; Mitra and Paul, 2011) reveal that a significant decrease in strike-slip motion will appear when the faults approach these bends or offsets and as a result, slip will be transferred to en echelon normal faults or uplifts depending on the type of step-over. However, based on the overall fault geometry in this area, I favour

the first model (linking damage zone) over the left step-over (constraining bend). Furthermore, small lensoidal and linear vegetated or water filled depressions (basins) are common (Fig. 1.10; see grabens). I think that these features have formed following the subsidence of their small-scale intervening blocks bounded by the normal faults rather than being sag-ponds formed by strike-slip motion. These depressions are rooted in a shallow depth ~10 m (see cross section JJ'). To test the validity of the related cross-section, I use the empirical relationship of Gurbuz (2010) which defines as:

$$d= 0.1104* l- (8.7550*10^{-2}) *w$$

Where d, l and w are the depth, length, and width of the basins. Although this relationship has originally been obtained for pull apart basins formed along strike-slip systems, it roughly estimates that the basin along cross-section JJ', with L= 77 m and W= 26 m, has a depth of ~6 m consistent with what I can obtain from the cross-section. Auguring one of these depressions up to 2 m depth shows that it has been filled by sand, silt, and clay sediments of probable Holocene age.

Abundant curvilinear structures (Fig. 1.10; pink lines), found at the northern side of the Hope Valley, could probably be attributed to gravitational collapse since they don't display appropriate orientation to the PSZ as other fault-related structures do. In the Hope Valley, downcutting by the Hope River has abandoned flights of terraces during the Holocene. This results in mass wasting of upper slopes which have already been faulted and are unstable. Therefore, the width of the damage zone gradually evolves within this area due to actively producing gravity faults. This supports the argument about the existence of a linking damage zone in this area since these curvilinear features (gravity faults) are closely-spaced nearby the fault tips on the Hope River cut bank. Formation of gravity faults in this site is attributed to changes in local stresses, resulting from interaction between topography and eroding Hope River, and considerable thickness of cover deposits as first and second order controls.

## S1.5 References


Barth, N.C., Toy, V.G., Langridge, R.M., Norris, R.J., 2012. Scale dependence of oblique plate-boundary partitioning: New insights from LiDAR, central Alpine fault, New Zealand. Lithosphere doi: 10.1130/L201.1.

Crowell, J.C., 1974. Origin of late cenozoic basins in southern california. Tectonics and Sedimentations 22, 190-204.

Eusden, J.D., Pettinga, J.R., Campbell, J.K., 2000. Structural evolution and landscape development of a collapsed transpressive duplex on the Hope Fault, North Canterbury, New Zealand. New Zeal J Geol Geop 43, 391-404.

Eusden, J.D., Pettinga, J.R., Campbell, J.K., 2005. Structural collapse of a transpressive hanging-wall fault wedge, Charwell region of the Hope Fault, South Island, New Zealand. New Zeal J Geol Geop 48, 295-309.

Gurbuz, A., 2010. Geometric characteristics of pull-apart basins. Lithosphere 2, 199-206.

Kim, Y.S., Peacock, D.C.P., Sanderson, D.J., 2004. Fault damage zones. Journal of Structural Geology 26, 503-517.

Langridge, R.M., Almond, P.C., Duncan, R.P., 2013. Timing of late Holocene paleoearthquakes on the Hurunui segment of the Hope fault: Implications for plate boundary strain release through South Island, New Zealand. Bulletin of the Geological Society of America 125, 756-775.

Langridge, R.M., Berryman, K.R., 2005. Morphology and slip rate of the Hurunui section of the Hope Fault, South Island, New Zealand. New Zeal J Geol Geop 48, 43-57.

Mitra, S., Paul, D., 2011. Structural geometry and evolution of releasing and restraining bends: Insights from laser-scanned experimental models. AAPG Bulletin 95, 1147-1180.

Royden, L.H., 1985. The Vienna Basin: a thin-skinned pull-apart basin. Strike-slip deformation, basin formation, and sedimentation, 319-338.

# SUPPLEMENT TO CHAPTER 2: LATE HOLOCENE RUPTURE BEHAVIOUR AND EARTHQUAKE CHRONOLOGY ON THE HOPE FAULT, NEW ZEALAND

# Supplementary Information

This file is composed of 7 main parts: (1) A picture of the extracted seeds from one peat sample; (2) Details of the Matagouri bush on the low gradient Holocene fan; (3) Pit logs and their interpretations; (4) Details of the Schmidt hammering technique; (5) Pictures of the fault bend and the basin formed behind it east of the trench site; (6) Parakeet Stream data; and (7) details of calculating mean recurrence interval (MRI) and its uncertainty.

## S2.1 Supplementary data: beech seeds in peat sample

I tried to select the most suitable materials for radiocarbon dating including small twigs, leaves, and seeds from every peat sample. If I couldn't find such materials, I selected bigger woody fragments and if none of the above existed, a bulk sample of peat or some rooty fragments were submitted for dating.


Figure. S2.1. Beech seeds extracted from peat samples for dating (scale bar in mm). As the seeds were small, five to six seeds were submitted to reach the necessary sample mass.

## S2.2 Supplementary data: Matagouri bush

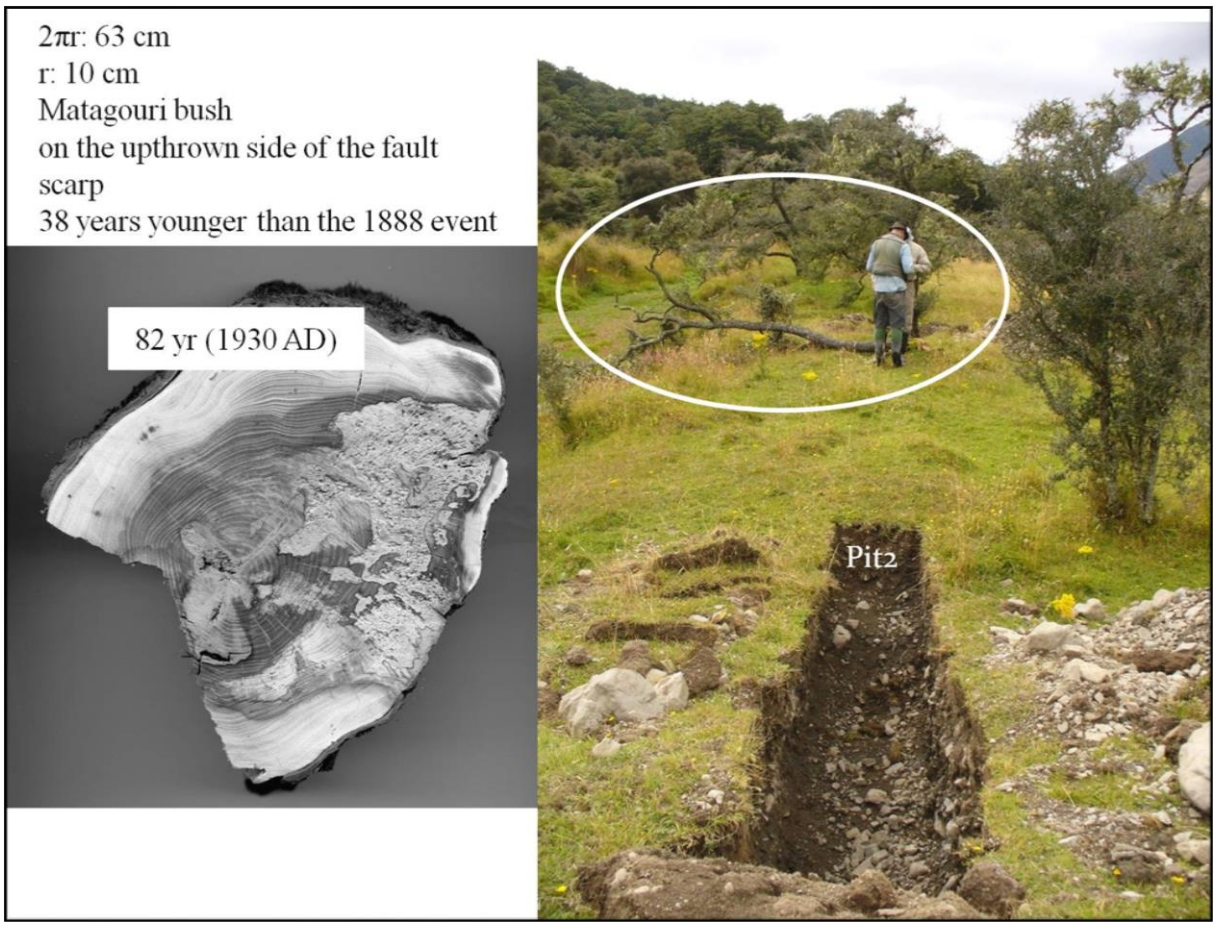


Figure. S2.2. The largest Matagouri bush was cut down. The bush has ring count of 82 yr and a colonization age of A.D. ~1930. This probably provides an age related to the clearance of forest at the Hope Shelter it, and gives us no insights into the timing of earthquake there.

## S2.3 Supplementary data: pit logs

These data are provided as they show extra information about the geomorphology and age of the site. However, the OSL ages from the pits are looking older than the estimated age of the low gradient fan using the downcutting rate of the Hope River estimated by Cowan (1989) and the height of the fan with respect to the current position of the Hope River.

### S2.3.1 Pit 1 (branch trench)

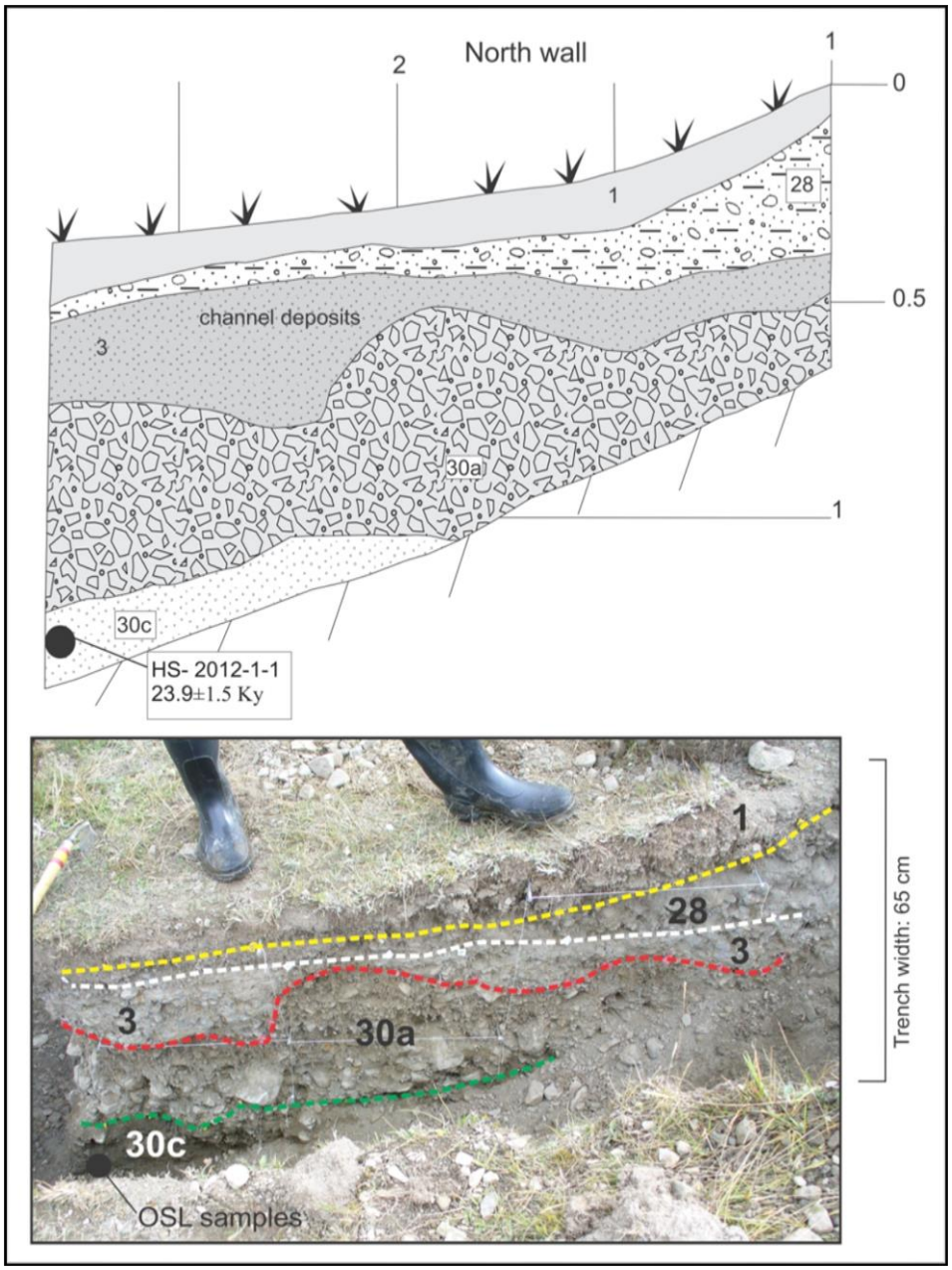


Figure. S2.3. Graphic and photo logs of the branch trench (Pit 1). This branch trench was 2.4 m long, 65 cm wide and 0.5-1 m deep. The second unit from top and the lower units are named 28, 30a and 30c respectively because they are correlated with units 28, 30a and 30c in Trench 1. Depositional units are described in section "Unit description of Pit 1". The ground surface marks the cross-sectional profile of the channel forming the wind gap. The current wind gap is erosional, but is underlain by an older channel, filled by unit 3.

Unit 3 shows geometry of the abandoned channel on the fault scarp. One OSL sample was taken from unit 30c at depth 92 cm below the surface to estimate the age of the fan.

Unit description of Pit1:

1-Top soil [soil]

28- Light reddish grey pebbly silty sand, maximum clast size: 7cm, average clast size: 1cm, moderately loose, matrix: loamy sand, some iron oxidation along root traces, gravely loamy (clay, silt, sand) sand [fan alluvium]

3- Sandy silt, subrounded pebbles, some bedding, maximum grain size: 5 cm [channel deposits]

30a- Light olive grey sandy gravel, maximum clast size: 18cm, average clast size: 3cm, matrix: medium-coarse sand, moderately loose, large clast iron stained [fan alluvium]

30c- Dark grey medium to coarse sand, very well sorted, moist [fan alluvium]

**S2.3.2 Pit 3**

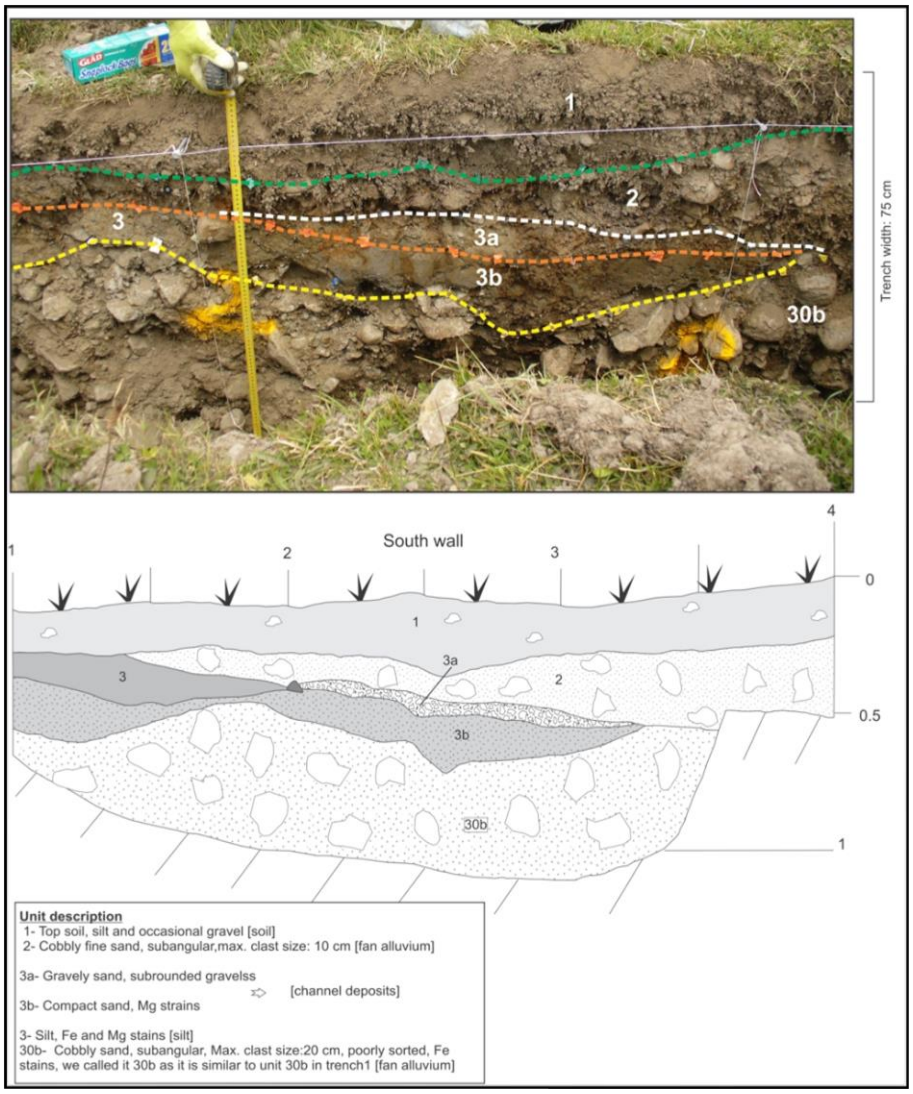


Figure. S2.4. Graphic and photo logs of Pit 3. This pit was 3 m long, 75 cm wide and 1 m deep. The lowest unit is named 30b because it is correlated with unit 30b in trench1. Units 3a and 3b show geometry of the abandoned channel on the fault scarp.

### S2.3.3 Pit 4

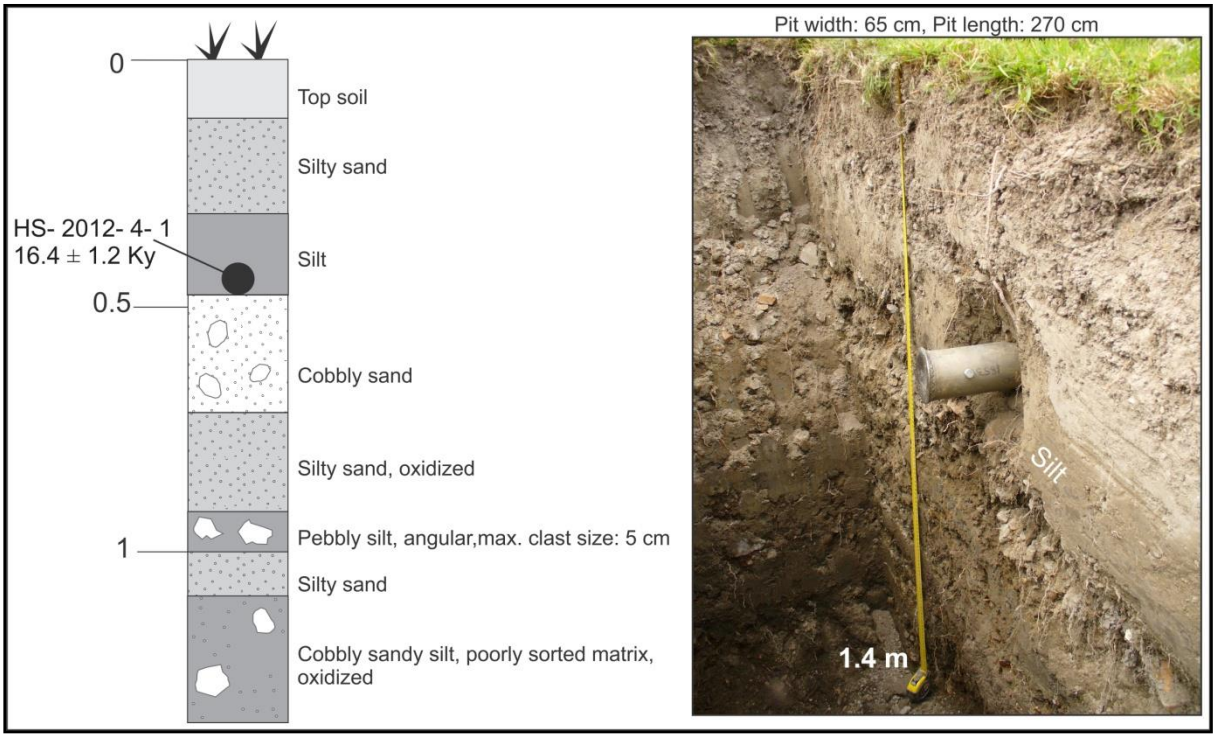


Figure. S2.5. Graphic and photo logs of Pit 4. This pit was 2.7 m long, 65 cm wide and 1.4 m deep. Unit description is done on the log. One OSL sample was taken from the silty unit at depth 45 cm below the surface to estimate the age of the fan.

## S2.4 Supplementary data: Schmidt hammering

### S2.4.1 Schmidt hammer

The Schmidt hammer (SH) was designed in 1948 to test the hardness of concrete (Goudie, 2006). It has been used in geomorphological studies for relative dating of the Holocene surfaces for nearly four decades (Winkler, 2005; Goudie, 2006, Shakesby et al., 2011). When applied on a rock surface, it measures the rebound (r-value) of a spring-loaded mass impacting against the surface of the rock. The rebound value is dependent to the hardness and compressional strength of the rock surface (Winkler, 2005; Goudie, 2006; Shakesby et al., 2006).

### S2.4.2 Methodology

In this study, an N-type SH with a calibrated energy of 2.207 Nm was first calibrated and then applied to the surfaces of 75 boulders within a debris deposit near the Hope-Kiwi confluence and 79 boulders within the debris deposit at the Hope Shelter site. Both debris

deposits are located ~5 km apart within the Hope Valley and are composed of boulders with the same lithology; i.e., sandstone of the Torlesse formation (Fig. S2. 6). At each site, one SH impact was implemented on each boulder (Winkler, 2000, 2005, Stahl et al., 2013). I selected very large and stable boulder to prevent boulder movement during tests, and avoided edges of the boulders and surfaces with joints, lichen and moss (Winkler, 2005). I compared the mean values of the SH from the two deposits using one way ANOVA (analysis of varience). The results are presented in Table S2.1. The results of ANOVA imply no significant age difference between the two groups. However, in relative age dating with SH, a maximum time resolution of ~300 years is common (Winkler, 2005). The mean value of the Hope Shelter deposit is slightly higher (47.4) with respect to the Hope-Kiwi site (46). Taking the slight differences in the mean values of the two sites and the time resolution of the SH into account, it can be concluded that the Hope Shelter debris deposit could possibly be younger (300? yr) than the Hope-Kiwi deposit. However, based on the ANOVA results, I can argue that the two debris deposits could have occurred around the same time in the Hope Valley and they are valuable for earthquake studies.

The appearance of a similar debris deposit near the Hope-Kiwi confluence, which was documented by McKay (1890) following the 1888 event (Figs. 2.2-2.3, and Appendix 2.1: 14), helped us to better understand the debris deposit and forest pattern at the Hope Shelter site. The Hope Shelter debris deposit showed an equivalent Schmidt Hammer mean rebound value to the examined debris deposits (older than the 1888) located near the Hope-Kiwi confluence to the south of the 1888 failure (Fig. S2.6). Therefore, the results strongly suggest that the debris deposit at the Hope Shelter site was not generated during the 1888 event, consistent with the dendrochronologic results. Therefore, I allocated a minimum age of ~275 years and a maximum age of <800 years to the Hope Shelter debris deposit based on the minimum age of the trees grown on the debris deposit and the age of the unconformity below unit 12 in T-2 because unit 12 could possibly represent a signal of the debris deposit in the swamp.

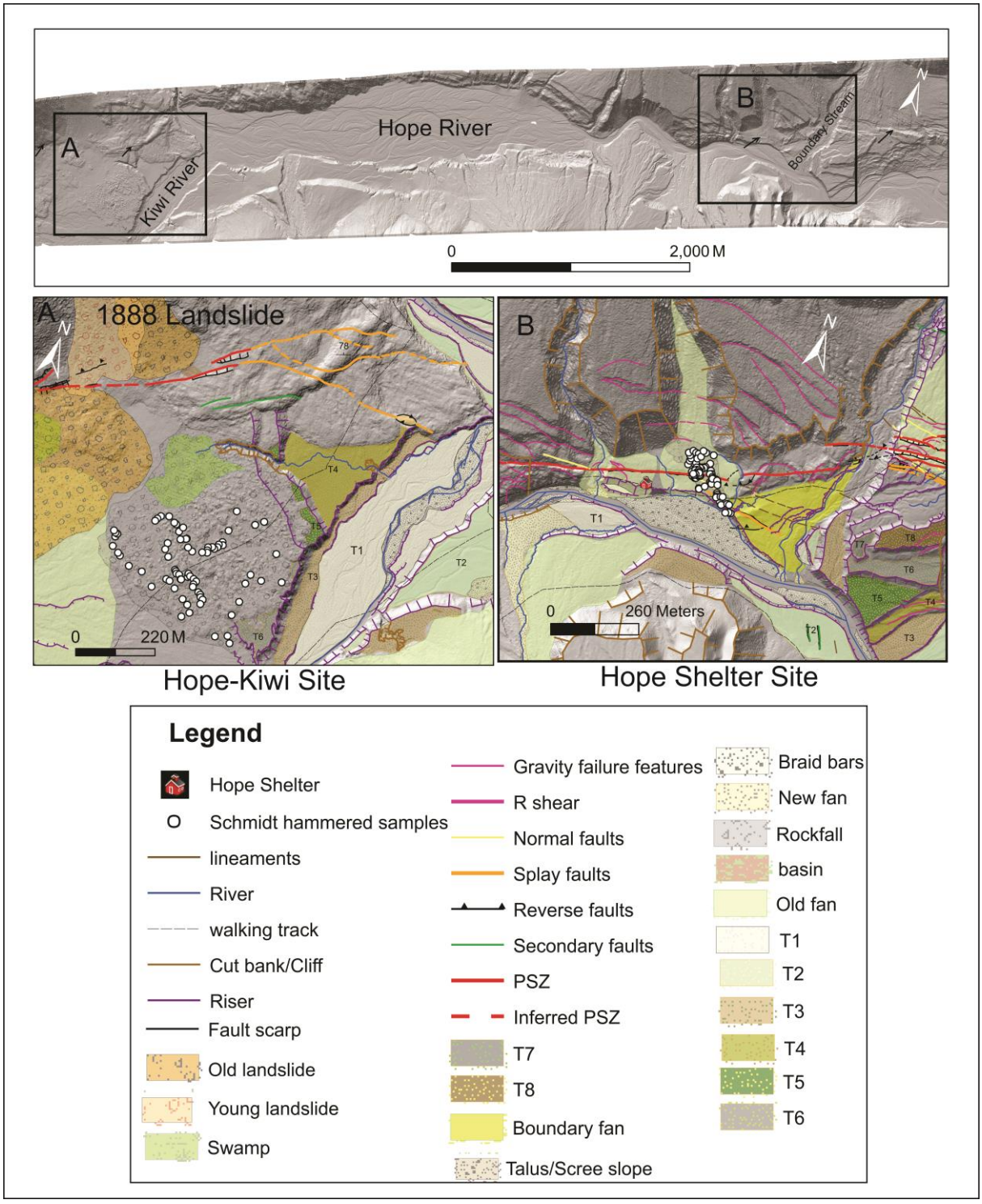


Figure. S2.6. Locations of the two sites relative to each other in the Hope Valley are shown on the uninterpreted LiDAR strip. Location of the Schmidt hammered sites are shown on the interpreted windows of LiDAR. Location of the landslide caused by the 1888 earthquake (McKay, 1890) has been shown on A. Black arrows on the uninterpreted LiDAR strip point out to the fault.

The results of this work could be useful for further investigations of paleoearthquakes if combined with accurately dated surfaces nearby the debris deposits and known earthquake chronologies, but by the analysis I have done, I only know that the debris are about the same age.

Table S2.1. Details of the SH data of the two debris deposits are presented. The results of the ANOVA analysis are also included.

| **Site** | **N** | **R-values: mean** | **Median** | **Skewness** | **Kurtosis** | **Minimum age of the debris deposit**<br>**Maximum age of the debris deposits** |
|---|---|---|---|---|---|---|
| Hope-Kiwi | 75 | 46 | 46 | 0.29 | -0.68 | N/A |
| Hope Shelter | 79 | 47.4 | 48 | 0.32 | 0.64 | Min ~200 (from dendrochronology)<br>Max ~ 1700 yr (from base of the swamp) |

| **ANOVA results** | | | | | | |
|---|---|---|---|---|---|---|
| **Descriptive** | | | | | | |
| **Groups** | **N** | **Mean** | **Std. Deviation** | **Std. Error** | **95% Confidence interval for mean** | |
| | | | | | **Lower bound** | **Upper bound** |
| HK | 75 | 46 | 5.22722 | 0.60359 | 44.7973 | 47.2027 |
| HS | 79 | 47.4051 | 6.19867 | 0.69741 | 46.0166 | 48.7935 |
| Total | 154 | 46.7208 | 5.77067 | 0.46501 | 45.8021 | 47.6395 |

| **ANOVA** | | | | | |
|---|---|---|---|---|---|
| | **Sum of squares** | **df** | **Mean square** | **F** | **Sig.** |
| Between groups | 75.956 | 1 | 75.956 | 2.300 | 0.131 |
| Within groups | 5019.038 | 125 | | | |
| Total | 5094.994 | 135 | | | |

### S2.4.3 References


Goudie, A. S., 2006, The Schmidt hammer in geomorphological research: Progress in Physical Geography, v. 30, no. 6, p. 703-718.

Shakesby, R. A., Matthews, J. A., Karlén, W., and Los, S. O., 2011, The Schmidt hammer as a Holocene calibrated-age dating technique: Testing the form of the R-value-age relationship and defining the predicted-age errors: Holocene, v. 21, no. 4, p. 615-628.

Shakesby, R. A., Matthews, J. A., and Owen, G., 2006, The Schmidt hammer as a relative-age dating tool and its potential for calibrated-age dating in Holocene glaciated environments: Quaternary Science Reviews, v. 25, no. 21-22, p. 2846-2867.

Stahl, T., Winkler, S., Quigley, M., Bebbington, M., Duffy, B., and Duke, D., 2013, Schmidt hammer exposure-age dating (SHD) of late Quaternary fluvial terraces in New Zealand: Earth Surface Processes and Landforms, v. 38, no. 15, p. 1838-1850.

Winkler, S., 2005, The Schmidt hammer as a relative-age dating technique: Potential and limitations of its application on Holocene moraines in Mt Cook National Park, Southern Alps, New Zealand: New Zeal J Geol Geop, v. 48, no. 1, p. 105-116.

## S2.5 Supplementary data: fault bend


Figure. S2.7. A huge displaced boulder was found at the base of the fault scarp near the fault bend. Location: ~2.8 km from Boundary stream towards east at approximate X and Y: 1545892.667 and 5282807.323 (Reference: NZGD_2000_TM) respectively.


Figure. S2.8. Fallen boulders were found at the base of the fault scarp (within the basin) near the fault bend. Location: ~2.7 km from Boundary stream towards east at approximate X and Y: 154511.79 and 5282879.733 (Reference: NZGD_2000_TM) respectively. Scarp height is ~5 m. Basin width is 22.2 m. Picture was taken in January 2012.

## S2.6 Supplementary data: Parakeet Stream site

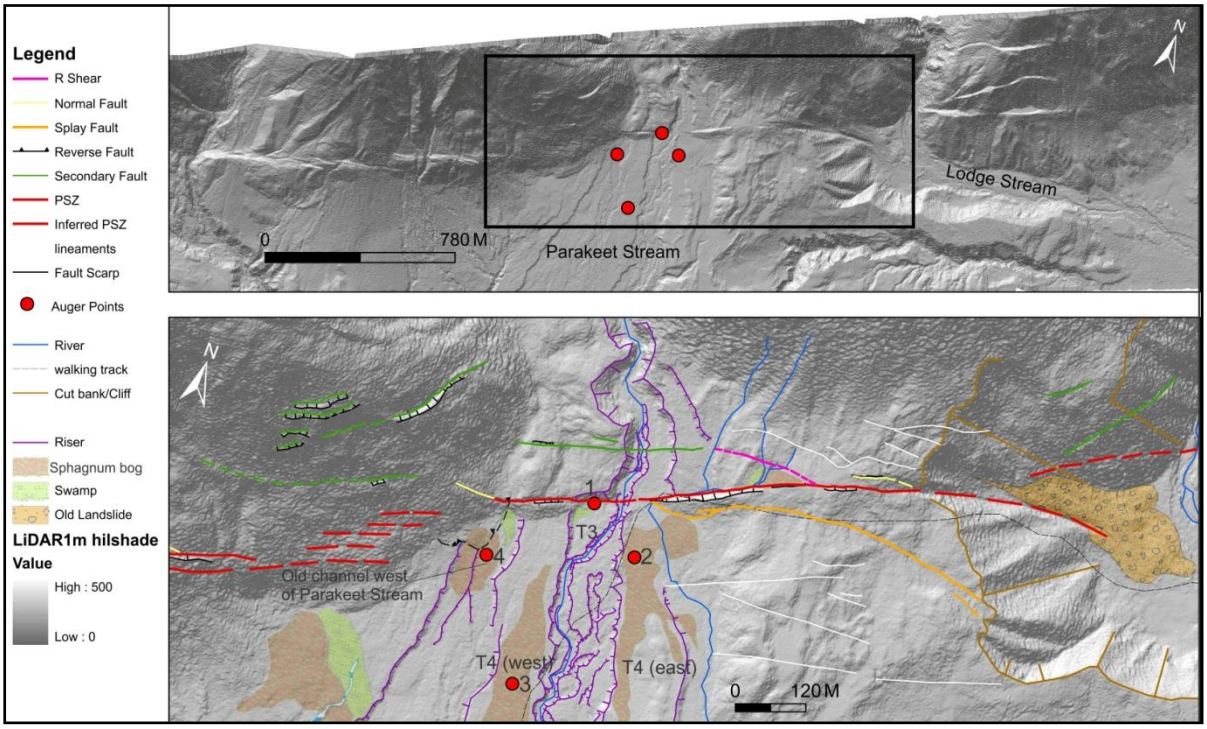


Figure. S2.9. Uninterpreted and interpreted LiDAR hillshade model of the Parakeet Stream site. Location: ~4 km west of the Hope-Kiwi confluence. Closed Red circles show the augur points (pits). Abbreviation PSZ: Principal Slip Zone. Term "old landslide" was used in the legend because the landslide deposit was colonised by very old beech trees. Secondary Faults are parallel to subparallel faults to the PSZ with dextral and or vertical displacements. Lineaments are the faults with no discernible displacement. All the pits and auger holes were excavated into the sphagnum bog surfaces.

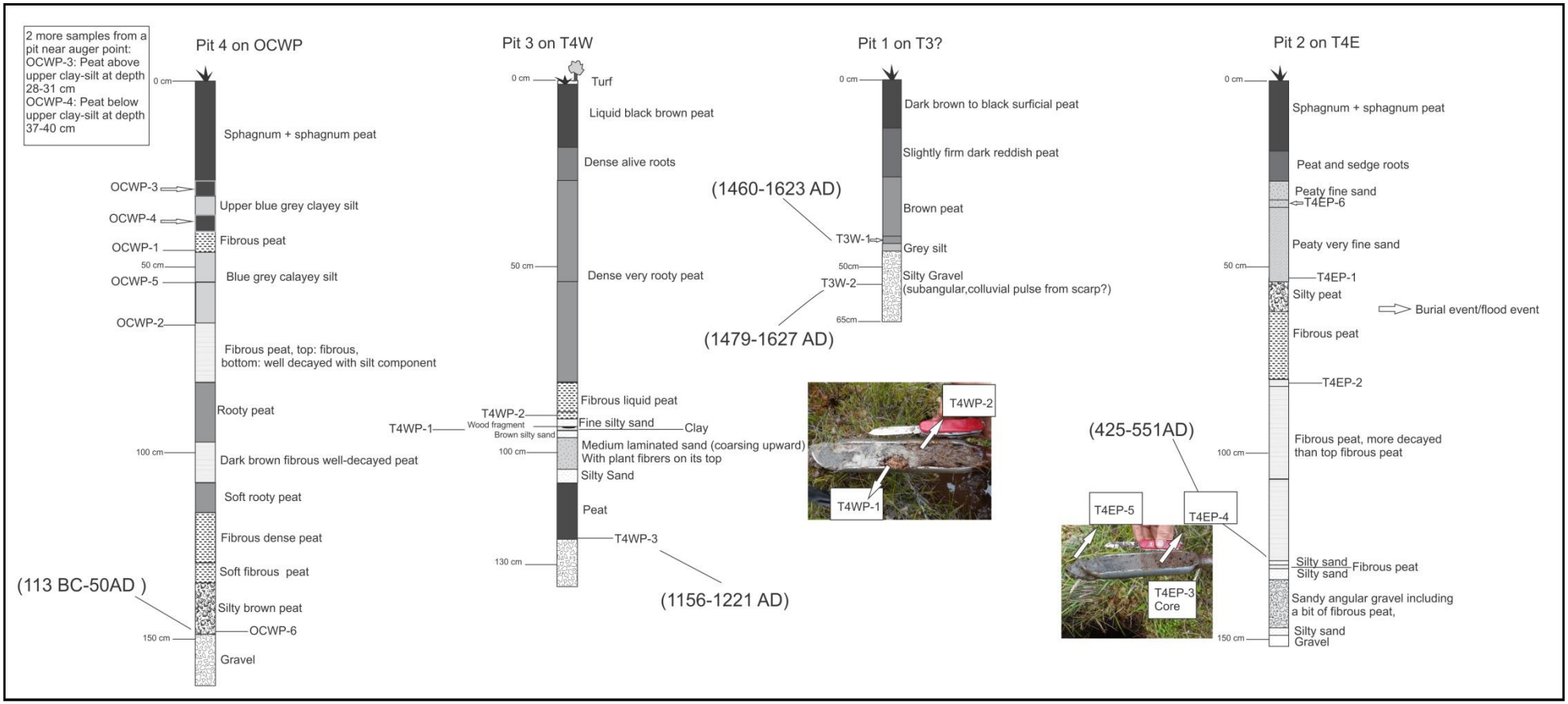


Figure. S2.10. Pit logs at the Parakeet Stream site. I collected samples from every peat horizon as indicated. In total, five samples were C-14 dated from the logs. These samples are from the deepest parts of the pits, above the gravel units, to identify the maximum ages of the swamps. The dated samples display the minimum age for the gravel deposit.

### S2.6.1 Fallen boulder due to the coseismic shaking associated with the 1888 event?

At the base of the fault scarp, on the surface of terrace T3 (Fig. S2.9), I found a large spheroid boulder (Fig. S2.11). The boulder was situated on a fallen tree. I found a young Silver beech grown on the fallen tree. The young tree was cut down at 46 cm height from its base. The tree postdates the 1888 event. As it normally takes 17-47 years for beech trees to colonize at high elevation or sloping surfaces (Langridge et al. 2007), this probably provides evidence for severe shaking at the Parakeet Stream site during the 1888 event; however, it does not give us any direct insight into the 1888 surface rupture extension.

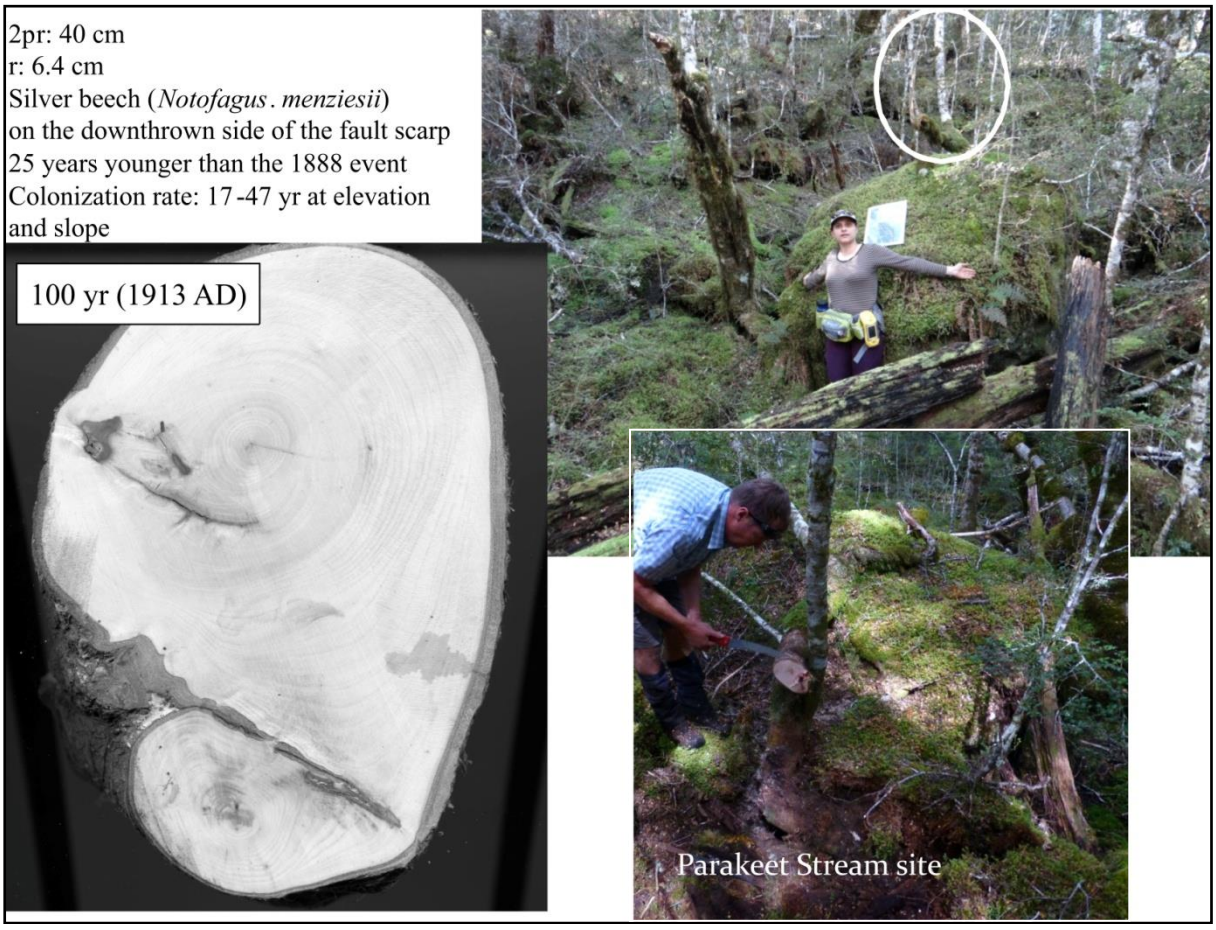


Figure. S2.11. The young Silver beech was cut down. The tree has ring count of 100 yr and a colonization age of A.D. ~1913.

### S2.6.2 References

Langridge, R., Duncan, R., and Almond, P., 2007, Indicators of recent paleoseismic activity along the western Hope Fault: GNS Science Consultancy Report 2006/151, p. 99.+appendices.

## S2.7 Supplementary data: calculating the mean recurrence interval time for the preferred earthquakes timings

To estimate the mean recurrence interval (MRI) and its uncertainty, I followed the methodology employed by Parsons (2008), and the calculations used by Nicol et al. (2012). To calculate the MRI, the Monte Carlo procedure is used to generate a recurrence interval histogram from earthquake input data. In this study, event timings of the earthquakes and their uncertainties, presented in years before 2013 (i.e., sampling year), were used in the calculations. The recurrence interval histogram for the Hurunui segment of the Hope fault is shown in Fig. S2.12. The MRI (~298 years) and Standard deviation (~199 years) calculated from the histogram are presented in Table. S2. The uncertainty in the MRI is the Standard deviation divided by the square root of the number of intervals. Based on this analysis, the MRI is reported 298 ± 88 years. The associated uncertainty includes both process and dating uncertainties.

| **Events timing** | **Event timing (presented in years before 2013) with uncertainty** |
|---|---|
| 1-E1 (1888) | 1- 125±1 |
| 2-E2 (1740-1840) | 2- 223±50 |
| 3-E3 (1479-1609) | 3- 469±65 |
| 4-E4 (819-1092) | 4- 1057±137 |
| 5-E5 (439-551) | 5- 1518±56 |
| 6-E6 (373-419) | 6- 1617±23 |
| **Differences** | |
| 1- E1-E2= 98 | |
| 2- E2-E3=246 | |
| 3- E3-E4= 588 | |
| 4- E4-E5=461 | |
| 5- E5-E6=99 | |

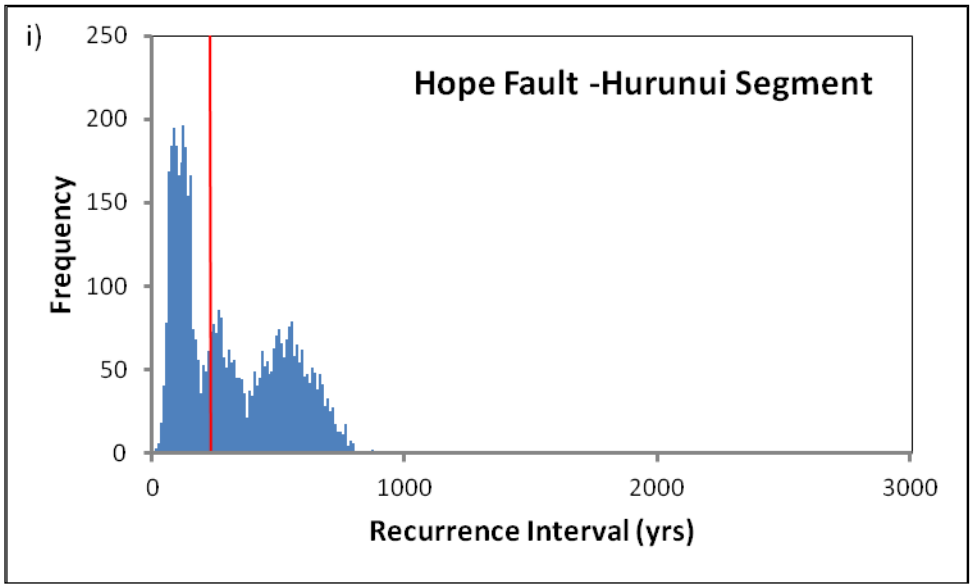


Fig. S2.12. Recurrence interval histogram for the Hurunui segment of the Hope fault generated using the earthquake data and the Monte Carlo method.

Table. S2.2. Calculated parameters from the histogram generated by the Monte Carlo procedure. The MRI and Standard deviation are highlighted.

| Mean | generated mean | generated mode | generated median | generated min | generated max | generated stdev | Min | Max | Stdev | Events |
|---|---|---|---|---|---|---|---|---|---|---|
| **298.4** | 298.1550849 | | 247.00 | 3.53130725 | 863.6074743 | 207.3594521 | 98 | 588 | **198.9267** | 6 |

## S2.7.1 References

Parsons, T., 2008, Monte Carlo method for determining earthquake recurrence parameters from short paleoseismic catalogues: Example calculations from California: Journal of geophysical research, v. 113, no. B03302

Nicol, A., Robinson, R., Van Dissen, R. J., and Harvison, A., 2012, Variability of single event slip and recurrence intervals for large magnitude paleoearthquakes on New Zealand's active faults: GNS Science Report 2012/41, p. 57 p.

# SUPPLEMENT TO CHAPTER 4: SEISMICALLY INDUCED BOULDER DISPLACEMENT IN THE PORT HILLS, NEW ZEALAND DURING THE 2010 DARFIELD (CANTERBURY) EARTHQUAKE

**Supplementary data associated with this article can be found in the online version, at http://www.tandfonline.com/doi/suppl/10.1080/00288306.2012.698627#tabModule.**

This file is composed of three main parts: (1) the dataset acquired in field including two tables; (2) the 2D FLAC methodology and its supplementary table and figure; (3) the complete results of topographic amplification modelling have been shown in the last figure.

## S4.1 Supplementary tables

Table S4.1. Characteristics of displaced boulders and ground damage in the Port Hills. These data have been collected a month after the September 2010 earthquake.

| Displaced boulders in the Port Hills | | | | | | | | |
|---|---|---|---|---|---|---|---|---|
| **Location** | **Length (cm)** | **Width (cm)** | **Height (cm)** | **Movement Distance (cm)** | **Movement Direction (Azimuth)** | **GPS. Height (m, a.s.l.)** | **Northing (NZMG)** | **Easting (NZMG)** |
| Hoon Hay | 24 | 21 | 18 | 48 | 240 | 484.067 | 5731794.025 | 2480652.122 |
| Hoon Hay | 44 | 40 | 38 | 113 | 325 | 487.61 | 5731833.742 | 2480670.613 |
| Hoon Hay | 50 | 25 | 30 | 30 | 345 | 487.975 | 5731830.342 | 2480671.344 |
| Hoon Hay | 30 | 25 | 25 | 13 | 300 | 487.75 | 5731831.231 | 2480670.114 |
| Hoon Hay | 80 | 50 | 60 | 140 | 140 | 488.058 | 5731815.459 | 2480663.972 |
| Hoon Hay | 220 | 110 | 70 | 15 | 225 | 488.764 | 5731820.758 | 2480666.674 |
| Hoon Hay | 60 | 50 | 35 | 8 | 270 | 488.074 | 5731820.395 | 2480663.771 |
| Hoon Hay | 140 | 110 | 70 | 9 | 305 | 487.796 | 5731824.235 | 2480658.901 |
| Hoon Hay | 91 | 59 | 48 | 160 | 236 | 487.822 | 5731808.245 | 2480669.752 |
| Hoon Hay | 165 | 75 | 58 | 25 | 240 | 487.18 | 5731809.653 | 2480669.441 |
| Hoon Hay | 57 | 52 | 28 | 35 | 235 | 488.346 | 5731816.301 | 2480667.86 |
| Hoon Hay | 80 | 47 | 45 | 120 | 255 | 488.374 | 5731822.278 | 2480668.427 |
| Hoon Hay | 125 | 60 | 50 | 25 | 300 | 488.821 | 5731820.986 | 2480671.308 |
| Hoon Hay | 111 | 52 | 36 | 20 | 255 | 488.821 | 5731820.986 | 2480671.308 |
| Hoon Hay | 80 | 36 | 25 | 85 | 240 | 483.822 | 5731800.684 | 2480646.746 |
| Hoon Hay | 48 | 37 | 41 | 75 | 255 | 485.672 | 5731800.831 | 2480648.85 |
| Hoon Hay | 105 | 63 | 43 | 75 | 240 | 486.025 | 5731792.655 | 2480654.595 |
| Hoon Hay | 45 | 23 | 25 | 45 | 260 | 474.68 | 5731983.212 | 2480622.278 |
| Hoon Hay | 52 | 40 | 20 | 18 | 220 | 481.779 | 5731894.631 | 2480656.396 |
| Hoon Hay | 43 | 26 | 43 | 20 | 50 | 482.055 | 5731891.617 | 2480657.186 |
| Hoon Hay | 60 | 50 | 50 | 20 | 265 | 482.055 | 5731891.617 | 2480657.186 |
| Hoon Hay | 120 | 75 | 36 | 38 | 225 | 486.124 | 5731843.67 | 2480668.751 |

| | | | | | | | | |
|---|---|---|---|---|---|---|---|---|
| Hoon Hay | 91 | 67 | 35 | 12 | 315 | 486.873 | 5731838.412 | 2480668.524 |
| Hoon Hay | 27 | 58 | 42 | 10 | 270 | 487.366 | 5731834.426 | 2480668.104 |
| Hoon Hay | 30 | 20 | 34 | 145 | 110 | 486.836 | 5731829.812 | 2480679.821 |
| Hoon Hay | 110 | 70 | 24 | 19 | 70 | 486.836 | 5731829.812 | 2480679.821 |
| Hoon Hay | 54 | 40 | 26 | 8 | 175 | 486.836 | 5731829.812 | 2480679.821 |
| Hoon Hay | 30 | 15 | 26 | 12 | 215 | 487.05 | 5731828.643 | 2480679.937 |
| Hoon Hay | 62 | 40 | 18 | 195 | 75 | 486.309 | 5731832.119 | 2480681.794 |
| Hoon Hay | 86 | 30 | 30 | 34 | 40 | 486.577 | 5731833.256 | 2480680.802 |
| Hoon Hay | 150 | 77 | 57 | 160 | 75 | 485.154 | 5731837.614 | 2480680.139 |
| Hoon Hay | 139 | 100 | 63 | 13 | 8 | 488.363 | 5731827.364 | 2480670.199 |
| Hoon Hay | 41 | 33 | 34 | 90 | 240 | 484.001 | 5731795.387 | 2480649.048 |
| Hoon Hay | 24 | 16 | 17 | 105 | 240 | 484.001 | 5731795.387 | 2480649.048 |
| Hoon Hay | 125 | 60 | 45 | 476 | 25 | 482.803 | 5731831.503 | 2480689.009 |
| Hoon Hay | 120 | 95 | 80 | 210 | 270 | 435.675 | 5731623.485 | 2480512.076 |
| Hoon Hay | 100 | 63 | 57 | 235 | 35 | 432.975 | 5731985.483 | 2480739.462 |
| Hoon Hay | 95 | 70 | 50 | 970 | 20 | 416.695 | 5731999.775 | 2480762.764 |
| Kennedy Bush | 105 | 65 | 35 | 25 | 90 | 447.123 | 5731501.537 | 2479431.038 |
| Kennedy Bush | 34 | 15 | 18 | 5 | 140 | 446.024 | 5731501.09 | 2479434.887 |
| Kennedy Bush | 38 | 35 | 25 | 7 | 120 | 446.476 | 5731497.324 | 2479428.78 |
| Kennedy Bush | 62 | 42 | 32 | 35 | 145 | 447.261 | 5731494.657 | 2479422.564 |
| Kennedy Bush | 44 | 40 | 27 | 15 | 130 | 444.429 | 5731487.49 | 2479412.901 |
| Kennedy Bush | 63 | 40 | 60 | In Situ | NO | 444.981 | 5731487.5 | 2479400.614 |
| Sugar Loaf | 140 | 100 | 100 | 75 | 240 | 407.23 | 5734031.934 | 2481395.509 |
| Gibraltar | 35 | 30 | 16 | 630? | 340 | 472.076 | 5727442.695 | 2478887.769 |
| East of Gibraltar | 25 | 20 | 10 | 2560? | 260 | 565.015 | 5727294.644 | 2479743.283 |
| Mitchells Track | 400 | 350 | 500 | 130 | 75 | 378.811 | 5732873.424 | 2481404.466 |
| Castle Rock | 67 | 37 | 20 | 24 | 240 | 376.043 | 5735474.89 | 2485613.744 |
| Castle Rock | 25 | 14 | 10 | 30 | 250 | 393.367 | 5735459.87 | 2485633.563 |
| Castle Rock | 95 | 30 | 25 | 10 | 335 | 393.367 | 5735459.87 | 2485633.563 |
| Castle Rock | 450 | 300 | 350 | 45 | 95 | 374.501 | 5735455.441 | 2485720.84 |
| Watlings Track | 128 | 48 | 30 | 16 | 73 | 412.945 | 5731502.866 | 2480481.219 |
| Crater Rim | 38 | 30 | 25 | 7 | 180 | 429.77 | 5731361.256 | 2480328.246 |
| Hoon Hay | One rockfall, SE facing, Volume c. 10.7 $m^3$ caused vegetation damage | | | | | 433? | 5732093.479 | 2480755.98 |
| Hoon Hay | One soil slumping, SE facing, Volume c. 4.8 $m^3$ | | | | | 395.089 | 5732068.888 | 2480747.111 |
| Kennedy Bush | Rockfall, NE facing , Located on the Ellas Track | | | | | 455? | 5731132.906 | 2480005.392 |
| Castle Rock | One rockfall, NE facing, Volume c. 1300 $m^3$ | | | | | 410? | 5735499.888 | 2485716.883 |
| Hoon Hay | A shattered ridge was recorded with a length and width of 5 and 4.6 m respectively | | | | | 488.821 | 5731820.986 | 2480671.308 |
| Hoon Hay | A crack was found with a length and width of 3.25m and 1.5 cm respectively | | | | | 483.713 | 5731798.291 | 2480646.701 |
| Hoon Hay | Scattered gaps between turf and surface soil were observed on a ridge crest | | | | | 450.509 | 5731591.394 | 2480609.751 |
| Gibraltar | One rockfall occurred at southeast of the Gibraltar spur on the Port Hills | | | | | 563.94 | 5727306.62 | 2479754.8 |

Table S4.2. Characteristics of some of the non-displaced boulders at the Hoon Hay site in the vicinity of displaced boulders. These boulders have almost similar geometry to displaced boulders.

| Some of the non-displaced boulders at the Hoon Hay site in the vicinity of displaced boulders | | | | | | | | |
|---|---|---|---|---|---|---|---|---|
| **Location** | **Length (cm)** | **Width (cm)** | **Height (cm)** | **Movement Distance (cm)** | **Movement Direction (Azimuth)** | **GPS. Height (m, a.s.l.)** | **Northing (NZMG)** | **Easting (NZMG)** |
| 1 | 52 | 34 | 23 | No | No | 448.399 | 5731614 | 2480601.145 |
| 2 | 53 | 27 | 14 | No | No | 451.154 | 5731586 | 2480605.95 |
| 3 | 64 | 57 | 52 | No | No | 451.348 | 5731673 | 2480590.442 |
| 4 | 43 | 39 | 34 | No | No | 454.878 | 5731690 | 2480588.424 |
| 5 | 46 | 30 | 23 | No | No | 479.771 | 5731768 | 2480648.036 |
| 6 | 73 | 55 | 66 | No | No | 478.803 | 5731768 | 2480644.245 |
| 7 | 69 | 34.5 | 30 | No | No | 480.795 | 5731772 | 2480646.278 |
| 8 | 62 | 34 | 50 | No | No | 482.709 | 5731783 | 2480647.916 |
| 9 | 71 | 41 | 25 | No | No | 484.348 | 5731790 | 2480651.617 |
| 10 | 64 | 46 | 25 | No | No | 486.259 | 5731803 | 2480655.935 |
| 11 | 126 | 37 | 32 | No | No | 487.753 | 5731834 | 2480667.786 |
| 12 | 51 | 35 | 28 | No | No | 485.822 | 5731845 | 2480666.396 |
| 13 | 80 | 62 | 34 | No | No | 485.363 | 5731847 | 2480665.136 |
| 14 | 39 | 30 | 18 | No | No | 484.104 | 5731867 | 2480663.99 |
| 15 | 57 | 39 | 18 | No | No | 483.076 | 5731888 | 2480659.84 |
| 16 | 80 | 55 | 46 | No | No | 482.054 | 5731897 | 2480655.138 |
| 17 | 60 | 46 | 23 | No | No | 481.741 | 5731906 | 2480655.362 |
| 18 | 81 | 57 | 30 | No | No | 482.23 | 5731908 | 2480655.874 |
| 19 | 69 | 55 | 46 | No | No | 483.374 | 5731917 | 2480655.731 |
| 20 | 81 | 67 | 34 | No | No | 482.51 | 5731916 | 2480650.953 |
| 21 | 62 | 44 | 41 | No | No | 483.428 | 5731923 | 2480651.57 |
| 22 | 161 | 81 | 92 | No | No | 481.701 | 5731921 | 2480646.937 |
| 23 | 37 | 35 | 30 | No | No | 480.751 | 5731932 | 2480640.232 |
| 24 | 69 | 57 | 57 | No | No | 448.205 | 5731613 | 2480601.755 |

## S4.2 Supplementary methodology used in the 2D FLAC modelling

1- The zone size for the model grids is 10 $m^2$ at the base and progressively smaller in the vertical dimension towards the ridge crest. Boundary conditions ('quiet' and 'free-field', Itasca Consulting Group, 2008) at the base and edges of all model grids eliminated wave interference at the grid boundary and ensured that energy was radiated as if the model extended indefinitely.

2- Seismometers were chosen due to their vicinity and similarity of their rock-type conditions (basalt and andesite, ASNZS1170: B, Rock) to the examined sites. The CRLZ seismometer, which is located in a cavern excavated almost level into steeply rising basaltic hillside at height of 55 m a.s.l. and at a closer distance to the sites, perhaps provides a more realistic seismic ground motion source than the LPCC since the latter is located at height of 5 m a.s.l. and on a very thin soil (less than 5 m) overlaying andesitic bedrock. Seismometers at CRLZ site are 20-30 m from the surface which could be far enough to remove the surface effects. Interestingly, fallen rocks from the cavern ceiling and wall collapsing were observed within the cave, but no evidence of displaced boulders was found on the ground surface.

3- Vertically propagating horizontally-polarized shear waves were applied to the model base as shear stresses calculated by:

$$\sigma s = 2(\rho\ Cs)\ vs \qquad (1)$$

where, $\rho$ = mass density (of the rock); Cs =speed of shear-wave propagation through medium and vs = input shear particle velocity (1 m/s), with the factor of two accounting for dividing the energy into an upward and a downward propagating wave at the grid boundary. The shear particle velocity was taken as the velocity time-history for an individual (i.e. north-south or east-west) component of horizontal ground motion recorded at the seismometers. Vertical shear waves could not be applied due to modelling constraints.

### S4.2.1 References

Itasca Consulting Group Itd 2008. FLAC - Fast Lagrangian Analysis of Continua, Ver. 6.0 User's Manual. Minneapolis, Itasca.

Table S4.3. Rock mass and soil properties used in numerical models. Uniaxial compressive strength (UCS), density, intact elastic modulus (Ei) and poisson's ratio were estimated based on typical values found in the literature. Geological Strength Index (GSI) was estimated from field observation. The rock mass elastic modulus (Erm) was calculated using equations given by Hoek et al. (2002).

| | **BASALT** | | **SOIL** |
|---|---|---|---|
| **PROPERTIES** | **Lower bound** | **Upper bound** | |
| UCS (MPa) | 150 | 200 | |
| Density $\rho$ (kg/m$^3$) | 2700 | 2700 | 1900 |
| GSI | 60 | 80 | |
| Intact elastic modulus, $E_i$ (GPa) | 40 | 80 | |
| Poissons ratio, $\upsilon$ | 0.20 | 0.30 | |
| Rock mass elastic mod $E_{rm}$ (GPa) | 21 | 70 | |
| Rock mass shear mod $G_{rm}$ (GPa) | 9 | 27 | 0.3 |
| Rock mass bulk mod $K_{rm}$ (GPa) | 12 | 58 | 0.5 |
| Shear wave velocity, $C_s = \sqrt{(G/\rho)}$ (m/s) | 1800 | 3160 | 400 |
| Shear stress, $\sigma_s = 2(\rho\ C_s)\ v_s$ (MPa) | 9.72 | 17.06 | |

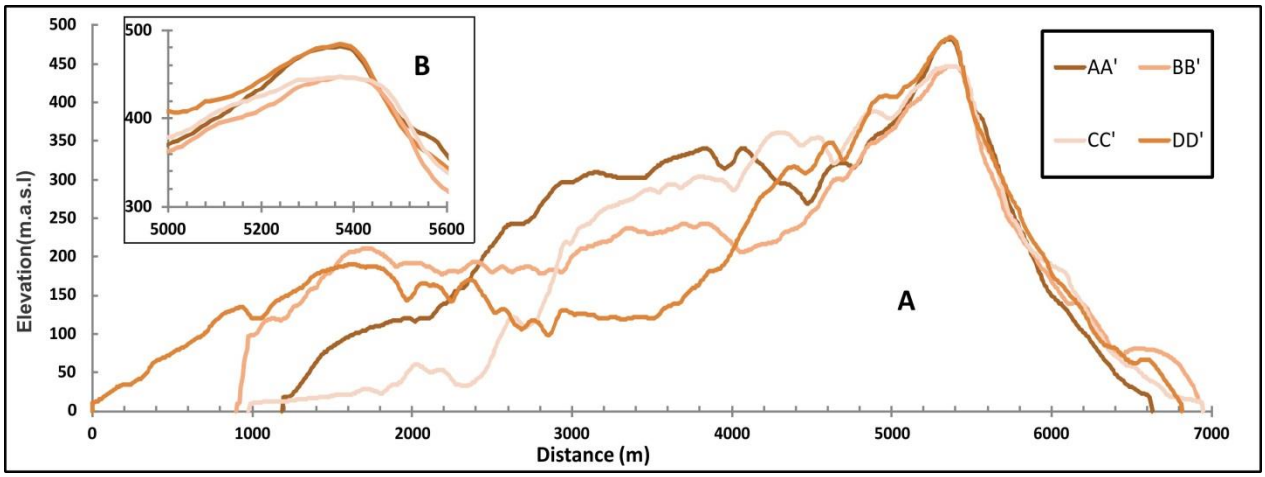


Figure S.4.1. Geometry of the hill along profiles AA'-DD' at the Hoon Hay site. (A), Full view of profiles (the vertical scale is exaggerated two times). (B), Detailed geometry of the peaks (both axis scales are the same).

## S4.3 Complete results of topographic amplification models

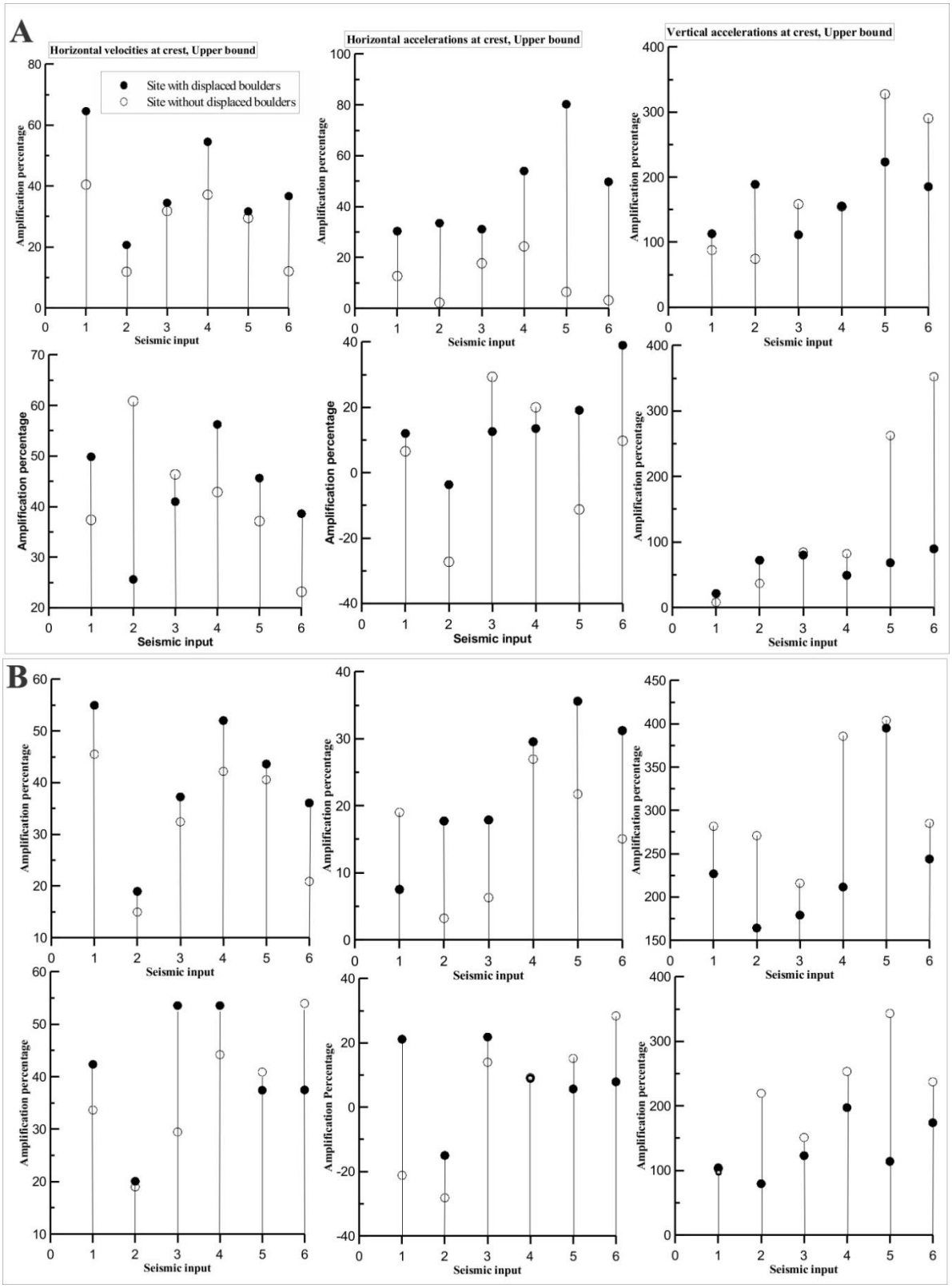

Figure S4.2. Results of four analyzed profiles (AA'-DD') have been compared on two sets of graphs (A-B). Both sets show amplification percentages of horizontal velocities, horizontal accelerations and vertical accelerations versus seismic inputs respectively. From left to right, the first three graphs of both A and B sets represent amplification percentages for upper bound rock properties and the second three graphs are their equivalents for lower boundary rock properties. Numbers 1-6 on the X axes show the different seismic inputs; 1-2: LPCC data of S80W and N10W components recorded for the Darfield earthquake, 3-4: CRLZ data of E and N components for the same earthquake, 5-6: LPCC data of similar components recorded for the Christchurch earthquake. Solid and open circles show amplification percentages for sites with and without displaced boulders.

## S4.4 Selected pictures of broken and displaced boulders and rockfalls in the Port Hills


Trimble
N